



HAL
open science

Optimisation structurale vis-à-vis de la fatigue des structures en alliages à mémoire de forme.

Xiaojun Gu

► **To cite this version:**

Xiaojun Gu. Optimisation structurale vis-à-vis de la fatigue des structures en alliages à mémoire de forme.. Mechanics of materials [physics.class-ph]. Université Paris Saclay (COmUE), 2017. English. NNT : 2017SACLY012 . tel-01617547

HAL Id: tel-01617547

<https://pastel.hal.science/tel-01617547>

Submitted on 16 Oct 2017

HAL is a multi-disciplinary open access archive for the deposit and dissemination of scientific research documents, whether they are published or not. The documents may come from teaching and research institutions in France or abroad, or from public or private research centers.

L'archive ouverte pluridisciplinaire **HAL**, est destinée au dépôt et à la diffusion de documents scientifiques de niveau recherche, publiés ou non, émanant des établissements d'enseignement et de recherche français ou étrangers, des laboratoires publics ou privés.

NNT : 2017SACLY012

THÈSE DE DOCTORAT
DE
L'UNIVERSITÉ PARIS-SACLAY
PRÉPARÉE À
L'ENSTA PARISTECH

ÉCOLE DOCTORALE N°579

Sciences mécaniques et énergétiques, matériaux et géosciences (SMEMaG)

Spécialité de doctorat : Mécanique des solides

Par

M. GU Xiaojun

Optimization of Shape Memory Alloy Structures
with Respect to Fatigue

Thèse présentée et soutenue à Palaiseau, le 25 septembre 2017

Composition du Jury :

Président: M. Andrei CONSTANTINESCU, Directeur de recherche, Ecole Polytechnique
Rapporteur: M. Günay ANLAS, Professeur, Boğaziçi University
M. Michaël PEIGNEY, Chercheur, IFSTTAR
Examineur: M. Etienne PATOOR, Professeur, Georgia Tech-Lorraine
M. ZHANG Weihong, Professeur, Northwestern Polytechnical University
Invité: M. Ky DANG VAN, Ancien Directeur de Recherche, CNRS
Co-directeur: M. Wael ZAKI, Professeur associé, Khalifa University
Directeur: M. Ziad MOUMNI, Professeur, ENSTA ParisTech

谨以此论文
献给我挚爱的父母和妻子

Acknowledgements

First of all, I would like to thank Prof. Ziad Moumni and Dr. Wael Zaki, my thesis supervisors, for your guidance and support, and valuable discussions we had during the whole work with this thesis. I am especially grateful to Dr. Wael Zaki, for his advice and assistance in keeping my progress on schedule and improving my research abilities in many ways.

I would also like to thank Prof. Zhang Weihong and Prof. Zhu Jihong, who give me constant support during my studies in Northwestern Polytechnical University. Without your guidance and encouragement, I could not have the chance to pursue my research.

I would like to thank my jury members Dr. Constantinescu, Prof. Patoor, Prof. Dang Van and reporters of the thesis Prof. Anlas and Dr. Peigney, for your time and efforts devoted to evaluate my work.

It is a pleasure to thank all the faculty and staff. The director of UME, Prof. Habibou Maitournam, thank you for your efforts to advance my work. Alain Van Herpen and Lahcène Cherfa, thanks for your help and support. And all the fellow PhD students and postdocs, Oana-Zenaida Pascan, Selçuk Hazar, Zheng Lin, Wang Jun, Quentin Pierron, Nicolas Thurieau, Yin Hao, Zhang Yahui, Zhang Shaobin. I have been fortunate to share the common moments in the lab with all of you.

Finally, I wish to thank my dear wife, Jia Nan, for your encouragement and love, and my parents-in-law. This dissertation would have been only a dream if my parents had not given me constant support and their unconditional love.

Publications

The publications associated with this PhD work are the following:

- About nonproportional loading, developed in Chapter 2:

Gu, X., Zaki, W., Morin, C., Moumni, Z., and Zhang, W. (2015). [Time integration and assessment of a model for shape memory alloys considering multiaxial nonproportional loading cases](#). *International Journal of Solids and Structures*, 54:82–99.

Gu, X., Zaki, W., Morin, C., Moumni, Z., and Zhang, W. (2014). Time integration and assessment of a model for shape memory alloys considering multiaxial nonproportional loading cases. In *Multi-physics Modeling of Solids an International Colloquium (MPMS 2014)*, Palaiseau, France.

- About LATIN method, detailed in Chapter 3:

Gu, X., Zhang, W., Zaki, W., and Moumni, Z. (2017). [Numerical simulation of pseudoelastic shape memory alloys using the large time increment method](#). *Smart Materials and Structures*, 26(4):045016.

Gu, X., Zaki, W., Moumni, Z., and Zhang, W. (2015). [Implementation of the large time increment method for the simulation of pseudoelastic shape memory alloys](#). In *ASME 2015 Conference on Smart Materials, Adaptive Structures and Intelligent Systems*. ASME.

- About cyclic loading, developed in Chapter 4:

Gu, X., Zhang, W., Zaki, W., and Moumni, Z. (2017). [An extended thermomechanically coupled 3D rate-dependent model for pseudoelastic SMAs under cyclic loading](#). *Smart Materials and Structures*, 26(9):095047.

- About high-cycle fatigue, topic in Chapter 5:

Gu, X., Moumni, Z., Zaki, W., and Zhang, W. (2016). [Shakedown based model for high-cycle fatigue of shape memory alloys](#). *Smart Materials and Structures*, 25(11):115012.

Zaki, W., **Gu, X.**, Moumni, Z., and Zhang, W. (2016). [High-cycle fatigue criterion for shape memory alloys based on shakedown theory](#). In *ASME 2016 Conference on Smart Materials, Adaptive Structures and Intelligent Systems*. ASME.

Gu, X., Moumni, Z., Zaki, W., and Zhang, W. (2016). [Shakedown based model for high cycle fatigue of shape memory alloys](#). In *European Congress on Computational Methods in Applied Sciences and Engineering*, Crete, Greece.

Abstract

This thesis presents a comprehensive and efficient structural optimization approach for shape memory alloys (SMAs) with respect to fatigue. The approach consists of three steps: First, the development of a suitable constitutive model capable of predicting, with good accuracy, the stabilized thermomechanical stress state of a SMA structure subjected to multiaxial nonproportional cyclic loading. The dependence of the saturated residual strain on temperature and loading rate is discussed. In order to overcome numerical convergence problems in situations where the phase transformation process presents little or no positive hardening, the large time increment method (LATIN) is utilized in combination with the ZM (Zaki-Moumni) model to simulate SMA structures instead of conventional incremental methods. Second, a shakedown-based fatigue criterion analogous to the Dang Van model for elastoplastic metals is derived for SMAs to predict whether a SMA structure subjected to high-cycle loading would undergo fatigue. The proposed criterion computes a fatigue factor at each material point, indicating its degree of safeness with respect to high-cycle fatigue. Third, a structural optimization approach, which can be used to improve the fatigue lifetime estimated using the proposed fatigue criterion is presented. The prospects of this work include the validation of the optimization approach with experimental data.

Keywords: shape memory alloys, high-cycle fatigue, structural optimization, nonproportional loading, thermomechanical coupling, cyclic loading, shakedown analysis.

Contents

List of Figures	xv
List of Tables	xix
Nomenclature	xxi
1 Introduction	1
1.1 Introduction and motivation	1
1.2 Overview of shape memory alloys	3
1.2.1 The martensitic transformation	3
1.2.2 Mechanical and functional properties of SMAs	4
1.2.3 Applications of shape memory alloys	6
1.3 Objectives and outline	7
2 Time integration and assessment of the ZM model in presence of nonproportional loading	9
2.1 Literature review of SMAs subjected to nonproportional loading	9
2.2 Summary of the ZM model	11
2.3 Boundary value problem and algorithmic setup	13
2.3.1 Boundary value problem	13
2.3.2 Derivation of the continuous material Jacobian	16
2.3.3 Algorithmic setup	17
2.4 Results and discussions	20
2.4.1 Simulation of proportional loading cases	20
2.4.2 Multiaxial reorientation tests	23
2.4.3 Validation of the model	26
2.5 Conclusion	35
3 Numerical simulation of pseudoelastic SMAs using the large time increment method	37
3.1 Integration of constitutive relations using LATIN	38
3.1.1 Initialization	39
3.1.2 Enforcing equilibrium	40

3.1.3	Enforcing consistency with the loading conditions	40
3.1.4	Error and stopping criteria	41
3.1.5	Algorithmic setup	41
3.2	Numerical examples and discussions	42
3.2.1	SMA element subjected to uniaxial tension	43
3.2.2	SMA element subjected to multiaxial loading cases	44
3.2.3	SMA cylinder subjected to stress-controlled nonproportional loading	46
3.2.4	SMA plate with a hole	47
3.2.5	Crimping of a SMA stent	52
3.3	Conclusion	56
4	A 3D rate-dependent model for pseudoelastic SMAs subjected to multiaxial and cyclic loading	57
4.1	Literature review on cyclic behavior of SMAs	57
4.2	The extended 3D constitutive model for pseudoelastic SMAs	58
4.3	Boundary value problem and algorithmic setup	63
4.3.1	Boundary value problem	63
4.3.2	Time-discrete formulation	64
4.3.3	Algorithmic setup	67
4.4	3D computational analysis and discussions	68
4.4.1	Thin-walled cylinder subjected to tensile loading	68
4.4.2	Strain-controlled loading	71
4.4.3	SMA tube subjected to cyclic loading	74
4.4.4	Crack tip opening in a SMA sample	77
4.5	Conclusion	79
5	Shakedown-based model for high-cycle fatigue of SMAs	81
5.1	Literature review on the fatigue of SMAs	81
5.2	Constitutive model	83
5.3	Shakedown analysis of SMAs	85
5.4	Fatigue analysis based on a multiscale approach	87
5.5	Non-smoothness of the safe domain	94
5.6	Example of SMA applications	96
5.6.1	Identification of material constants	96
5.6.2	Fatigue analysis of a SMA brick under multiaxial nonproportional loading	97
5.7	Conclusion	100
6	Shape optimization of SMA structures with respect to fatigue	101
6.1	Fatigue criterion for SMAs	102
6.1.1	Energy based low-cycle fatigue criterion for SMAs	102

6.1.2	Shakedown based high-cycle fatigue criterion for SMAs	103
6.2	Optimization methods	104
6.2.1	Boundary value problem	104
6.2.2	Shape optimization problem	105
6.2.3	Description of the optimization process and tools	106
6.3	Optimization case 1: SMA plate with a hole in the center	107
6.4	Optimization case 2: self-expanding SMA stent	109
6.4.1	FEM implementation	110
6.4.2	High-cycle fatigue analysis	114
6.4.3	Simulation results and optimization process	114
6.5	Conclusion	121
7	Conclusions	123
Appendix A	Derivation of the continuous tangent operators for Chapter 4	125
Appendix B	Mathematical derivations for Chapter 5	129
B.1	Dimensions of the elastic domain	129
B.2	Material constants	130
	Bibliography	131

List of Figures

1.1	Temperature-induced phase transformation.	3
1.2	The detwinning of martensitic SMAs with applied stress.	4
1.3	Schematic illustration of the one-way shape memory effect.	4
1.4	Schematic illustration of the assisted two-way shape memory effect.	5
1.5	Schematic illustration of pseudoelasticity.	6
2.1	Stress-controlled proportional loading cases.	20
2.2	Simulated stress-strain behavior for pure tension and pure shear loading.	21
2.3	Simulated response for loading path 3.	22
2.4	Simulated response for loading path 4.	22
2.5	Experimental setup used in Bouvet et al. (2004)	22
2.6	Stress-strain behavior in the axial and hoop directions due to loading in Fig. 2.5b	23
2.7	Simulation of martensite reorientation under multiaxial loading.	24
2.8	Biaxial non-proportional loading.	25
2.9	Evolution of the martensite volume fraction and orientation strain.	25
2.10	Numerical prediction of stress and strain behavior and comparison with numerical simulation results from (Stebner and Brinson, 2013).	27
2.11	Evolution of the von Mises equivalent stress and martensite volume fraction with loading time.	27
2.12	Comparison of experimental and simulation results for the butterfly loading in Fig. 2.12a	29
2.13	Tensile and shear stress-strain curves used to determine the parameters of the ZM model.	30
2.14	Experimental versus simulation results for the square tension-shear loading in Fig. 2.14a	31
2.15	Experimental versus simulation results for the loading shown in Fig. 2.15a	32
2.16	Sample used in Bouvet et al. (2002)	33
2.17	Stress variation in the radial direction for the cylinder used for numerical simulations.	34
2.18	Simulation of the experimental data of Bouvet et al. (2002)	34
3.1	Graphic illustration of the algorithmic integration procedure. (A) and (CL) respectively denote admissible and consistent solutions.	38
3.2	Simulation of uniaxial stress-strain behavior using LATIN.	43

3.3	Three stress-controlled proportional loading cases.	44
3.4	Simulated stress-strain behavior in pure tension (loading path 1).	45
3.5	Simulated stress-strain behavior in pure shear (loading path 2).	45
3.6	Simulated stress-strain behavior and shear versus axial strain for mixed tensile-shear loading (loading path 3).	45
3.7	Strain behaviors. For comparison, the results obtained using the incremental method are from Chapter 2, the experimental data is from Bouvet et al. (2002).	46
3.8	Axial stress vs. strain. For comparison, the results obtained using the incremental method are from Chapter 2, the experimental data is from Bouvet et al. (2002).	47
3.9	Hoop stress vs. strain. For comparison, the results obtained using the incremental method are from Chapter 2, the experimental data is from Bouvet et al. (2002).	47
3.10	Geometry of the plate and loading conditions.	48
3.11	The convergence curve of the residual \mathcal{R} (blue) and the change of maximum stress difference $\bar{\mathcal{R}}$ (red) in the model of SMA plate using the material parameters in Table 2.1.	48
3.12	Comparison of von Mises stress distribution computed using LATIN (left) and the step-by-step integration algorithm (right) at time step 0.5.	49
3.13	Comparison of von Mises stress distribution computed using LATIN (left) and the step-by-step integration algorithm (right) at time step 0.75.	49
3.14	Comparison of von Mises stress distribution computed using LATIN (left) and the step-by-step integration algorithm (right) at time step 1.0.	50
3.15	The convergence curve of the residual \mathcal{R} (blue) and the change of maximum stress difference $\bar{\mathcal{R}}$ (red) in the model of SMA plate using the material parameters in Table 3.1.	50
3.16	The distributions of von Mises stress at time step 0.5 (left), 0.75 (middle) and 1.0 (right).	51
3.17	The distributions of maximum principle strain at time step 0.5 (left), 0.75 (middle) and 1.0 (right).	51
3.18	The distributions of martensite volume fraction at time step 0.5 (left), 0.75 (middle) and 1.0 (right).	52
3.19	Geometry of the stent cell used for simulation using the repeated unit cell (RUC) method.	53
3.20	The convergence curve of the residual \mathcal{R} (blue) and the change of maximum stress difference $\bar{\mathcal{R}}$ (red) in the model of SMA stent using the material parameters in Table 3.1.	54
3.21	The pressure versus current radius response of the stent during the compression and release process.	54
3.22	Distribution of stress in the stent cell.	55
3.23	Distribution of the martensite volume fraction in the stent cell.	55
4.1	Mechanical and thermal boundary conditions for the SMA cylinder.	68
4.2	Comparison of isothermal uniaxial stress–strain responses with the experimental and simulation data from from Andani and Elahinia (2014) at different temperatures.	69

4.3	Comparison of simulations using the proposed model against reference experimental and simulation data taken from Andani and Elahinia (2014)	70
4.4	Stress-strain response comparison of simulated results against reference experimental data taken from Dunić et al. (2014) at strain rate of: (a) 10^{-1} s^{-1} , (b) 10^{-2} s^{-1} and (c) 10^{-3} s^{-1}	71
4.5	Strain-temperature response comparison of simulated results against reference experimental data taken from Dunić et al. (2014) at strain rate of: (a) 10^{-1} s^{-1} , (b) 10^{-2} s^{-1} and (c) 10^{-3} s^{-1}	72
4.6	Stress-strain response comparison of simulated results against reference experimental data taken from Grabe and Bruhns (2008) at strain rate of: (a) 10^{-3} s^{-1} , (b) 10^{-4} s^{-1} and (c) 10^{-5} s^{-1}	72
4.7	Strain-temperature response comparison of simulated results against reference experimental data taken from Grabe and Bruhns (2008) at strain rate of: (a) 10^{-3} s^{-1} , (b) 10^{-4} s^{-1} and (c) 10^{-5} s^{-1}	73
4.8	Multiaxial nonproportional loading cases under different loading rates.	74
4.9	Temperature variation with respect to tensile and shear strain.	74
4.10	Simulated material behavior at different temperatures under cyclic loading.	76
4.11	Comparison of the stress-strain curves obtained at different strain rates.	77
4.12	Simulation of crack opening under cyclic loading.	77
4.13	Simulated results of crack opening under cyclic loading: (a) transformation zone near the tip; (b) stress distribution near the tip.	78
4.14	Simulated results of crack opening under cyclic loading: (a) residual strain near the tip; (b) residual stress near the tip.	79
5.1	Possible responses of SMAs under varying loads.	86
5.2	Multiscale representation of SMA volume elements.	88
5.3	Projections parallel and normal to the orientation strain.	90
5.4	Admissible stress domains.	91
5.5	Elastic domain containing the loading path.	92
5.6	The cases when the factor $G(x)$ changes to different values.	93
5.7	Elastic domain.	94
5.8	Fatigue tests for different mean stress/strain values (Tabanlı et al., 1999).	95
5.9	Fatigue tests with fixed nominal strain amplitude (Zheng et al., 2016).	96
5.10	Influence of temperature on the radius of the elastic domain for $z = 0$	96
5.11	Uniaxial fatigue experiments needed for the determination of the material constants α_{-1} , β_0 , γ_{-1} and β'_{-1}	97
5.12	Two loading path: (a) the rhombic type and (b) the square type.	98
5.13	Uniaxial stress-strain response of the material.	98
5.14	Responses to the rhombic and square loading cases in Fig. 5.12.	99

5.15	Fatigue factor $G(\mathbf{x})$ for different loading paths.	100
6.1	Evolution of the hysteresis area with the number of cycles.	102
6.2	Energy based low-cycle fatigue criterion from Morin (2011)	103
6.3	Design nodes update strategy.	106
6.4	Optimization process.	107
6.5	The convergence history of the objective function (blue) and the constraint (red).	108
6.6	Comparison of the low-cycle fatigue factor distribution before and after optimization.	109
6.7	Comparison of the stress distribution at step time 0.5 before and after optimization.	109
6.8	Comparison of the martensite volume fraction distribution at step time 0.5 before and after optimization.	109
6.9	Stent and artery modeling.	111
6.10	Material parameters of Nitinol used for manufacturing stent.	112
6.11	Stress-strain curve at different temperatures.	113
6.12	Simulated martensite volume fraction for the original stent design under: (a) fully crimped loading; (b) systolic pressure; (c) diastolic pressure.	115
6.13	Simulated results for the original stent design: (a) stress distribution fully crimped; (b) stress distribution under systolic pressure; (c) stress distribution under diastolic pressure; (d) high-cycle fatigue factor distribution.	115
6.14	The single strut reduced stent model considered for the optimization problem.	116
6.15	The convergence history of the objective function (blue) and the constraint (red).	117
6.16	Evolution of the high-cycle fatigue factor in iterations 1 to 8, corresponding to Figs. (a) to (h).	117
6.17	Evolution of the von Mises stress in the stent under systolic pressure in iterations 1 to 8, corresponding to Figs. (a) to (h).	118
6.18	Evolution of the von Mises stress in the stent under diastolic pressure in iterations 1 to 8, corresponding to Figs. (a) to (h).	118
6.19	Evolution of the maximum martensite volume fraction in the stent in iterations 1 to 8, corresponding to Figs. (a) to (h).	119
6.20	Geometric comparison of the original and new stent designs.	119
6.21	Simulated martensite volume fraction of the new stent design under: (a) fully crimped loading; (b) systolic pressure; (c) diastolic pressure.	120
6.22	Simulated results of the new stent design: (a) stress distribution fully crimped; (b) stress distribution under systolic pressure; (c) stress distribution under diastolic pressure; (d) high-cycle fatigue factor distribution.	120

List of Tables

2.1	Material parameters used for the finite element simulations in Section 2.4.1.	21
2.2	Material parameters obtained using data form Bouvet et al. (2004)	23
2.3	Material parameters used for simulating SMA behavior in presence of nonproportional loading following Stebner and Brinson (2013)	26
2.4	Material parameters used for the simulations following Grabe and Bruhns (2009)	28
2.5	Material parameters used for the simulation of nonproportional loading of SMAs following Sittner et al. (1995)	30
2.6	Material parameters used for simulating the experimental data in Sittner et al. (1995) for the loading case in Fig. 2.15a.	32
3.1	Material parameters used for finite element analysis of the SMA element subjected to uniaxial tension.	43
4.1	Material parameters calibrated using the experimental data in Fig. 4.2.	69
4.2	Material parameters calibrated using the experimental data in Fig. 4.3a from Andani and Elahinia (2014)	70
4.3	Material parameters calibrated using the experimental data from Dunić et al. (2014)	72
4.4	Material parameters calibrated using the experimental data in Figure 4.6 from Grabe and Bruhns (2008)	73
4.5	Material parameters calibrated using experimental data from Yu et al. (2014)	75
5.1	Material parameters used for simulating SMA brick.	98
6.1	Material parameters used for finite element simulations.	112

Nomenclature

Roman Symbols

a, b, G, Y	material parameters of the ZM model
A_f^0	austenitic finish temperature at zero stress
A_s^0	austenitic start temperature at zero stress
$\bar{a}, \bar{b}, \bar{c}, \bar{b}'$	material constants in the high-cycle fatigue criterion
\mathcal{A}_α	thermodynamic force associated associated to the dissipative variable α
a, m, p	material constants in low-cycle fatigue criterion
A_f^σ	austenitic finish temperature under stress σ
A_s^σ	austenitic start temperature under stress σ
B	internal stress
C_p	specific heat capacity
\mathcal{D}	pseudopotential of dissipation
E	macroscopic strain tensor
q	heat influx vector
e	internal energy
r	external heat source
E_A	Young's modulus of austenite
E_M	Young's modulus of martensite
El_{MA}	$(1 + \nu)(1/E_M - 1/E_A)$
E_{ori}	macroscopic martensite orientation strain tensor

\mathbf{f}	body forces
$f_{\text{high}}(\mathbf{x})$	high-cycle fatigue factor at material point \mathbf{x}
$f_{\text{low}}(\mathbf{x})$	low-cycle fatigue factor at material point \mathbf{x}
\mathcal{F}_z^1	forward phase transformation yield function
\mathcal{F}_z^2	reverse phase transformation yield function
\mathcal{F}_{ori}	orientation yield function
$G(\mathbf{x})$	high-cycle fatigue factor at material point \mathbf{x}
$g(\mathbf{X})$	inequality constraint for design variables \mathbf{X}
h	heat transfer coefficient
$h(\mathbf{X})$	equality constraint for design variables \mathbf{X}
\mathcal{J}	continuous material Jacobian
J	number of integration points in a SMA model
$\mathcal{J}_{\sigma\varepsilon}$	tangent stiffness tensor with respect to the increment of stress
$\mathcal{J}_{Q\varepsilon}$	tangent stiffness tensor with respect to the increment of internal heat generation
$\mathcal{J}_{\sigma\theta}$	tangent thermal modulus tensor with respect to the increment of stress
$\mathcal{J}_{Q\theta}$	tangent thermal modulus with respect to the increment of internal heat generation
\mathbf{K}	equivalent elastic stiffness tensor
k	thermal conductivity
\mathbf{K}_A	austenite elastic stiffness tensor
\mathbf{K}_M	martensite elastic stiffness tensor
\mathbb{K}_q	heat transfer and convection boundary condition
\mathbb{K}_σ	static admissibility
\mathbb{K}_θ	specified temperature boundary condition
\mathbb{K}_u	kinematic admissibility
\mathbf{L}	macroscopic elastic stiffness tensor

\mathbf{l}	mesoscopic elastic stiffness tensor
\mathcal{L}	Lagrangian
M_f^0	martensitic finish temperature at zero stress
M_s^0	martensitic start temperature at zero stress
M_f^σ	martensitic finish temperature under stress σ
M_s^σ	martensitic start temperature under stress σ
\mathbf{n}	outward unit vector normal to the boundary
P	hydrostatic pressure
P_{MA}	$\nu/E_A - \nu/E_M$
\mathbb{P}_{ori}	axis of the hypercylinder of the elastic region
\mathbb{P}_z	central hyperplane of the elastic region
Q	inner heat generation
Q_{el}	thermoelastic heat generation
Q_{in}	intrinsic dissipation
Q_{latent}	latent heat
\mathcal{R}	residual
\mathbb{R}^3	three-dimensional Euclidean space
$\bar{\mathcal{R}}$	maximum von Mises difference throughout a model
\mathbf{S}	macroscopic stress deviator tensor
\mathbf{s}	stress deviator
s	entropy
\mathcal{S}_n	boundary value problem solution at increment n
t, T	time
\mathbf{T}^d	contact forces
tol_1, tol_2, tol_3	numerical tolerances

\mathbf{u}	displacement vector
\mathbf{u}^d	prescribed displacement on volume Ω
u_ρ, u_ϕ, u_z	displacements in cylindrical coordinates
V	volume of a SMA structure
\bar{V}	volume of the original design
$W_d(\mathbf{x})$	hysteresis area of the stabilized cycle at material point \mathbf{x}
\mathbf{X}	design variables
\mathbf{x}	point in volume Ω
Z	macroscopic martensite volume fraction
z	martensite volume fraction
z_e	cumulative martensite fraction

Greek Symbols

$\alpha, \beta, \kappa, \xi, \tau$	material parameters of the ZM model
α_{-1}	fully reversed bending fatigue limit ($\theta > A_f$)
α	equivalent thermal expansion coefficient tensor
α_A	thermal expansion coefficient tensor for austenite
α_M	thermal expansion coefficient tensor for martensite
β_0	repeated torsion fatigue limit ($\theta = A_f$)
β'_{-1}	alternate torsion fatigue limit ($\theta > A_f$)
ε_0	maximum orientation strain
ε_{eq}^{ori}	equivalent orientation strain
ε^{ori}	martensite orientation strain tensor
ε	total strain tensor
ε_r	residual strain tensor
η	inelastic multiplier for martensite reorientation

Γ	total boundary of volume Ω
γ_{-1}	alternate torsion fatigue limit ($\theta < M_f$)
Γ_d	design boundary
Γ_h	convection boundary
Γ_T	boundary for contact force
Γ_θ	specified temperature boundary
Γ_u	boundary for displacement
γ	maximum inelastic strain
ν	Poisson's ratio
ν_1, ν_2	Lagrange multipliers
Ω	a volume in three-dimensional Euclidean space
Ω_d	design space
$\phi(t)$	loading path
ϕ, ν	material parameters related to saturated residual strain
Ψ	Helmholtz free energy density
Ψ_A	free energy densities of austenite
Ψ_M	free energy densities of martensite
Ψ_I	free energy density contributed by austenite-martensite interaction
Ψ_θ	free energy density related to temperature
ρ	density
ρ	mesoscopic residual stress tensor
ρ, ϕ, z	three directions in cylindrical coordinates
Σ	macroscopic stress tensor
σ	stress tensor
σ_{af}	completion stress for reverse transformation into austenite

σ_{as}	initiation stress for reverse transformation into austenite
σ_{mf}	completion stress for forward transformation into martensite
σ_{ms}	initiation stress for forward transformation into martensite
σ_{rf}	stress for completion of martensitic reorientation
σ_{rs}	stress for initiation of martensitic reorientation
θ	temperature
θ^d	temperature applied on boundary Γ_θ
θ_r	reference temperature

Superscripts

(0)	value prior to loading
(sat)	saturated value
el	elastic
k	iteration
*	time-independent value

Subscripts

n	load increment
o	projection normal to the orientation strain
p	projection parallel to the orientation strain
VM	von Mises equivalent norm

Acronyms / Abbreviations

3D	three-dimensional
A	austenitic phase
DCM	direct cyclic method
DOE	design of experiments
FDA	Food and Drug Administration

FEM	finite element method
LATIN	large time increment
M	martensitic phase
OWSME	one-way shape memory effect
REV	representative elementary volume
RUC	repeated unit cell
SMA	shape memory alloy
SMA _s	shape memory alloys
SME	shape memory effect
TWSME	two-way shape memory effect
UMAT	user material
ZM	Zaki-Moumni

Chapter 1

Introduction

1.1 Introduction and motivation

Shape memory alloys (SMAs) are a group of metallic materials exhibiting unique characteristics and, accordingly, drawing the interest of scientific communities and of industries. These alloys are known for their ability to undergo extensive inelastic deformation that can be recovered by heating. The underlying physical mechanism for this ability is a solid–solid phase transformation known as the martensitic transformation. It is responsible for several unusual behaviors observed in SMAs that have promoted their use in a wide range of engineering applications, such as aerospace industry, biomedical field and transportation industry.

In many of these applications, shape memory alloy (SMA) structures are used in situations involving cyclic load variations, for which the possibility of failure by fatigue is an important design consideration. In this respect, two types of fatigue are generally distinguished: functional fatigue, which characterizes a functional degradation in SMAs such as the decrease in maximum recoverable deformation or the modification of transformation temperatures, and structural fatigue, which refers to the degradation of mechanical SMA properties by means of nucleation and propagation of defects that can potentially lead to ultimate failure.

Structural fatigue, in particular, is usually classified in terms of the number of cycles to failure as either low- or high-cycle. The achievable fatigue life is influenced by many factors, including material composition, loading history, surface condition, thermomechanical processing, as well as size effects at smaller length scales (Siredey-Schwaller et al., 2009; He and Sun, 2010). The ultimate number of cycles typically ranges from 10^4 cycles in temperature-controlled cyclic one-way shape memory applications (Hornbogen, 2004) to a nominal 4×10^8 cycles for pseudoelastic endovascular stents (ASTM F2477-07, 2013). In particular, high-cycle fatigue can take place at load levels well below common physical thresholds, for which the material is seemingly elastic with no observable dissipative processes at the macroscopic scale.

Fatigue of SMAs deals with high-cycle fatigue, as we are mainly interested in fatigue occurring in the pseudoelastic domain. A typical example of SMA devices expected to withstand a high number of

loading cycles is the SMA stent. According to US Food and Drug Administration (FDA) guidelines, endovascular stents are required to withstand the equivalent of 400 million cycles of pulsatile blood pressure, or an equivalent of 10 years in the human body (ASTM F2477-07, 2013). Fatigue analysis in this case is particularly important for proper design of the stent. High-cycle fatigue in SMAs remains poorly understood and virtually unaccounted for by current fatigue models. This is especially true for SMAs subjected to nonproportional loading, which may undergo simultaneous phase transformation and martensite reorientation. Moreover, the studies for design optimization methods with respect to fatigue of SMAs remain scattered.

This thesis aims to fill this gap by proposing an efficient approach for fatigue design and optimization of SMA structures. To this end, a precise constitutive law, reproducing all main effects displayed by the SMAs, is required for determining the thermomechanical asymptotic state of the material with good accuracy. Indeed, it is well known that for many types of metallic structures, the fatigue lifetime is investigated using the stabilized thermomechanical state as an input to a fatigue criterion. A multiaxial high-cycle fatigue criterion should then be defined and validated for three-dimensional (3D) structures, and should account for all the observed thermomechanical effects of SMAs, which cannot be captured using a conventional Wöhler curve approach. Finally, structural optimization approach, capable of accounting for the predefined fatigue criterion to improve the fatigue performance of SMA structures should be developed.

In the present work, a fatigue design and optimization procedure is proposed and implemented in three steps:

The first step is devoted to the computing the stabilized stress state under cyclic loading. It involves proposing a constitutive model accounting for key SMA effects and capable of predicting the stabilized stress state of a SMA structure. This is accomplished by extending the Zaki-Moumni (ZM) model (Zaki and Moumni, 2007a,b) to account for nonproportional loading and rate-dependent residual strain under cyclic loading. Moreover, a numerical procedure using the large time increment (LATIN) method (Boisse et al., 1990) is developed to solve numerical convergence problems in situations where the phase transformation process presents little or lack of hardening.

The second step concerns the prediction of the fatigue lifetime of the structure using the thermomechanical stabilized stress state computed in the first step. To this end, a shakedown based high-cycle fatigue criterion for shape memory alloys is developed. Using a multiscale approach, a shakedown based high-cycle fatigue criterion analogous to the Dang Van model (Dang Van, 1973) for elastoplastic metals is derived for SMAs obeying the ZM model. The proposed criterion computes a fatigue factor at each material point, indicating its degree of safeness with respect to high cycle fatigue.

The third step deals with the development of an efficient structural optimization approach to improve fatigue behavior. Both high-cycle fatigue computed in step two and energy-based low-cycle fatigue developed by Moumni et al. (2005); Morin (2011) are considered.

The next section is devoted to a brief description of the unique behaviors and the applications of SMAs. A literature review is then given, following the outline of the dissertation.

1.2 Overview of shape memory alloys

Shape memory alloys (SMAs) are a group of metallic materials capable of sustaining severe inelastic deformation that can be recovered by heating (Otsuka and Wayman, 1999). This behavior is explained by the ability of SMAs to undergo transformation between a higher symmetry austenite phase and a lower symmetry martensite phase. The martensite phase can be inelastically deformed by detwinning and reorientation of variants characterized by different crystallographic orientations (Funakubo, 1987). Starting from the 1970's, the use of SMAs in engineering applications has seen significant development (Van Humbeeck, 1999) and it now spans a number of important fields ranging from biomedicine to civil engineering and aeronautics (Duerig et al., 1999).

1.2.1 The martensitic transformation

The origin of the unique properties of SMAs is in their crystalline structure, which can undergo martensitic transformation. This martensitic transformation is a first-order diffusionless solid-to-solid phase change, from its high crystallographic symmetry, usually cubic austenitic phase (A) to a low symmetry martensitic phase (M), shown in Fig. 1.1. The low symmetry martensite enables the existence of several martensite variants defined by the orientation of their habit plane (Otsuka and Wayman, 1999; Morin, 2011). The existence of a martensitic variant depends on the thermomechanical state. In the absence of applied stress, the variants of martensite usually arrange themselves in a self-accommodating manner through twinning (self-accommodating martensite), resulting in no observable macroscopic strain. As shown in Fig. 1.2, by applying mechanical loading the martensitic variants are forced to reorient (detwin) into a single variant (detwinned martensite), leading to the presence of large macroscopic inelastic strain. Uniaxial or multiaxial loading of shape memory alloys can induce phase

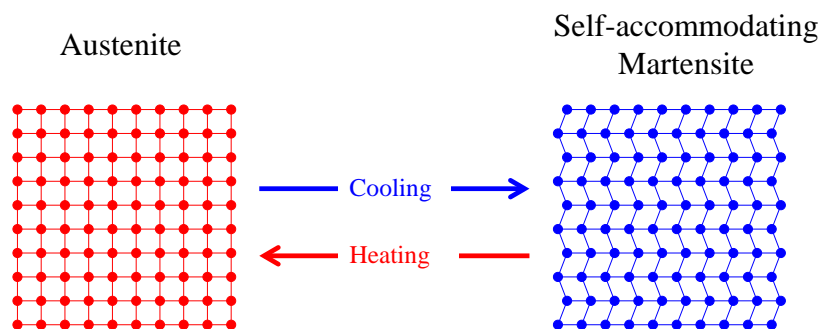


Figure 1.1 Temperature-induced phase transformation.

transformation accompanied by the nucleation or shrinking of martensite variants (Bodaghi et al., 2013). When the loading direction changes, preferred martensite variants begin to form at the expense of others leading to a change in orientation of the inelastic strain in the martensitic phase. Both phase change and martensite reorientation can take place at the same time in presence of multiaxial nonproportional loading.

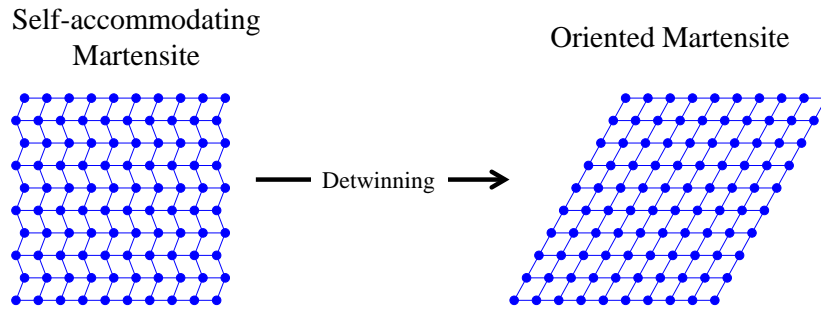


Figure 1.2 The detwinning of martensitic SMAs with applied stress.

1.2.2 Mechanical and functional properties of SMAs

Shape memory alloys are known for their ability to undergo extensive inelastic deformation that can be recovered by heating. Among the unique functional properties of SMAs are the shape memory effect (SME) and pseudoelasticity. Two different kinds of shape memory effect are commonly distinguished, namely one-way shape memory effect (OWSME) and two-way shape memory effect (TWSME).

One-way shape memory effect

A shape memory alloy is able to remember its original configuration, after it has been deformed, by heating the material above characteristic transition temperatures. The unique effect is known as one-way shape memory effect. The material response is shown in Fig. 1.3. When an austenitic SMA is cooled down to a self-accommodating Martensite state without macroscopic strain (temperature below M_f^0 , path 1 \rightarrow 2 in Figs. 1.3a and 1.3b). A deformation is then applied (path 2 \rightarrow 3), the martensite gets detwinned and undergo extensive inelastic deformation, which remain after unloading. Upon heating above a temperature A_f^0 (path 3 \rightarrow 4), the material shape recover to its original.

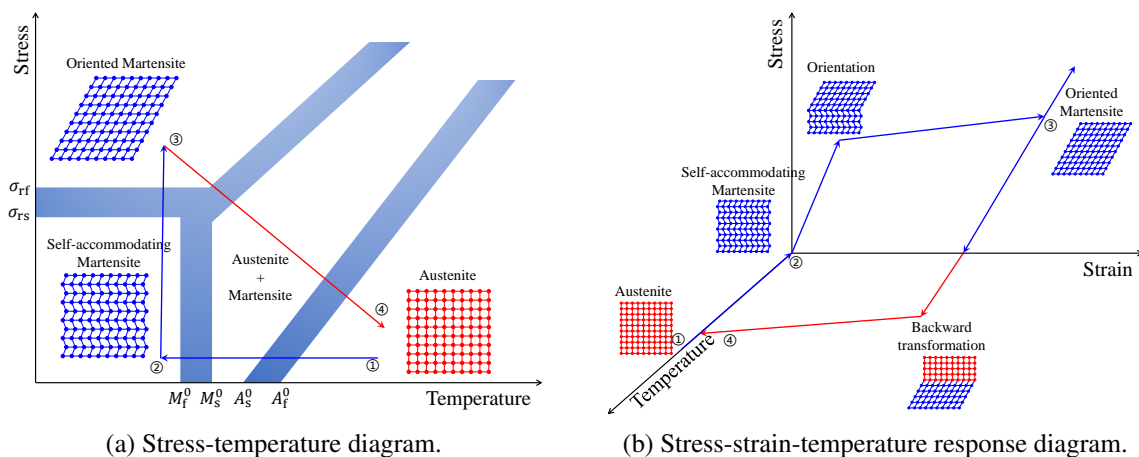


Figure 1.3 Schematic illustration of the one-way shape memory effect.

Two-way shape memory effect

The mechanism of one-way shape memory effect is described above, only the configuration of the austenitic phase is remembered. However, it is possible to remember the shape of the martensitic phase under certain conditions. A material that shows a shape memory effect during both heating and cooling is said to have two-way shape memory effect. Contrary to the previous effect, it is not an intrinsic property to Shape Memory Alloys, it can be exhibited after specific thermomechanical treatment known as “training”. When the material is trained, cooling the material to induce transformation to a martensitic phase in the absence of external stress produces inelastic strain because of the internal stress existing inside the material, which is introduced by training. The other type of two-way shape memory alloys is associated with temperature induced transformation above constant stress corresponding to complete martensite variants orientation σ_{rf} , namely assisted two-way shape memory effect (shown in Fig. 1.4). Under an applied uniaxial stress σ , the new transformation temperatures are represented as M_s^σ , M_f^σ , A_s^σ and A_f^σ for martensite start, martensite finish, austenite start and austenite finish temperatures, respectively.

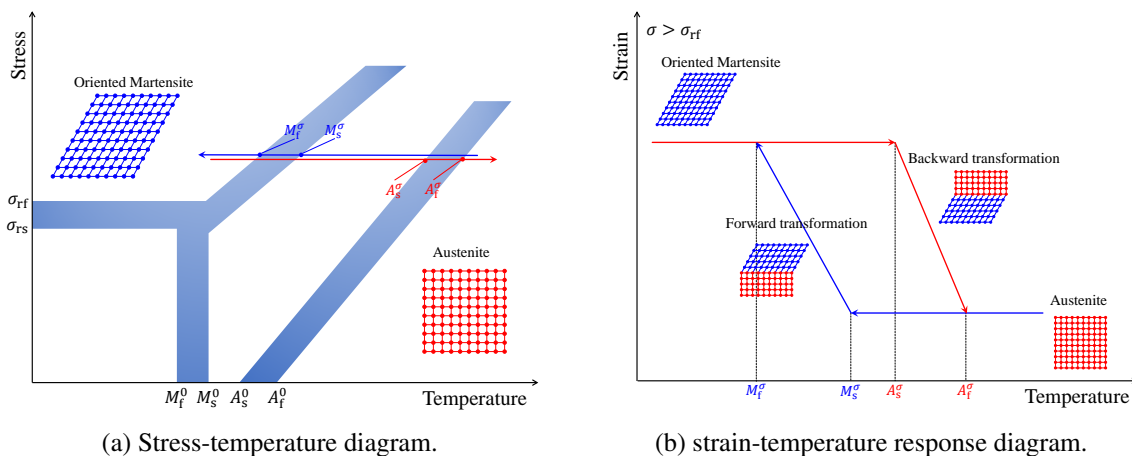


Figure 1.4 Schematic illustration of the assisted two-way shape memory effect.

Pseudoelasticity

In addition to thermally induced phase transformation, transformation can also be induced by applying mechanical loading to the material in the austenitic phase. The result is fully oriented martensite created from austenite. This material behavior is called pseudoelasticity, which refers to the ability of these materials to deform substantially when subjected to mechanical loading and to recover their undeformed shape completely once the load is removed if the temperature of the material is above A_f^0 . The stress-temperature response and stress-strain are schematically represented on Figs. 1.5a and 1.5b, respectively. The transformation stresses are represented as σ_{ms} , σ_{mf} , σ_{as} , and σ_{af} for martensitic yield start, martensitic yield finish, austenitic yield start and austenitic yield finish stresses, respectively. During a pseudoelastic transformation, a considerable amount of heat can be generated and absorbed

due to phase change, which can result in temperature variations that readily impact the behavior of the SMA, a manifestation of thermomechanical coupling effects.

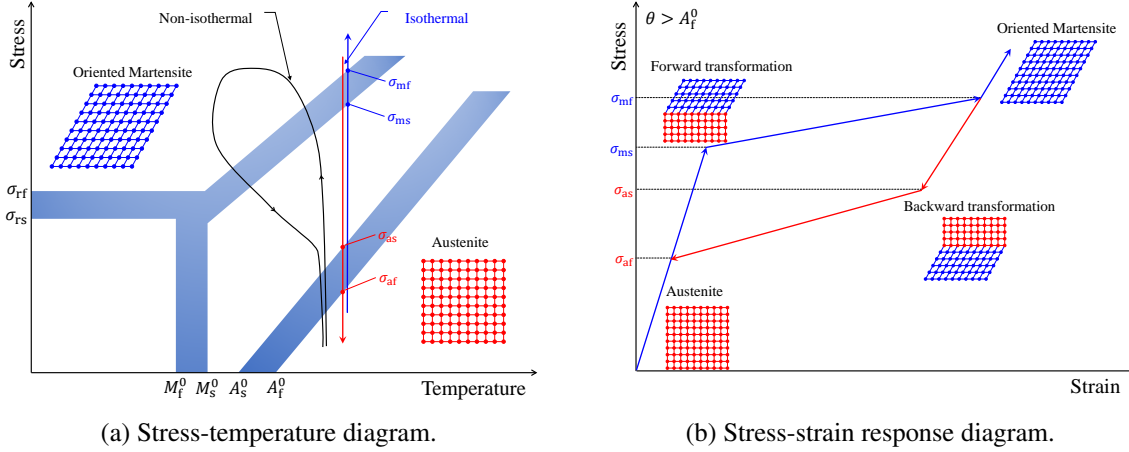


Figure 1.5 Schematic illustration of pseudoelasticity.

1.2.3 Applications of shape memory alloys

Although iron-based and copper-based SMAs, such as Fe-Mn-Si, Cu-Zn-Al and Cu-Al-Ni, are low-cost and easy to machine, due to their poor stability in cyclic applications and poor thermomechanical response (Huang, 2002), NiTi-based SMAs are the most widely used on a commercial scale. Generally, SMA applications can be divided into two categories according to their primary function of their material, where the shape memory effect can be used to generate motion and/or force, and pseudoelasticity can be store the deformation energy (Jani et al., 2014). The unique behaviors of SMAs have motivated increased usage of these materials in engineering applications, namely:

- In aerospace industry, SMAs are used as active and adaptive structures with morphing capability and system-level optimization under various flight conditions (Jani et al., 2014). Boeing developed an active serrated aerodynamic device with SMA actuators, which is known as a variable geometry chevron and has been installed on a GE90–115B jet engine for Boeing 777–300 ER commercial aircraft. This device has proven to be very effective in reducing noise during take-off by maximizing the chevron deflection, and also increasing the cruise efficiency by minimizing the chevron deflection during cruise phase (Hartl et al., 2009a,b). Several other SMA applications for aerospace are the shape morphing wing (Sofla et al., 2010), retractable landing gear (Kutlucinar, 2005), telescopic wing system (Knowles and Bird, 2004) and so on.
- In the biomedical field, devices such as stents take advantage of the pseudoelasticity and biocompatibility of NiTi SMAs, which capable to recover large strains elastically allows for self-expandable structures to be compressed down to very small sizes and deployed into an obstructed passage. Moreover, SMA stents are much more compliant to bends in the vessel and contours in the lumen,

whereas stainless steel stents tend to force blood vessel straight (Jani et al., 2014). Besides, SMAs are used for manufacturing orthodontic braces (Andreasen and Hilleman, 1971), eyeglass frames (Zider and Krumme, 1990), artificial myocardium (Shiraishi et al., 2007) and so on.

- In transportation industry, a SMA actuation system is incorporated in the Shinkansen Nozomi-500 and 700 series bullet train gearbox where the temperature in the gearbox is monitored and a SMA spring opens/closes the two-way valve unit of Automatic oil valve adjusting equipment for gearbox according to oil temperature, the volume of oil flow lubricating the pinion gears is optimized (Otsuka and Kakeshita, 2002). Many other SMA applications that have been developed for the automotive industry can be found in Jani et al. (2014).

1.3 Objectives and outline

A good understanding of fatigue in SMAs is important to improve the safety of the SMA materials in industrial applications as SMAs usually operate under cyclic loading. Designing and optimizing structures against fatigue requires precise prediction of the thermomechanical stabilized stress state as well as a reliable fatigue criterion. The aim of this work is to develop an efficient approach for design and optimize SMA structures with respect to fatigue. The approach is split into three major steps:

- the development of a suitable constitutive law, that can predict with good accuracy the cyclic thermomechanical response of SMAs,
- the development of a fatigue criterion to predict whether a SMA structure submitted to high-cycle loading would undergo or not fatigue,
- the study of a structural optimization approach, which can be used to improve the fatigue lifetime measured by the predefined fatigue criterion.

The dissertation is organized as following:

Chapter 2 is devoted to time integration and assessment of the ZM model for shape memory alloys under multiaxial nonproportional loading. Detailed derivation of the time-discrete implicit integration algorithm is provided, including an explicit closed-form expression for the continuous material Jacobian. The algorithm is used for finite element simulations using Abaqus, in which the model is implemented by means of a user material subroutine. Extensive validation of the model is provided against multiple sets of experimental and numerical simulation data taken from the literature.

Chapter 3 introduces a numerical approach to solve numerical convergence problems, in situations where the phase transformation process presents little or lack of hardening, using LATIN method. In contrast to the conventional incremental method, the LATIN method solves the global equilibrium and local consistency conditions sequentially for the entire loading path. The achieved solution must satisfy the conditions of static and kinematic admissibility and consistency simultaneously after several iterations. 3D numerical implementation is accomplished using an implicit algorithm and is then used

for finite element simulation using the software Abaqus. Computational tests demonstrate the ability of this approach to simulate SMAs presenting flat phase transformation plateaus and subjected to complex loading cases, such as the quasi-static behavior of a stent structure. Some numerical results are contrasted to those obtained using step-by-step incremental integration.

Chapter 4 proposes an extended thermomechanically coupled 3D rate-dependent model for pseudoelastic SMAs under cyclic loading, including the influence of load rate and temperature on both the rate and value at saturation of residual strain. The derivation of the model follows a procedure similar to the one used in (Gu et al., 2015). In the proposed model, a new evolution rule is introduced for residual strain, which takes into account thermomechanical coupling. The influence of thermal expansion is also introduced for the first time into the ZM model. Finite element implementation of the new model is provided, with detailed implicit time-discrete formulation of the constitutive equations in a 3D setting and closed-form formulation of the continuous tangent stiffness and thermal moduli. The time-integration procedure is programmed into the software Abaqus by means of a user material (UMAT) subroutine and several simulation cases are presented and discussed.

Chapter 5 presents a high-cycle fatigue criterion for SMAs based on shakedown analysis. The analysis accounts for phase transformation as well as reorientation of martensite variants as possible sources of fatigue damage. In the case of high-cycle fatigue, once the structure has reached an asymptotic state, damage is assumed to become confined at the mesoscopic scale, or the scale of the grain, with no discernable inelasticity at the macroscopic scale. The proposed criterion can be used to predict whether a SMA structure submitted to high cycle loading would undergo or not fatigue. To this end, the model permits to compute a fatigue factor in each material point indicating its degree of safeness with respect to high cycle fatigue. Hence, the proposed criterion can localize the critical points with respect to fatigue, and be used to design SMA structures against high-cycle fatigue.

Chapter 6 deals with structural optimization of SMA structures with respect of fatigue. Both low- and high-cycle fatigue is considered. The proposed approach is used to optimize two 3D SMA structures, significant fatigue safety improvement is obtained with new designed configurations.

General conclusions and outlook are finally provided in Chapter 7, including a summary and review of the presented approach, as well as some prospects.

Chapter 2

Time integration and assessment of the ZM model in presence of nonproportional loading

Fatigue analysis of SMAs requires the computation of the stabilized response of a structure subject to nonproportional and cyclic thermomechanical loading. The ZM model is selected as the analytical model to reproduce the actual behavior of a SMA structure. This chapter presents a numerical implementation of the ZM model for SMAs (Zaki and Mounni, 2007a) that fully accounts for nonproportional loading and its influence on martensite reorientation and phase transformation. Detailed derivation of the time-discrete implicit integration algorithm is provided, including an explicit closed-form expression for the continuous material Jacobian. The algorithm is used for finite element simulations using Abaqus, in which the model is implemented by means of a user material subroutine (UMAT). Extensive validation of the model is provided against multiple sets of experimental and numerical simulation data taken from the literature.

This chapter is organized as following: Section 2.1 presents a general literature review on SMAs subjected to nonproportional loading. A brief review of the ZM models is provided in Section 2.2 followed by a general presentation of the boundary value problem and time-discrete equations for a SMA subjected to isothermal loading in Section 2.3, including a closed-form expression for the continuous material Jacobian. Numerical simulations are then carried out in Section 2.4 for a number of loading cases, many of which are taken from the literature and shown to be properly simulated by the model. A general conclusion and outlook are finally provided in Section 2.5.

2.1 Literature review of SMAs subjected to nonproportional loading

Uniaxial or multiaxial loading of SMAs can induce phase transformation accompanied by the nucleation or shrinking of martensite variants (Otsuka and Wayman, 1999; Bodaghi et al., 2013). When the

loading direction changes, preferred martensite variants begin to form at the expense of others leading to a change in orientation of the inelastic strain in the martensitic phase. Both phase change and martensite reorientation can take place at the same time in presence of multiaxial nonproportional loading, which motivates the need for SMA models capable of accounting for these processes simultaneously. Numerical integration of the constitutive equations in this case is particularly challenging because it typically involves solving highly nonlinear equations while satisfying multiple consistency conditions and intrinsic constraints on the state variables. Proper numerical integration of SMA models is of special importance in such areas as the mechanics of fracture of SMAs, where multiaxial loading conditions and severe stress gradients are experienced by the material in the neighbourhood of the crack tip, as well as in analyzing fatigue of SMA structures, where accurate simulation of the multiaxial behavior of the material is needed for numerical prediction of fatigue life using appropriate failure criteria.

In the literature, the behavior of SMAs subjected to nonproportional loading has been the subject of intense investigation. [Sittner et al. \(1995\)](#) performed biaxial tension-torsion experiments on polycrystalline Cu-Al-Zn-Mn SMA samples considering rectangular and triangular stress- and strain-controlled loading cases. In both cases, the inelastic deformation of the material was found to be fully recoverable by unloading. [Lim and McDowell \(1999\)](#) reported several biaxial proportional and nonproportional loading experiments for thin-walled tubes of pseudoelastic Nitinol (Ni-Ti) SMAs under circular normal/shear stress- and strain-controlled loading. The material response was found to exhibit tensile-compressive asymmetry when subjected to cyclic tensile-compressive loading. Moreover, force- and strain-controlled experiments were conducted at different strain rates, with and without hold times, and the results were reported including the influence of thermomechanical coupling. [Bouvet et al. \(2002\)](#) carried out tension/internal pressure tests and biaxial compression tests using Cu-Al-Be SMA samples where the authors also observed tensile compressive asymmetry in the material behavior. A model was later proposed ([Bouvet et al., 2004](#)) that takes into account this asymmetry, as well as the influence of temperature, return point memory and the nonproportionality of the applied load on SMA behavior. The model was validated against experimental data obtained under general multiaxial loading cases. [Panico and Brinson \(2007\)](#) proposed a macroscopic phenomenological model based on the framework of thermodynamics of irreversible processes. The model accounts for the influence of multiaxial stress states and non-proportional loading histories and was shown to reasonably agree with the experimental data in [Sittner et al. \(1995\)](#). [Grabe and Bruhns \(2009\)](#) reported experimental results for polycrystalline Nitinol subjected to several multiaxial loading cases in a wide temperature range in order to investigate pseudoelasticity and the one-way shape memory effect of the material. Based on these experiments, the use of von Mises equivalent stress in deriving loading functions for phase transformation and martensite reorientation was found inappropriate as it failed to capture tensile-compressive and tensile-torsional asymmetries. [Arghavani et al. \(2010\)](#) presented a phenomenological constitutive model that accounts for key features of SMA behavior when the material is subjected to proportional as well as non-proportional loading. The model was successfully used to simulate a number of experimental results taken from the literature. [Chemisky et al. \(2011\)](#) derived a model for shape memory alloys based on earlier work by the authors. The model focuses on SMA behavior at lower stress levels and takes into account several effects

associated with SMA behavior such as tensile-compressive asymmetry and temperature-driven phase transformation. Simulation results are reported, without validation, at different temperatures for a case of multiaxial loading consisting of a square tension-shear loading path. Another model was developed by [Stebner and Brinson \(2013\)](#). The model was numerically integrated using an explicit scheme. Care was taken in eliminating the need for user-calibration of the numerical integration parameters and reducing the sensitivity of the integration algorithm to mass scaling for faster computation. [Bodaghi et al. \(2013\)](#) derived a simple and robust phenomenological model for SMAs using the framework of continuum thermodynamics of irreversible processes. The model was used to simulate SMAs subjected to uniaxial and biaxial loading, including proportional and nonproportional tensile-torsional loading. Good agreement with experimental data was achieved for these loading cases. [Auricchio et al. \(2014\)](#) recently proposed a model for SMAs that accounts for several aspects of SMA behavior in presence of multiaxial loading. The model was numerically integrated using Fischer-Burmeister functions to account for the Kuhn-Tucker conditions governing the evolution of several state variables, including the volume fractions of single- and multi-variant martensites and the directional orientation of single-variant martensite. The use of the Fischer-Burmeister functions allowed the authors to dispense with the conventional search for active loading surfaces by substituting the Kuhn-Tucker inequalities with a set of equivalent nonlinear equalities. The model is validated against experimental data for several loading cases, including a case of combined tension-torsion involving a helical SMA spring. A recent model was also proposed by [Mehrabi et al. \(2014\)](#), which consisted of a thermodynamically acceptable evolution of the microplane model for SMAs. In the spirit of the microplane theory, the authors considered different stress projection methods to resolve the three-dimensional constitutive material behavior into a combination of uniaxial models defined in specific spatial directions. The model was then used to simulate experiments on a thin hollow SMA cylinder subjected to tension, torsion and combined tension-torsion loading cases. Only proportional loading was considered for the combined loading case. [Zaki and Moumni \(2007a,b\)](#) and [Moumni et al. \(2008\)](#) derived a phenomenological model that can simultaneously account for phase transformation and martensite detwinning and reorientation. The model was improved to account for tensile-compressive asymmetry ([Zaki, 2010](#); [Zaki et al., 2011](#)), plastic yielding ([Zaki et al., 2010](#)), and thermomechanical coupling ([Morin et al., 2011a](#)) including cyclic effects ([Moumni et al., 2009](#); [Morin et al., 2011a,b,c](#)). However, numerical integration of the model in presence of non-proportional multiaxial loading was only considered so far in the case of martensitic SMAs ([Zaki, 2012a,b](#)).

2.2 Summary of the ZM model

The ZM model for SMAs is developed based on the framework of generalized standard materials ([Halphen and Nguyen, 1974](#)) that was slightly extended to account for constraints on the state variables ([Moumni, 1995](#); [Moumni et al., 2008](#)). Using standard index notation for tensor representation and implied summation over repeated indices, the derivation of the model gives the following stress-strain

relation:

$$\boldsymbol{\sigma} = \mathbf{K} : (\boldsymbol{\varepsilon} - z\boldsymbol{\varepsilon}_{\text{ori}}), \quad (2.1)$$

where $\boldsymbol{\sigma}$ and $\boldsymbol{\varepsilon}$ are the stress and total strain tensors, z is the volume fraction of martensite and $\boldsymbol{\varepsilon}_{\text{ori}}$ is the inelastic strain caused by martensite detwinning and reorientation. The elastic stiffness tensor \mathbf{K} is a function of phase composition. It is given by the expression

$$\mathbf{K} = [(1-z)\mathbf{K}_A^{-1} + z\mathbf{K}_M^{-1}]^{-1}, \quad (2.2)$$

in which \mathbf{K}_A and \mathbf{K}_M are the elastic stiffness matrices of austenite and martensite, respectively.

The volume fraction of martensite cannot be less than zero or greater than one and the recoverable inelastic deformation of martensite is limited by a maximum ε_0 that depends on the material used. These constraints are mathematically expressed as

$$z \geq 0, \quad 1 - z \geq 0, \quad \text{and } \varepsilon_0 - \varepsilon_{\text{eq}}^{\text{ori}} \geq 0, \quad (2.3)$$

where $\varepsilon_{\text{eq}}^{\text{ori}}$ is an equivalent orientation strain taken in this paper to be

$$\varepsilon_{\text{eq}}^{\text{ori}} = \sqrt{\frac{2}{3} \boldsymbol{\varepsilon}_{\text{ori}} : \boldsymbol{\varepsilon}_{\text{ori}}}. \quad (2.4)$$

The evolution of the dissipative variables z and $\boldsymbol{\varepsilon}_{\text{ori}}$ are governed by the Kuhn-Tucker conditions

$$\mathcal{F}_z^1(\boldsymbol{\sigma}, z, \boldsymbol{\varepsilon}_{\text{ori}}) \leq 0, \quad \dot{z} \geq 0, \quad \dot{z}\mathcal{F}_z^1 = 0, \quad (2.5)$$

for forward transformation, in which $0 \leq z < 1$;

$$\mathcal{F}_z^2(\boldsymbol{\sigma}, z, \boldsymbol{\varepsilon}_{\text{ori}}) \leq 0, \quad -\dot{z} \geq 0, \quad -\dot{z}\mathcal{F}_z^2 = 0, \quad (2.6)$$

for reverse transformation, in which $0 < z \leq 1$;

$$\mathcal{F}_{\text{ori}}(\boldsymbol{\sigma}, z, \boldsymbol{\varepsilon}_{\text{ori}}) \leq 0, \quad \eta \geq 0, \quad \eta\mathcal{F}_{\text{ori}} = 0, \quad (2.7)$$

for martensite detwinning and reorientation, in which η is the inelastic multiplier and the rate of orientation strain is provided by the normality rule

$$\dot{\boldsymbol{\varepsilon}}_{\text{ori}} = \eta \frac{\partial \mathcal{F}_{\text{ori}}}{\partial \mathbf{X}} = \frac{3}{2} \eta \frac{\mathbf{X}}{\mathbf{X}_{\text{vm}}} = \eta \mathbf{N}. \quad (2.8)$$

In the above equation, \mathbf{X}_{vm} is the von Mises equivalent of the thermodynamic force \mathbf{X} , conjugate to the orientation strain $\boldsymbol{\varepsilon}_{\text{ori}}$, and $\mathbf{N} = \frac{3}{2} \frac{\mathbf{X}}{\mathbf{X}_{\text{vm}}}$ is a vector indicating the direction of the orientation strain rate $\dot{\boldsymbol{\varepsilon}}_{\text{ori}}$ in strain space. To simplify numerical integration, martensite is assumed to be fully oriented by the applied stress as soon as the phase transformation from austenite to martensite takes place. This

simplification is in accordance with results in the literature (Patoor et al., 2006). For the ZM model used, this assumption is equivalent to considering that the stress σ_{rf} needed for complete detwinning of martensite is less than the stress σ_{ms} required to initiate forward phase transformation.

2.3 Boundary value problem and algorithmic setup

2.3.1 Boundary value problem

A pseudoelastic SMA structure occupying a volume $\Omega \in \mathbb{R}^3$ is subjected to isothermal loading in the time interval $[0, T]$. The load consists of body forces $\mathbf{f}(\mathbf{x}, t)$ acting over $\Omega \times [0, T]$ and contact forces $\mathbf{T}^{\text{d}}(\mathbf{x}, t)$ acting over $\Gamma_{\text{T}} \times [0, T]$. The remaining part $\Gamma_{\text{u}} = \Gamma - \Gamma_{\text{T}}$ of the boundary is subjected to prescribed displacement $\mathbf{u}^{\text{d}}(\mathbf{x}, t)$. Starting from an initial configuration at time $t = 0$ in which the state variables are known, the problem consists of solving the following set of equations over Ω for $t \in [0, T]$:

Static and kinematic admissibility

$$\boldsymbol{\sigma} \in \mathbb{K}_{\boldsymbol{\sigma}}, \quad \mathbf{u} \in \mathbb{K}_{\mathbf{u}}, \quad (2.9)$$

where the sets $\mathbb{K}_{\boldsymbol{\sigma}}$, $\mathbb{K}_{\mathbf{u}}$ are defined as

$$\begin{aligned} \mathbb{K}_{\boldsymbol{\sigma}} &= \{ \boldsymbol{\sigma} \mid \text{div} \boldsymbol{\sigma} + \mathbf{f} = 0 \text{ in } \Omega, \boldsymbol{\sigma} \mathbf{n} = \mathbf{T}^{\text{d}} \text{ on } \Gamma_{\text{T}} \}, \\ \mathbb{K}_{\mathbf{u}} &= \{ \mathbf{u} \mid \mathbf{u} = \mathbf{u}^{\text{d}} \text{ on } \Gamma_{\text{u}} \}, \end{aligned} \quad (2.10)$$

where \mathbf{n} is the outward unit vector normal to the boundary Γ_{T} , \mathbf{u} is the displacement vector.

Infinitesimal strain tensor $\boldsymbol{\varepsilon}$ is used and defined as

$$\boldsymbol{\varepsilon} = \frac{1}{2} (\nabla \mathbf{u} + {}^t \nabla \mathbf{u}) \text{ in } \Omega. \quad (2.11)$$

The stress-strain relation is given by

$$\boldsymbol{\sigma} = \mathbf{K} : (\boldsymbol{\varepsilon} - z \boldsymbol{\varepsilon}_{\text{ori}}) \text{ in } \Omega, \quad (2.12)$$

where \mathbf{K} is given by Eq. (2.2), and z and $\boldsymbol{\varepsilon}_{\text{ori}}$ are governed by Eqs. (2.3) to (2.8).

The boundary value problem above is solved using the finite element method. Time integration of the constitutive equations is done using an implicit algorithm that takes into account the possibility of simultaneous phase transformation and martensite detwinning and reorientation in presence of nonproportional multiaxial loading.

The assumption of complete orientation of martensite as soon as it forms reduces the constraint on the orientation strain to the equality $\varepsilon_0 - \varepsilon_{\text{eq}}^{\text{ori}} = 0$. In terms of modeling, this means that the magnitude of the inelastic strain is fully governed by the volume fraction of martensite. Numerical implementation is simplified in this case because of the reduced number of test cases considered for the detection of active loading. In particular, situations where the magnitude of the orientation strain varies at constant

martensite volume fraction no longer appear. The loading function \mathcal{F}_{ori} governing the orientation of martensite can be written in this case as

$$\mathcal{F}_{\text{ori}} = X_{\text{vm}} - zY, \text{ where } X = \boldsymbol{\sigma} - \frac{2}{3\varepsilon_0^2} (\boldsymbol{\sigma} : \boldsymbol{\varepsilon}_{\text{ori}}) \boldsymbol{\varepsilon}_{\text{ori}}, \quad (2.13)$$

in which Y is a material parameter that defines the stress onset of martensite detwinning in uniaxial tension. The expressions of the phase transformation functions remain unchanged with respect to the original ZM model. They are given by

$$\mathcal{F}_z^1 = \frac{1}{2} \left[El_{\text{MA}} \boldsymbol{\sigma} : \boldsymbol{\sigma} + P_{\text{MA}} (\text{tr} \boldsymbol{\sigma})^2 \right] - C(\theta) + \boldsymbol{\sigma} : \boldsymbol{\varepsilon}_{\text{ori}} - (G + b)z - a(1 - z) - \left[(\alpha - \beta)z + \frac{\beta}{2} \right] \left(\frac{2}{3} \boldsymbol{\varepsilon}_{\text{ori}} : \boldsymbol{\varepsilon}_{\text{ori}} \right), \quad (2.14)$$

$$\mathcal{F}_z^2 = -\frac{1}{2} \left[El_{\text{MA}} \boldsymbol{\sigma} : \boldsymbol{\sigma} + P_{\text{MA}} (\text{tr} \boldsymbol{\sigma})^2 \right] + C(\theta) - \boldsymbol{\sigma} : \boldsymbol{\varepsilon}_{\text{ori}} + (G - b)z - a(1 - z) + \left[(\alpha - \beta)z + \frac{\beta}{2} \right] \left(\frac{2}{3} \boldsymbol{\varepsilon}_{\text{ori}} : \boldsymbol{\varepsilon}_{\text{ori}} \right), \quad (2.15)$$

where El_{MA} , P_{MA} , α , β , a , b , and G are material parameters and $C(\theta)$ is a function of temperature.

Considering a discretization of the time interval $[0, T]$ into N intervals, the increments of the state variables z and $\boldsymbol{\varepsilon}_{\text{ori}}$ for load increment $n + 1$, $n \in \{0, N - 1\}$, are determined by enforcing the appropriate consistency conditions assuming z and $\boldsymbol{\varepsilon}_{\text{ori}}$ are known at load increment n . In the equations below, the load increments n and $n + 1$ are indicated in the subscript and the solution iteration k is indicated in the superscript of the relevant variable. The incremental equations are solved using a classical predictor-corrector strategy (Simo and Hughes, 1998) as follows:

- An elastic stress increment is first determined that achieves static equilibrium:

$$z_{n+1}^{(0)} = z_n, \text{ and } \boldsymbol{\varepsilon}_{\text{ori},n+1}^{(0)} = \boldsymbol{\varepsilon}_{\text{ori},n}, \quad (2.16)$$

$$\boldsymbol{\sigma}_{n+1}^{(0)} = \mathbf{K}_{n+1}^{(0)} : \left(\boldsymbol{\varepsilon}_{n+1} - z_{n+1}^{(0)} \boldsymbol{\varepsilon}_{\text{ori},n+1}^{(0)} \right). \quad (2.17)$$

- The stress increment is then corrected and the state variables are updated in accordance with the consistency conditions. If \mathcal{F}_z is any of the two loading functions \mathcal{F}_z^1 and \mathcal{F}_z^2 governing phase change, these conditions must satisfy

$$\mathcal{F}_z \left(\boldsymbol{\sigma}^{(k)}, z^{(k)}, \boldsymbol{\varepsilon}_{\text{ori}}^{(k)} \right) \leq 0, \quad (2.18)$$

$$\mathcal{F}_{\text{ori}} \left(\boldsymbol{\sigma}^{(k)}, z^{(k)}, \boldsymbol{\varepsilon}_{\text{ori}}^{(k)} \right) \leq 0, \quad (2.19)$$

where the subscript $n+1$ is eliminated for readability and where each inequality reduces to a strict equality when the relevant process is active. The equalities can be approximated using first-order Taylor series expansions of the loading functions \mathcal{F}_z and \mathcal{F}_{ori} in the neighbourhood of $\left(\boldsymbol{\sigma}^{(k-1)}, z^{(k-1)}, \boldsymbol{\varepsilon}_{\text{ori}}^{(k-1)} \right)$, which

can then be solved iteratively. The Taylor series approximations are written explicitly as follows:

$$\mathcal{F}_z^{(k-1)} + \frac{\partial \mathcal{F}_z^{(k-1)}}{\partial \boldsymbol{\sigma}} : \Delta \boldsymbol{\sigma}^{(k)} + \frac{\partial \mathcal{F}_z^{(k-1)}}{\partial z} \Delta z^{(k)} + \frac{\partial \mathcal{F}_z^{(k-1)}}{\partial \boldsymbol{\varepsilon}_{\text{ori}}} : \Delta \boldsymbol{\varepsilon}_{\text{ori}}^{(k)} = 0, \quad (2.20)$$

$$\mathcal{F}_{\text{ori}}^{(k-1)} + \frac{\partial \mathcal{F}_{\text{ori}}^{(k-1)}}{\partial \boldsymbol{\sigma}} : \Delta \boldsymbol{\sigma}^{(k)} + \frac{\partial \mathcal{F}_{\text{ori}}^{(k-1)}}{\partial z} \Delta z^{(k)} + \frac{\partial \mathcal{F}_{\text{ori}}^{(k-1)}}{\partial \boldsymbol{\varepsilon}_{\text{ori}}} : \Delta \boldsymbol{\varepsilon}_{\text{ori}}^{(k)} = 0, \quad (2.21)$$

where $\Delta v^{(k)} = v^{(k)} - v^{(k-1)}$ is the increment of variable v at iteration k . If phase transformation and martensite orientation are active at the same time, $\Delta z^{(k)}$ and $\Delta \eta^{(k)}$ are obtained by solving the time-discrete Eqs. (2.20) and (2.21) simultaneously, where $\Delta \eta^{(k)}$ is the discrete inelastic multiplier used to express the discrete normality rule at iteration k as

$$\Delta \boldsymbol{\varepsilon}_{\text{ori}}^{(k)} = \Delta \eta^{(k)} \mathbf{N}^{(k-1)}. \quad (2.22)$$

\mathbf{N} in the previous equation is approximated at iteration k by its value at the previous iteration $k-1$, with the initial value corresponding to an elastic prediction. Substituting Eq. (2.22) into Eqs. (2.20) and (2.21) gives

$$\mathcal{F}_z^{(k-1)} + \frac{\partial \mathcal{F}_z^{(k-1)}}{\partial \boldsymbol{\sigma}} : \Delta \boldsymbol{\sigma}^{(k)} + \frac{\partial \mathcal{F}_z^{(k-1)}}{\partial z} \Delta z^{(k)} + \frac{\partial \mathcal{F}_z^{(k-1)}}{\partial \boldsymbol{\varepsilon}_{\text{ori}}} : \mathbf{N}^{(k-1)} \Delta \eta^{(k)} = 0, \quad (2.23)$$

$$\mathcal{F}_{\text{ori}}^{(k-1)} + \frac{\partial \mathcal{F}_{\text{ori}}^{(k-1)}}{\partial \boldsymbol{\sigma}} : \Delta \boldsymbol{\sigma}^{(k)} + \frac{\partial \mathcal{F}_{\text{ori}}^{(k-1)}}{\partial z} \Delta z^{(k)} + \frac{\partial \mathcal{F}_{\text{ori}}^{(k-1)}}{\partial \boldsymbol{\varepsilon}_{\text{ori}}} : \mathbf{N}^{(k-1)} \Delta \eta^{(k)} = 0. \quad (2.24)$$

The time-discrete stress-strain relation can then be written as

$$\Delta \boldsymbol{\sigma}^{(k)} = \mathbf{K}^{(k-1)} : \left[\Delta \boldsymbol{\varepsilon}^{(k)} - \left(\Delta \mathbf{K}^{-1,(k)} : \boldsymbol{\sigma}^{(k-1)} + \Delta z^{(k)} \boldsymbol{\varepsilon}_{\text{ori}}^{(k-1)} + z^{(k-1)} \Delta \boldsymbol{\varepsilon}_{\text{ori}}^{(k)} \right) \right], \quad (2.25)$$

where $\Delta \boldsymbol{\varepsilon}^{(k)} = \mathbf{0}$ because $\boldsymbol{\varepsilon}$ is not updated in the corrector step and the increment of the elastic compliance tensor is given by

$$\Delta \mathbf{K}^{-1,(k)} = \left(K_{\text{M}}^{-1} - K_{\text{A}}^{-1} \right) \Delta z^{(k)}. \quad (2.26)$$

Combining Eqs. (2.22), (2.25) and (2.26) gives

$$\Delta \boldsymbol{\sigma}^{(k)} = -\mathbf{K}^{(k-1)} : \left[\mathbf{R}^{(k-1)} \Delta z^{(k)} + z^{(k-1)} \mathbf{N}^{(k-1)} \Delta \eta^{(k)} \right], \quad (2.27)$$

where

$$\mathbf{R}^{(k-1)} = \left(K_{\text{M}}^{-1} - K_{\text{A}}^{-1} \right) : \boldsymbol{\sigma}^{(k-1)} + \boldsymbol{\varepsilon}_{\text{ori}}^{(k-1)}. \quad (2.28)$$

The increments of the martensite volume fraction $\Delta z^{(k)}$ and the multiplier $\eta^{(k)}$ can now be calculated as

$$\Delta z^{(k)} = \frac{A_{\text{ori}}^{(k-1)} \mathcal{F}_{\text{ori}}^{(k-1)} - B_{\text{ori}}^{(k-1)} \mathcal{F}_z^{(k-1)}}{A_z^{(k-1)} B_{\text{ori}}^{(k-1)} - B_z^{(k-1)} A_{\text{ori}}^{(k-1)}}, \quad (2.29)$$

$$\Delta \eta^{(k)} = \frac{B_z^{(k-1)} \mathcal{F}_z^{(k-1)} - A_z^{(k-1)} \mathcal{F}_{\text{ori}}^{(k-1)}}{A_z^{(k-1)} B_{\text{ori}}^{(k-1)} - B_z^{(k-1)} A_{\text{ori}}^{(k-1)}}, \quad (2.30)$$

where

$$A_z^{(k-1)} = \partial_z \mathcal{F}_z^{(k-1)} - \partial_{\sigma} \mathcal{F}_z^{(k-1)} : \mathbf{K}^{(k-1)} : \mathbf{R}^{(k-1)}, \quad (2.31)$$

$$A_{\text{ori}}^{(k-1)} = \partial_{\varepsilon_{\text{ori}}} \mathcal{F}_z^{(k-1)} : \mathbf{N}^{(k-1)} - z^{(k-1)} \partial_{\sigma} \mathcal{F}_z^{(k-1)} : \mathbf{K}^{(k-1)} : \mathbf{N}^{(k)}, \quad (2.32)$$

$$B_z^{(k-1)} = \partial_z \mathcal{F}_{\text{ori}}^{(k-1)} - \partial_{\sigma} \mathcal{F}_{\text{ori}}^{(k-1)} : \mathbf{K}^{(k-1)} : \mathbf{R}^{(k-1)}, \quad (2.33)$$

$$B_{\text{ori}}^{(k-1)} = \partial_{\varepsilon_{\text{ori}}} \mathcal{F}_{\text{ori}}^{(k-1)} : \mathbf{N}^{(k-1)} - z^{(k-1)} \partial_{\sigma} \mathcal{F}_{\text{ori}}^{(k-1)} : \mathbf{K}^{(k-1)} : \mathbf{N}^{(k)}. \quad (2.34)$$

For phase transformation without martensite reorientation, the increment of martensite volume fraction at iteration k is given by the simple equation

$$\Delta z^{(k)} = - \frac{\mathcal{F}_z^{(k-1)}}{A_z^{(k-1)}}. \quad (2.35)$$

Similarly, the inelastic multiplier at iteration k in the case of martensite reorientation without phase transformation is given by

$$\Delta \eta^{(k)} = - \frac{\mathcal{F}_{\text{ori}}^{(k-1)}}{B_{\text{ori}}^{(k-1)}}. \quad (2.36)$$

2.3.2 Derivation of the continuous material Jacobian

For small volume changes, the continuous material Jacobian at the beginning of increment $n + 1$ is given by

$$\mathcal{J} = \frac{d\sigma}{d\varepsilon}, \quad (2.37)$$

where the right-hand term is evaluated at the end of increment n .

The time-continuous stress-strain relation can be written in differential form as

$$d\sigma = \mathbf{K} : [d\varepsilon - (\mathbf{R}dz + z\mathbf{N}d\eta)]. \quad (2.38)$$

For combined phase transformation and martensite reorientation, substituting dz and $d\eta$ in the above

with the expressions

$$dz = \frac{A_{\text{ori}} \partial_{\sigma} \mathcal{F}_{\text{ori}} - B_{\text{ori}} \partial_{\sigma} \mathcal{F}_z}{A_z B_{\text{ori}} - B_z A_{\text{ori}}} : \mathbf{K} : d\boldsymbol{\varepsilon}, \quad (2.39)$$

$$d\eta = \frac{B_z \partial_{\sigma} \mathcal{F}_z - A_z \partial_{\sigma} \mathcal{F}_{\text{ori}}}{A_z B_{\text{ori}} - B_z A_{\text{ori}}} : \mathbf{K} : d\boldsymbol{\varepsilon}, \quad (2.40)$$

leads to the following closed-form expression of the continuous material Jacobian:

$$\begin{aligned} \mathcal{J} = \frac{d\boldsymbol{\sigma}}{d\boldsymbol{\varepsilon}} = & \mathbf{K} - \mathbf{R} : \mathbf{K} \otimes \frac{(A_{\text{ori}} \partial_{\sigma} \mathcal{F}_{\text{ori}} - B_{\text{ori}} \partial_{\sigma} \mathcal{F}_z) : \mathbf{K}}{A_z B_{\text{ori}} - B_z A_{\text{ori}}} \\ & - {}_z \mathbf{N} : \mathbf{K} \otimes \frac{(B_z \partial_{\sigma} \mathcal{F}_z - A_z \partial_{\sigma} \mathcal{F}_{\text{ori}}) : \mathbf{K}}{A_z B_{\text{ori}} - B_z A_{\text{ori}}}. \end{aligned} \quad (2.41)$$

The same procedure gives the following expressions of the material Jacobian for the case of phase transformation with no reorientation of martensite and for the case of martensite reorientation without phase transformation:

$$\mathcal{J} = \frac{d\boldsymbol{\sigma}}{d\boldsymbol{\varepsilon}} = \mathbf{K} + \mathbf{R} : \mathbf{K} \otimes \frac{\partial_{\sigma} \mathcal{F}_z : \mathbf{K}}{A_z}, \quad (2.42)$$

and

$$\mathcal{J} = \frac{d\boldsymbol{\sigma}}{d\boldsymbol{\varepsilon}} = \mathbf{K} + {}_z \mathbf{N} : \mathbf{K} \otimes \frac{\partial_{\sigma} \mathcal{F}_{\text{ori}} : \mathbf{K}}{B_{\text{ori}}}, \quad (2.43)$$

respectively.

2.3.3 Algorithmic setup

A ‘‘User Material’’ subroutine is developed for the simulation of phase transformation and martensite reorientation in the finite element analysis software Abaqus. The subroutine uses the implicit integration algorithm presented below in order to update the stress components and the state variables at the end of each load increment. The parameters tol_1 , tol_2 and tol_3 that appear in the algorithm are numerical tolerances, which are set to very small values directly in the subroutine.

Algorithm 1: Algorithm of UMAT

-
- 1 Read the parameters of the model;
 - 2 Determine the elastic trial state: calculate the increment of trial stress $\sigma_{n+1}^{(0)}$ using Eq. (2.17);
calculate initial trial values for the loading functions $\mathcal{F}_{z,n+1}^{(0)}, \mathcal{F}_{\text{ori},n+1}^{(0)}$;
 - 3 **if** $(\mathcal{F}_{z,n+1}^{(0)} \leq \text{tol}_1 \text{ and } \mathcal{F}_{\text{ori},n+1}^{(0)} \leq \text{tol}_2)$ **or** $(\mathcal{F}_{z,n+1}^{1,(0)} > \text{tol}_1 \text{ and } \mathcal{F}_{\text{ori},n+1}^{(0)} \leq \text{tol}_2 \text{ and } z_{n+1}^{(0)} = 1)$ **or**
 $(\mathcal{F}_{z,n+1}^{2,(0)} > \text{tol}_1 \text{ or } \mathcal{F}_{\text{ori},n+1}^{(0)} > \text{tol}_2 \text{ and } z_{n+1}^{(0)} = 0)$, *(the trial solution is acceptable)* **then**
 - 4 Set the stress vector equal to the trial stress vector;
 - 5 Set the state variables to their values at the beginning of the increment;
 - 6 Set the material Jacobian \mathcal{J} equal to the elastic stiffness tensor \mathbf{K} ;
 - 7 **else if** $(\mathcal{F}_{z,n+1}^{(0)} \leq \text{tol}_1 \text{ and } \mathcal{F}_{\text{ori},n+1}^{(0)} > \text{tol}_2 \text{ and } z_{n+1}^{(0)} > 0)$ **or**
 $(\mathcal{F}_{z,n+1}^{1,(0)} > \text{tol}_1 \text{ and } \mathcal{F}_{\text{ori},n+1}^{(0)} > \text{tol}_2 \text{ and } z_{n+1}^{(0)} = 1)$, *(only martensite reorientation is active)* **then**
 - 8 Set iteration counter $k = 0$;
 - 9 **while** $|\mathcal{F}_{\text{ori},n+1}^{(k)}| > \text{tol}_2$ **do**
 - 10 Calculate the increment of the inelastic multiplier $\Delta\eta_{n+1}^{(k+1)}$ using Eq. (2.30);
 - 11 Set $k = k + 1$;
 - 12 Update the state variables;
 - 13 Calculate the material Jacobian \mathcal{J} using Eq. (2.43);
 - 14 **else if** $\mathcal{F}_{z,n+1}^{(0)} > \text{tol}_1 \text{ and } \mathcal{F}_{\text{ori},n+1}^{(0)} \leq \text{tol}_2$, *(only phase transformation is active)* **then**
 - 15 Set iteration counter $k = 0$;
 - 16 **while** $|\mathcal{F}_{z,n+1}^{1,(k)}| > \text{tol}_1 \text{ and } z_{n+1}^{(k)} < 1$ **do**
 - 17 Calculate the increment of martensite volume fraction $\Delta z_{n+1}^{(k+1)}$ using Eq. (2.29);
 - 18 Set $z_{n+1}^{(k+1)} = z_{n+1}^{(k)} + \Delta z_{n+1}^{(k+1)}$;
 - 19 **if** $z_{n+1}^{(k+1)} > 1$ **then**
 - 20 set $z_{n+1}^{(k+1)} = 1$;
 - 21 Set $k = k + 1$;
 - 22 **while** $|\mathcal{F}_{z,n+1}^{2,(k)}| > \text{tol}_1 \text{ and } z_{n+1}^{(k)} > 0$ **do**
 - 23 Calculate the increment of martensite volume fraction $\Delta z_{n+1}^{(k+1)}$ using Eq. (2.29);
 - 24 Set $z_{n+1}^{(k+1)} = z_{n+1}^{(k)} + \Delta z_{n+1}^{(k+1)}$;
 - 25 **if** $z_{n+1}^{(k+1)} < 0$ **then**
 - 26 Set $z_{n+1}^{(k+1)} = 0$;
 - 27 Set $k = k + 1$;
 - 28 Update the state variables;
 - 29 Calculate the material Jacobian \mathcal{J} using Eq. (2.42);
-

Continued on next page

Continued from previous page

```

30 else if  $\mathcal{F}_{z,n+1}^{-1,(0)} > tol_1$  and  $\mathcal{F}_{ori,n+1}^{(0)} > tol_2$  and  $z_{n+1}^{(0)} < 1$ , (martensite reorientation or phase
    transformation or both) then
31   Set iteration counter  $k = 0$ ;
32   while  $\left( \left| \mathcal{F}_{z,n+1}^{-1,(k)} \right| > tol_1 \text{ and } z_{n+1}^{(k)} < 1 \right)$  or  $\left( \left| \mathcal{F}_{ori,n+1}^{(k)} \right| > tol_2 \text{ and } z_{n+1}^{(k)} > 0 \right)$  do
33     Calculate the increment of the inelastic multiplier  $\Delta\eta_{n+1}^{(k+1)}$  and the increment of martensite
        volume fraction  $\Delta z_{n+1}^{(k+1)}$  using Eqs. (2.29) and (2.30);
34     Set  $z_{n+1}^{(k+1)} = z_{n+1}^{(k)} + \Delta z_{n+1}^{(k+1)}$ ;
35     if  $z_{n+1}^{(k+1)} > 1$  then
36       Set  $z_{n+1}^{(k+1)} = 1$ ;
37     Set  $k = k + 1$ ;
38   if  $\Delta z_{n+1} > tol_3$  and  $\Delta\eta_{n+1} > tol_3$ , (simultaneous phase transformation and martensite
    reorientation) then
39     Update the stress vector and the state variables;
40     Calculate the material Jacobian  $\mathcal{J}$  using Eq. (2.41);
41   else if  $\Delta z_{n+1} > tol_3$  and  $\Delta\eta_{n+1} \leq tol_3$ , (phase transformation only) then
42     Reset the state variables to their values at the beginning of the increment, goto 15;
43   else if  $\Delta z_{n+1} \leq tol_3$  and  $\eta_{n+1} > tol_3$ , (martensite reorientation only) then
44     Reset the state variables to their values at the beginning of the increment, goto 8;
45 else if  $\mathcal{F}_{z,n+1}^{-2,(0)} > tol_1$  and  $\mathcal{F}_{ori,n+1}^{(0)} > tol_2$  and  $z_{n+1}^{(0)} > 0$ , (martensite reorientation or phase
    transformation or both) then
46   Set iteration counter  $k = 0$ ;
47   while  $\left( \left| \mathcal{F}_{z,n+1}^{-2,(k)} \right| > tol_1 \text{ and } z_{n+1}^{(k)} > 0 \right)$  or  $\left( \left| \mathcal{F}_{ori,n+1}^{(k)} \right| > tol_2 \text{ and } z_{n+1}^{(k)} > 0 \right)$  do
48     Calculate the increment of the inelastic multiplier  $\Delta\eta_{n+1}^{(k+1)}$  and the increment of martensite
        volume fraction  $\Delta z_{n+1}^{(k+1)}$  using Eqs. (2.29) and (2.30);
49     Set  $z_{n+1}^{(k+1)} = z_{n+1}^{(k)} + \Delta z_{n+1}^{(k+1)}$ ;
50     if  $z_{n+1}^{(k+1)} < 0$  then
51       Set  $z_{n+1}^{(k+1)} = 0$ ;
52     Set  $k = k + 1$ ;
53   if  $\Delta z_{n+1} < -tol_3$  and  $\Delta\eta_{n+1} > tol_3$ , (simultaneous phase transformation and martensite
    reorientation) then
54     Update the stress vector and the state variables;
55     Calculate the material Jacobian  $\mathcal{J}$  using Eq. (2.41);
56   else if  $\Delta z_{n+1} < -tol_3$  and  $\Delta\eta_{n+1} \leq tol_3$ , (phase transformation only) then
57     Reset the state variables to their values at the beginning of the increment, goto 15;
58   else if  $\Delta z_{n+1} \geq -tol_3$  and  $\Delta\eta_{n+1} > tol_3$ , (martensite reorientation only) then
59     Reset the state variables to their values at the beginning of the increment, goto 8;
60 return: stress, state variables, tangent operators.

```

2.4 Results and discussions

The problem defined in the previous section is solved by means of the finite element method for several pseudoelastic SMA structures subjected to uniaxial and multiaxial proportional and nonproportional loading. For cases involving comparison to experimental data, the parameters of the ZM model are determined according to a deterministic procedure described in [Zaki and Mousni \(2007a\)](#). The section is organized as follows:

- Proportional loading is considered in Section 2.4.1, which includes numerical simulation results for pure tension, pure torsion, as well as multiaxial tension-torsion and tension-internal pressure loading that are compared to experimental data from [Bouvet et al. \(2004\)](#).
- A hypothetical situation involving nonproportional loading is presented in Section 2.4.2 in order to investigate the ability of the model to account for multiaxial loading in presence of simultaneous phase transformation and martensite reorientation.
- In Section 2.4.3, the model is used to simulate a number of numerical as well as experimental results available in the literature for SMAs subjected to nonproportional multiaxial loading. The reference data used for the validation are those reported by [Sittner et al. \(1995\)](#), [Bouvet et al. \(2002\)](#), [Panico and Brinson \(2007\)](#), [Grabe and Bruhns \(2009\)](#), [Arghavani et al. \(2010\)](#) and [Stebner and Brinson \(2013\)](#). In each case, the parameters used for the simulations using the ZM model were obtained by curve fitting to a subset of the reported data.

2.4.1 Simulation of proportional loading cases

The four loading cases shown in Fig. 2.1 are considered in this section, ranging from pure tension (path 1) to pure shear (path 2). Paths 3 and 4 represent combined tensile-shear loading where tension is dominant for path 3 and shear is dominant for path 4.

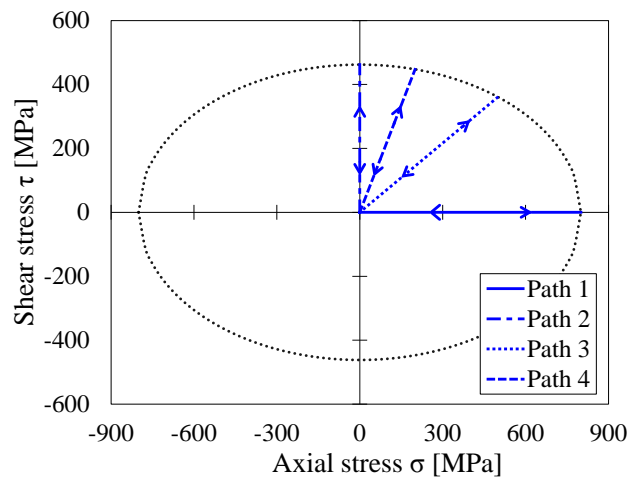


Figure 2.1 Stress-controlled proportional loading cases.

The simulations are performed on a single 8-node hexahedral element with reduced integration. A maximum von Mises equivalent stress of 800 MPa is achieved in each loading case and a constant temperature $T = 340$ K is considered for which the shape memory alloy is pseudoelastic. The parameters used for the simulations are listed in Table 2.1.

Table 2.1 Material parameters used for the finite element simulations in Section 2.4.1.

E_A	30 340	MPa	E_M	18 000	MPa
a	5.16	MPa	b	6.36	MPa
ν	0.3		ε_0	0.04	
Y	30	MPa	G	13.17	MPa
α	500	MPa	β	1250	MPa
ξ	0.20	MPa K ⁻¹	κ	4.16	MPa
A_f^0	320	K	θ	340	K

The simulated uniaxial response of the material is shown in Fig. 2.2a for tensile loading and Fig. 2.2b for shear loading. The obtained pseudoelastic loops are identical in shape up to a scaling factor of $\sqrt{3}$ along the coordinate axes.

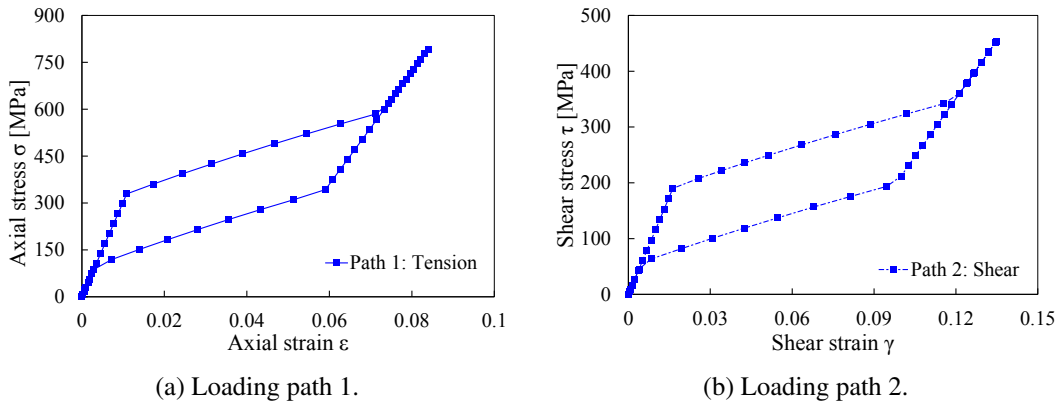


Figure 2.2 Simulated stress-strain behavior for pure tension and pure shear loading.

Simulation results for the combined loading cases corresponding to the loading paths 3 and 4 on Fig. 2.1 are shown in Figs. 2.3 and 2.4. In both cases, tensile and shear pseudoelasticity is obtained with full inelastic strain recovery when the load is removed.

The model is now used to simulate the behavior of a thin-walled SMA cylinder following Bouvet et al. (2004). The cylinder is subjected to proportional multiaxial loading consisting of a combination of axial loading and internal pressure. Taking advantage of radial symmetry, the finite element model consists of a portion of a thin-walled tube, 10 mm in length, for which the cross section is shown in Fig. 2.5a. The dimensions are chosen such that the thickness is much smaller than the other dimensions in order for the sample to qualify as thin-walled. The model is meshed using 90 hexahedral linear

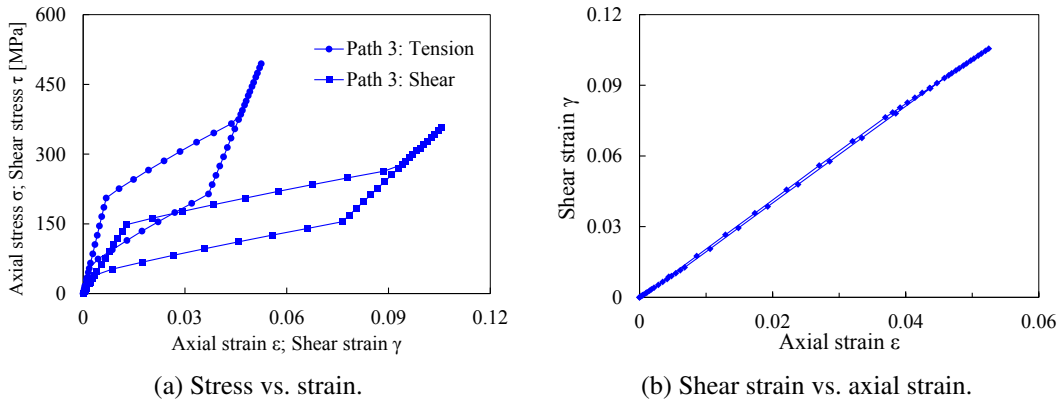


Figure 2.3 Simulated response for loading path 3.

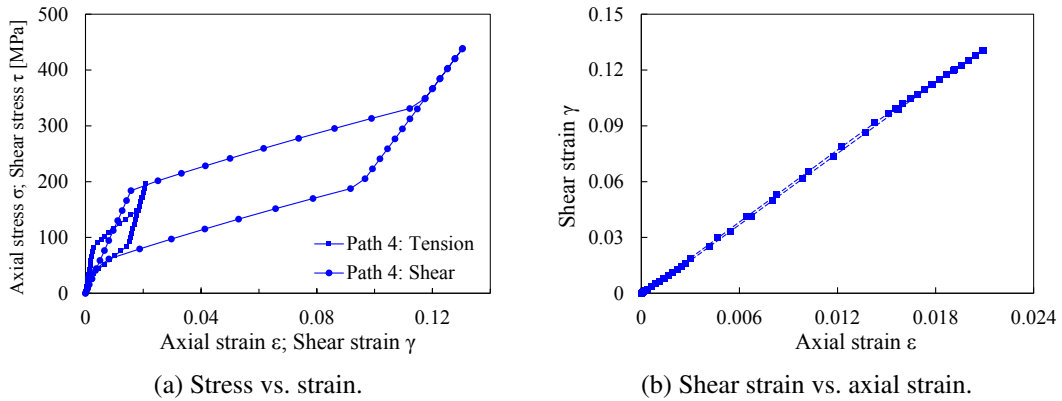


Figure 2.4 Simulated response for loading path 4.

elements (C3D8 in Abaqus terminology) without reduced integration for a total of 1320 degrees of freedom. Conditions of radial symmetry are prescribed on the boundaries of the section as shown in the figure.

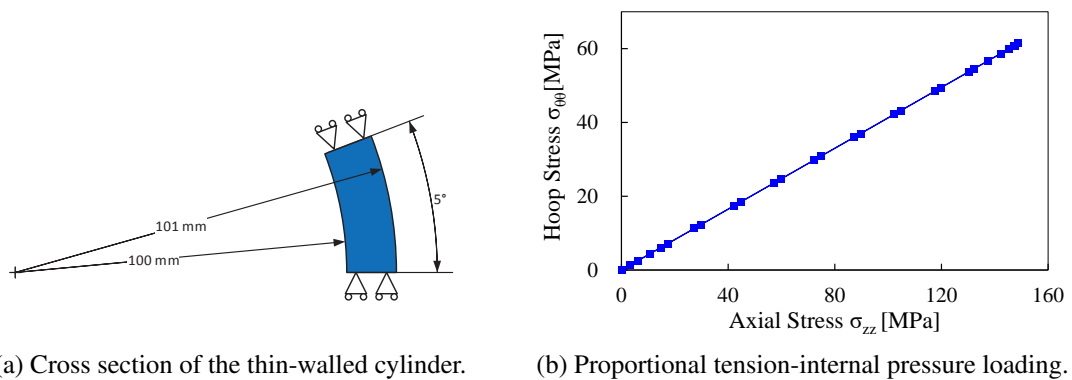


Figure 2.5 Experimental setup used in Bouvet et al. (2004).

The parameters used for the simulations are determined using the experimental stress-strain curve

in Fig. 2.6a. They are listed in Table 2.2. The loading considered in this case corresponds to the hoop versus axial stress shown in Fig. 2.5b, in which a constant slope is obtained because of the proportional nature of the load.

Table 2.2 Material parameters obtained using data form Bouvet et al. (2004).

E_A	45 200	MPa	E_M	26 400	MPa
a	0.24	MPa	b	0.096	MPa
ν	0.3		ε_0	0.08	
Y	30	MPa	G	0.92	MPa
α	2500	MPa	β	6250	MPa
ξ	0.0145	MPa K ⁻¹	κ	0.038	MPa
A_f^0	320	K	θ	340	K

The resulting stress-strain behavior of the material is shown in Fig. 2.6 where two pseudoelastic stress-strain loops are shown representing the material behavior in the axial and hoop directions respectively. The simulations are in good agreement with the experimental data in both cases. In particular, the

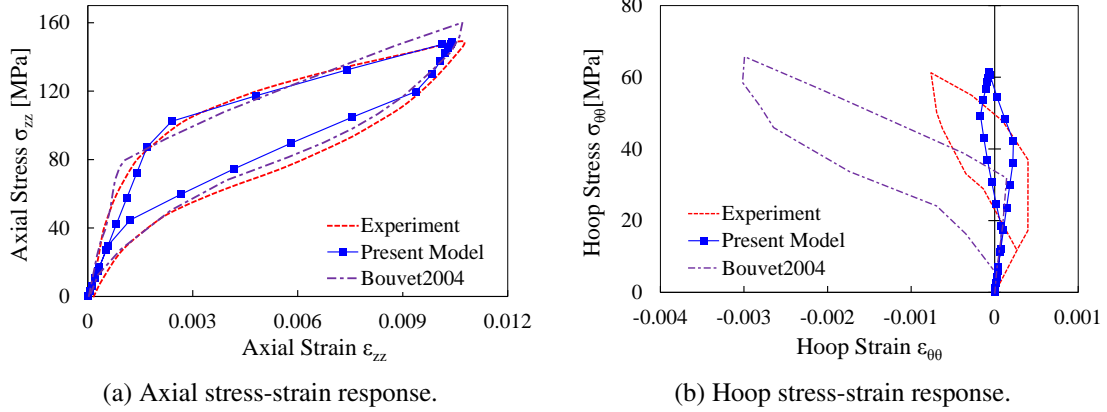


Figure 2.6 Stress-strain behavior in the axial and hoop directions due to loading in Fig. 2.5b.

model provides improved prediction of the material behavior in the hoop direction. Deviation from the experimental data may be due to the use of von Mises equivalent stress in the present version of the model, which cannot reproduce the asymmetry in the material response.

2.4.2 Multiaxial reorientation tests

A preliminary numerical simulation test is performed in this section in order to illustrate the ability of the model to simulate simultaneous phase transformation and martensite reorientation and to account for martensite reorientation at saturation, in which case the equivalent orientation strain reaches its maximum value ε_0 . In case the loading magnitude continues to increase beyond the saturation point,

the components of the orientation strain tensor ε_{ori} may continue to evolve to accommodate possible modifications in the loading direction while the equivalent orientation strain remains constant.

The parameters used in this section are those listed in Table 2.1. The proposed simulation involves an axial loading corresponding to a maximum normal stress of 600 MPa followed by an increase in shear stress from 0 to 195 MPa as shown in Fig. 2.7a. The maximum normal stress is such that maximum inelastic strain is achieved in tension (complete transformation of austenite to fully oriented martensite) as shown in Fig. 2.7b. The superposition of shear stress leads to an increase in the yz strain component at the expense of the normal xx strain in such way that the total equivalent orientation strain remains constant (same figure). The evolution of the inelastic strain components is an expression of the physical process of martensite reorientation, in which preferred martensite variants form at the expense of other variants that are less-favorably oriented with respect to the applied load. From a phenomenological point of view, within the frame of the ZM model for shape memory alloys, this behavior is captured through the use of the loading function for martensite orientation \mathcal{F}_{ori} .

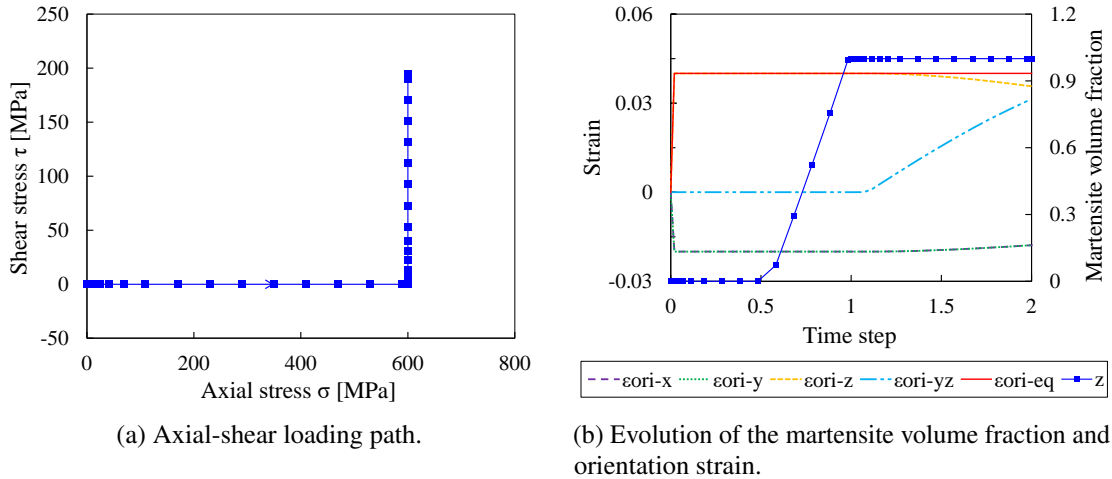


Figure 2.7 Simulation of martensite reorientation under multiaxial loading.

Further testing of the model is carried out using the square loading path shown in Fig. 2.8a, which consists of the following loading steps starting from an unloaded state:

1. Tensile loading up to a maximum tensile stress of 250 MPa (segment AB on the figure),
2. Shear loading up to a maximum shear stress of 250 MPa (segment BC),
3. Compression up to a maximum compressive normal stress of 250 MPa (segment CD),
4. Shear reversal (segment DE),
5. Tensile loading up to a maximum tensile stress of 250 MPa (segment EF),
6. Unloading of shear stress (segment FG),
7. Unloading of tensile stress (segment GA), leading to complete unloading of the material.

The parameters used are those listed in Table 2.5. The results of the simulation are reported in Fig. 2.8b as shear strain in terms of normal strain. An elastic response is also shown in the same figure for reference.

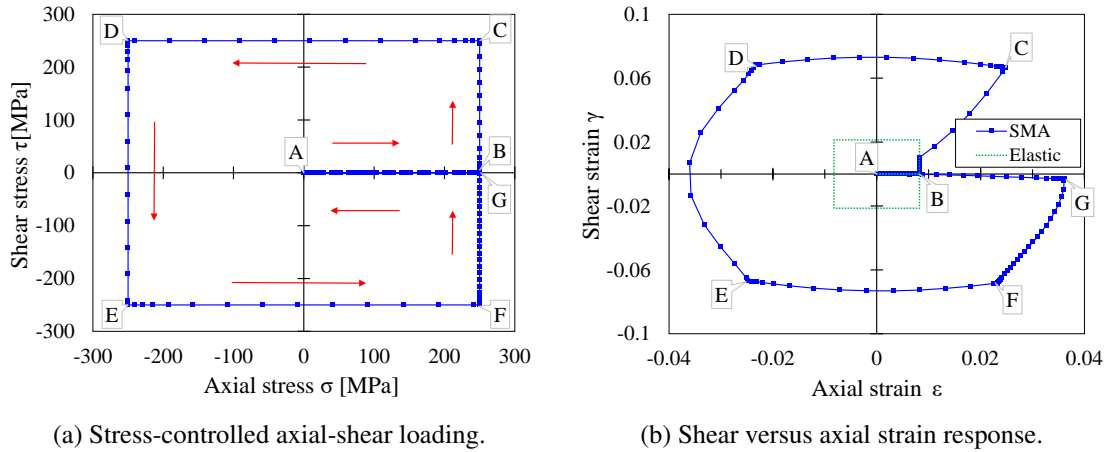


Figure 2.8 Biaxial non-proportional loading.

The evolution with the loading time of the martensite volume fraction and the orientation strain is shown in Fig. 2.9. It is clear from the figures that the initial tensile loading is not sufficient to cause

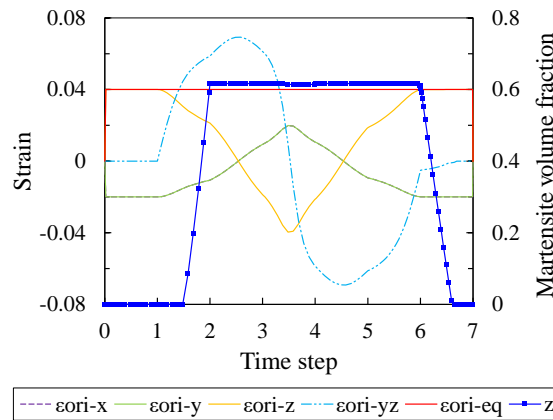


Figure 2.9 Evolution of the martensite volume fraction and orientation strain.

inelastic deformation. The material behavior for loading step 1 therefore coincides with the reference elastic behavior. The superposition of shear in load step 2 increases the values taken by the loading functions for phase change and martensite reorientation leading to shear-dominated inelastic deformation as shown in Fig. 2.9. The onset of this deformation corresponds to a deviation from the vertical direction of the portion BC of the shear versus tensile strain curve in Fig. 2.8b as shear orientation strain starts to develop at the expense of normal strain (Fig. 2.9, step time 1–2). Further tensile/shear loading in load steps 3 to 7 results in the evolution of the inelastic strain along the elliptic arcs CD, DE, EF and FG in Fig. 2.8b. Complete strain recovery is then obtained upon complete unloading in load step 8. It can be

observed that the strain at point G in Fig. 2.8b, corresponding to time step 6 in Fig. 2.9, still comprises a residual shear component despite the removal of shear loading. This observation is a manifestation of martensite reorientation in presence of nonproportional loading, which results in the inelastic strain not being aligned with the stress. Despite the total inelastic strain being recoverable by unloading, individual strain components do not vanish if the corresponding stress components are unloaded. Rather, the components of the inelastic strain tensor are scaled down in magnitude when the volume fraction of martensite decreases. This is consistent with the physics of pseudoelastic deformation in SMAs, where shape recovery results from the transformation of martensite into austenite, not from the inelastic deformation being recovered within the martensite phase.

2.4.3 Validation of the model

The model is used to simulate a number of cases reported in the literature involving pseudoelastic shape memory alloys subjected to nonproportional loading. Both stress- and strain-controlled experiments are considered using data obtained by several research groups including [Sittner et al. \(1995\)](#), [Bouvet et al. \(2002\)](#), [Stebner and Brinson \(2013\)](#), [Panico and Brinson \(2007\)](#), [Arghavani et al. \(2010\)](#) and [Grabe and Bruhns \(2009\)](#).

Strain-controlled tension-shear loading

Following the recently published work of [Stebner and Brinson \(2013\)](#), a SMA sample modelled as a single hexahedral mesh element, is subjected to the displacement-driven loading shown in Fig. 2.10a. The loading involves nonproportional tensile-shear strain in which a maximum tensile strain of 0.04 is achieved. The material parameters used for the simulation, equivalent to those in [Stebner and Brinson \(2013\)](#), are listed in Table 2.3. The temperature used for the simulation is artificial and is only meant to guarantee pseudoelastic behavior of the shape memory alloy.

Table 2.3 Material parameters used for simulating SMA behavior in presence of nonproportional loading following [Stebner and Brinson \(2013\)](#).

E_A	82 675	MPa	E_M	35 000	MPa
a	4.79	MPa	b	5.39	MPa
ν	0.4		ε_0	0.038	
Y	30	MPa	G	4.48	MPa
α	789.5	MPa	β	3421	MPa
ξ	0.19	MPa K ⁻¹	κ	2.32	MPa
A_f^0	300	K	θ	340	K

The displacement-controlled loading results in square-shaped shear strain versus normal strain behavior. The stress curve in Fig. 2.10b has a more complicated shape, which underlines the well-established nonlinearity in SMA behavior. Numerical simulations are in agreement with those obtained

by [Stebner and Brinson \(2013\)](#). A better fit can likely be obtained by fine-tuning the parameters of the ZM model. Some deviation is inevitable however because of intrinsic differences between the two models.

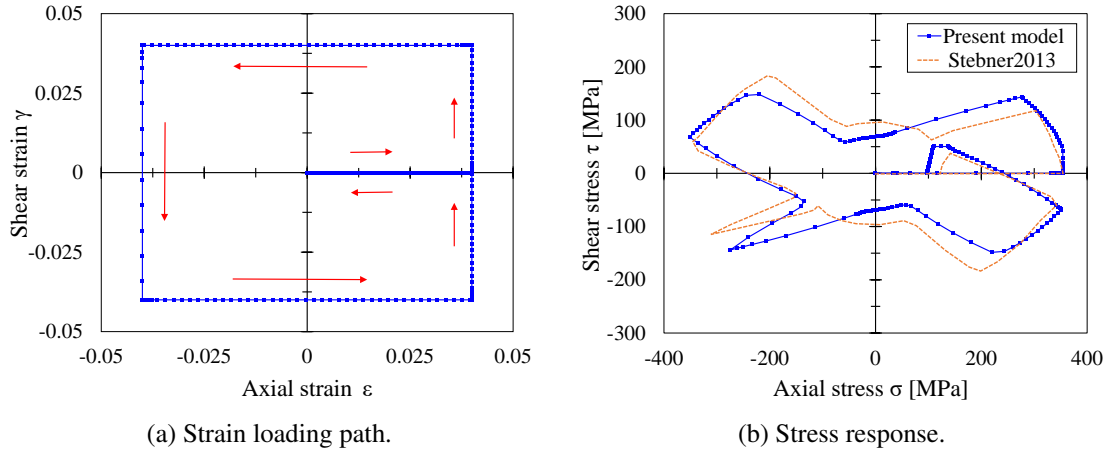


Figure 2.10 Numerical prediction of stress and strain behavior and comparison with numerical simulation results from ([Stebner and Brinson, 2013](#)).

The time evolution of the equivalent von Mises stress and the martensite volume fraction is shown in [Fig. 2.11](#). Notable differences between the simulation results of the two models include a steeper increase

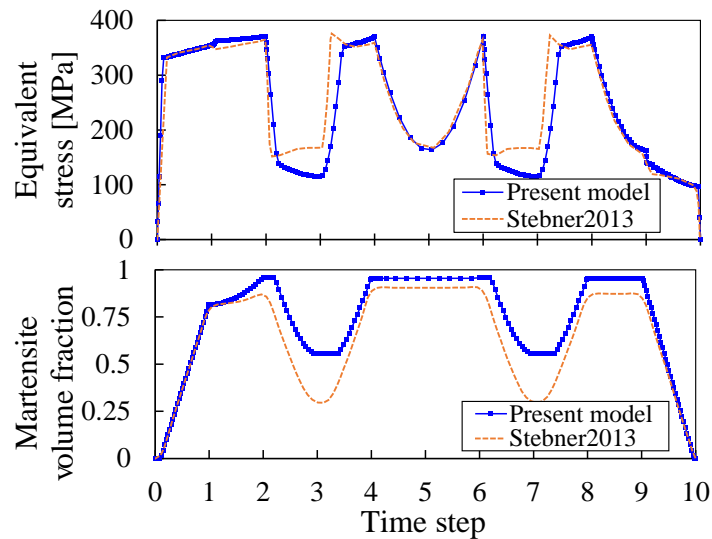


Figure 2.11 Evolution of the von Mises equivalent stress and martensite volume fraction with loading time.

in the volume fraction of martensite from time step 1 to 2, which indicates that a more pronounced hardening is predicted by the ZM model leading to higher maximum value of the martensite volume fraction z at time step 2 that persists in subsequent load steps. In addition, the curve predicted by the ZM model features flat portions that indicate a delay in martensite reorientation with respect to changes

in the loading direction. The delay is related to the formulation of the phase transformation function, which decreases slightly when the shear or tensile strain components decrease at the beginning of load steps 3, 4 and 8 (time steps 2–3, 3–4 and 7–8 respectively). The flat portions are indeed accompanied with a decrease of the von Mises equivalent stress, which strongly influences the phase transformation functions. Such decrease is not observed in the simulations of [Stebner and Brinson \(2013\)](#), which results in the absence of flat plateaus.

Strain-controlled tension-torsion loading

Experimental data reported by [Grabe and Bruhns \(2009\)](#) shows a strong dependence of the material behavior on the loading history. The loading considered by the authors is the one shown in Fig. 2.12a, which consists in two strain-controlled butterfly loading paths that start and end at the same unloaded state. The maximum axial and shear strains reached in each case are $\varepsilon = \gamma' = \gamma/\sqrt{3} = 0.015$. Path 2 follows the loading sequence for path 1 in reverse order, such that the same intermediate states of shear and axial strain are achieved. The resulting material response in Fig. 2.12b shows a clear difference in terms of the shear stress, plotted as $\tau' = \tau/\sqrt{3}$, versus axial stress curves corresponding to the two loading cases.

The experiments by [Grabe and Bruhns \(2009\)](#) are simulated using the ZM model with the parameters listed in Table 2.4. The material parameters were obtained from uniaxial experimental data reported in [Grabe and Bruhns \(2008\)](#) using the same SMA material at the same temperature and loading rate as in [\(Grabe and Bruhns, 2009\)](#). Since the original ZM model is used, in which asymmetry in the material behavior is not considered, the simulations could not predict the tensile-compressive asymmetry seen in Fig. 2.12b. The overall agreement with the experimental data remains satisfactory nevertheless and does produce a trend similar to the one observed in the Fig. 2.12b, where the first load path results in shear stresses with higher magnitudes in the second and third quadrants and lower magnitudes in the first and fourth quadrants compared to the shear stresses obtained with the second load path for extremal values $\gamma' = \pm 0.015$ of the shear strain. A good fit is also achieved for the stress-strain behavior in shear shown in Fig. 2.12d. The difference between the experimental and simulation results is more pronounced, however, for the axial stress-strain curves in Fig. 2.12c.

Table 2.4 Material parameters used for the simulations following [Grabe and Bruhns \(2009\)](#).

E_A	46 800	MPa	E_M	18 800	MPa
a	0.85	MPa	b	0.31	MPa
ν	0.3		ε_0	0.01	
Y	30	MPa	G	2.19	MPa
α	2000	MPa	β	5000	MPa
ξ	0.22	MPa K ⁻¹	κ	0.6	MPa
A_f^0	300	K	θ	340	K

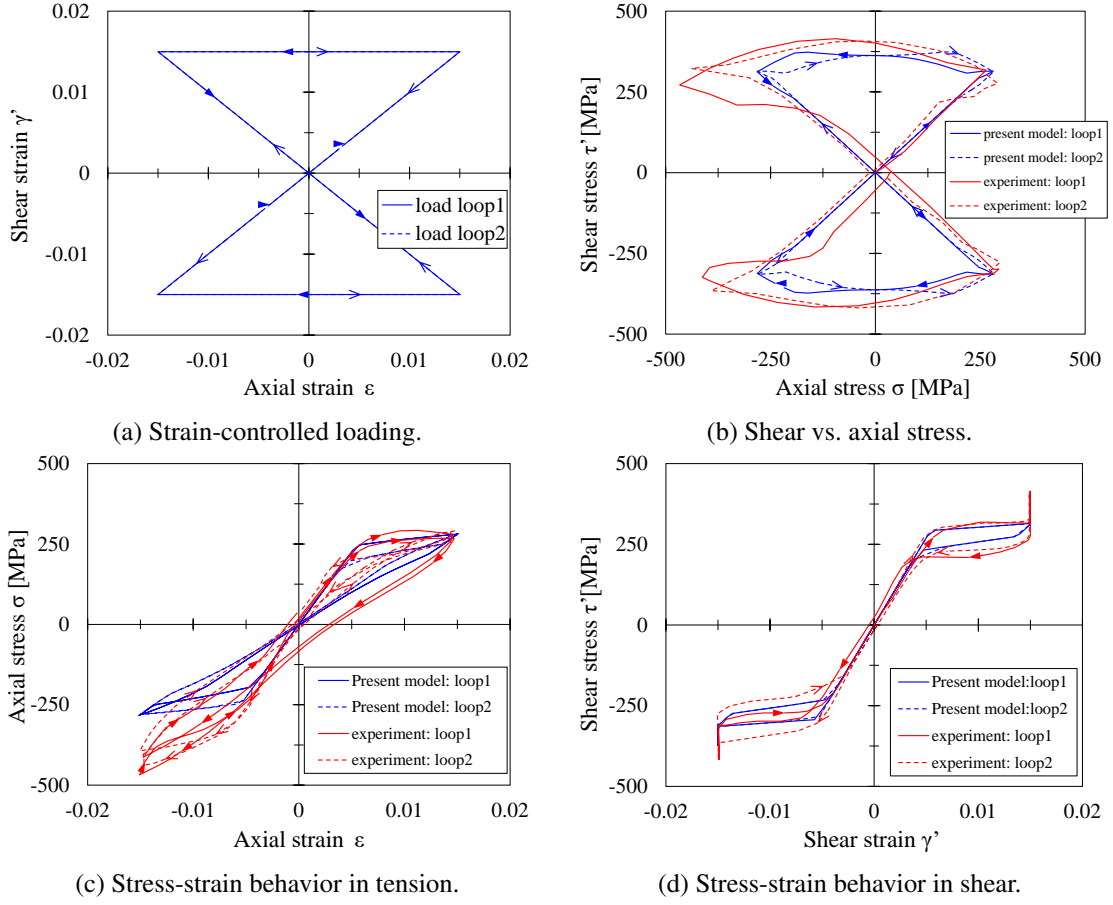


Figure 2.12 Comparison of experimental and simulation results for the butterfly loading in Fig. 2.12a.

Stress-controlled tension-torsion loading

Experimental data from [Sittner et al. \(1995\)](#) is used to validate the model for the case of nonproportional stress-controlled loading in tension and torsion. The experiments were carried out on thin-walled cylindrical SMA samples. The authors used the following expressions for the equivalent stress and strain in reporting their results:

$$\sigma_{\text{eq}} = \sqrt{\sigma^2 + \tau_{\text{inv}}^2}, \quad \tau_{\text{inv}} = C^S \tau, \quad (2.44)$$

$$\epsilon_{\text{eq}} = \sqrt{\epsilon^2 + \gamma_{\text{inv}}^2}, \quad \gamma_{\text{inv}} = \frac{\gamma}{C^E}, \quad (2.45)$$

where τ_{inv} and γ_{inv} are energetically equivalent shear stress and strain and C^S and C^E are empirical coefficients. von Mises equivalent stress and strain are obtained for $C^S = C^E = \sqrt{3}$. Since different expressions are used for σ_{eq} and ϵ_{eq} in the ZM model, two different loading cases are considered for the finite element simulations:

1. The first loading case is shown in Fig. 2.14a, in which the normal and shear stress used for the

simulation are exactly those reported in [Sittner et al. \(1995\)](#), but the equivalent stress is not the same.

- The second loading case is shown in [Fig. 2.15a](#), in which the shear stress used for the simulation produces an equivalent stress identical to the one in ([Sittner et al., 1995](#)).

For the first loading case, the material parameters used for the simulations are listed in [Table 2.5](#). They were determined using the experimental tensile response of the SMA shown in [Fig. 2.13](#).

Table 2.5 Material parameters used for the simulation of nonproportional loading of SMAs following [Sittner et al. \(1995\)](#).

E_A	30 340	MPa	E_M	18 000	MPa
a	1.84	MPa	b	1.395	MPa
ν	0.3		ε_0	0.02	
Y	30	MPa	G	11.46	MPa
α	1000	MPa	β	2500	MPa
ξ	0.116	MPa K ⁻¹	κ	1.34	MPa
A_f^0	300	K	θ	340	K

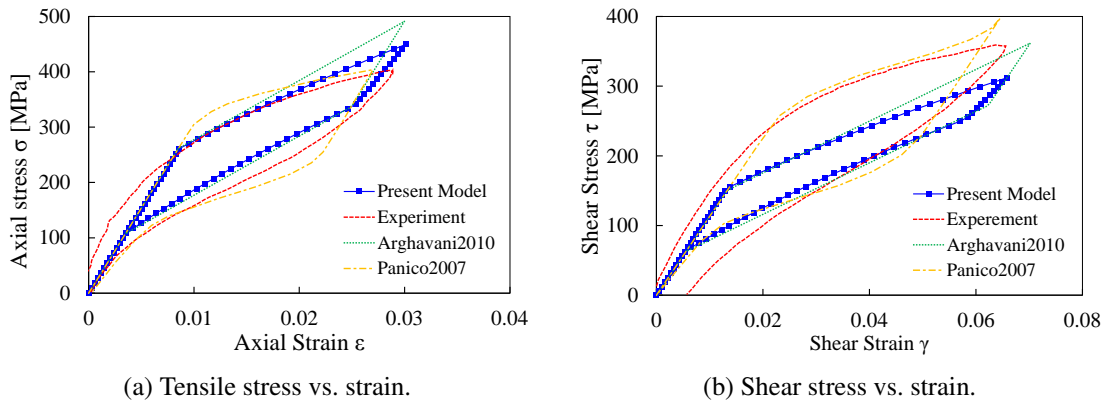


Figure 2.13 Tensile and shear stress-strain curves used to determine the parameters of the ZM model.

The experimental results of [Sittner et al. \(1995\)](#) as well as numerical simulations by [Arghavani et al. \(2010\)](#); [Panico and Brinson \(2007\)](#) are reported on the same figures for comparison. The results are in good agreement overall, with the model predictions being particularly consistent with those of [Arghavani et al. \(2010\)](#). This is likely because both the ZM model and the model by [Arghavani et al. \(2010\)](#) propose similar loading functions and evolution rules for the inelastic deformation of SMAs. Because of the intrinsically different expressions used for the equivalent stress and strain, it is not possible to accurately fit the material behavior in tension and shear simultaneously to those reported by [Sittner et al. \(1995\)](#).

In order to validate the model for the case of nonproportional loading, the loading shown in [Fig. 2.14a](#) is considered. The sample is first subjected to tensile loading corresponding to an increase in normal

stress from 0 to 240 MPa. Shear is then applied up to a maximum shear stress of 195 MPa and then removed. The model used for finite element simulation consists of a single hexahedral element with linear integration (C3D8). The material behavior predicted by the model is shown in terms of shear versus axial strain in Fig. 2.14b. The stress-strain behavior in tension and shear is shown in Figs. 2.14c and 2.14d, respectively. In these figures, the results of numerical simulations using the ZM model are in good agreement overall with the experimental data and with the predictions of the other models considered. From Fig. 2.14b, the material response appears to remain elastic throughout the tensile loading step and starts to become inelastic during the subsequent shear loading step where a deviation from the vertical direction is observed at an approximate shear strain of 0.005. In addition, it is interesting to observe that the predicted axial strain continues to increase during tensile unloading at constant shear stress, which is inconsistent with the experimental curve. A similar observation can also be made for the results obtained by Panico and Brinson (2007). The stress-strain behavior of the material in tension and in shear is shown in Figs. 2.14c and 2.14d, respectively. In Fig. 2.14c, it is interesting to see that the experimental curve appears to be nonlinear during the final unloading step, suggesting either an inelastic or a nonlinear elastic behavior of the material, which is not predicted by any of the models.

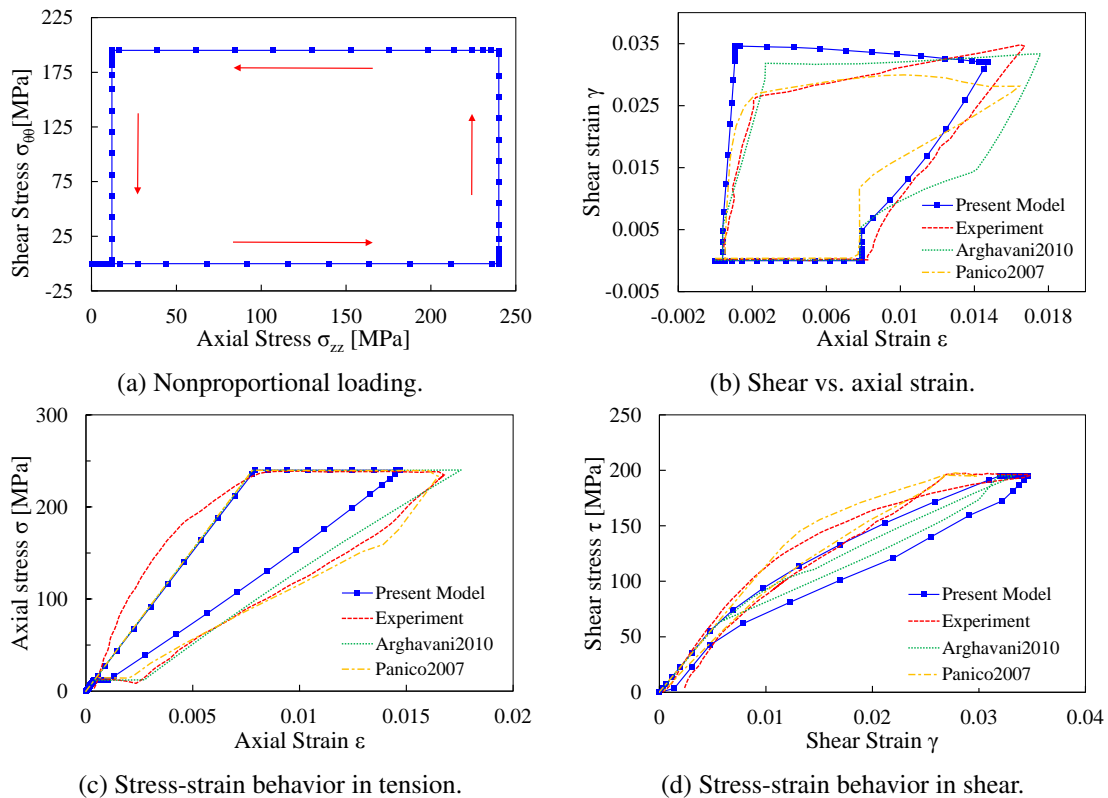
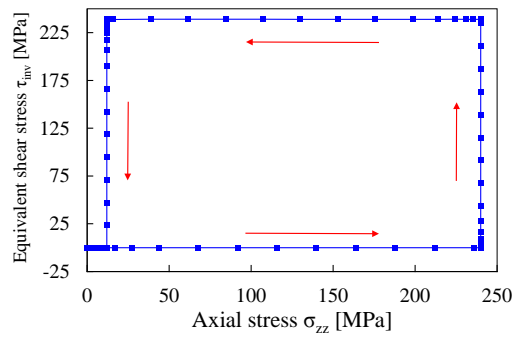


Figure 2.14 Experimental versus simulation results for the square tension-shear loading in Fig. 2.14a.

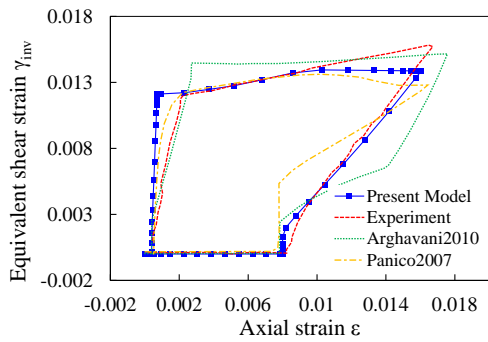
For the second loading case shown in Fig. 2.15a, the parameters of the model are those in Table 2.6. The parameters are chosen to properly fit the *equivalent* stress-strain curve in Fig. 2.15e. As shown in Figs. 2.15b and 2.15d, a better agreement with the experimental data is achieved in this case.

Table 2.6 Material parameters used for simulating the experimental data in [Sittner et al. \(1995\)](#) for the loading case in Fig. 2.15a.

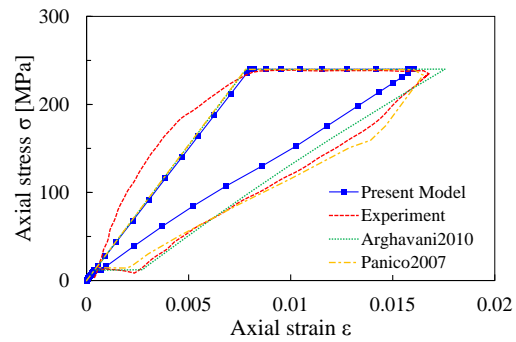
E_A	30 000	MPa	E_M	18 000	MPa
a	0.99	MPa	b	0.25	MPa
ν	0.3		ε_0	0.001	
Y	30	MPa	G	3.5	MPa
α	2000	MPa	β	50 000	MPa
ξ	0.0028	MPa K ⁻¹	κ	0.97	MPa
A_f^0	300	K	θ	340	K



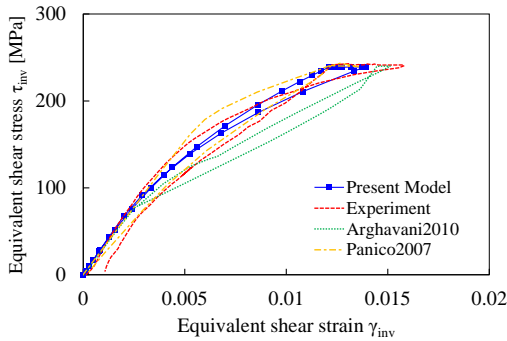
(a) Square loading.



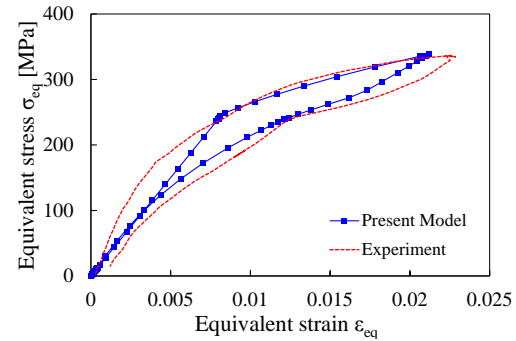
(b) Shear vs. axial strain.



(c) Stress-strain behavior in tension.



(d) Stress-strain behavior in shear.

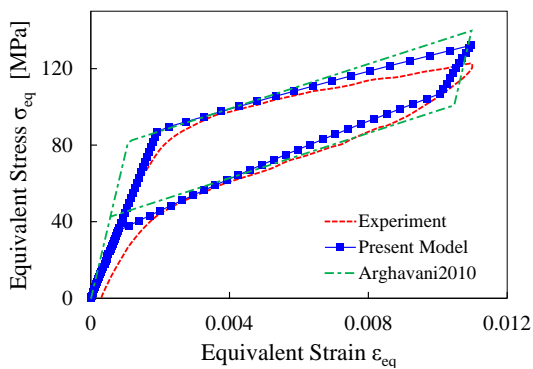


(e) Equivalent stress-strain curve.

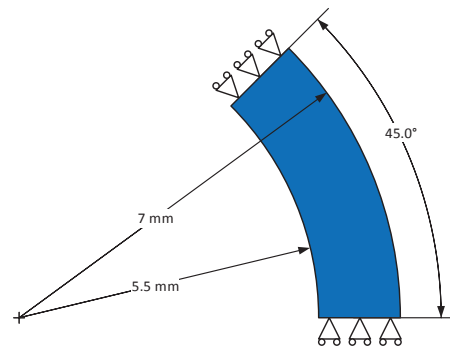
Figure 2.15 Experimental versus simulation results for the loading shown in Fig. 2.15a.

Stress-controlled tension-internal pressure loading

For this last validation, the reference experimental data are those obtained by Bouvet et al. (2002) for a tubular Cu-Al-Be SMA sample subjected to nonproportional loading consisting of combined tension and internal pressure. The parameters used for the simulation are listed in Table 2.2. They are determined using the tensile stress-strain curve in Fig. 2.16a. Because of radial symmetry, only part of the cylinder corresponding to the cross section shown in Fig. 2.16b is used for finite element simulation. The section is 11 mm in internal diameter and 1.5 mm in thickness and the sample is 18 mm long. The mesh consists of 36 hexahedral elements with linear integration (C3D8) for a total of 600 degrees of freedom.



(a) Uniaxial tensile curve used to determine the parameters of the ZM model.



(b) Cross section of the sample used for finite element simulation of the thin-walled cylinder.

Figure 2.16 Sample used in Bouvet et al. (2002).

Because of the relatively high radius-to-thickness ratio, the stress gradient across the thickness for the highest applied load is not negligible as shown in Fig. 2.17. The sample is subjected to the loading shown in Fig. 2.18a, which corresponds to an increase in axial stress to 140 MPa, followed by an increase in the hoop stress to 140 MPa as well. The load is then removed in accordance with the square path shown. The results are calculated by averaging along the thickness of the sample of the computed stress and strain for a point far from the two ends of the cylinder. The predicted strain response is shown in terms of hoop versus axial strain in Fig. 2.18b.

The simulated strain curve is in agreement with the experimental data and with numerical results from Arghavani et al. (2010). Strain curves corresponding to the interior and exterior surfaces of the cylinder are shown for reference on the same figure. The simulation results that better represent the experimental data are those obtained for a point located on the external wall of the sample.

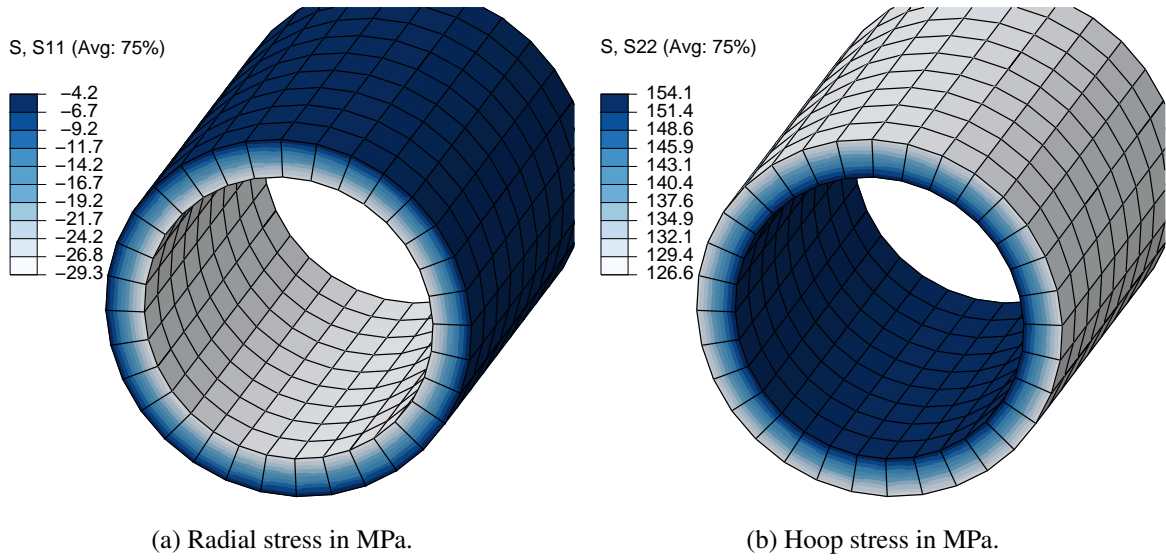


Figure 2.17 Stress variation in the radial direction for the cylinder used for numerical simulations.

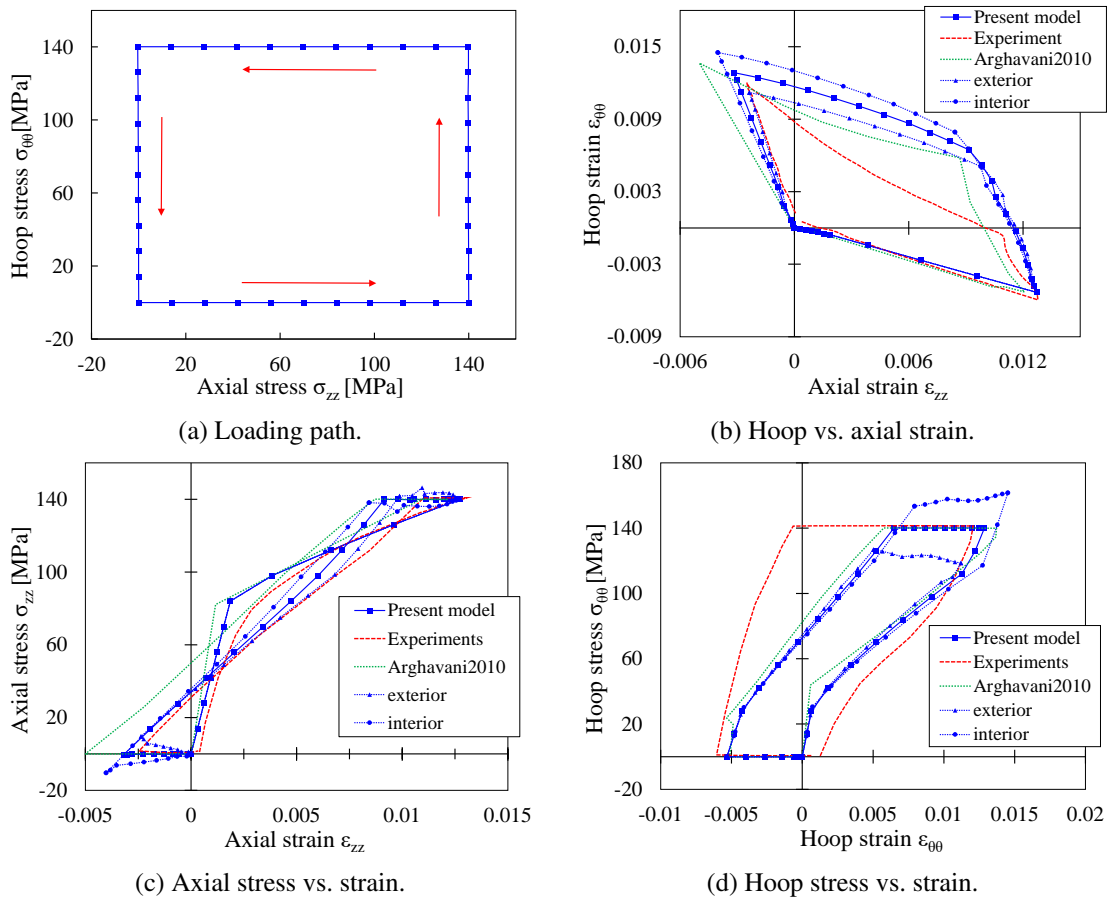


Figure 2.18 Simulation of the experimental data of Bouvet et al. (2002).

2.5 Conclusion

Numerical integration of the ZM model was presented in detail for the general case of SMAs undergoing phase transformation and martensite detwinning and reorientation. The proposed derivations include an analytical expression for the continuous material Jacobian. The algorithmic aspects needed to properly detect active loading states for phase transformation and martensite reorientation, which may potentially take place at the same time, were properly explained. The algorithm was then implemented for use in finite element analysis by means of a user material subroutine. The model was successfully used in predicting experimental and numerical data obtained by several research groups for SMA samples subjected to different types of multiaxial nonproportional loading. The samples ranged from a simple rectangular brick, meshed with a single linear element, to a Nitinol thin-walled cylinder. The loading cases considered varied from simple tension and shear, to combined loading involving tension, shear, and internal pressure leading to complex distributions of stress states within the material. In all these cases, the predictions of the model were in reasonable agreement with the reference data.

The proposed developments are part of an effort to develop numerical simulation capabilities that can be later used to analyze crack propagation and failure by fatigue of SMA devices in presence of heterogeneous and multiaxial stress states. Despite a marked ability to simulate very complex loading scenarios, convergence difficulties were encountered for SMAs with essentially flat phase transformation plateaus. Moreover, the influence of thermomechanical coupling and cyclic loading is not taken into account. These issues are addressed in the following chapters.

Chapter 3

Numerical simulation of pseudoelastic SMAs using the large time increment method

The numerical integration procedure proposed in Chapter 2 (Gu et al., 2015) can simulate very complex loading scenarios. In practice, however, convergence difficulties were encountered for SMAs with essentially flat phase transformation plateaus. To overcome the convergence difficulties, a numerical implementation of the large time increment (LATIN) method for the simulation of shape memory alloys in the pseudoelastic range is presented in this chapter. The method was initially proposed as an alternative to the conventional incremental approach for the integration of nonlinear constitutive models (Boisse et al., 1990). It is adapted here for the simulation of pseudoelastic SMA behavior using the ZM model and is shown to be especially useful in situations where the phase transformation process presents little or lack of hardening. In these situations, a slight stress variation in a load increment can result in large variations of strain and local state variables (Nicola et al., 2008), which may lead to difficulties in numerical convergence. In contrast to the conventional incremental method, the LATIN method solve the global equilibrium and local consistency conditions sequentially for the entire loading path. The achieved solution must satisfy the conditions of static and kinematic admissibility and consistency simultaneously after several iterations. 3D numerical implementation is accomplished using an implicit algorithm and is then used for finite element simulation using the software Abaqus. Computational tests demonstrate the ability of this approach to simulate SMAs presenting flat phase transformation plateaus and subjected to complex loading cases, such as the quasi-static behavior of a stent structure. Some numerical results are contrasted to those obtained using step-by-step incremental integration.

In this chapter, detailed time-discrete equations for the ZM model, adapted for use with the LATIN method are then presented in Section 3.1, in which algorithmic considerations are also introduced. Numerical simulations are carried out in Section 3.2 for a number of loading cases, many of which contrasted with results from the literature. General conclusions and outlook are finally provided in

Section 3.3.

3.1 Integration of constitutive relations using LATIN

The boundary value problem described in Section 2.3.1 can be solved using finite-elements in a step-by-step incremental approach. Time integration of the constitutive equations can be done in this case using an implicit algorithm, like in Chapter 2, which can take into account the possibility of simultaneous phase transformation and martensite detwinning and reorientation. If a solution $\mathcal{S}_n = (\Delta\boldsymbol{\varepsilon}_n, \boldsymbol{\sigma}_n, \Delta z_n, \Delta\boldsymbol{\varepsilon}_{\text{ori},n})$ is known at increment n , a solution \mathcal{S}_{n+1} at increment $n+1$ is obtained by enforcing static and kinematic admissibility as well as consistency conditions simultaneously at this increment. This is typically accomplished using a classical predictor-corrector strategy (Simo and Hughes, 1998) as follows: An elastic stress increment achieving static equilibrium is first determined; the stress increment is then corrected and the state variables adjusted *in the same step* in accordance with the consistency conditions.

As stated in the beginning of this chapter, the algorithm provided in Chapter 2 allows proper simulation of SMAs subjected to complex loading but encounters convergence difficulties in situations where the phase transformation plateaus are exceedingly shallow. To overcome this issue, the LATIN method is used in this chapter for the integration of the ZM model. The method involves two major steps:

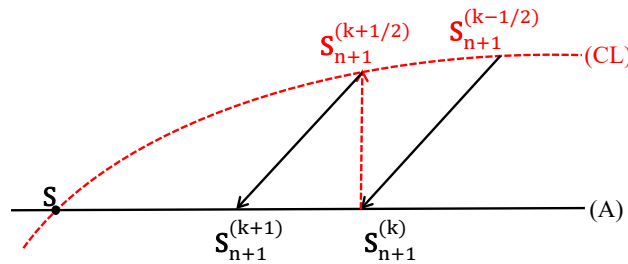


Figure 3.1 Graphic illustration of the algorithmic integration procedure. (A) and (CL) respectively denote admissible and consistent solutions.

1. For each load increment and *for the entire loading path*, find $\mathcal{S} = (\Delta\boldsymbol{\varepsilon}, \boldsymbol{\sigma}, 0, 0)$ in the set of admissible solutions A that satisfies the conditions of static and kinematic admissibility. Requirements of consistency with the loading conditions are relaxed and therefore the dissipative state variables are kept constant in this step.
2. For each load increment and *for the entire loading path*, find $\mathcal{S} = (0, \boldsymbol{\sigma}, \Delta z, \Delta\boldsymbol{\varepsilon}_{\text{ori}})$ in the set of solutions CL consistent with the loading conditions. Conditions of static admissibility are relaxed in this step and the obtained solution does not have immediate physical relevance but rather serves as an intermediate step in the iterative numerical integration process.

The two steps are repeated until a solution is achieved that satisfies the conditions of static and kinematic admissibility in step 1 and the conditions of consistency in step 2 simultaneously.

In the original LATIN method proposed by [Boisse et al. \(1990\)](#), the step for finding admissible solutions involves solving a linear problem. Based on this method, [Maitournam et al. \(2002\)](#) proposed the direct cyclic method (DCM) to directly calculate the stabilized state of an elastoplastic structure under cyclic thermomechanical loading taking advantage of the requirement of periodicity on the state variables to achieve a stable state. [Morin et al. \(2011c\)](#) extended the DCM for SMAs, starting with the weak form of the equilibrium problem written as

$$\forall \omega \in C, \quad \int_{\Omega} (\boldsymbol{\varepsilon} - \boldsymbol{\varepsilon}^{\text{in}}) : \mathbf{K} : \boldsymbol{\varepsilon}[\omega] dV = \int_{\Omega} \rho \mathbf{f} \cdot \omega dV + \int_{\partial\Omega} \mathbf{T} \cdot \omega dS, \quad (3.1)$$

where ω is a test function belonging to the set C of displacement fields, \mathbf{f} is the body force acting over Ω , \mathbf{T} is the contact force acting over the boundary $\partial\Omega$, $\boldsymbol{\varepsilon}$ and $\boldsymbol{\varepsilon}^{\text{in}}$ are the total strain and inelastic strain respectively. In order to linearize the global step, a generalized external force is computed that takes into account the part due to the inelastic strain which is constant during the global step:

$$\forall \omega \in C, \quad \int_{\Omega} \boldsymbol{\varepsilon} : \mathbf{K} : \boldsymbol{\varepsilon}[\omega] dV = \int_{\Omega} \rho \mathbf{f} \cdot \omega dV + \int_{\partial\Omega} \mathbf{T} \cdot \omega dS + \int_{\Omega} \boldsymbol{\varepsilon}^{\text{in}} : \mathbf{K} : \boldsymbol{\varepsilon}[\omega] dV. \quad (3.2)$$

The problem then becomes “linear-elastic” but with different generalized external force for each increment. In this work and in contrast to ([Morin et al., 2011c](#)), the global step in which admissible solutions are determined is still nonlinear as shown in Eq. (3.1), but with known state variables $\boldsymbol{\varepsilon}^{\text{in}}$, which are kept constant in each increment. On the one hand, the only unknown in this step is the statically admissible stress field, which is easy to compute; on the other hand, the procedure can be implemented using a standard “User Material” subroutine like Abaqus’ UMAT. The main drawback of this iterative procedure is an inferior convergence rate compared to the incremental method using an operator split strategy and an exact material Jacobian, it is therefore mostly intended for situations where the incremental approach fails to converge because of, *e.g.*, shallow phase transformation plateaus. The time integration of the ZM model using LATIN method proceeds as follows:

3.1.1 Initialization

The complete loading history is divided into N increments. At the beginning of the iterative procedure, *i.e.* for $k = 0$ where k denotes the iteration number, all the dissipative variables are set to zero for every load increment n .

$$\forall n \in \{1, \dots, N\}, \quad z_n^{(k=0)} = 0, \quad \text{and} \quad \boldsymbol{\varepsilon}_{\text{ori},n}^{(k=0)} = 0. \quad (3.3)$$

3.1.2 Enforcing equilibrium

For each load increment $n + 1$, the solution

$$\mathbf{S}_{n+1}^{(k)} = \left(\Delta \boldsymbol{\varepsilon}_{n+1}^{(k)}, \boldsymbol{\sigma}_{n+1}^{(k)}, \Delta z_{n+1}^{(k)} = 0, \Delta \boldsymbol{\varepsilon}_{\text{ori},n+1}^{(k)} = 0 \right) \quad (3.4)$$

is computed using values of the dissipative variables from the previous iteration ($k - 1/2$):

$$z_{n+1}^{(k)} = z_{n+1}^{(k-1/2)}, \text{ and } \boldsymbol{\varepsilon}_{\text{ori},n+1}^{(k)} = \boldsymbol{\varepsilon}_{\text{ori},n+1}^{(k-1/2)}. \quad (3.5)$$

These fixed variables introduce an imbalance in the system that is accounted for in solving the boundary value problem for equilibrium. The strain is given by the following equation:

$$\boldsymbol{\varepsilon}_{n+1}^{(k)} = \boldsymbol{\varepsilon}_n^{(k)} + \Delta \boldsymbol{\varepsilon}_{n+1}^{(k)}. \quad (3.6)$$

The statically admissible stress fields $\boldsymbol{\sigma}_{n+1}^{(k)}$ are given by the relation

$$\boldsymbol{\sigma}_{n+1}^{(k)} = \mathbf{K}_{n+1}^{(k)} : \left(\boldsymbol{\varepsilon}_{n+1}^{(k)} - z_{n+1}^{(k-1/2)} \boldsymbol{\varepsilon}_{\text{ori},n+1}^{(k-1/2)} \right). \quad (3.7)$$

Since the only unknown in this case is the statically admissible stress field, this problem is easier to solve than the original one that includes additional requirements of consistency with the loading conditions.

3.1.3 Enforcing consistency with the loading conditions

Active loading surfaces are detected in this step and the dissipative variables are updated accordingly for each load increment. The solution in this step is defined as

$$\mathbf{S}_{n+1}^{(k+1/2)} = \left(\Delta \boldsymbol{\varepsilon}_{n+1}^{(k+1/2)} = 0, \boldsymbol{\sigma}_{n+1}^{(k+1/2)}, \Delta z_{n+1}^{(k+1/2)}, \Delta \boldsymbol{\varepsilon}_{\text{ori},n+1}^{(k+1/2)} \right). \quad (3.8)$$

The iteration number ($k + 1/2$) indicates an intermediate iteration between (k) and ($k + 1$). Since the increment of strain is zero, the strain $\boldsymbol{\varepsilon}_{n+1}^{(k+1/2)}$ at this iteration is such that

$$\boldsymbol{\varepsilon}_{n+1}^{(k+1/2)} = \boldsymbol{\varepsilon}_{n+1}^{(k)}. \quad (3.9)$$

The increments of the martensite volume fraction $\Delta z_{n+1}^{(k+1/2)}$ and the inelastic multiplier $\eta_{n+1}^{(k+1/2)}$ are determined using the following iterative scheme described in Eqs. (2.29) and (2.30), obtained by solving the linearized consistency conditions for phase transformation and martensite reorientation. Detailed derivation procedure can be found in Section 2.3.1. Simplified expressions of Δz and η are obtained when only one of the two dissipative processes, phase transformation and orientation, is active. The following values of the state variables are obtained in this case:

$$z_{n+1}^{(k+1/2)} = z_n^{(k+1/2)} + \Delta z_{n+1}^{(k+1/2)}, \quad (3.10)$$

$$\boldsymbol{\varepsilon}_{\text{ori},n+1}^{(k+1/2)} = \boldsymbol{\varepsilon}_{\text{ori},n}^{(k+1/2)} + \Delta \boldsymbol{\varepsilon}_{\text{ori},n+1}^{(k+1/2)}. \quad (3.11)$$

Upon convergence, the stress is determined $\forall n \in \{1, \dots, N\}$ using the relation

$$\boldsymbol{\sigma}_{n+1}^{(k+1/2)} = \mathbf{K}_{n+1}^{(k+1/2)} : \left(\boldsymbol{\varepsilon}_{n+1}^{(k)} - z_{n+1}^{(k+1/2)} \boldsymbol{\varepsilon}_{\text{ori},n+1}^{(k+1/2)} \right). \quad (3.12)$$

3.1.4 Error and stopping criteria

At the end of each iteration $k + 1/2$ over the complete loading path, a residual \mathcal{R} is computed using the relation

$$\mathcal{R} = \frac{1}{J} \sum_{j=1}^J \max_{1 \leq n \leq N} \frac{\left\| \boldsymbol{\sigma}_{n+1}^{(k+1/2)} - \boldsymbol{\sigma}_{n+1}^{(k)} \right\|}{\left\| \boldsymbol{\sigma}_{n+1}^{(k+1/2)} \right\| + \left\| \boldsymbol{\sigma}_{n+1}^{(k)} \right\|}, \quad (3.13)$$

where $\boldsymbol{\sigma}_{n+1}^{(k)}$ and $\boldsymbol{\sigma}_{n+1}^{(k+1/2)}$ are given by Eqs. (3.7) and (3.12), j is the integration point number in the simulated FE model and J is the number of integration points. The iterative process is stopped when \mathcal{R} becomes sufficiently small.

3.1.5 Algorithmic setup

A ‘‘User Material’’ subroutine (UMAT) is developed for the integration of the constitutive equations of the ZM model using the LATIN method in the finite element analysis software Abaqus. The iterative process described in the previous section is implemented by means of Python scripts and repeated until the stopping condition in the previous section is met. The subroutine itself uses the implicit integration algorithm presented below in order to update the stress components and the local state variables separately at the end of each load increment in a given iteration covering a complete loading path. The parameters tol_1 , tol_2 , and tol_3 that appear in the algorithm are numerical tolerances. The algorithm itself is summarized as follows:

Algorithm 2: algorithm of the LATIN method for UMAT.

- 1 Read the parameters of the model and discretize the loading path;
 - 2 Determine the stress field $\sigma_{n+1}^{(k)}$ for load increment $n + 1$ at iteration k using Eq. (3.7);
 - 3 **if** $\mathcal{F}_{z,n+1}^{(k+1/2,0)} \leq tol_1$ and $\mathcal{F}_{ori,n+1}^{(k+1/2,0)} \leq tol_2$ **then**
 - 4 the stress solution is acceptable: Set the state variables to their values at the previous increment for the same iteration:

$$z_{n+1}^{(k+1/2)} = z_n^{(k+1/2)}, \text{ and } \epsilon_{ori,n+1}^{(k+1/2)} = \epsilon_{ori,n}^{(k+1/2)};$$
 - 5 **else if** $\mathcal{F}_{z,n+1}^{(k+1/2,0)} > tol_1$ or $\mathcal{F}_{ori,n+1}^{(k+1/2,0)} > tol_2$ **then**
 - 6 Determine the increment $\Delta z_{n+1}^{(k+1/2)}$ of the martensite volume fraction and the increment $\eta_{n+1}^{(k+1/2)}$ of the inelastic multiplier using Eqs. (2.29) and (2.30);
 - 7 Update the state variables $z_{n+1}^{(k+1/2)}$ and $\epsilon_{ori,n+1}^{(k+1/2)}$ using Eqs. (3.10) and (3.11), set $z = 0$ if $z < 0$ and $z = 1$ if $z > 1$;
 - 8 Determine the stress field $\sigma_{n+1}^{(k+1/2)}$ using Eq. (3.12);
 - 9 Compute the residual \mathcal{R} using Eq. (3.13);
 - 10 Check for convergence:
 - 11 **if** $n = N$ (i.e. *at the last increment*) **then**
 - 12 **if** $\mathcal{R} \leq tol_3$ (*convergence*) **then end then**
 - 13 **goto** 18;
 - 14 **else**
 - 15 Set $k = k + 1$ and $n = 1$ and **goto** 2;
 - 16 **else**
 - 17 Set $n = n + 1$ and **goto** 2;
 - 18 **return**.
-

3.2 Numerical examples and discussions

The UMAT in the previous section is used to simulate several pseudoelastic SMA structures subjected to different loading conditions. The following cases are considered: A single hexahedral SMA element subjected to tensile loading is considered in Section 3.2.1, material parameters resulting in perfectly flat phase transformation plateaus are used in order to illustrate numerical convergence of the proposed UMAT in this case; A cylinder subjected to nonproportional stress-controlled loading cases is presented in Section 3.2.2 for validation against results obtained using the conventional incremental method. The reference data used for the validation are those reported in Gu et al. (2015); In Section 3.2.3, a SMA cylinder is used to simulate stress-controlled nonproportional loading and the numerical result are compared with experimental results available in the literature. The reference data used for the validation are reported by Gu et al. (2015) and Bouvet et al. (2002). The material parameters used for the simulation are obtained by curve fitting to a subset of the reported data; In order to investigate the ability of the present approach to simulate complex structures with large stress gradients in the presence of flat phase transformation plateaus, a SMA plate with a hole in its center subjected to alternating pressure is

considered in Section 3.2.4; Finally, a repeated unit cell (RUC) of stent subjected to radial pressure is presented in Section 3.2.5. A desktop equipped with Intel hexa-core Xeon processors @1.6 GHz and 16 GB of RAM was used to run the simulations. Only one core was used each time.

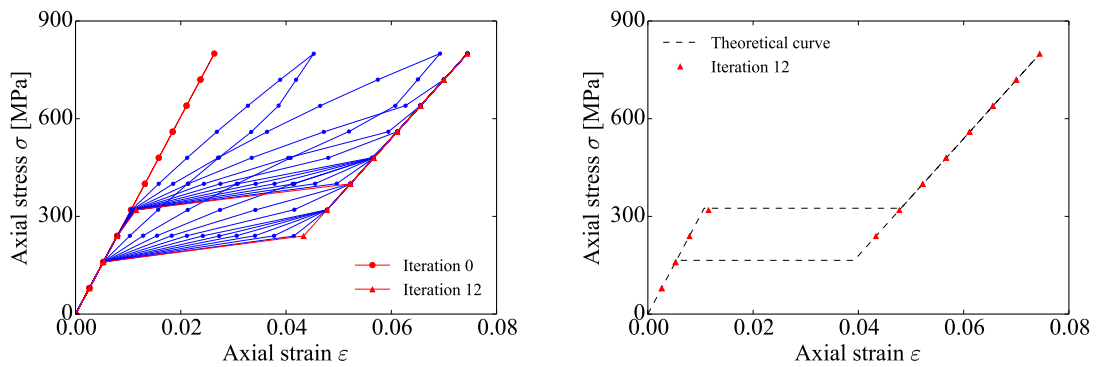
3.2.1 SMA element subjected to uniaxial tension

A single 8-node hexahedral SMA element (Abaqus designation C3D8) is subjected to tensile loading that increases monotonically from 0 to 800 MPa. The reference stress-strain curve for the material is reported in Fig. 3.2b and shows perfectly flat phase transformation plateaus. The simulation completes in this case in 12 iterations using the parameters in Table 3.1 and a tolerance of 0.4 % on the residual \mathcal{R} . Additional iterations are required if a smaller tolerance is desired.

Table 3.1 Material parameters used for finite element analysis of the SMA element subjected to uniaxial tension.

E_A	30 340	MPa	E_M	18 000	MPa
a	2.84	MPa	b	2.84	MPa
ν	0.3		ε_0	0.03	
Y	30	MPa	G	0.9	MPa
α	666.67	MPa	β	1666.67	MPa
ξ	0.26	MPa K ⁻¹	κ	2.09	MPa
A_f^0	280	K	θ	340	K

As shown in Fig. 3.2a, the computed intermediate stress-strain curves are initially perfectly linear, corresponding to dissipative state variables equal to zero, then gradually approach the reference curve in subsequent iterations until a converged solution is obtained as illustrated in Fig. 3.2b.



(a) Intermediate statically admissible behavior. (b) Final iterative solution vs. the reference curve.

Figure 3.2 Simulation of uniaxial stress-strain behavior using LATIN.

With the same material parameters, simulation using the conventional incremental method reported

in Chapter 2 (Gu et al., 2015) aborts at time increment 0.198, corresponding to a stress value of 317.1 MPa and zero martensite volume fraction, exactly at the onset of forward phase transformation. Beyond this point, a slight increase in stress would result in large variation of the strain and other state variables, as the material immediately and completely transforms to martensite. This large variation in a potentially small load increment results in important imbalance that can be challenging to accommodate numerically. Convergence issues can be resolved by introducing some measure of phase transformation hardening and/or making adjustments to the default solver parameters such as the maximum number of iterations per increment. In contrast to the step-by-step incremental method, the LATIN method avoids large variations of strain and state variables in a given increment as shown in Fig. 3.2a.

3.2.2 SMA element subjected to multiaxial loading cases

The three loading cases in Fig. 3.3 are considered in this section. Path 1 corresponds to pure tension,

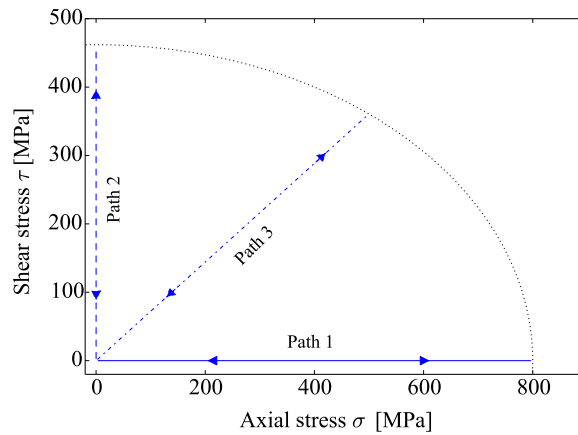
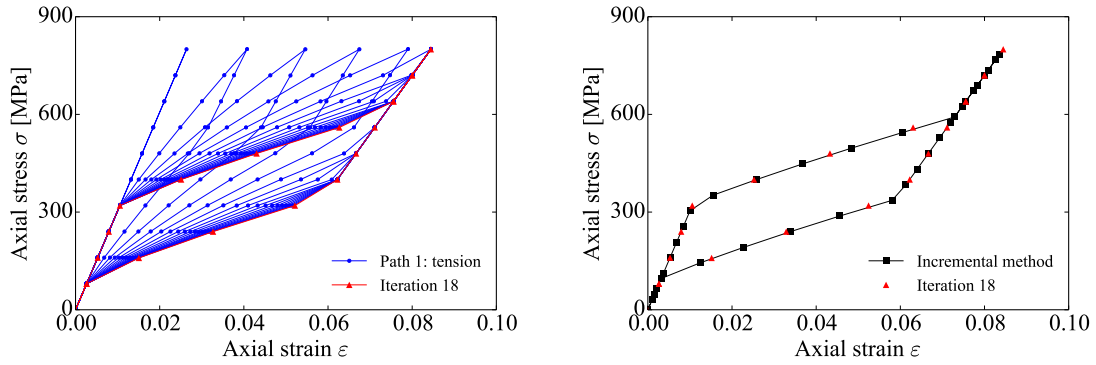


Figure 3.3 Three stress-controlled proportional loading cases.

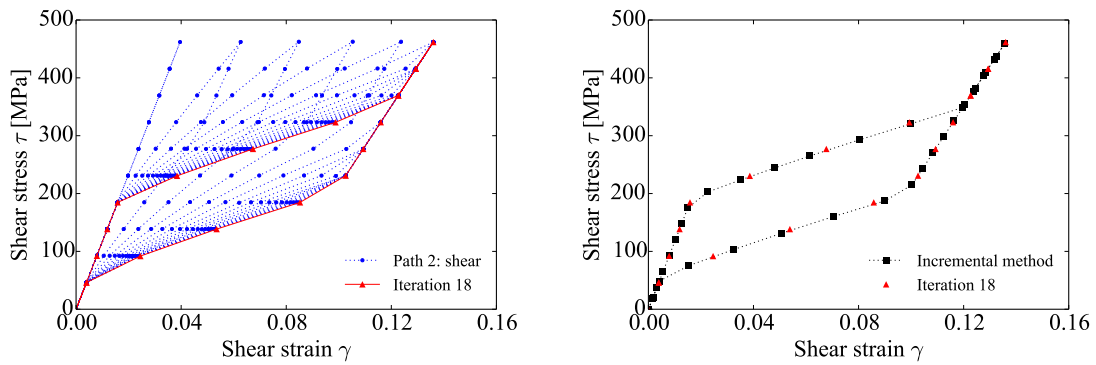
path 2 to pure shear, and path 3 is a combination of both. The simulations are performed on a single fully integrated 8-node hexahedral element (Abaqus designation C3D8) up to a maximum von Mises equivalent stress of 800 MPa in each case. A constant temperature $\theta = 340$ K is considered for which the shape memory alloy is pseudoelastic. The parameters used for the simulations are listed in Table 2.1 and the tolerance on the residual \mathcal{R} is set to 1 %.

18 iterations were required for convergence in these simulations. Intermediate approximations of the stress-strain behavior using the LATIN method are shown in Fig. 3.4a for loading case 1 and comparison of the converged solution with the one obtained using the conventional incremental algorithm in Chapter 2 is shown in Fig. 3.4b. Similar results are reported in Figs. 3.5 and 3.6 for the second and third loading cases. Like in the previous simulations, the first iteration of the stress-strain curve is purely elastic with all the state variables equal to zero. The intermediate curves are similar to those obtained using DCM in Morin et al. (2011c). The results perfectly fit those obtained using the algorithm in Chapter 2.



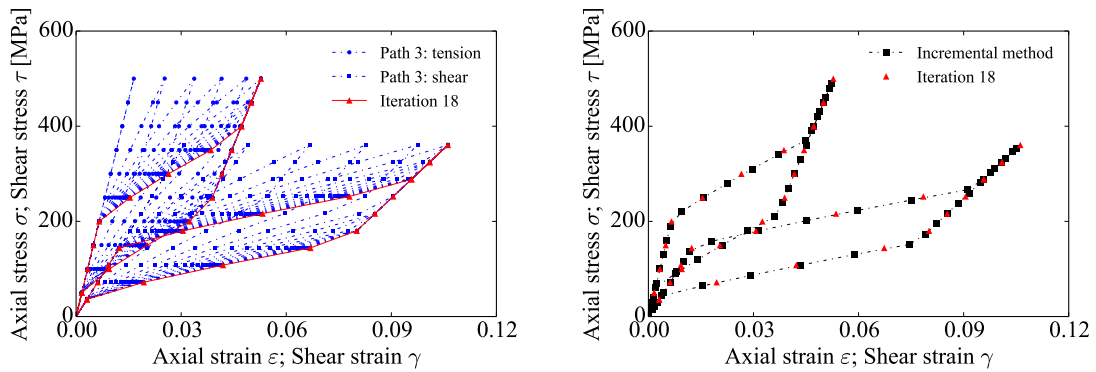
(a) Intermediate statically admissible behavior. (b) Final iterative solution vs. the reference curves.

Figure 3.4 Simulated stress-strain behavior in pure tension (loading path 1).



(a) Intermediate statically admissible behavior. (b) Final iterative solution vs. the reference curves.

Figure 3.5 Simulated stress-strain behavior in pure shear (loading path 2).



(a) Intermediate statically admissible behavior. (b) Final iterative solution vs. the reference curves.

Figure 3.6 Simulated stress-strain behavior and shear versus axial strain for mixed tensile-shear loading (loading path 3).

3.2.3 SMA cylinder subjected to stress-controlled nonproportional loading

For this simulation case, experimental data obtained by [Bouvet et al. \(2002\)](#) are used as reference. The data are obtained using tubular Cu-Al-Be SMA samples subjected to nonproportional loading consisting of mixed tension and internal pressure. The parameters used for the simulation are listed in [Table 2.2](#). Because of radial symmetry, only part of the cylinder corresponding to the cross section shown in [Fig. 2.16b](#) is used for finite element simulation. The section is 11 mm in internal diameter and 1.5 mm in thickness and the sample is 18 mm long. The mesh consists of 36 hexahedral elements with linear integration (C3D8) for a total of 600 degrees of freedom.

The sample is subjected to the loading shown in [Fig. 2.18a](#), which corresponds to an increase in axial stress to 140 MPa, followed by an increase in the hoop stress to 140 MPa as well. The load is then removed in accordance with the square path shown. The results are calculated by averaging along the thickness of the sample of the computed stress and strain for a point far from the two ends of the cylinder. Intermediate transformations of the stress-strain behavior using the LATIN method are shown in terms of hoop versus axial strain in [Fig. 3.7a](#). The comparison of the converged solution with the one obtained using the algorithm in [Chapter 2](#) is shown in [Fig. 3.7b](#). As shown in [Fig. 3.7a](#), the axial-hoop strain

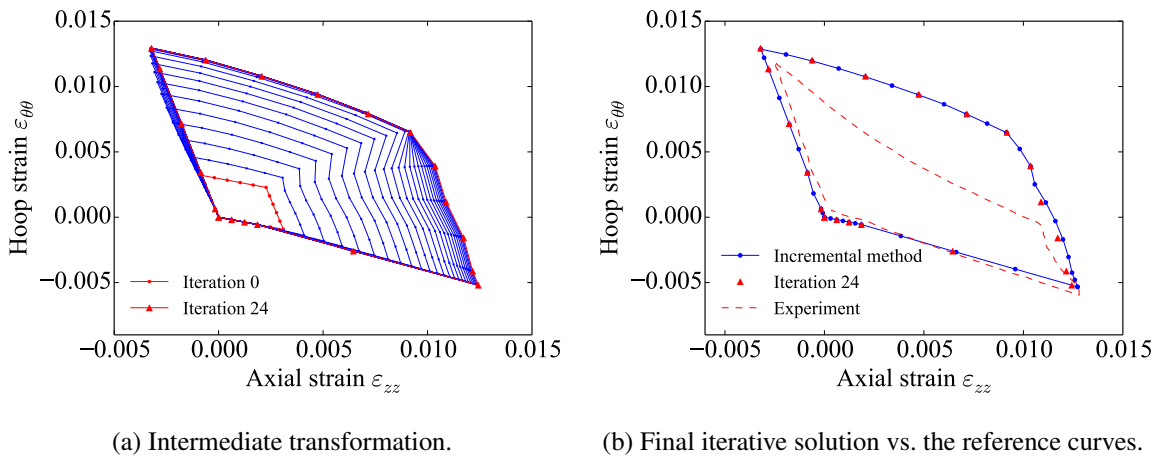


Figure 3.7 Strain behaviors. For comparison, the results obtained using the incremental method are from [Chapter 2](#), the experimental data is from [Bouvet et al. \(2002\)](#).

curve increases in size until convergence, at which point both admissibility and consistency conditions are satisfied simultaneously. The inelastic strain $z\varepsilon_{ori}$ at every point increases from zero to the value in the converged iteration. Similar results are reported in [Figs. 3.8](#) and [3.9](#) in terms of axial stress versus axial strain and hoop stress versus hoop strain.

The converged solution perfectly fits the one obtained using the algorithm in [Chapter 2](#). The red triangular markers representing converged data points obtained using LATIN fall exactly on the reference curves shown in blue in [Figs. 3.7b](#), [3.8b](#) and [3.9b](#). Since the original ZM model is used, in which asymmetry in the material behavior is not considered, the simulations could not predict the tensile-compressive asymmetry in the hoop direction seen in [Figs. 3.7b](#) and [3.9b](#).

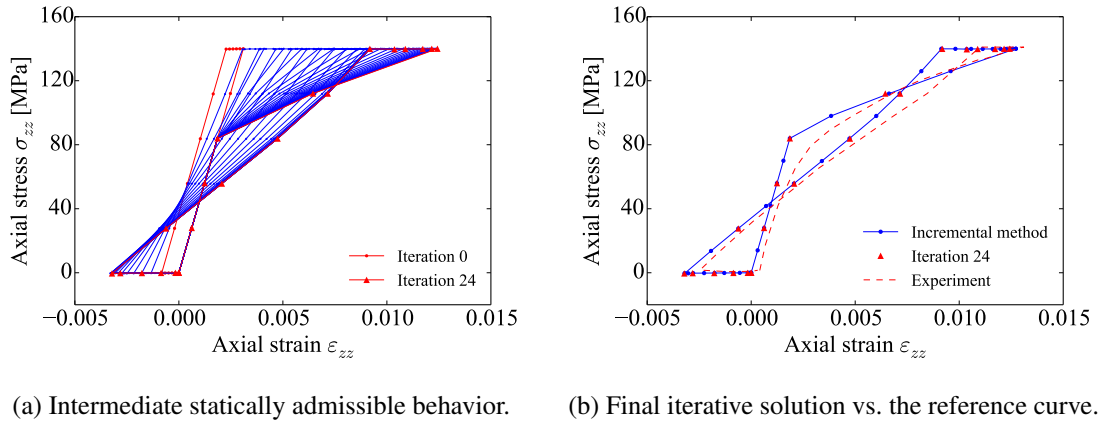


Figure 3.8 Axial stress vs. strain. For comparison, the results obtained using the incremental method are from Chapter 2, the experimental data is from Bouvet et al. (2002).

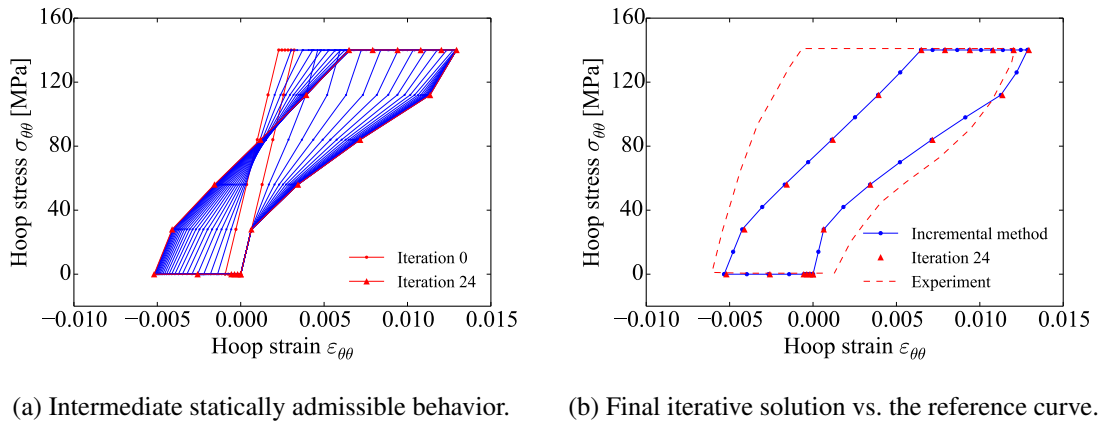


Figure 3.9 Hoop stress vs. strain. For comparison, the results obtained using the incremental method are from Chapter 2, the experimental data is from Bouvet et al. (2002).

3.2.4 SMA plate with a hole

The rectangular SMA plate in Fig. 3.10a is considered in this section to illustrate the ability of the proposed algorithm to simulate complex structures in presence of flat phase transformation plateaus and steep stress gradients. The plate is $100 \text{ mm} \times 120 \text{ mm} \times 15 \text{ mm}$ in size and contains a hole 25 mm in radius at the center. The mesh consists of 128 hexahedral elements with linear integration (C3D8) for a total of 747 degrees of freedom. Biaxial loading is considered, involving horizontal and vertical tractions P1 and P2 as shown in Fig. 3.10. Conditions of isothermal loading are assumed with $\theta = 340 \text{ K}$, for which the material is pseudoelastic.

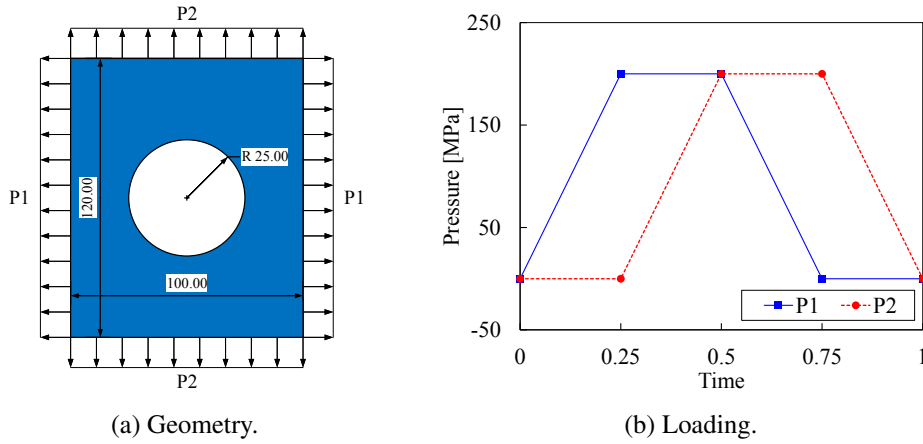


Figure 3.10 Geometry of the plate and loading conditions.

Comparison with step-by-step incremental integration

The comparison is made against simulations using the algorithm in Chapter 2 with the material parameters in Table 2.1. Numerical tolerance on the residual \mathcal{R} is set to 0.1 %, for which 26 iterations are required for convergence. The total solution time was 12 min. The results are shown in Figs. 3.12 to 3.14, which illustrate the distribution of von Mises stress using both integration algorithms at time steps 0.5, 0.75 and 1. The convergence curve of the residual \mathcal{R} is shown as the blue line in Fig. 3.11, in which the red line is the maximum von Mises difference throughout the model and is defined as follows:

$$\bar{\mathcal{R}} = \max_{1 \leq n \leq N} \frac{\|\sigma_{n+1}^{(k+1/2)} - \sigma_{n+1}^{(k)}\|}{\|\sigma_{n+1}^{(k+1/2)}\| + \|\sigma_{n+1}^{(k)}\|}. \tag{3.14}$$

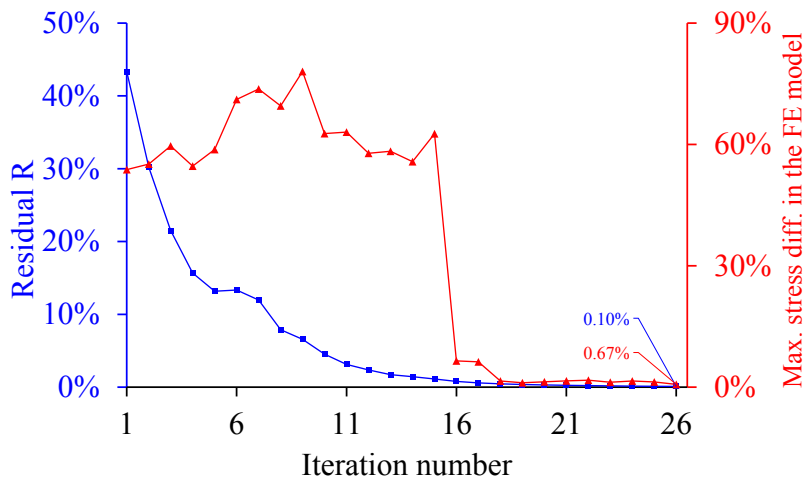


Figure 3.11 The convergence curve of the residual \mathcal{R} (blue) and the change of maximum stress difference $\bar{\mathcal{R}}$ (red) in the model of SMA plate using the material parameters in Table 2.1.

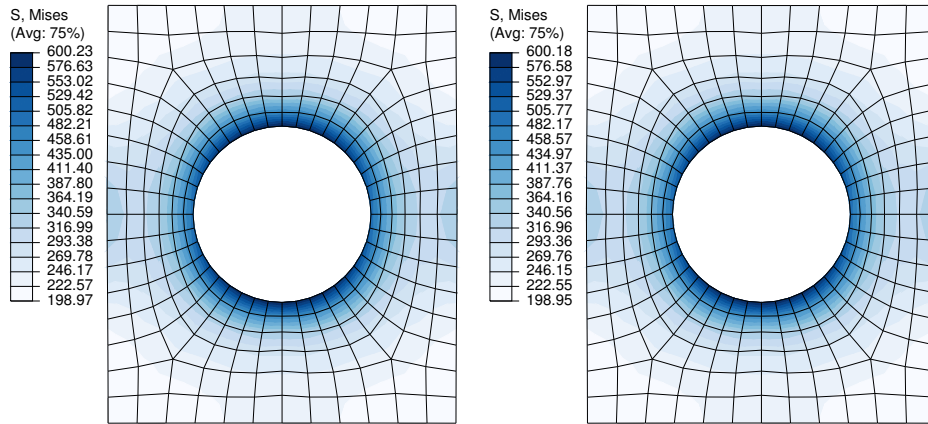


Figure 3.12 Comparison of von Mises stress distribution computed using LATIN (left) and the step-by-step integration algorithm (right) at time step 0.5.

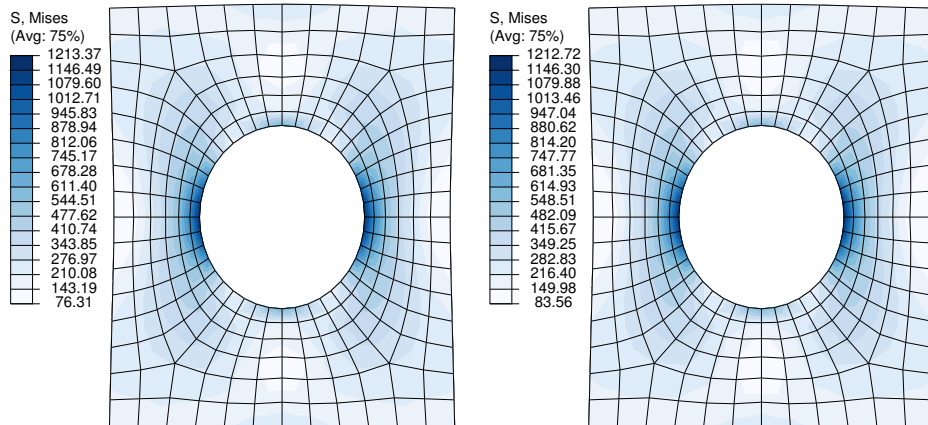


Figure 3.13 Comparison of von Mises stress distribution computed using LATIN (left) and the step-by-step integration algorithm (right) at time step 0.75.

In all cases, very low deviation from the incremental is observed. It is worth noting that the values of stress at time step 1.0 are very small and therefore they are essentially zero, as shown in Fig. 3.14.

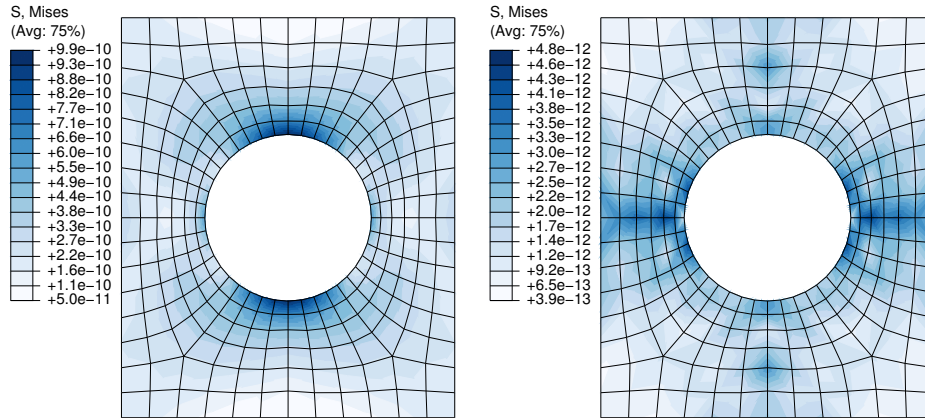


Figure 3.14 Comparison of von Mises stress distribution computed using LATIN (left) and the step-by-step integration algorithm (right) at time step 1.0.

Simulation with flat phase transformation plateaus

In this case, the material parameters used are those in Table 3.1, for which the phase transformation plateaus are perfectly flat. Using the algorithm in Chapter 2, the simulation aborted at time step 0.88 because of convergence difficulty. However, using the LATIN-based algorithm, the simulation completes in 60 iterations with a tolerance of 0.1 % on the residual \mathcal{R} . The total solution time was 28 min and the convergence curve of the residual \mathcal{R} is shown in Fig. 3.15, in which also shown the maximum stress difference $\bar{\mathcal{R}}$. The computed distributions of von Mises stress, maximum principle strain and the volume fraction of martensite in the plate are reported in Figs. 3.16 to 3.18 at time step 0.5, for which the surface tractions P1 and P2 are both maximal, and at time step 0.75 for which P1 decreases to zero with P2 maximum, finally at time step 1.0 for which P1 and P2 are both decrease to zero.

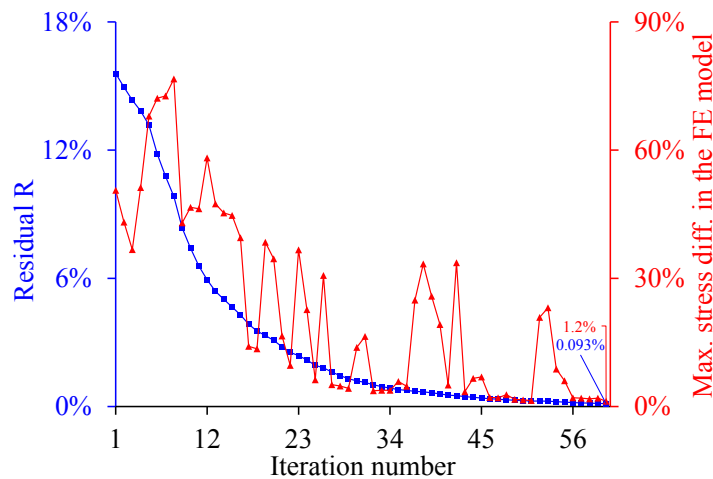


Figure 3.15 The convergence curve of the residual \mathcal{R} (blue) and the change of maximum stress difference $\bar{\mathcal{R}}$ (red) in the model of SMA plate using the material parameters in Table 3.1.

It is worth noting that values of the martensite volume fraction reported outside the interval $[0, 1]$ are a result of the data interpolation carried out by Abaqus in representing the volume fraction contours. The actual values, computed at individual integration points, are well within the acceptable range to a user-specified numerical tolerance. From Figs. 3.17 and 3.18, it is seen that after complete unloading, the strain is completely recovered and the volume fraction of martensite becomes zero throughout the SMA plate.

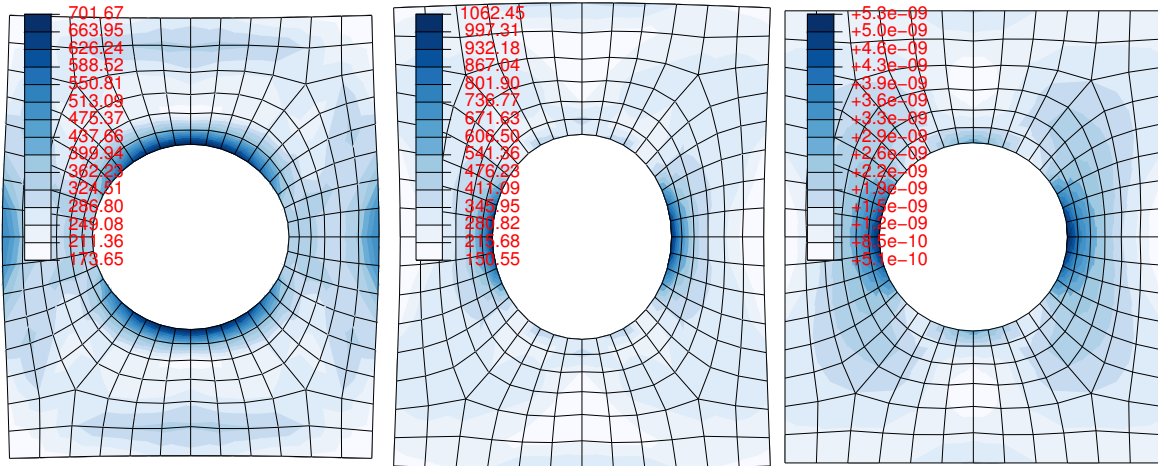


Figure 3.16 The distributions of von Mises stress at time step 0.5 (left), 0.75 (middle) and 1.0 (right).

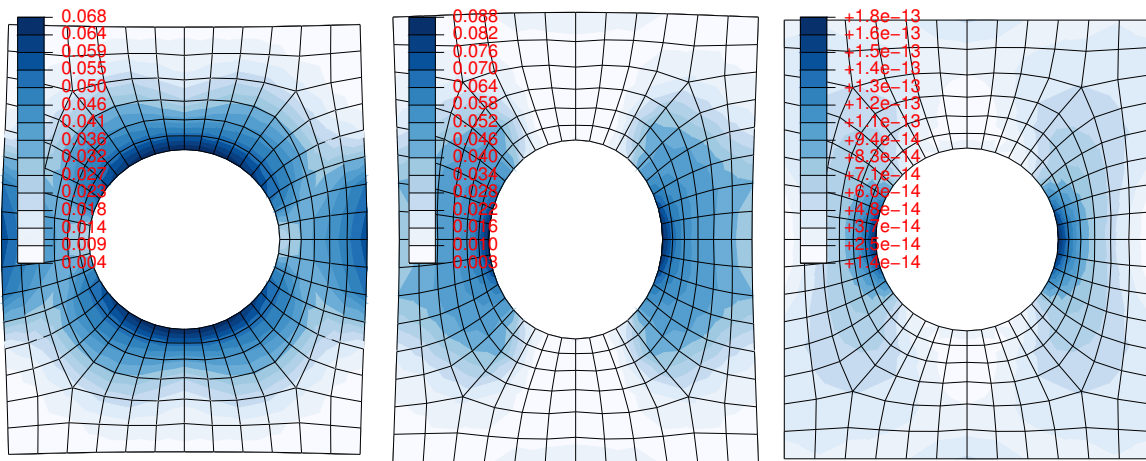


Figure 3.17 The distributions of maximum principle strain at time step 0.5 (left), 0.75 (middle) and 1.0 (right).

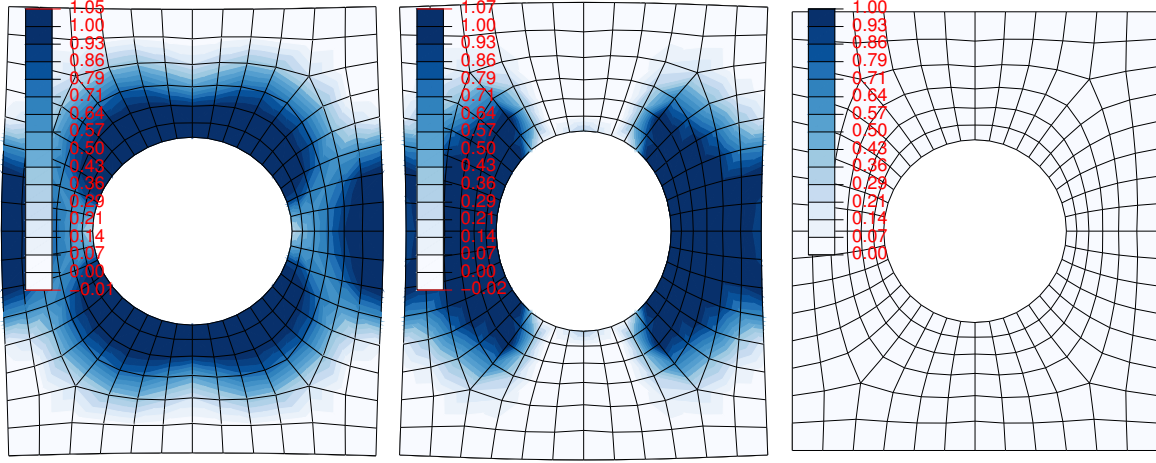


Figure 3.18 The distributions of martensite volume fraction at time step 0.5 (left), 0.75 (middle) and 1.0 (right).

3.2.5 Crimping of a SMA stent

The geometry of the stent¹ considered in this section was obtained through the open source stent design project “Open Stent”, available from <https://github.com/cbonsig/open-stent>. The stent is 11 mm in length and 4 mm in outer radius, with the strut thickness of 0.11 mm. The mesh consists of 4308 hexahedral elements with linear integration (C3D8) for a total of 22 932 degrees of freedom. As shown in Fig. 3.19b Crimping of the stent is accomplished by means of 0.25 MPa pressure on the outer surface of the stent, which is then removed.

Because of symmetry and geometric periodicity of the stent design, a single unit cell of the stent is simulated using a repeated unit cell (RUC). The geometry of the unit cell is shown in Fig. 3.19. Following Xia et al. (2007), unified periodic boundary conditions are imposed on the RUC boundary, as shown in Fig. 3.19a. In this regard, the periodic conditions on the planes K+ and K– are such that

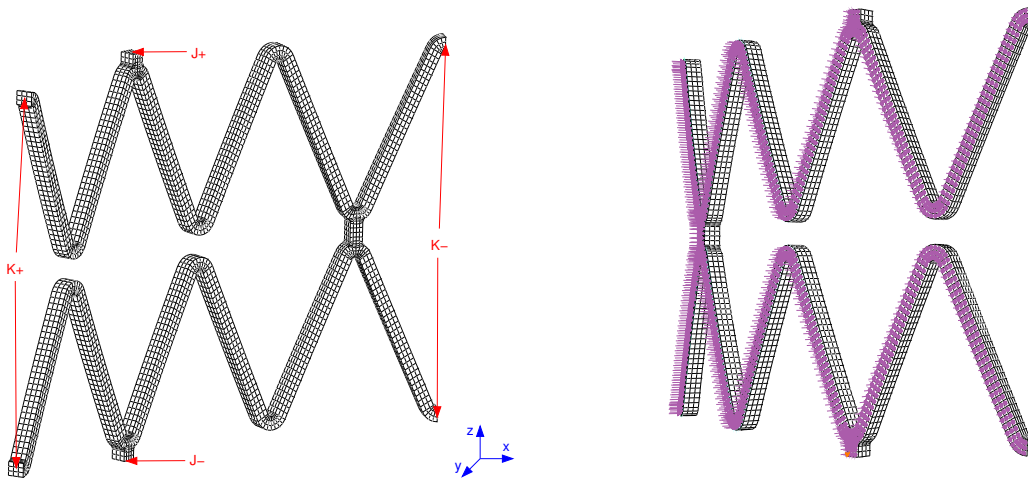
$$u_{\rho}^{K+} = u_{\rho}^{K-}, u_{\phi}^{K+} = u_{\phi}^{K-}, \text{ and } u_z^{K+} = u_z^{K-}, \quad (3.15)$$

where u_{ρ} , u_{ϕ} and u_z are the displacements along the ρ , ϕ and z directions in cylindrical coordinates, respectively. The constraints in Eq. (3.15) imply that a pair of corresponding nodes on the planes K+ and K– experience the same displacements. Similarly, the periodic boundary conditions on the boundary planes J+ and J– can be written as

$$u_{\rho}^{J+} = u_{\rho}^{J-}, u_{\phi}^{J+} = u_{\phi}^{J-}, \text{ and } u_z^{J+} - u_z^{J-} = \Delta l, \quad (3.16)$$

indicating that a pair of corresponding nodes on the planes J+ and J– experience the same displacements in the circumferential and radial directions. Moreover, the difference Δl in the displacement along the

¹Derived from Open Stent Design, Craig Bonsignore, <https://nitinol.com>. (CC BY-SA 3.0)



(a) Planes that applied periodic boundary conditions. (b) Uniform pressure on the outer surface of the stent.

Figure 3.19 Geometry of the stent cell used for simulation using the repeated unit cell (RUC) method.

axial direction is constant for any pair of corresponding points on the two planes $J+$ and $J-$ because the two planes are parallel.

In this case, the material parameters used are those in Table 3.1, for which the phase transformation plateaus are perfectly flat. Using the algorithm in Chapter 2, the simulation aborted at time step 0.49. In contrast, the same simulation carried out using LATIN completed in 49 iterations with 0.1 % tolerance on the residual \mathcal{R} . The total solution time is 56 minutes and the convergence curve of the residual \mathcal{R} is shown in Fig. 3.20. The pressure versus current radius response of the stent during the compression and release process is shown in Fig. 3.21.

The resulting deformation and volume distribution of the von Mises stress are shown in Fig. 3.22. The distribution of the martensite volume fraction in the stent is illustrated in Fig. 3.23. The complete stent shown in the above figures was obtained by patterning the unit cell around the z -axis for improved visibility.

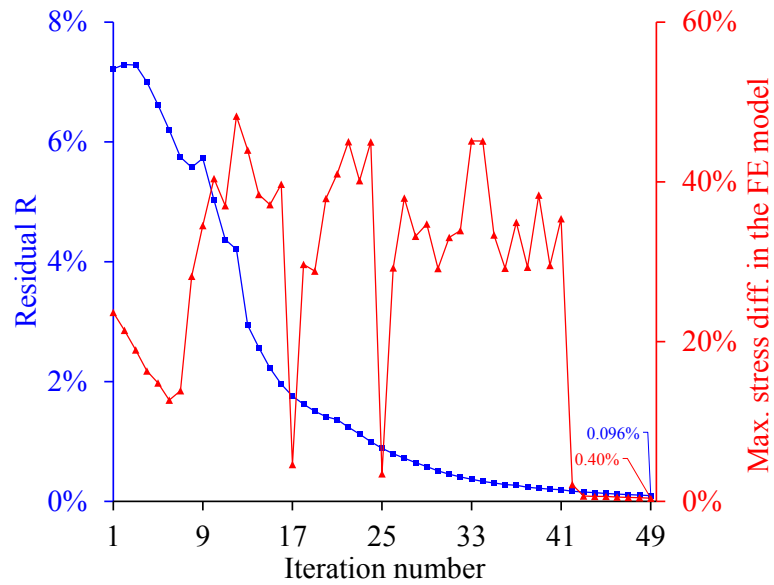


Figure 3.20 The convergence curve of the residual \mathcal{R} (blue) and the change of maximum stress difference $\bar{\mathcal{R}}$ (red) in the model of SMA stent using the material parameters in Table 3.1.

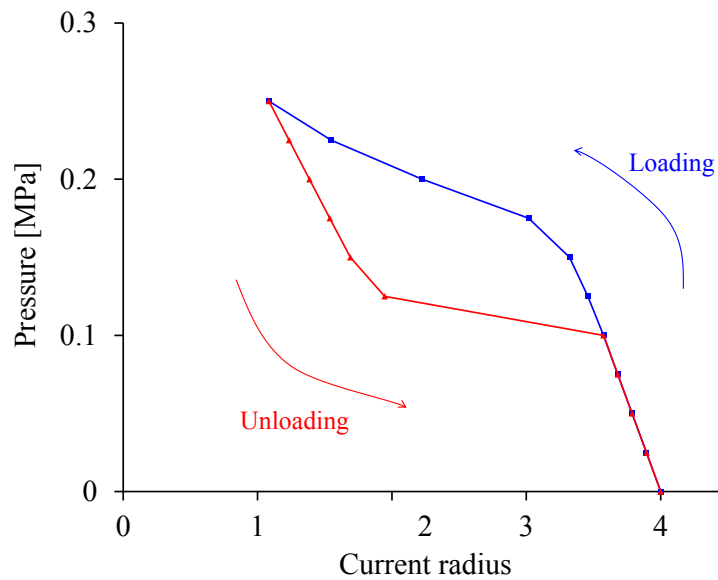


Figure 3.21 The pressure versus current radius response of the stent during the compression and release process.

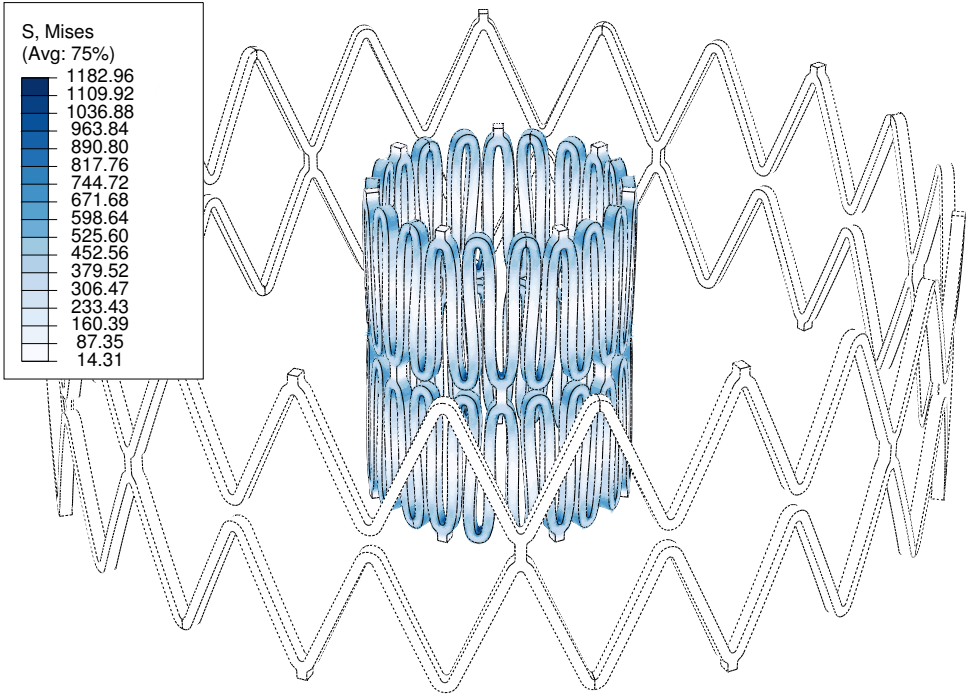


Figure 3.22 Distribution of stress in the stent cell.

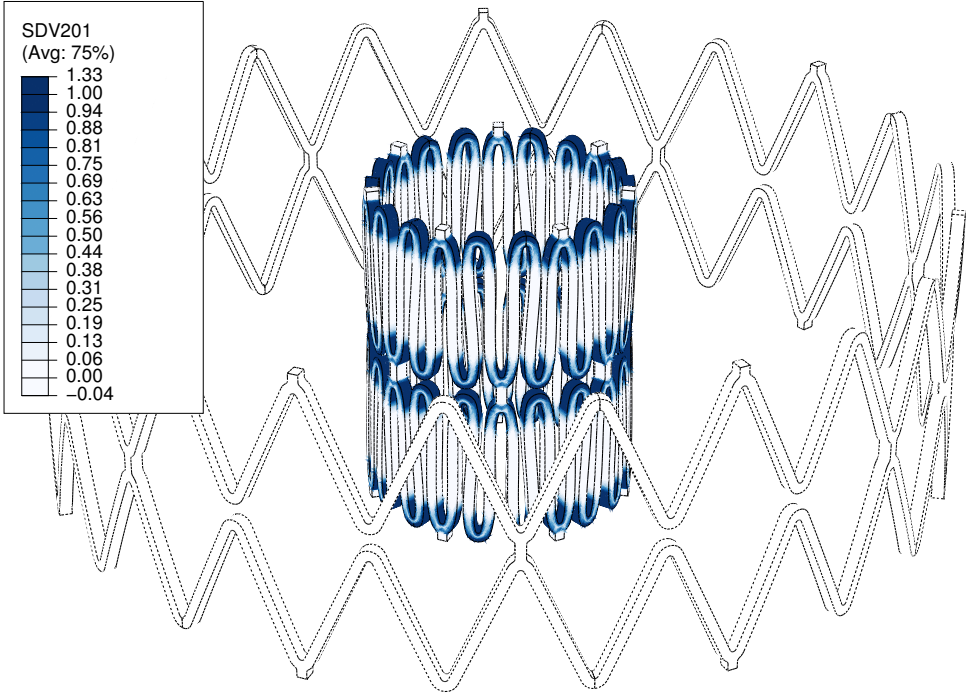


Figure 3.23 Distribution of the martensite volume fraction in the stent cell.

3.3 Conclusion

An implementation of the large time increment method for the integration of constitutive relations for SMAs was presented for the first time in this chapter. The presented approach was demonstrated the ability to overcome the convergence difficulties on simulating SMAs presenting flat phase transformation plateaus. The ZM model was used to illustrate the practicability of the proposed method, which can well be utilized for the integration of similar SMA constitutive models. The LATIN method was programmed into a user material subroutine (UMAT) that was used in several finite element simulations in Abaqus. The UMAT was successful in simulating the behavior of shape memory alloys presenting flat phase transformation plateaus, including samples with complex geometries subjected to nonproportional loading resulting in steep stress gradients. It was also shown to provide results consistent with those obtained using the conventional incremental algorithm in Chapter 2.

Chapter 4

A 3D rate-dependent model for pseudoelastic SMAs subjected to multiaxial and cyclic loading

The previous two chapters deal with non-cyclic behavior of SMAs. As our aim is the design and optimization with respect to fatigue, it is necessary to develop a cyclic model, in order to allow computing a stabilized thermomechanical state under multiaxial and cyclic loading. In this chapter, an extended model is developed to account for cyclic loading effects and thermomechanical coupling in SMAs, including the influence of load rate and temperature on both the rate and value at saturation of residual strain. It is the first such comprehensive model to be successfully utilized for relatively complex simulations involving SMAs subjected to multiaxial nonproportional loading. The derivation of the constitutive equations as well as the time-integration and relevant algorithmic considerations were presented in detail. The model was shown to allow reasonable agreement with several sets of reference experimental and simulation data taken from the literature.

This chapter is organized as follows: Section 4.1 presents a brief review on cyclic behavior and modeling of SMAs. Section 4.2 introduces the extended 3D constitutive model, derived within the framework of generalized standard materials with internal variables (Moumni et al., 2008). The numerical implementation of the model is then presented in Section 4.3, including the derivation of state variable increments and continuous tangent moduli. Several numerical examples are presented and discussed in Section 4.4, and a general conclusion and outlook are finally provided in Section 4.5.

4.1 Literature review on cyclic behavior of SMAs

The stress-strain curve of pseudoelastic SMAs shows a notable hysteresis loop and, usually, a certain amount of residual strain resulting from incomplete strain recovery. If the material is subjected to cyclic loading, the amount of residual strain that accumulates in each cycle (Miyazaki et al., 1986;

Kan et al., 2016) tends to decrease until an asymptotic state is reached in which hysteresis becomes stable and residual strain saturates. The deformation process, including the rate at which residual strain accumulates, is known to be affected by the loading rate (Morin et al., 2011a,b; Saleeb et al., 2015; Dunić et al., 2016) due to strong thermomechanical coupling (Shaw and Kyriakides, 1995; Grabe and Bruhns, 2008; Dunić et al., 2014). In addition, recent experimental evidence (Kan et al., 2016) suggests that the observed rate dependence also extends to the maximum amount of residual strain that can be achieved at saturation.

Several models capable of describing the cyclic behavior of SMAs have been proposed in the literature. The usual modeling approach involves the introduction of a dedicated state variable to represent residual strain. Depending on the chemical composition of the SMA and the extent of mechanical loading (Saint-Sulpice et al., 2009), the formation of residual strain is explained either as a consequence of plastic slip (e.g. Bo and Lagoudas, 1999; Lagoudas and Entchev, 2004; Hartl et al., 2010; Yu et al., 2013), or a manifestation of jammed martensite that could not transform back to austenite upon unloading (e.g. Tanaka et al., 1995; Lexcellent and Bourbon, 1996; Lexcellent et al., 2000; Auricchio et al., 2003; Moumni et al., 2005; Zaki and Moumni, 2007a; Kang et al., 2009; Morin et al., 2011b). The presence of jammed martensite is explained by the appearance, within the SMA, of localized residual stress fields because of dislocation arrangements required to maintain strain compatibility at grain boundaries. A model that simultaneously accounts for residual strain and the presence of jammed martensite was proposed by Kan and Kang (2010). The influence of loading rate on residual strain was more recently considered by Yu et al. (2015) who proposed a macroscopic 3D model in which the rate dependence is interpreted as a consequence of physical interaction between phase transformation and plastic slip in the austenite phase. However, the simulations presented by the authors were limited to uniaxial loading cases. In this work, we proposed an extended constitutive model in which the magnitude of the residual strain at saturation is influenced by temperature. As the loading rate changes, the temperature of the SMA is affected because of strong thermomechanical coupling. More specifically, the competition of dissipated energy due to inelastic processes and latent heat exchange due to first-order phase transformation results in temperature variations that affect the amount of residual strain predicted by the model at saturation.

4.2 The extended 3D constitutive model for pseudoelastic SMAs

The model is developed based on the generalized standard materials framework (Halphen and Nguyen, 1974) that was extended to account for constraints on the state variables (Moumni, 1995; Moumni et al., 2008). The Helmholtz free energy density Ψ at a material point can be written as

$$\Psi = (1 - z)\Psi_A + z\Psi_M + \Psi_I + \Psi_\theta, \quad (4.1)$$

where z is the local martensite volume fraction, Ψ_A and Ψ_M are the free energy densities of austenite and martensite, respectively. Ψ_I is the free energy density contributed by austenite-martensite interaction

and Ψ_θ is the free energy density related to temperature.

Following [Zaki and Moumni \(2007a\)](#) and including the effect of thermal expansion, the free energy densities of austenite and martensite are written as

$$\Psi_A = \frac{1}{2}(\boldsymbol{\varepsilon}_A - \boldsymbol{\varepsilon}_r - \boldsymbol{\alpha}_A \Delta\theta) : \mathbf{K}_A : (\boldsymbol{\varepsilon}_A - \boldsymbol{\varepsilon}_r - \boldsymbol{\alpha}_A \Delta\theta), \quad (4.2)$$

$$\Psi_M = \frac{1}{2}(\boldsymbol{\varepsilon}_M - \boldsymbol{\varepsilon}_{\text{ori}} - \boldsymbol{\varepsilon}_r - \boldsymbol{\alpha}_M \Delta\theta) : \mathbf{K}_M : (\boldsymbol{\varepsilon}_M - \boldsymbol{\varepsilon}_{\text{ori}} - \boldsymbol{\varepsilon}_r - \boldsymbol{\alpha}_M \Delta\theta) + C(\theta) - \frac{2}{3} \mathbf{B} : \boldsymbol{\varepsilon}_{\text{ori}}, \quad (4.3)$$

where $\boldsymbol{\varepsilon}_A$ and $\boldsymbol{\varepsilon}_M$ are the local austenite and martensite strain tensors, $\boldsymbol{\varepsilon}_{\text{ori}}$ and $\boldsymbol{\varepsilon}_r$ are the martensite orientation and residual strain tensors. $\Delta\theta = \theta - \theta_r$ is the deviation of the material temperature θ from a reference value θ_r . \mathbf{K}_A , \mathbf{K}_M , $\boldsymbol{\alpha}_A$, and $\boldsymbol{\alpha}_M$ are material constants representing the elastic stiffness tensors of austenite and martensite, and the tensors of thermal expansion coefficients for these phases, respectively. \mathbf{B} is a measure of internal stress that develops during cyclic training and allows unassisted transformation of austenite into oriented martensite. $C(\theta)$ is an energy density that depends on temperature according to the relation

$$C(\theta) = \xi \left(\theta - A_f^0 \right) + \kappa, \quad (4.4)$$

where ξ and κ are material parameters and A_f^0 is the reverse phase transformation finish temperature at zero stress.

The free energy density contributed by austenite-martensite interaction is proposed to have the following expression:

$$\Psi_I = G \frac{z^2}{2} + \frac{z}{2} [\alpha z + \beta(1-z)] \left(\frac{2}{3} \boldsymbol{\varepsilon}_{\text{ori}} : \boldsymbol{\varepsilon}_{\text{ori}} \right), \quad (4.5)$$

where α , β and G are material parameters that control the shape of the pseudoelastic hysteresis loop and the stress-strain curve slopes during phase transformation.

Following [Morin et al. \(2011a\)](#), the free energy density related to temperature can be written as

$$\Psi_\theta = \rho C_p \left[\Delta\theta - \theta \ln \left(\frac{\theta}{\theta_r} \right) \right], \quad (4.6)$$

where ρ and C_p are the mass density and specific heat capacity, respectively.

The cumulative martensite fraction z_e , used to account for the effects of training, is defined as

$$z_e = \int_0^t |\dot{z}| dt. \quad (4.7)$$

The parameters α , β , ξ , κ , and G are functions of the cumulative martensite fraction z_e . They are defined using the relation,

$$f = f^{(0)} + \left(f^{(\text{sat})} - f^{(0)} \right) \left(1 - \exp(-z_e/\tau) \right), \quad (4.8)$$

where $f = \{\alpha, \beta, \xi, \kappa, G\}$, $f^{(0)}$ is the initial value of f prior to loading and $f^{(\text{sat})}$ its asymptotic value.

The procedure for characterizing the material parameters is identical to the one described in Zaki and Moumni (2007b).

The derivation of the model gives the following stress-strain relation:

$$\boldsymbol{\sigma} = \mathbf{K} : [\boldsymbol{\varepsilon} - z\boldsymbol{\varepsilon}_{\text{ori}} - \boldsymbol{\varepsilon}_r - \boldsymbol{\alpha}\Delta\theta], \quad (4.9)$$

where $\boldsymbol{\sigma}$ and $\boldsymbol{\varepsilon}$ are the Cauchy stress tensor and total strain tensor. The elastic stiffness tensor \mathbf{K} and thermal expansion tensor $\boldsymbol{\alpha}$ are functions of phase composition:

$$\mathbf{K} = [(1-z)\mathbf{K}_A^{-1} + z\mathbf{K}_M^{-1}]^{-1}, \quad (4.10)$$

$$\boldsymbol{\alpha} = (1-z)\boldsymbol{\alpha}_A + z\boldsymbol{\alpha}_M. \quad (4.11)$$

The volume fraction of martensite is constrained to the interval $[0, 1]$, and the recoverable inelastic deformation of martensite is limited by a maximum ε_0 that depends on the material used. The further assumption of complete orientation of stress-induced martensite once it forms reduces the constraint on the orientation strain to an equality. These constraints can be expressed as

$$z \geq 0, \quad 1 - z \geq 0, \quad \text{and} \quad \varepsilon_0 - \sqrt{\frac{2}{3}\boldsymbol{\varepsilon}_{\text{ori}} : \boldsymbol{\varepsilon}_{\text{ori}}} = 0, \quad (4.12)$$

where ε_0 is a scalar that depends on z_e according to Eq. (4.8):

$$\varepsilon_0^{(0)} = \gamma^{(0)}, \quad \text{and} \quad \varepsilon_0^{(\text{sat})} = \gamma^{(\text{sat})} - \varepsilon_r^{(\text{sat})}, \quad (4.13)$$

where $\gamma^{(0)}$ and $\gamma^{(\text{sat})}$ are the maximum inelastic strain prior to the first loading cycle and upon stabilization, respectively.

The thermodynamic forces associated with z and $\boldsymbol{\varepsilon}_{\text{ori}}$ are taken as sub-gradients of a pseudopotential of dissipation

$$\mathcal{D} := D(\dot{z}, \dot{\boldsymbol{\varepsilon}}_{\text{ori}}) = [a(1-z) + bz]|\dot{z}| + z^2 Y \sqrt{\frac{2}{3}\dot{\boldsymbol{\varepsilon}}_{\text{ori}} : \dot{\boldsymbol{\varepsilon}}_{\text{ori}}}, \quad (4.14)$$

where a , b , and Y are material parameters. The loading functions for forward and reverse phase transfor-

mation \mathcal{F}_z^1 and \mathcal{F}_z^2 and for martensite reorientation \mathcal{F}_{ori} can be defined as

$$\begin{aligned} \mathcal{F}_z^1 = & \frac{1}{2} \left[El_{\text{MA}} \boldsymbol{\sigma} : \boldsymbol{\sigma} + P_{\text{MA}} (\text{tr} \boldsymbol{\sigma})^2 \right] + \left(\boldsymbol{\sigma} + \frac{2}{3} \mathbf{B} \right) : (\boldsymbol{\varepsilon}_{\text{ori}} + \boldsymbol{\alpha}_{\text{MA}} \Delta \theta) \\ & - C(\theta) - (G + b)z - a(1 - z) - \left[(\alpha - \beta)z + \frac{\beta}{2} \right] \varepsilon_0^2, \end{aligned} \quad (4.15)$$

$$\begin{aligned} \mathcal{F}_z^2 = & -\frac{1}{2} \left[El_{\text{MA}} \boldsymbol{\sigma} : \boldsymbol{\sigma} + P_{\text{MA}} (\text{tr} \boldsymbol{\sigma})^2 \right] - \left(\boldsymbol{\sigma} + \frac{2}{3} \mathbf{B} \right) : (\boldsymbol{\varepsilon}_{\text{ori}} + \boldsymbol{\alpha}_{\text{MA}} \Delta \theta) \\ & + C(\theta) + (G - b)z - a(1 - z) + \left[(\alpha - \beta)z + \frac{\beta}{2} \right] \varepsilon_0^2, \end{aligned} \quad (4.16)$$

$$\mathcal{F}_{\text{ori}} = \left\| \left(\boldsymbol{\sigma} + \frac{2}{3} \mathbf{B} \right) - \frac{2}{3\varepsilon_0^2} \left[\left(\boldsymbol{\sigma} + \frac{2}{3} \mathbf{B} \right) : \boldsymbol{\varepsilon}_{\text{ori}} \right] \boldsymbol{\varepsilon}_{\text{ori}} \right\|_{\text{VM}} - zY, \quad (4.17)$$

where El_{MA} , P_{MA} , and $\boldsymbol{\alpha}_{\text{MA}}$ are material constants. The evolution of the martensite volume fraction z (forward and reverse phase transformation) and martensite orientation strain tensor $\boldsymbol{\varepsilon}_{\text{ori}}$ are governed by the consistency conditions associated with the loading functions. They can be expressed in terms of the Kuhn-Tucker conditions as

$$\begin{aligned} \dot{z} \geq 0, \quad \mathcal{F}_z^1(\boldsymbol{\sigma}, \boldsymbol{\varepsilon}_{\text{ori}}, z, \theta) \leq 0, \quad \dot{z} \mathcal{F}_z^1 &= 0, \\ \dot{z} \leq 0, \quad \mathcal{F}_z^2(\boldsymbol{\sigma}, \boldsymbol{\varepsilon}_{\text{ori}}, z, \theta) \leq 0, \quad -\dot{z} \mathcal{F}_z^2 &= 0, \\ \eta \geq 0, \quad \mathcal{F}_{\text{ori}}(\boldsymbol{\sigma}, \boldsymbol{\varepsilon}_{\text{ori}}, z) \leq 0, \quad \eta \mathcal{F}_{\text{ori}} &= 0, \end{aligned} \quad (4.18)$$

where η is positive scalar, so that $\dot{\boldsymbol{\varepsilon}}_{\text{ori}} = N\eta$, and N is a vector indicating the direction of the orientation strain rate. The evolution of the residual strain $\boldsymbol{\varepsilon}_r$ and of the internal stress \mathbf{B} are governed by the following empirical laws:

$$\dot{\boldsymbol{\varepsilon}}_r = \frac{\boldsymbol{\varepsilon}_r^{(\text{sat})}}{\tau} \left(\frac{3}{2} \frac{s}{\sigma_{\text{VM}}} \right) \exp(-z_e/\tau) \dot{z}_e, \quad (4.19)$$

$$\dot{\mathbf{B}} = \frac{\mathbf{B}^{(\text{sat})}}{\tau} \frac{\boldsymbol{\varepsilon}_{\text{ori}}}{\varepsilon_0} \exp(-z_e/\tau) \dot{z}_e, \quad (4.20)$$

where $\boldsymbol{\varepsilon}_r^{(\text{sat})}$ and $\mathbf{B}^{(\text{sat})}$ are positive scalars. $\boldsymbol{\varepsilon}_r^{(\text{sat})}$ is associated with the saturated residual strain in tension under isothermal conditions. Recent experimental data shows that the residual strain can be influenced by strain rate (Kan et al., 2016) and temperature (Yu et al., 2014). The saturated residual strain increases with the increase of test temperature or strain rate. The main reason for this coupling is the dependence of the phase transformation stress on temperature. Higher transformation stress increases the dislocation density and slipping, which could jam more martensite after unloading to zero stress and increase the residual strain at the macroscopic scale. In order to model the coupling between residual strain and temperature, $\boldsymbol{\varepsilon}_r^{(\text{sat})}$ is defined to be dependent on temperature in linearized form:

$$\boldsymbol{\varepsilon}_r^{(\text{sat})} = \phi\theta + \nu, \quad (4.21)$$

where ϕ and ν are material parameters. In Eq. (4.21), the term θ accounts for the influence of temperature on the residual strain due to thermomechanical coupling. Indeed, loading rate and stress level can also influence the value of saturated residual strain. But these influence is already added in by the temperature term in Eq. (4.21) due to thermomechanical coupling. The two material parameters ϕ and ν can be obtained by two isothermal cyclic tensile experiments under different test temperatures. Every cyclic tensile experiment gives a data point $\{\theta, \varepsilon_r^{(\text{sat})}\}$. A series of such data points can be substituted into Eq. (4.21) to calculate the two material parameters $\{\phi, \nu\}$.

The mechanical response of pseudoelastic SMA structure has strong loading rate dependence. From an experimental point of view, the dependence is due to the internal heat generation and absorption during phase transformation. The first law of thermodynamics gives:

$$\dot{e} - \boldsymbol{\sigma} : \dot{\boldsymbol{\varepsilon}} - r + \nabla \mathbf{q} = 0, \quad (4.22)$$

where e and r are internal energy and external heat source, respectively. \mathbf{q} is the heat influx vector. The Helmholtz free energy Ψ and its time differentiation $\dot{\Psi}$ in the spatial configuration are given by

$$\Psi = e - s\theta, \text{ and } \dot{\Psi} = \dot{e} - \dot{s}\theta - s\dot{\theta}, \quad (4.23)$$

where s is the entropy. Combining Eqs. (4.22) and (4.23), one can eliminate the internal energy to get

$$\dot{\Psi} = \boldsymbol{\sigma} : \dot{\boldsymbol{\varepsilon}} + r - \nabla \mathbf{q} - \dot{s}\theta - s\dot{\theta}. \quad (4.24)$$

The Helmholtz free energy Ψ and entropy s are assumed here to depend on the same state variables

$$\Psi = \psi(\boldsymbol{\varepsilon}, \boldsymbol{\varepsilon}_{\text{ori}}, \boldsymbol{\varepsilon}_r, \mathbf{B}, z, \theta), \quad (4.25)$$

$$s = s(\boldsymbol{\varepsilon}, \boldsymbol{\varepsilon}_{\text{ori}}, \boldsymbol{\varepsilon}_r, \mathbf{B}, z, \theta). \quad (4.26)$$

The time differentiation of Ψ and s then gives

$$\dot{\Psi} = \frac{\partial \psi}{\partial \boldsymbol{\varepsilon}} : \dot{\boldsymbol{\varepsilon}} + \frac{\partial \psi}{\partial \boldsymbol{\varepsilon}_{\text{ori}}} : \dot{\boldsymbol{\varepsilon}}_{\text{ori}} + \frac{\partial \psi}{\partial \boldsymbol{\varepsilon}_r} : \dot{\boldsymbol{\varepsilon}}_r + \frac{\partial \psi}{\partial \mathbf{B}} : \dot{\mathbf{B}} + \frac{\partial \psi}{\partial z} \dot{z} + \frac{\partial \psi}{\partial \theta} \dot{\theta}, \quad (4.27)$$

$$\dot{s} = \frac{\partial s}{\partial \boldsymbol{\varepsilon}} : \dot{\boldsymbol{\varepsilon}} + \frac{\partial s}{\partial \boldsymbol{\varepsilon}_{\text{ori}}} : \dot{\boldsymbol{\varepsilon}}_{\text{ori}} + \frac{\partial s}{\partial \boldsymbol{\varepsilon}_r} : \dot{\boldsymbol{\varepsilon}}_r + \frac{\partial s}{\partial \mathbf{B}} : \dot{\mathbf{B}} + \frac{\partial s}{\partial z} \dot{z} + \frac{\partial s}{\partial \theta} \dot{\theta}. \quad (4.28)$$

Taking into account

$$\frac{\partial \psi}{\partial \boldsymbol{\varepsilon}} = \boldsymbol{\sigma}, \quad -\frac{\partial \psi}{\partial \theta} = s, \text{ and } \theta \frac{\partial s}{\partial \theta} = \rho C_p, \quad (4.29)$$

Eqs. (4.24), (4.27) and (4.28) give the heat equation

$$\rho C_p \dot{\theta} + \nabla \mathbf{q} = \dot{Q}_{\text{latent}} + \dot{Q}_{\text{el}} + \dot{Q}_{\text{in}} + r, \quad (4.30)$$

where \dot{Q}_{latent} , \dot{Q}_{el} , and \dot{Q}_{in} are the latent heat, thermoelastic heat generation and intrinsic dissipation,

respectively. They are defined as follows:

$$\dot{Q}_{\text{latent}} = \theta \frac{\partial \psi^2}{\partial z \partial \theta} \dot{z}, \quad (4.31)$$

$$\dot{Q}_{\text{el}} = \theta \frac{\partial \psi^2}{\partial \boldsymbol{\varepsilon} \partial \theta} \dot{\boldsymbol{\varepsilon}}, \quad (4.32)$$

$$\dot{Q}_{\text{in}} = -\frac{\partial \psi}{\partial \boldsymbol{\varepsilon}_{\text{ori}}} : \dot{\boldsymbol{\varepsilon}}_{\text{ori}} - \frac{\partial \psi}{\partial \boldsymbol{\varepsilon}_{\text{r}}} : \dot{\boldsymbol{\varepsilon}}_{\text{r}} - \frac{\partial \psi}{\partial \mathbf{B}} : \dot{\mathbf{B}} - \frac{\partial \psi}{\partial z} : \dot{z}. \quad (4.33)$$

Morin et al. (2011b) considered four major heat sources during phase transformation: latent heat, and dissipation due to phase transformation and the formation of residual stress and residual strain. In the present work, nonproportional loading conditions and thermal expansion are considered. The heat generation due to martensite reorientation and to thermoelastic effects are taken into account. The rate of latent heat and energy dissipation are given by

$$\dot{Q}_{\text{latent}} = (\xi - \boldsymbol{\sigma} : \boldsymbol{\alpha}_{\text{MA}}) \theta \dot{z}, \quad (4.34)$$

$$\dot{Q}_{\text{el}} = -\theta \boldsymbol{\alpha} : \mathbf{K} : \dot{\boldsymbol{\varepsilon}}, \quad (4.35)$$

$$\dot{Q}_{\text{in}} = [a(1-z) + bz] |\dot{z}| + z^2 Y \eta + \left(\frac{\mathbf{B}^{(\text{sat})}}{\tau} z \boldsymbol{\varepsilon}_0 + \frac{\boldsymbol{\varepsilon}_{\text{r}}^{(\text{sat})}}{\tau} \sigma_{\text{VM}} \right) \exp(-z_c/\tau) |\dot{z}|. \quad (4.36)$$

4.3 Boundary value problem and algorithmic setup

4.3.1 Boundary value problem

The boundary value problem described below governs the quasi-static evolution of a SMA structure occupying a volume $\Omega \in \mathbb{R}^3$ and subjected to prescribed loading in the time interval $[0, T]$. The SMA is subjected to a body force density $\mathbf{f}(\mathbf{x}, t)$ acting in the domain Ω . The contact forces $\mathbf{T}^{\text{d}}(\mathbf{x}, t)$ are applied on part Γ_{T} of the boundary Γ , and displacement $\mathbf{u}^{\text{d}}(\mathbf{x}, t)$ is prescribed over the remaining boundary Γ_{u} . Using Fourier's law of heat conduction $\mathbf{q}(\mathbf{x}, t) = -k \nabla \theta(\mathbf{x}, t)$, the thermal boundary conditions are defined as follows: The inner heat generation $Q(\mathbf{x}, t)$ is acting over Ω . The heat convection conditions are acting on portion Γ_{h} of the boundary Γ , and the temperature $\theta^{\text{d}}(\mathbf{x}, t)$ is prescribed over the remaining portion Γ_{θ} such that $\Gamma_{\theta} \cup \Gamma_{\text{h}} = \Gamma$. Starting from an initial configuration at time $t = 0$ in which the state variables are known, the problem consists in solving the following set of equations over Ω for $t \in [0, T]$:

Static and kinematic admissibility

$$\boldsymbol{\sigma} \in \mathbb{K}_{\boldsymbol{\sigma}}, \quad \mathbf{u} \in \mathbb{K}_{\mathbf{u}}, \quad (4.37)$$

where the sets $\mathbb{K}_{\boldsymbol{\sigma}}$, $\mathbb{K}_{\mathbf{u}}$ are defined as

$$\begin{aligned} \mathbb{K}_{\boldsymbol{\sigma}} &= \{ \boldsymbol{\sigma} \mid \text{div} \boldsymbol{\sigma} + \mathbf{f} = 0 \text{ in } \Omega, \boldsymbol{\sigma} \cdot \mathbf{n} = \mathbf{T}^{\text{d}} \text{ on } \Gamma_{\text{T}} \}, \\ \mathbb{K}_{\mathbf{u}} &= \{ \mathbf{u} \mid \mathbf{u} = \mathbf{u}^{\text{d}} \text{ on } \Gamma_{\text{u}} \}, \end{aligned} \quad (4.38)$$

and \mathbf{n} is an outward unit vector normal to the boundary Γ_T .

Heat equations

$$\mathbf{q} \in \mathbb{K}_q, \theta \in \mathbb{K}_\theta, \quad (4.39)$$

where the sets \mathbb{K}_q , \mathbb{K}_θ are defined as

$$\begin{aligned} \mathbb{K}_q &= \{ \mathbf{q} \mid -\operatorname{div} \mathbf{q} + \dot{Q} = \rho C_p \dot{\theta} \text{ in } \Omega, \mathbf{q} \cdot \mathbf{n} = h(\theta - \theta_r) \text{ on } \Gamma_h \}, \\ \mathbb{K}_\theta &= \{ \theta \mid \theta = \theta^d \text{ on } \Gamma_\theta \}, \end{aligned} \quad (4.40)$$

where θ_r is the ambient temperature of the surrounding environment and h is the heat transfer coefficient. \mathbf{n} is an outward unit vector normal to the boundary Γ_h .

Infinitesimal strain tensor $\boldsymbol{\varepsilon}$ is used and defined as

$$\boldsymbol{\varepsilon} = \frac{1}{2} (\nabla \mathbf{u} + {}^t \nabla \mathbf{u}) \text{ in } \Omega. \quad (4.41)$$

The stress-strain relation is given by

$$\boldsymbol{\sigma} = \mathbf{K} : [\boldsymbol{\varepsilon} - z \boldsymbol{\varepsilon}_{\text{ori}} - \boldsymbol{\varepsilon}_r - \boldsymbol{\alpha}(\theta - \theta_r)] \text{ in } \Omega, \quad (4.42)$$

where \mathbf{K} is given by Eq. (4.10), z and $\boldsymbol{\varepsilon}_{\text{ori}}$ are governed by Eq. (4.18), $\boldsymbol{\varepsilon}_r$ is governed by Eq. (4.19).

The mechanical state variables z and $\boldsymbol{\varepsilon}_{\text{ori}}$ influence the temperature solution θ of Eq. (4.39) because of the rate of inner heat generation \dot{Q} of Eqs. (4.34) to (4.36). Similarly, the solution of the mechanical problem Eq. (4.37) depends on the temperature field through the energy density $C(\theta)$ in Eq. (4.4) and $\boldsymbol{\varepsilon}_r^{(\text{sat})}$ in Eq. (4.21). Therefore, the problem defined by Eqs. (4.37) and (4.39) is strongly thermomechanically coupled.

4.3.2 Time-discrete formulation

Finite element analysis is used to solve the boundary volume problem outlined in the previous section. Time discretization of the constitutive equations is carried out using an implicit algorithm (Zaki, 2012a,b) that takes into account the mechanical part of Eq. (4.37) and the thermal part of Eq. (4.39) simultaneously. Meanwhile, the mechanical part also takes into account the possibility of simultaneous phase transformation and martensite detwinning and reorientation in presence of nonproportional multiaxial loading. Considering a time history $[0, T]$ discretized into N intervals $t_1 < t_2 < \dots < t_n$, the increments of the fields $(\boldsymbol{\sigma}, \boldsymbol{\varepsilon}, \theta, z, \boldsymbol{\varepsilon}_{\text{ori}})$ for load increment $n + 1$, $n \in \{0, N - 1\}$, are determined by enforcing the appropriate consistency and heat conditions assuming these fields are known at load increment n . In order to simplify the numerical implementation, the parameters $\{\alpha, \beta, \xi, \kappa, G\}$, the residual strain $\boldsymbol{\varepsilon}_r$ and the internal stress \mathbf{B} are updated at the beginning of increment $n + 1$ and kept constant throughout the increment. In the equations below, the load increment numbers n and $n+1$ are indicated in the subscript and the solution iteration number (k) is indicated in the superscript of the relevant variable.

To calculate the increments of stress and internal variables for given strain and temperature increments, a predictor-corrector strategy (Simo and Hughes, 1998) is used. First, a thermoelastic predictor problem is solved by assuming that the increments of the martensite volume fraction z and the orientation strain $\boldsymbol{\varepsilon}_{\text{ori}}$ are zero. Under this assumption,

$$z_{n+1}^{(0)} = z_n, \quad \text{and} \quad \boldsymbol{\varepsilon}_{\text{ori},n+1}^{(0)} = \boldsymbol{\varepsilon}_{\text{ori},n}, \quad (4.43)$$

the increment of total strain $\Delta\boldsymbol{\varepsilon}_n$, temperature $\Delta\theta_n$ and the cumulative martensite fraction z_e are specified prior to engaging the predictor step and are kept constant through increment $n + 1$. With $v^{(0)}$ indicating the value of a variable v obtained in the predictor step, one has

$$\boldsymbol{\varepsilon}_{n+1} = \boldsymbol{\varepsilon}_n + \Delta\boldsymbol{\varepsilon}_n, \quad \theta_{n+1} = \theta_n + \Delta\theta_n, \quad \text{and} \quad z_{e,n+1} = z_{e,n} + \Delta z_{e,n}. \quad (4.44)$$

In this fashion, the parameters $\{\alpha, \beta, \xi, \kappa, G\}$, internal stress \mathbf{B} and the residual strain $\boldsymbol{\varepsilon}_r$ are constant throughout increment $n + 1$, and will be updated at the beginning of the next increment. This two-time-scale solution strategy considerably simplifies the numerical solution of the constitutive equations.

The trial thermoelastic stress is expressed as

$$\boldsymbol{\sigma}_{n+1}^{(0)} = \mathbf{K}_{n+1}^{(0)} : \left[\boldsymbol{\varepsilon}_{n+1} - \boldsymbol{\varepsilon}_{r,n+1} - z_{n+1}^{(0)} \boldsymbol{\varepsilon}_{\text{ori},n+1}^{(0)} - \boldsymbol{\alpha}_{n+1}^{(0)} (\theta_{n+1} - \theta_r) \right], \quad (4.45)$$

where the material properties \mathbf{K} and $\boldsymbol{\alpha}$ are dependent on z .

The loading functions $\mathcal{F}_{n+1}^{(0)} \left(\boldsymbol{\sigma}_{n+1}^{(0)}, \theta_{n+1}, z_{n+1}^{(0)}, \boldsymbol{\varepsilon}_{\text{ori},n+1}^{(0)} \right)$ are then determined, for $\mathcal{F} = \{\mathcal{F}_z^1, \mathcal{F}_z^2, \mathcal{F}_{\text{ori}}\}$. The thermoelastic trial state is accepted if one of the following conditions is satisfied

$$\begin{aligned} \mathcal{F}_{z,n+1}^{1,(0)} &\leq 0, & \text{and} & \quad z_{n+1}^{(0)} = 0, \\ \mathcal{F}_{z,n+1}^{1,(0)}, \mathcal{F}_{z,n+1}^{2,(0)}, \mathcal{F}_{\text{ori},n+1}^{(0)} &\leq 0, \text{ and } 0 < z_{n+1}^{(0)} < 1, \\ \mathcal{F}_{z,n+1}^{2,(0)}, \mathcal{F}_{\text{ori},n+1}^{(0)} &\leq 0, & \text{and} & \quad z_{n+1}^{(0)} = 1. \end{aligned} \quad (4.46)$$

Otherwise, the trial state lies outside the loading surfaces defined by $\mathcal{F} = 0$. $\left\{ \boldsymbol{\sigma}_{n+1}^{(k)}, z_{n+1}^{(k)}, \boldsymbol{\varepsilon}_{\text{ori},n+1}^{(k)} \right\}$ need be determined in the corrector step to pull the state variables back onto the loading surfaces. An iterative scheme is then carried out to obtain the stress and internal variables in the corrector step, in which first-order Taylor series expansions are used to approximate the loading functions as follows:

$$\mathcal{F}_{z,n+1}^{(k-1)} + \partial_{\boldsymbol{\sigma}} \mathcal{F}_{z,n+1}^{(k-1)} : \Delta\boldsymbol{\sigma}_{n+1}^{(k)} + \partial_z \mathcal{F}_{z,n+1}^{(k-1)} \Delta z_{n+1}^{(k)} + \partial_{\boldsymbol{\varepsilon}_{\text{ori}}} \mathcal{F}_{z,n+1}^{(k-1)} : \Delta\boldsymbol{\varepsilon}_{\text{ori},n+1}^{(k)} + \partial_{\theta} \mathcal{F}_{z,n+1}^{(k-1)} \Delta\theta_{n+1} = 0, \quad (4.47)$$

$$\mathcal{F}_{\text{ori},n+1}^{(k-1)} + \partial_{\boldsymbol{\sigma}} \mathcal{F}_{\text{ori},n+1}^{(k-1)} : \Delta\boldsymbol{\sigma}_{n+1}^{(k)} + \partial_z \mathcal{F}_{\text{ori},n+1}^{(k-1)} \Delta z_{n+1}^{(k)} + \partial_{\boldsymbol{\varepsilon}_{\text{ori}}} \mathcal{F}_{\text{ori},n+1}^{(k-1)} : \Delta\boldsymbol{\varepsilon}_{\text{ori},n+1}^{(k)} = 0, \quad (4.48)$$

where $\Delta v^{(k)} = v^{(k)} - v^{(k-1)}$ is the increment of variable v at iteration k . If phase transformation and martensite orientation are active at the same time, $\Delta z_{n+1}^{(k)}$ and $\Delta\boldsymbol{\varepsilon}_{\text{ori},n+1}^{(k)}$ are obtained by solving the time-discrete Eqs. (4.47) and (4.48) simultaneously, where $\Delta\boldsymbol{\eta}_{n+1}^{(k)}$ is the discrete inelastic multiplier used to

express the discrete normality rule at iteration k as

$$\Delta \boldsymbol{\varepsilon}_{\text{ori},n+1}^{(k)} = \Delta \eta_{n+1}^{(k)} \mathbf{N}_{n+1}^{(k-1)}. \quad (4.49)$$

\mathbf{N} in the previous equation is approximated at iteration k by its value at the previous iteration $k - 1$, with the initial value corresponding to an elastic prediction. The time-discrete stress-strain relation can then be written as

$$\begin{aligned} \Delta \boldsymbol{\sigma}_{n+1}^{(k)} = & \mathbf{K}_{n+1}^{(k-1)} : \left[\Delta \boldsymbol{\varepsilon}_{n+1}^{(k)} - \left(\Delta \mathbf{K}_{n+1}^{(k),-1} : \boldsymbol{\sigma}_{n+1}^{(k-1)} + \Delta \boldsymbol{\varepsilon}_{r,n+1}^{(k)} \right. \right. \\ & \left. \left. + \Delta z_{n+1}^{(k)} \boldsymbol{\varepsilon}_{\text{ori},n+1}^{(k-1)} + z_{n+1}^{(k-1)} \Delta \boldsymbol{\varepsilon}_{\text{ori},n+1}^{(k)} + \Delta \boldsymbol{\alpha}_{n+1}^{(k)} \left(\theta_{n+1}^{(k-1)} - \theta_r \right) + \Delta \theta_{n+1}^{(k)} \boldsymbol{\alpha}_{n+1}^{(k-1)} \right) \right], \end{aligned} \quad (4.50)$$

where $\Delta \boldsymbol{\varepsilon}_{n+1}^{(k)}$, $\Delta \boldsymbol{\varepsilon}_{r,n+1}^{(k)}$ and $\Delta \theta_{n+1}^{(k)}$ equal zero because they are not updated in the corrector step and the increment of the elastic compliance tensor and the thermal expansion coefficient are given by

$$\Delta \mathbf{K}_{n+1}^{(k),-1} = \left(\mathbf{K}_M^{-1} - \mathbf{K}_A^{-1} \right) \Delta z_{n+1}^{(k)}, \quad (4.51)$$

$$\Delta \boldsymbol{\alpha}_{n+1}^{(k)} = (\boldsymbol{\alpha}_M - \boldsymbol{\alpha}_A) \Delta z_{n+1}^{(k)}. \quad (4.52)$$

Combining Eqs. (4.49) to (4.52) gives

$$\Delta \boldsymbol{\sigma}_{n+1}^{(k)} = -\mathbf{K}_{n+1}^{(k-1)} : \left[\mathbf{R}_{n+1}^{(k-1)} \Delta z_{n+1}^{(k)} + z_{n+1}^{(k-1)} \mathbf{N}_{n+1}^{(k-1)} \Delta \eta_{n+1}^{(k)} \right], \quad (4.53)$$

where

$$\mathbf{R}_{n+1}^{(k-1)} = \left(\mathbf{K}_M^{-1} - \mathbf{K}_A^{-1} \right) : \boldsymbol{\sigma}_{n+1}^{(k-1)} + \boldsymbol{\varepsilon}_{\text{ori},n+1}^{(k-1)} + (\boldsymbol{\alpha}_M - \boldsymbol{\alpha}_A) \left(\theta_{n+1}^{(k-1)} - \theta_r \right). \quad (4.54)$$

The increments of the martensite volume fraction $\Delta z_{n+1}^{(k)}$ and the multiplier $\Delta \eta_{n+1}^{(k)}$ can now be calculated using Eqs. (2.29) to (2.36). The iterative procedure stops if $\Delta z_{n+1}^{(k)}$ and $\Delta \eta_{n+1}^{(k)}$ are less than a specified tolerance. At the end of increment $n + 1$, the increment of cumulative martensite volume fraction is calculated by

$$\Delta z_{e,n+1} = \left| \Delta z_{n+1}^{(k)} \right|, \quad (4.55)$$

which will be used at the beginning of the next increment to update the cyclic parameters. In this fashion, the parameters $\{\alpha, \beta, \xi, \kappa, G\}$, internal stress \mathbf{B} and the residual strain $\boldsymbol{\varepsilon}_r$ remain constant during increment $n + 1$. A minimal error is introduced to the system's solutions due to the two-time-scale update strategy of the material parameters. The analytical solution of increment $n + 1$ can be defined as $\mathcal{S}_{n+1}(\hat{z}_{e,n+1})$, where $\hat{z}_{e,n+1}$ is analytical solution of the cumulative martensite volume fraction at increment $n + 1$

$$\hat{z}_{e,n+1} = z_{e,n+1} + \delta, \quad (4.56)$$

where δ is a small value that depends on how much martensite transformed in the current increment. The solution obtained using the algorithm above is $\mathcal{S}_{n+1}(z_{e,n+1})$. The error on the system's solution \mathcal{R} at

every increment can be shown to be bounded:

$$\mathcal{R} \leq \max_{0 \leq n \leq N-1} \|\mathcal{S}_{n+1}(z_{e,n+1} + \delta) - \mathcal{S}_{n+1}(z_{e,n+1})\|. \quad (4.57)$$

4.3.3 Algorithmic setup

A ‘‘User Material’’ subroutine (UMAT) is developed for the simulation of thermomechanical coupling in SMAs using the finite element analysis software Abaqus. The subroutine uses the implicit integration algorithm presented below to update the stress and state variables and the tangent operators at the end of each load increment.

Algorithm 3: Algorithm of UMAT

Input : Material parameters, $\boldsymbol{\varepsilon}_n$, $\Delta\boldsymbol{\varepsilon}_{n+1}$, θ_n , $\Delta\theta_{n+1}$, z_n , $\boldsymbol{\varepsilon}_{\text{ori},n}$, $z_{e,n}$, tolerances tol_1 , tol_2 , tol_3 .

Output : $\boldsymbol{\sigma}_{n+1}$, z_{n+1} , $\boldsymbol{\varepsilon}_{\text{ori},n+1}$, $\boldsymbol{\varepsilon}_{r,n+1}$, $z_{e,n+1}$, tangent operators $\mathcal{J}_{\sigma\varepsilon}$, $\mathcal{J}_{\sigma\theta}$, $\mathcal{J}_{Q\varepsilon}$, $\mathcal{J}_{Q\theta}$.

- 1 **Initialization**: Set the internal variables using equation (4.43), set the strain and temperature using equation (4.44), Determine a thermoelastic trial stress increment using equation (4.45).
 - 2 **if the Kuhn-Tucker conditions (4.18) are satisfied then**
 - 3 **goto 21**;
 - 4 **else if** $\mathcal{F}_{z,n+1}^{(0)} \leq tol_1$ **and** $\mathcal{F}_{\text{ori},n+1}^{(0)} > tol_2$, (only martensite reorientation is active) **then**
 - 5 Calculate the increment of the inelastic multiplier $\Delta\eta_{n+1}$ using (2.36);
 - 6 Calculate the tangent operators using (A.28) to (A.31);
 - 7 **else if** $\mathcal{F}_{z,n+1}^{(0)} > tol_1$ **and** $\mathcal{F}_{\text{ori},n+1}^{(0)} \leq tol_2$, (only phase transformation is active) **then**
 - 8 Calculate the increment of martensite volume fraction Δz_{n+1} using (2.35);
 - 9 Calculate the tangent modulus tensors using (A.24) to (A.27);
 - 10 **else if** $\mathcal{F}_{z,n+1}^{(0)} > tol_1$ **and** $\mathcal{F}_{\text{ori},n+1}^{(0)} > tol_2$, (phase transformation or reorientation or both) **then**
 - 11 Calculate the increment of the inelastic multiplier $\Delta\eta_{n+1}$ and the increment of martensite volume fraction Δz_{n+1} using (2.29) and (2.30);
 - 12 **if** $(\Delta z_{n+1} > tol_3$ **and** $\mathcal{F}_{z,n+1}^{1,(0)} > tol_1$ **and** $\Delta\eta_{n+1} > tol_3)$ **or**
 $(\Delta z_{n+1} < tol_3$ **and** $\mathcal{F}_{z,n+1}^{2,(0)} > tol_1$ **and** $\Delta\eta_{n+1} > tol_3)$, (simultaneous phase transformation and martensite reorientation) **then**
 - 13 Update the stress and the state variables;
 - 14 Calculate the tangent operators using (A.20) to (A.23);
 - 15 **else if** $(\Delta z_{n+1} < tol_3$ **and** $\mathcal{F}_{z,n+1}^{1,(0)} > tol_1)$ **or** $(\Delta z_{n+1} > tol_3$ **and** $\mathcal{F}_{z,n+1}^{2,(0)} > tol_1)$, (martensite reorientation only) **then**
 - 16 Reset the state variables to their values at the beginning of the increment;
 - 17 **goto 5**;
 - 18 **else if** $\eta_{n+1} < tol_3$ **and** $\mathcal{F}_{\text{ori},n+1}^{(0)} > tol_2$, (phase transformation only) **then**
 - 19 Reset the state variables to their values at the beginning of the increment;
 - 20 **goto 8**;
 - 21 **return**: stress, state variables, tangent operators.
-

4.4 3D computational analysis and discussions

To demonstrate the capabilities of this extended model, four simulation cases are presented here for SMA structures subjected to varying thermal and mechanical loadings. The first case represents a cylinder subjected to proportional tension. Three isothermal loading cases under different temperatures are used to calibrate the material parameters, followed by a tension loading case at room temperature, illustrating the influence of thermomechanical coupling. Experimental and simulation data from [Andani and Elahinia \(2014\)](#) are used for comparison. The second case considers a SMA cylinder subjected to multiaxial nonproportional loading and is used to validate the model against experimental results reported by [Grabe and Bruhns \(2008\)](#). The third case considers a SMA tube subjected to cyclic proportional tension at different test temperatures and loading rates. The simulation is validated against experimental data from ([Yu et al., 2014](#)). Thin-walled cylinder is used in all of the three simulation cases. Fig. 4.1 shows the boundary conditions and simplified heat transfer conditions of thin-walled cylinder proposed by [Yin et al. \(2014\)](#) and also used by [Yu et al. \(2015\)](#). The heat flow through the grips is considered to take place by conduction. Finally, the extended model is used to simulate crack tip opening in presence of cyclic loading. This example is chosen to demonstrate the ability of the model to simulate high stress gradients.

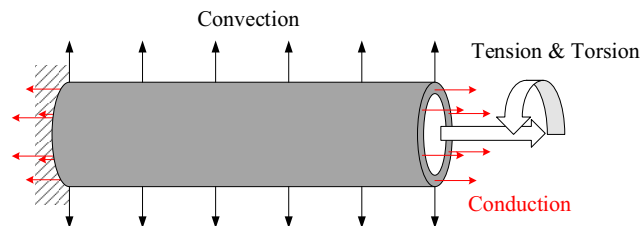


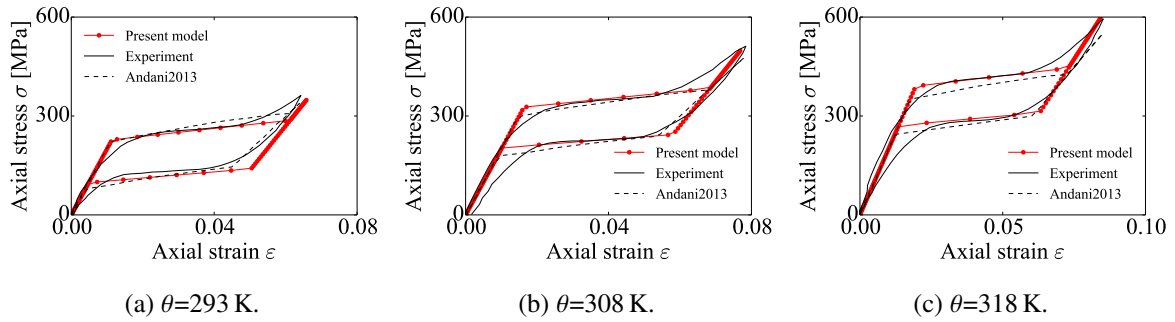
Figure 4.1 Mechanical and thermal boundary conditions for the SMA cylinder.

4.4.1 Thin-walled cylinder subjected to tensile loading

Following the recently published work of [Andani and Elahinia \(2014\)](#), a SMA thin-walled cylinder is subjected to tensile loading under isothermal conditions. The outer diameter, thickness and length of the cylinder are 4.5 mm, 0.3 mm and 14 mm, respectively. The model is meshed using 8-node linear hexahedral elements (C3D8 in Abaqus) for a total of 34 560 degrees of freedom. Three uniaxial isothermal loading conditions are simulated at the temperatures of 293 K, 308 K and 318 K, respectively. The material parameters calibrated from the experimental data of [Andani and Elahinia \(2014\)](#) are listed in Table 4.1. It's notable that the material constants such as density ρ , heat capacity C_p , heat convection and conduction coefficients h_{air} , k for all simulated case in this chapter are the values taken from [Morin et al. \(2011a\)](#). The simulation results shown in Fig. 4.2 are in good agreement with the experimental and simulation data of [Andani and Elahinia \(2014\)](#).

Table 4.1 Material parameters calibrated using the experimental data in Fig. 4.2.

E_A	20 000	MPa	E_M	13 500	MPa
ν	0.3		ρ	6500	kg m^{-3}
C_p	440	$\text{J kg}^{-1} \text{K}^{-1}$	$B^{(\text{sat})}$	0	MPa
α_A	11×10^{-6}	K^{-1}	α_M	6.6×10^{-6}	K^{-1}
k	18	$\text{W m}^{-1} \text{K}^{-1}$	τ	10	
σ_{rs}	30	MPa	σ_{rf}	80	MPa
$\sigma_{\text{ms}}^{(0)}$	241	MPa	$\sigma_{\text{ms}}^{(\text{sat})}$	241	MPa
$\sigma_{\text{mf}}^{(0)}$	300	MPa	$\sigma_{\text{mf}}^{(\text{sat})}$	300	MPa
$\sigma_{\text{as}}^{(0)}$	154	MPa	$\sigma_{\text{as}}^{(\text{sat})}$	154	MPa
$\sigma_{\text{af}}^{(0)}$	112	MPa	$\sigma_{\text{af}}^{(\text{sat})}$	112	MPa
$\gamma^{(0)}$	0.04		$\gamma^{(\text{sat})}$	0.04	
ϕ	0	K^{-1}	ν	0	
A_f^0	280	K	θ_r	293	K
h_{air}	50	$\text{W m}^{-2} \text{K}^{-1}$			

Figure 4.2 Comparison of isothermal uniaxial stress–strain responses with the experimental and simulation data from from [Andani and Elahinia \(2014\)](#) at different temperatures.

In order to investigate the influence of loading rate, a pseudoelastic SMA cylinder 1.5 mm in external diameter, 0.085 mm in wall thickness and 33.5 mm in length is considered. The SMA tube is meshed using 8-node linear hexahedral elements with coupled temperature–displacement (C3D8T in Abaqus) for a total of 40 560 degrees of freedom. The cylinder is subjected to a strain rate of $\dot{\epsilon} = 3 \times 10^{-3} \text{ s}^{-1}$. First, a set of isothermal uniaxial data, shown in Fig. 4.3a, are used to calibrate the model parameters in Table 4.2.

The simulated stress–strain behavior reported in Fig. 4.3b and the corresponding temperature evolution reported in Fig. 4.3c are compared with the experimental and simulation results of [Andani and Elahinia \(2014\)](#). As shown in Fig. 4.3b, the slopes of the phase transformation plateaus and the hysteresis size increase with increasing loading rate. In line with the experimental results in Figure 4.3c, the temperature of the specimen starts to increase during forward phase transformation because of latent heat and intrinsic dissipation. During the elastic unloading stage, the temperature decreases

Table 4.2 Material parameters calibrated using the experimental data in Fig. 4.3a from Andani and Elahinia (2014).

E_A	34 200	MPa	E_M	18 400	MPa
ν	0.3		ρ	6500	kg m ⁻³
C_p	440	J kg ⁻¹ K ⁻¹	$B^{(sat)}$	0	MPa
α_A	11×10^{-6}	K ⁻¹	α_M	6.6×10^{-6}	K ⁻¹
k	18	W m ⁻¹ K ⁻¹	τ	10	
σ_{rs}	30	MPa	σ_{rf}	80	MPa
$\sigma_{ms}^{(0)}$	312	MPa	$\sigma_{ms}^{(sat)}$	312	MPa
$\sigma_{mf}^{(0)}$	362	MPa	$\sigma_{mf}^{(sat)}$	362	MPa
$\sigma_{as}^{(0)}$	184	MPa	$\sigma_{as}^{(sat)}$	184	MPa
$\sigma_{af}^{(0)}$	139	MPa	$\sigma_{af}^{(sat)}$	139	MPa
$\gamma^{(0)}$	0.048		$\gamma^{(sat)}$	0.048	
ϕ	0	K ⁻¹	ν	0	
A_f^0	278	K	θ_r	293	K
h_{air}	50	W m ⁻² K ⁻¹			

because of air convection and heat conduction through the two ends of the specimen. When the reverse phase transformation begins, the temperature rapidly decreases to values below the ambient temperature because of latent heat absorption. The numerical simulation results in this case are in better agreement with the experimental data compared to those reported by Andani and Elahinia (2014), particularly true during the unloading phase. A notable temperature increase takes place during the last increment, even though the material behavior during this increment is elastic. In this case, the temperature increase is the result of heat influx from the surrounding medium, which takes place because of prior temperature drop in the specimen to below ambient due to latent heat.

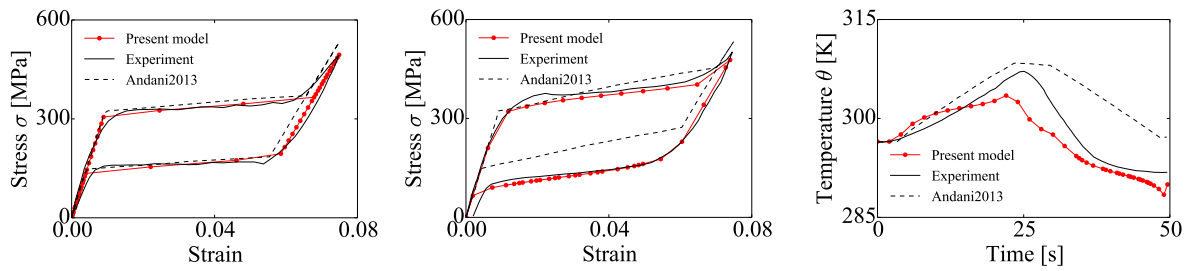
(a) Isothermal case at 296.5 K. (b) Stress-strain ($\dot{\epsilon} = 3 \times 10^{-3} \text{ s}^{-1}$). (c) Temperature ($\dot{\epsilon} = 3 \times 10^{-3} \text{ s}^{-1}$).

Figure 4.3 Comparison of simulations using the proposed model against reference experimental and simulation data taken from Andani and Elahinia (2014).

4.4.2 Strain-controlled loading

In this section, the thermomechanical responses of SMAs under strain-controlled loading are discussed. The range of strain rates is from 10^{-1} s^{-1} to 10^{-5} s^{-1} . Dunić et al. (2014) performed several strain-controlled experiments on belt type TiNi SMAs, which were applied tensile displacement along the length direction with strain rates of 10^{-1} s^{-1} , 10^{-2} s^{-1} and 10^{-3} s^{-1} . The dimensions of the specimen is $160 \text{ mm} \times 10 \text{ mm} \times 0.38 \text{ mm}$ and the working length limited by the testing machine grips is 100 mm. Grabe and Bruhns (2008) performed several strain-controlled experiments on thin-walled SMA tubes considering strain rates of 10^{-3} s^{-1} , 10^{-4} s^{-1} and 10^{-5} s^{-1} . The tubes are 50 mm in length, 9.6 mm in outer diameter, and 7.92 mm in inner diameter. Both literatures reported strong dependence of the mechanical behavior of the samples on temperature due to variation of the loading rates.

Simulations are carried out considering the same experimental setups. The SMA belt is meshed using 8-node linear hexahedral elements with coupled temperature-displacement (C3D8T in Abaqus) for a total of 5832 degrees of freedom. The SMA tube is meshed using the same elements for a total of 12 240 degrees of freedom. Displacements are applied along the length direction of the samples with different loading rate. The boundary conditions are identical to those used in Section 4.4.1 and shown in Fig. 4.1.

Simulation results for the SMA belt used in Dunić et al. (2014) with a maximum strain of 7.8 % is shown in Figs. 4.4 and 4.5. Material parameters are listed in Table 4.3. The model prediction for the stress-strain curve of Fig. 4.4 and strain-temperature response of Fig. 4.5 are compared with the experimental and simulation results of Dunić et al. (2014). Simulation results for a uniaxial tension test up used in Grabe and Bruhns (2008) with a maximum strain $\varepsilon = 3.5 \%$ is shown in Figs. 4.6 and 4.7. This particular simulation is used to calibrate the material parameters in Table 4.4. The model prediction for the stress-strain curve of Fig. 4.6 and strain-temperature response of Fig. 4.7 are compared with the experimental data from Grabe and Bruhns (2008). As shown in Figs. 4.4 to 4.7, the slopes of the phase transformation plateaus as well as the temperature variation are found to increase with increasing loading rate. Overall, the predictions are in good agreement with reference data.

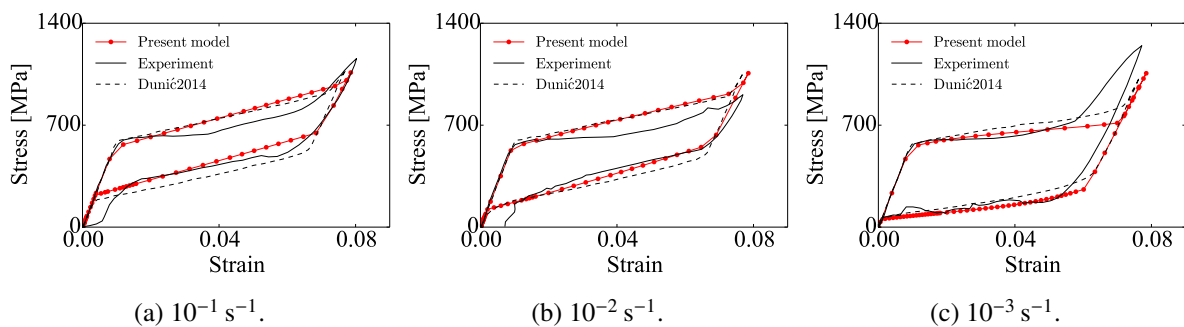


Figure 4.4 Stress-strain response comparison of simulated results against reference experimental data taken from Dunić et al. (2014) at strain rate of: (a) 10^{-1} s^{-1} , (b) 10^{-2} s^{-1} and (c) 10^{-3} s^{-1} .

Using the calibrated model parameters in Table 4.4, a multiaxial nonproportional loading case

Table 4.3 Material parameters calibrated using the experimental data from [Dunić et al. \(2014\)](#).

E_A	59 000	MPa	E_M	45 000	MPa
ν	0.3		ρ	6500	kg m^{-3}
C_p	440	$\text{J kg}^{-1} \text{K}^{-1}$	$B^{(\text{sat})}$	0	MPa
α_A	1.1×10^{-5}	K^{-1}	α_M	1.1×10^{-5}	K^{-1}
k	18	$\text{W m}^{-1} \text{K}^{-1}$	τ	10	
σ_{rs}	30	MPa	σ_{rf}	80	MPa
$\sigma_{ms}^{(0)}$	550	MPa	$\sigma_{ms}^{(\text{sat})}$	550	MPa
$\sigma_{mf}^{(0)}$	565	MPa	$\sigma_{mf}^{(\text{sat})}$	565	MPa
$\sigma_{as}^{(0)}$	219	MPa	$\sigma_{as}^{(\text{sat})}$	219	MPa
$\sigma_{af}^{(0)}$	178	MPa	$\sigma_{af}^{(\text{sat})}$	178	MPa
$\gamma^{(0)}$	0.055		$\gamma^{(\text{sat})}$	0.055	
ϕ	0	K^{-1}	ν	0	
A_f^0	276	K	θ_T	298	K
h_{air}	25	$\text{W m}^{-2} \text{K}^{-1}$			

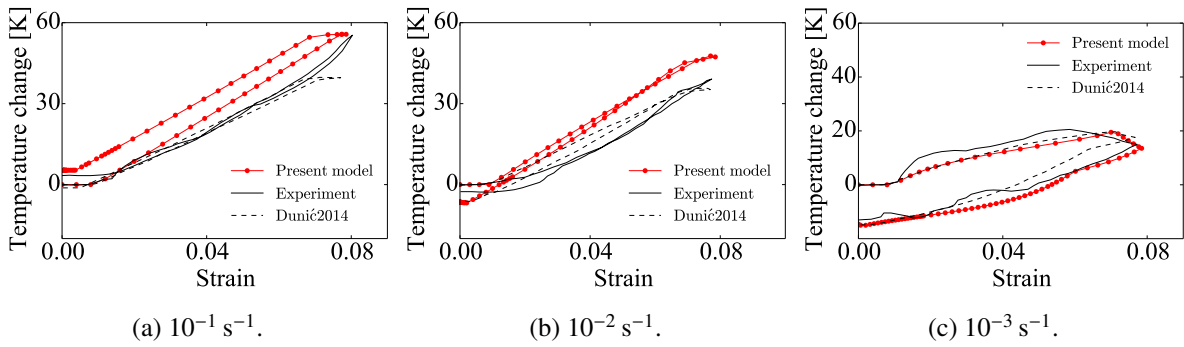


Figure 4.5 Strain-temperature response comparison of simulated results against reference experimental data taken from [Dunić et al. \(2014\)](#) at strain rate of: (a) 10^{-1} s^{-1} , (b) 10^{-2} s^{-1} and (c) 10^{-3} s^{-1} .

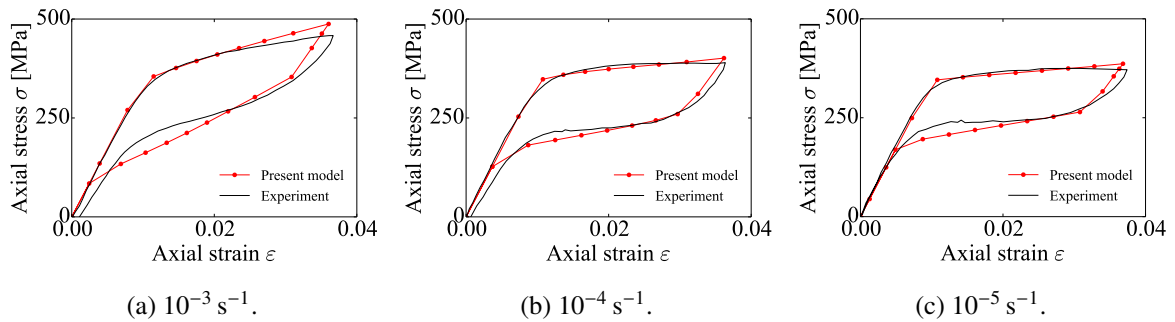
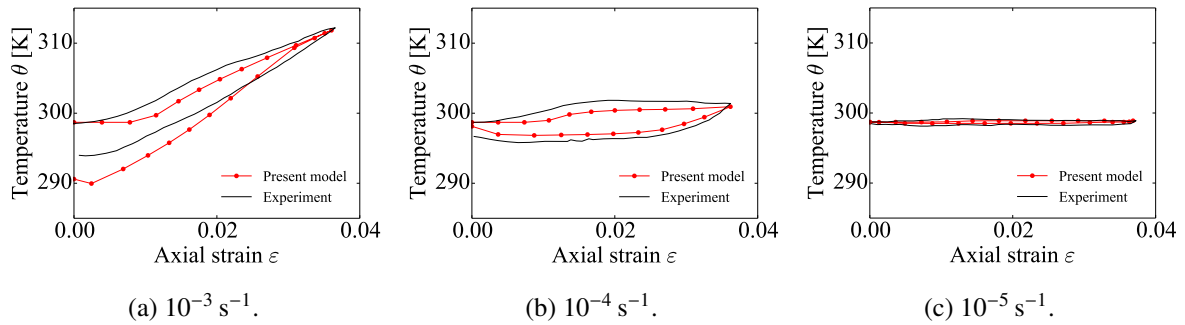


Figure 4.6 Stress-strain response comparison of simulated results against reference experimental data taken from [Grabe and Bruhns \(2008\)](#) at strain rate of: (a) 10^{-3} s^{-1} , (b) 10^{-4} s^{-1} and (c) 10^{-5} s^{-1} .

Table 4.4 Material parameters calibrated using the experimental data in Figure 4.6 from Grabe and Bruhns (2008).

E_A	34 500	MPa	E_M	24 400	MPa
ν	0.3		ρ	6500	kg m^{-3}
C_p	440	$\text{J kg}^{-1} \text{K}^{-1}$	$B^{(\text{sat})}$	0	MPa
α_A	11×10^{-6}	K^{-1}	α_M	6.6×10^{-6}	K^{-1}
k	18	$\text{W m}^{-1} \text{K}^{-1}$	τ	10	
σ_{rs}	30	MPa	σ_{rf}	80	MPa
$\sigma_{ms}^{(0)}$	338	MPa	$\sigma_{ms}^{(\text{sat})}$	338	MPa
$\sigma_{mf}^{(0)}$	378	MPa	$\sigma_{mf}^{(\text{sat})}$	378	MPa
$\sigma_{as}^{(0)}$	262	MPa	$\sigma_{as}^{(\text{sat})}$	262	MPa
$\sigma_{af}^{(0)}$	180	MPa	$\sigma_{af}^{(\text{sat})}$	180	MPa
$\gamma^{(0)}$	0.021		$\gamma^{(\text{sat})}$	0.021	
ϕ	0	K^{-1}	ν	0	
A_f^0	280	K	θ_r	298	K
h_{air}	50	$\text{W m}^{-2} \text{K}^{-1}$			

Figure 4.7 Strain-temperature response comparison of simulated results against reference experimental data taken from Grabe and Bruhns (2008) at strain rate of: (a) 10^{-3} s^{-1} , (b) 10^{-4} s^{-1} and (c) 10^{-5} s^{-1} .

corresponding to the square loading path shown in Fig. 4.8a is simulated. The loading consists of the following sequence, starting from an unloaded state: tension, torsion at fixed tensile strain, unloading in tension, and unloading in torsion. The maximum tensile and torsional strains reached in each case are $\epsilon = \gamma/\sqrt{3} = 2.0 \%$. The stress responses are shown in Fig. 4.8b. The disagreement of the tension-torsion stress curves compared to experimental data is likely due to the use of the von Mises equivalent stress in formulating the loading functions for the model, which is known from experimental observations not to be very accurate. The simulated strain-temperature responses are shown in Fig. 4.9, which shows good agreement with the experimental data from Grabe and Bruhns (2008).

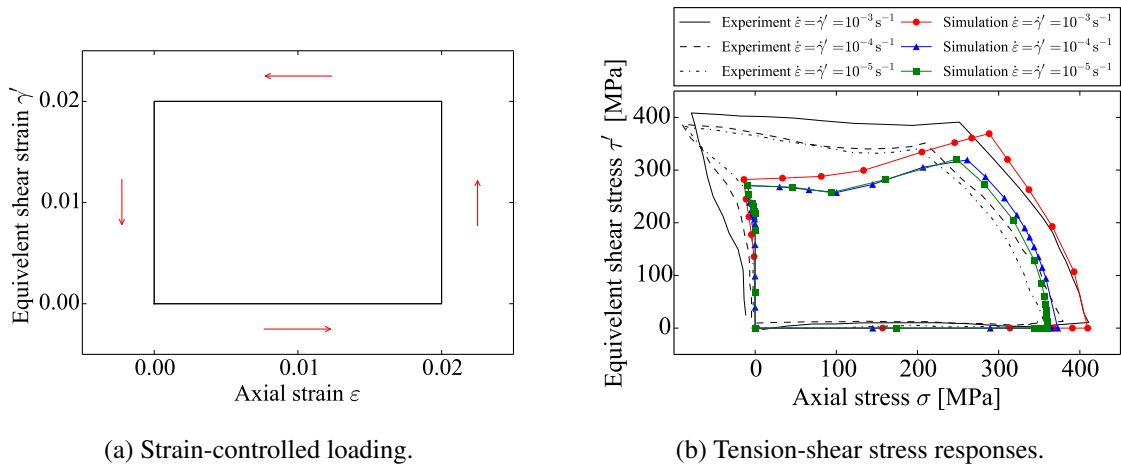


Figure 4.8 Multiaxial nonproportional loading cases under different loading rates.

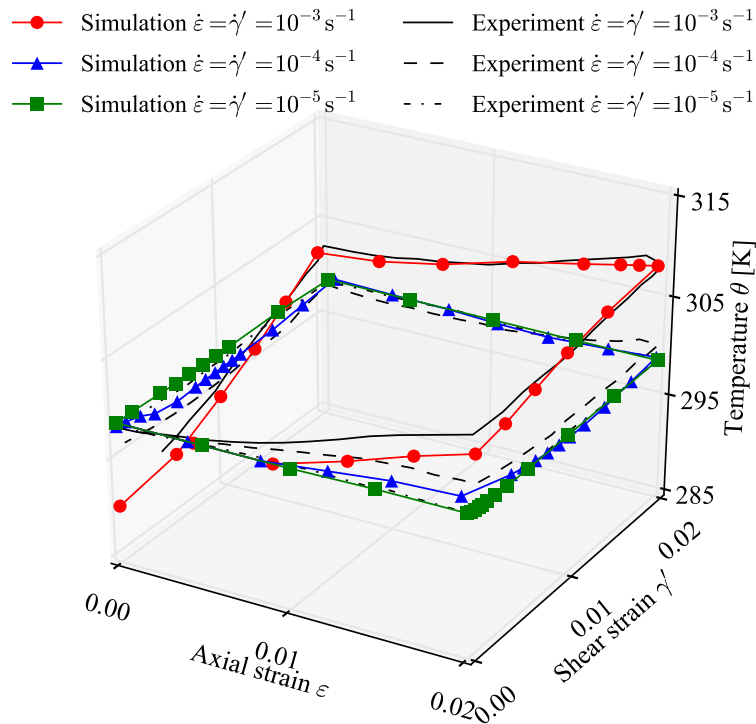


Figure 4.9 Temperature variation with respect to tensile and shear strain.

4.4.3 SMA tube subjected to cyclic loading

To investigate the influence of temperature on the stress-strain response of SMAs, the model is used to simulate a number of cases in the literature involving pseudoelastic SMAs subjected to cyclic loading at various temperatures. Of particular interest, in addition to strong thermomechanical coupling, is the dependence of residual strain on temperature reported by Yu et al. (2014). The authors carried out experiments on thin-walled tubular specimens 2.5 mm in outer diameter and 2.2 mm in inner diameter.

The total length of the specimen is 60 mm and the gauge length of the extensometer used is 15 mm. The model is meshed using 8-node linear hexahedral elements (C3D8) for a total of 2048 degrees of freedom.

Experimental data from Yu et al. (2014) is used to validate the present model for the case of uniaxial cyclic loading at different room temperatures. The experiments were carried out considering thin-walled tubes in a temperature-controlled chamber. The parameters used for the simulations are those in Table 4.5. The material parameters are obtained from a uniaxial tensile loading experiment at 333 K, and ϕ and ν are calculated using Eq. (4.21).

Table 4.5 Material parameters calibrated using experimental data from Yu et al. (2014).

E_A	28 000	MPa	E_M	17 000	MPa
ν	0.3		ρ	6500	kg m ⁻³
C_p	440	J kg ⁻¹ K ⁻¹	$B^{(sat)}$	100	MPa
α_A	11×10^{-6}	K ⁻¹	α_M	6.6×10^{-6}	K ⁻¹
k	18	W m ⁻¹ K ⁻¹	τ	9	
σ_{rs}	80	MPa	σ_{rf}	100	MPa
$\sigma_{ms}^{(0)}$	615	MPa	$\sigma_{ms}^{(sat)}$	472	MPa
$\sigma_{mf}^{(0)}$	672	MPa	$\sigma_{mf}^{(sat)}$	568	MPa
$\sigma_{as}^{(0)}$	428	MPa	$\sigma_{as}^{(sat)}$	392	MPa
$\sigma_{af}^{(0)}$	288	MPa	$\sigma_{af}^{(sat)}$	268	MPa
$\gamma^{(0)}$	0.063		$\gamma^{(sat)}$	0.063	
ϕ	0.000 375	K ⁻¹	ν	-0.106 375	
A_f^0	283	K	θ_r	333	K
h_{air}	50	W m ⁻² K ⁻¹			

In order to simulate the experiments proposed by Yu et al. (2014), simulations were carried out using thin-walled cylinder at temperature of 313 K, 333 K and 353 K, respectively. Tensile loading was applied on the end surface for 40 cycles, the magnitude was 570 MPa, 675 MPa and 770 MPa, respectively. The simulated uniaxial response of the material is shown in Figs. 4.10a to 4.10c for temperatures 313 K, 333 K and 353 K, respectively. Fig. 4.10d shows the evolution of the residual strain at different test temperatures. From the simulated results, it is seen that the amount of residual strain at saturation increases with increasing temperature and with the number of cycles. This observation is consistent with the those of from Yu et al. (2014).

For non-isothermal conditions, experimental data reported by Kan et al. (2016) shows strong dependence of the material behavior on the loading rate. In particular residual strain and transformation hardening increase with the increasing number of cycles and strain rate. The influence of loading rate on the residual strain is due to thermomechanical coupling, which can be explained as follows: at higher loading rates, heat is not released fast enough from the SMA in order to maintain temperature equilibrium with the surroundings. The material temperature therefore increases resulting in higher

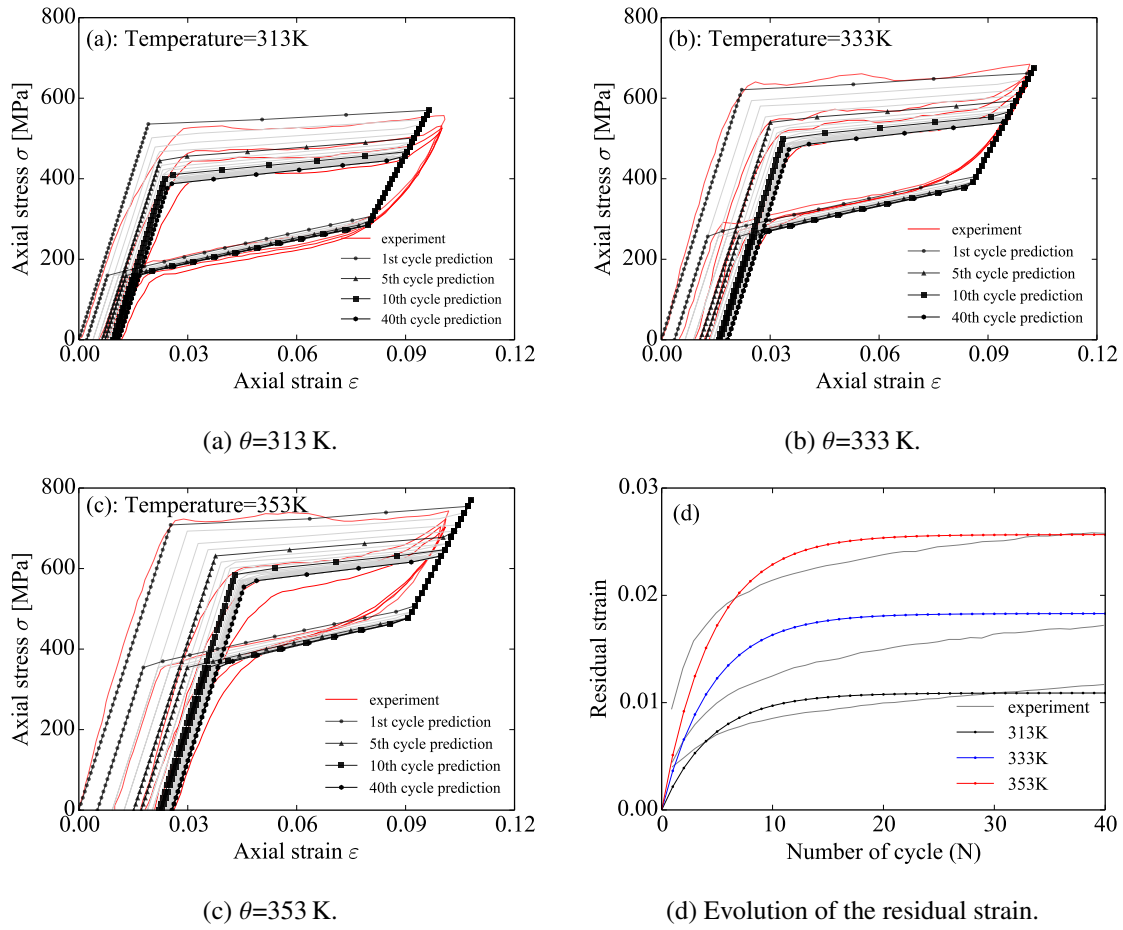


Figure 4.10 Simulated material behavior at different temperatures under cyclic loading.

transformation stress. This, in turn, favors increased plastic slip during phase transformation, which increases the amount of martensite trapped by dislocation fields upon unloading. Two different strain rates are considered for the simulations: $1 \times 10^{-3} \text{ s}^{-1}$ and $3.3 \times 10^{-3} \text{ s}^{-1}$. The experiments needed to calibrate the material parameters are not provided in Kan et al. (2016). Hence, we use the material parameters listed in Table 4.5. The experiments were carried out on thin-walled tubular specimens with an outer diameter of 2.5 mm and inner diameter of 2.2 mm. The total length of the specimen is 60 mm and the gauge length of the extensometer is 15 mm. The model is meshed using 8-node linear hexahedral element with temperature-displacement coupling (C3D8T in Abaqus) for a total of 2048 degrees of freedom. Tensile loading of 700 MPa was applied for 50 cycles. The boundary conditions are the same as those used in Section 4.4.1 and shown in Fig. 4.1. The simulated stress-strain curve in Fig. 4.11 shows 0.71% residual strain at $1 \times 10^{-3} \text{ s}^{-1}$ and 1.1% at $3.3 \times 10^{-3} \text{ s}^{-1}$ strain rates. The simulated residual strain is found to increase with the loading rate, in accordance with the experimental observations of Kan et al. (2016).

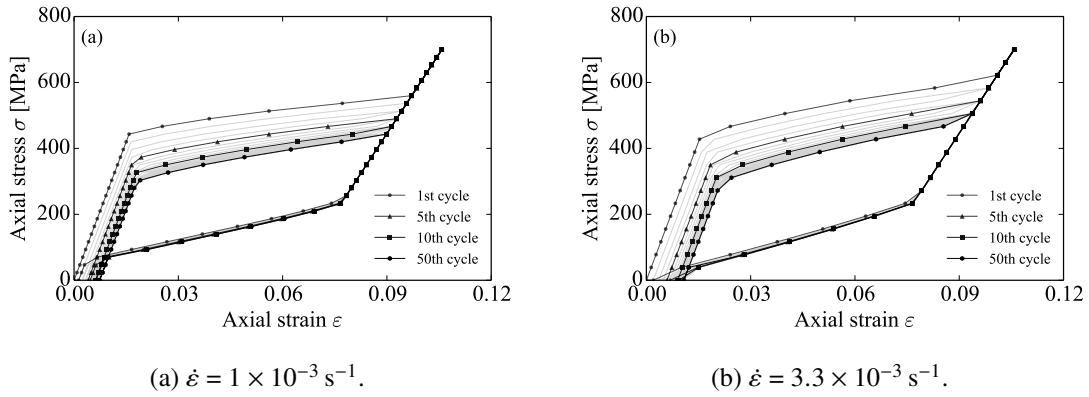


Figure 4.11 Comparison of the stress-strain curves obtained at different strain rates.

4.4.4 Crack tip opening in a SMA sample

Stress concentration at the tip of a crack in a SMA sample results in increased martensite transformation and reorientation (Hazar et al., 2015), which influence the growth of the crack. In this section, a simulation is provided for a SMA sample containing a crack and subjected to cyclic loading. The simulation takes into account ratcheting, which is not usually considered in existing work on fracture of SMAs. The geometry and mesh used for finite element analysis are shown in Fig. 4.12a, in which the dimensions are reported in mm. Only half of the sample is considered due to symmetry. The length of the pre-crack is assumed to be 1 mm. The model is meshed using 8-node linear hexahedral elements with reduced integration and coupled temperature-displacement (C3D8RT in Abaqus) for a total of 31 920 degrees of freedom. Symmetry boundary conditions are prescribed along the left side of the crack tip and a concentrated force of 593 N is applied at the center of the borehole in the y-direction and transferred to the upper half of the borehole via multi-point constraints. The heat convection conditions are acting on all the exterior surface of the sample. The loading prescribed increases linearly, reaching a maximum in 2 s before subsequently decreasing to zero. This load cycle is repeated 10 times for a total loading time of 40 s. The material parameters used for the simulation are those listed in Table 4.5.

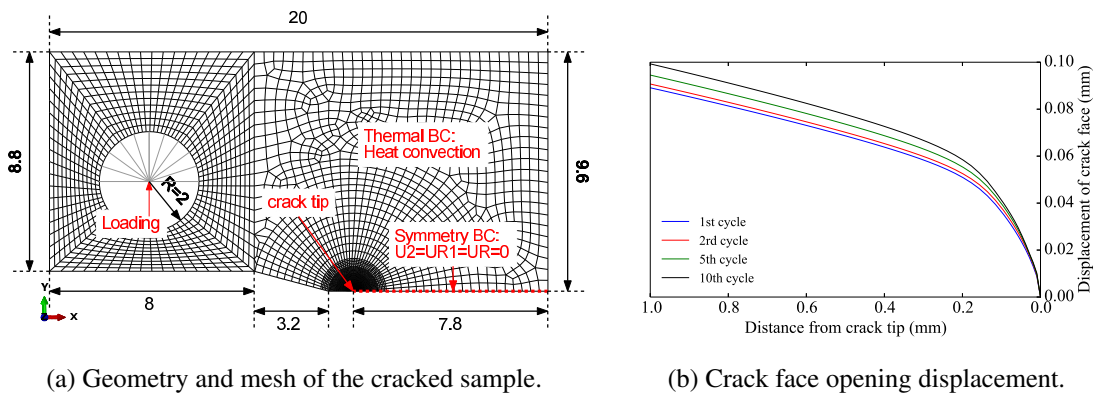


Figure 4.12 Simulation of crack opening under cyclic loading.

The simulation was performed on a laptop equipped with a quad-core CPU and 8GB RAM and was completed in 272 min of CPU time. Figs. 4.12b and 4.13 show the crack face opening displacement, the simulated phase transformation zone and stress distribution near the crack tip at loading times 2 s, 6 s, 18 s and 38 s, corresponding to the load maxima for cycles 1, 2, 5 and 10. Fig. 4.14 shows the residual strain and stress distribution near the crack tip at loading times 4 s, 8 s, 20 s and 40 s, corresponding to the load minima for cycles 1, 2, 5 and 10. Fig. 4.13a shows the phase transformation regions for different load cycles. The region inside the red line is fully martensitic, and the region outside the blue line is fully austenitic, with a zone of mixture in between the two. The size of the phase transformation region is found to increase with increasing number of cycles. This is explained by an accumulation of residual stress (shown in Fig. 4.14b), which facilitates phase transformation in subsequent cycles. Likewise, the crack face opening displacement is shown to increase (Fig. 4.12b).

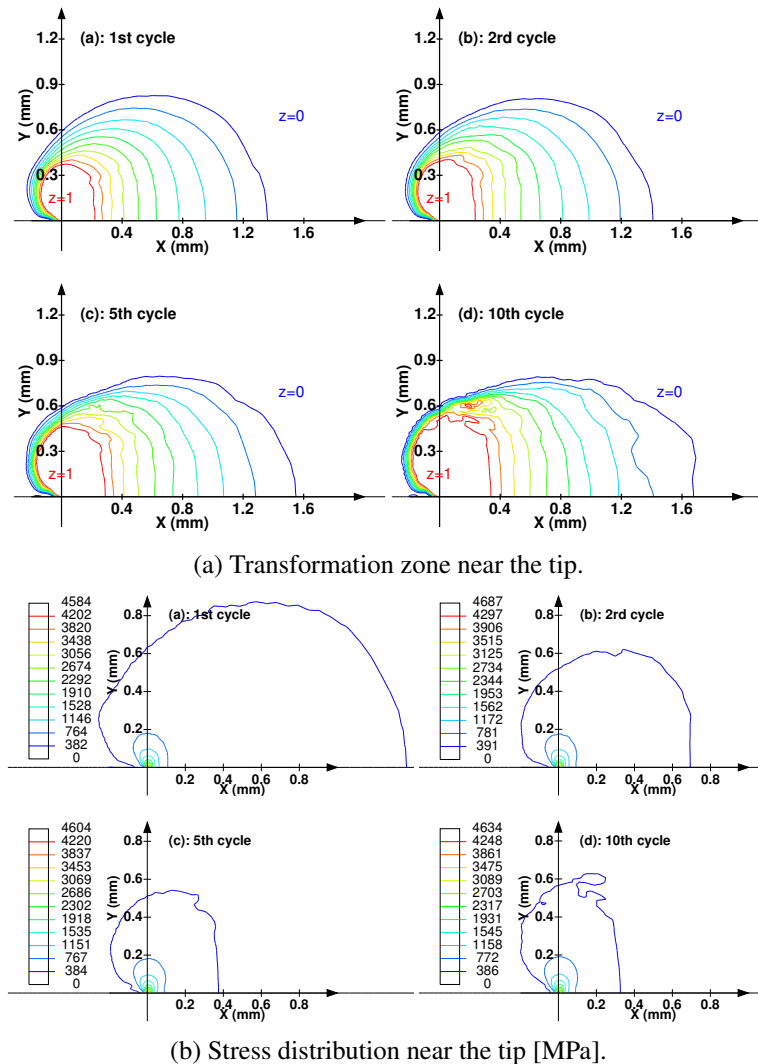


Figure 4.13 Simulated results of crack opening under cyclic loading: (a) transformation zone near the tip; (b) stress distribution near the tip.

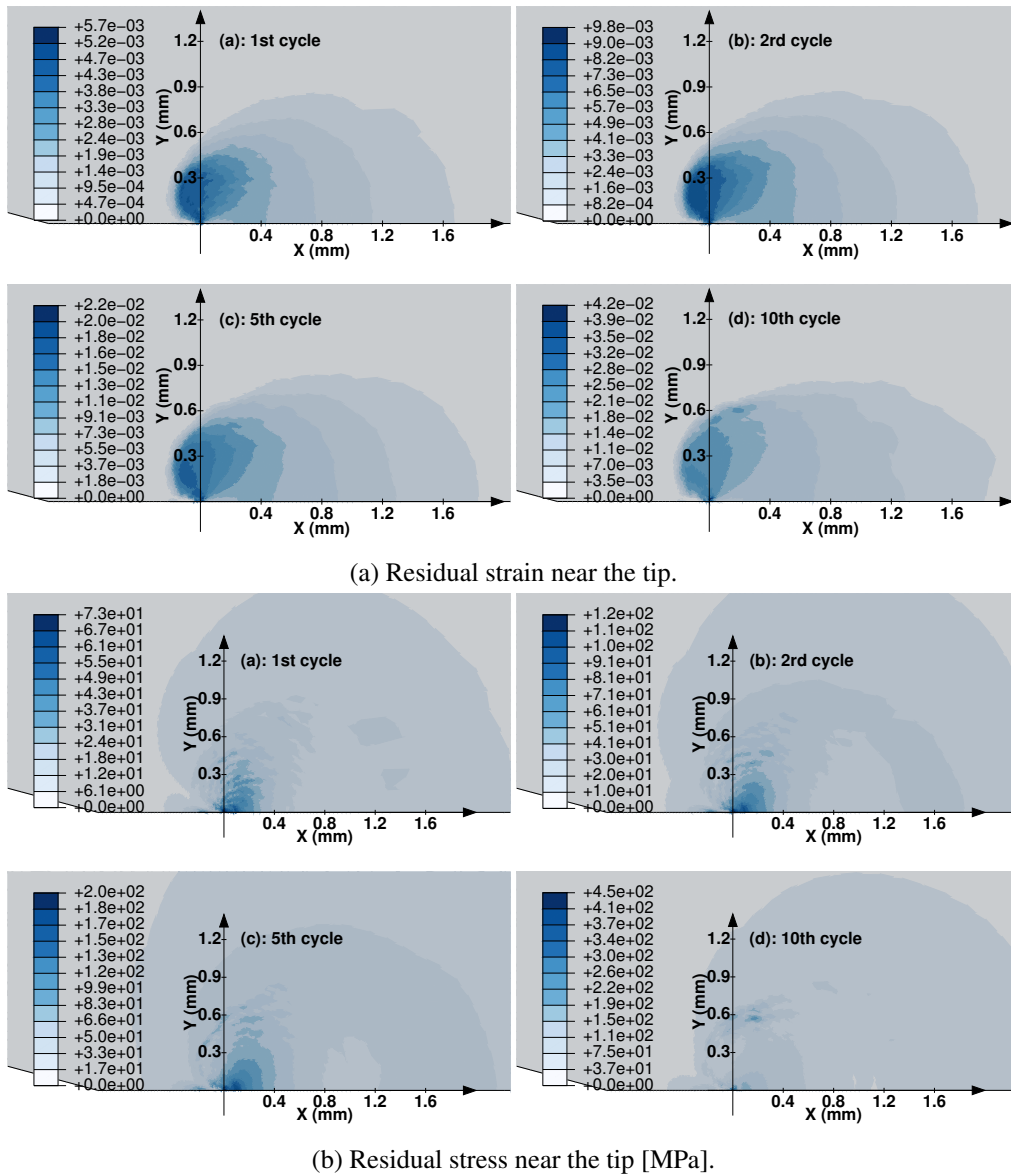


Figure 4.14 Simulated results of crack opening under cyclic loading: (a) residual strain near the tip; (b) residual stress near the tip.

4.5 Conclusion

The model presented in this chapter was shown to successfully account for cyclic loading effects and thermomechanical coupling in SMAs, including the influence of load rate and temperature on both the rate and value at saturation of residual strain. It is the first such comprehensive model to be successfully utilized for relatively complex simulations involving SMAs subjected to multiaxial nonproportional loading, possibly resulting in strong stress gradients. The derivation of the constitutive equations as well as the time-integration and relevant algorithmic considerations were presented in detail. The model was

shown to allow reasonable agreement with several sets of reference experimental and simulation data taken from the literature. Some deviation was noted, however, which can likely be improved in future work by considering tensile-compressive asymmetry. This can be achieved following a procedure similar to [Zaki \(2010\)](#); [Zaki et al. \(2011\)](#), in which von Mises stress and strain equivalents are substituted with asymmetric stress and strain measures.

So far, the developed constitutive law is capable to predict with good accuracy the cyclic thermomechanical response of SMAs. The next step focuses on developing a fatigue criterion to predict whether a SMA structure submitted to high-cycle loading would undergo fatigue.

Chapter 5

Shakedown-based model for high-cycle fatigue of SMAs

This chapter introduces the second step of the approach for fatigue design and optimization. The chapter presents a high-cycle fatigue criterion for SMAs based on shakedown analysis. The analysis accounts for phase transformation as well as reorientation of martensite variants as possible sources of fatigue damage. In the case of high-cycle fatigue, once the structure has reached an asymptotic state, damage is assumed to become confined at the mesoscopic scale, the scale of the grain, with no discernable inelasticity at the macroscopic scale. Using a multiscale approach, a high-cycle fatigue criterion analogous to the Dang Van model ([Dang Van, 1973](#)) for elastoplastic metals is derived for SMAs obeying the ZM model for shape memory alloys ([Zaki and Moumni, 2007b](#)). For these alloys, a safe domain is established in stress deviator space, consisting of a hypercylinder with axis parallel to the direction of martensite orientation at the mesoscopic scale. Safety with regard to high-cycle fatigue, upon elastic shakedown, is conditioned by the persistence of the macroscopic stress path at every material point within the hypercylinder, whose size depends on the volume fraction of martensite. The proposed criterion computes a fatigue factor at each material point, indicating its degree of safeness with respect to high cycle fatigue.

This chapter is organized as follows: after a literature review on the fatigue of SMAs in Section 5.1, a shakedown theory for shape memory alloys is developed in Section 5.3, followed by the derivation of the high-cycle fatigue criterion in Section 5.4 for SMAs obeying the ZM model. A procedure for characterizing the material parameters is then provided in Section 5.6.

5.1 Literature review on the fatigue of SMAs

SMAs are commonly used in situations involving cyclic load variations, fatigue is therefore an important design consideration that has attracted the interest of the scientific and engineering communities ([Melton and Mercier, 1979b](#); [Porter et al., 2001](#); [Hornbogen, 2004](#); [Robertson et al., 2012](#)). In this respect, two types of fatigue are generally distinguished: functional fatigue, which characterizes a functional

degradation in SMAs such as the decrease in maximum recoverable deformation or the modification of transformation temperatures, and structural fatigue, which refers to the degradation of mechanical SMA properties by means of nucleation and propagation of defects that can potentially lead to ultimate failure. [Eggeler et al. \(2004\)](#) investigated functional and structural fatigue of SMAs. They showed that functional fatigue is associated with increased residual strain resulting from incomplete reverse transformation and that structural fatigue is characterized by the nucleation and propagation of surface cracks. [Miyazaki et al. \(1986\)](#) and, later [Pelton et al. \(2012\)](#), showed that the transformation temperatures decrease with thermal loading cycles.

Structural fatigue, in particular, is usually classified in terms of the number of cycles to failure as either low- or high-cycle. The achievable fatigue life is influenced by many factors, including material composition, loading history, surface condition, thermomechanical processing, as well as size effects at smaller length scales ([He and Sun, 2010](#); [Siredey-Schwaller et al., 2009](#)). The ultimate number of cycles typically ranges from 10^4 cycles in temperature-controlled cyclic one-way shape memory applications ([Hornbogen, 2004](#)) to a nominal 4×10^8 cycles for pseudoelastic endovascular stents ([ASTM F2477-07, 2013](#)). In particular, high-cycle fatigue can take place at load levels well below common physical thresholds, for which the material is seemingly elastic with no observable dissipative processes at the macroscopic scale.

[Melton and Mercier \(1979a,b\)](#) investigated the influence of transformation temperature on the fatigue behavior of SMAs. They observed an increase in fatigue limit with decreasing transformation temperature in high cycle fatigue, while in low-cycle fatigue, the material followed a Coffin-Manson law. [Miyazaki et al. \(1989\)](#) performed stress controlled tension-tension fatigue tests on dog-bone SMA samples in which the fatigue limit at 10^6 cycles increased with increasing temperature. This was justified by the dependence on temperature of the martensite transformation stress σ_{ms} . [Miyazaki et al. \(1999\)](#) measured the fatigue life in rotary bending for SMAs with different compositions subjected to different strain amplitudes at different temperatures. The authors showed that low-cycle fatigue was largely influenced by the test temperature whereas high-cycle fatigue was not. [Tabanli et al. \(1999\)](#) examined the effect of mean stress and strain on the fatigue properties of NiTi SMA. They observed that the number of cycles to failure varied non-monotonically with mean strain at fixed amplitude, and the fatigue life for mixed-phase samples is an order of magnitude less than that of single-phase samples. [Moumni et al. \(2005, 2009\)](#) proposed an energy approach for analyzing fatigue in NiTi SMAs, which considers the energy dissipated in a complete stabilized loading cycle as the relevant parameter for the estimation of low-cycle fatigue life, later [Zhang et al. \(2016\)](#) investigated the influence of loading rate on failure and fatigue life. Alternative methods for low-cycle fatigue prediction included modified Coffin-Manson models, such as in the work of [Runciman et al. \(2011\)](#), who applied it to predict fatigue life for thin-walled Nitinol tubes subjected to cyclic torsion to various degrees of mean and alternating strain, and [Maletta et al. \(2012\)](#), who take into account the strain mechanisms involved during repeated stress-induced martensitic transformations.

In contrast to the abundant, if incomplete, research into low-cycle fatigue of SMAs, high-cycle fatigue in these materials has received little attention and is well under-investigated. A typical example

of SMA devices expected to withstand a high number of loading cycles is the SMA stent. According to US Food and Drug Administration (FDA) guidelines, stents are required to last 400 million cycles due to pulsatile blood pressure, or an equivalent of 10 years in the human body (ASTM F2477-07, 2013). Fatigue analysis in this case is particularly important for proper design of the stent and has been the topic of recent work (Hornbogen, 2004; Pelton et al., 2008; Pelton, 2011; Robertson et al., 2012; Dordoni et al., 2014, 2015; Meoli et al., 2014; Mahtabi et al., 2015). Even more recently, Auricchio et al. (2016) derived a Dang Van criterion for high-cycle fatigue in SMAs obeying the Souza-Auricchio model. The derivation uses shakedown analysis and considers phase transformation as the only dissipative mechanism.

5.2 Constitutive model

SMAs are simulated using the ZM model (Zaki and Moumni, 2007b; Moumni et al., 2008). For the purpose of this chapter and to simplify further analytical derivations, it is assumed that austenite and martensite have the same elastic stiffness,

$$\mathbf{K}_A = \mathbf{K}_M := \mathbf{K}. \quad (5.1)$$

Since the model is based on a rheological representation in series of the constituents, the total strain $\boldsymbol{\varepsilon}$ and the local strains in austenite and martensite, $\boldsymbol{\varepsilon}_A$ and $\boldsymbol{\varepsilon}_M$ are related by the equation

$$(1 - z)\boldsymbol{\varepsilon}_A + z\boldsymbol{\varepsilon}_M - \boldsymbol{\varepsilon} = 0. \quad (5.2)$$

Using this equation allows rewriting the free energy density as follows, for $0 < z < 1$:

$$\begin{aligned} \mathcal{W} &:= W(\boldsymbol{\varepsilon}, \theta, z, \boldsymbol{\varepsilon}_{\text{ori}}) \\ &= \frac{1}{2}(\boldsymbol{\varepsilon} - z\boldsymbol{\varepsilon}_{\text{ori}}) : \mathbf{K} : (\boldsymbol{\varepsilon} - z\boldsymbol{\varepsilon}_{\text{ori}}) + zC(\theta) + G\frac{z^2}{2} + \frac{z}{2}[\alpha z + \beta(1 - z)] \left(\frac{2}{3}\boldsymbol{\varepsilon}_{\text{ori}} : \boldsymbol{\varepsilon}_{\text{ori}} \right). \end{aligned} \quad (5.3)$$

The volume fraction of martensite is restricted to the interval $[0, 1]$, therefore

$$\begin{aligned} z &\geq 0, \\ 1 - z &\geq 0, \end{aligned} \quad (5.4)$$

and the orientation finish stress is considered to be lower than the critical stress for forward phase transformation, which means that the equivalent transformation strain $\sqrt{\frac{2}{3}\boldsymbol{\varepsilon}_{\text{ori}} : \boldsymbol{\varepsilon}_{\text{ori}}}$ immediately reaches its maximum value γ as soon as oriented martensite forms:

$$\sqrt{\frac{2}{3}\boldsymbol{\varepsilon}_{\text{ori}} : \boldsymbol{\varepsilon}_{\text{ori}}} = \gamma. \quad (5.5)$$

Using the theory of Lagrange multipliers, a constraints potential \mathcal{W}_1 is constructed such that

$$\mathcal{W}_1 := -\nu_1 z - \nu_2(1 - z) - \mu \left(\gamma - \sqrt{\frac{2}{3} \boldsymbol{\varepsilon}_{\text{ori}} : \boldsymbol{\varepsilon}_{\text{ori}}} \right), \quad (5.6)$$

where ν_1 and ν_2 are Lagrange multipliers obeying the Kuhn-Tucker conditions

$$\begin{aligned} \nu_1 &\geq 0, \quad \nu_1 z = 0, \\ \nu_2 &\geq 0, \quad \nu_2(1 - z) = 0, \\ \mu &> 0, \quad \mu \left(\gamma - \sqrt{\frac{2}{3} \boldsymbol{\varepsilon}_{\text{ori}} : \boldsymbol{\varepsilon}_{\text{ori}}} \right) = 0. \end{aligned} \quad (5.7)$$

The sum of Helmholtz free energy density \mathcal{W} and the constraints potential \mathcal{W}_1 gives the Lagrangian

$$\begin{aligned} \mathcal{L} &= \mathcal{W} + \mathcal{W}_1 \\ &= \frac{1}{2} (\boldsymbol{\varepsilon} - z \boldsymbol{\varepsilon}_{\text{ori}}) : \mathbf{K} : (\boldsymbol{\varepsilon} - z \boldsymbol{\varepsilon}_{\text{ori}}) + z C(\theta) + G \frac{z^2}{2} + \frac{z}{2} [\alpha z + \beta(1 - z)] \gamma^2 \\ &\quad - \nu_1 z - \nu_2(1 - z) - \mu \left(\gamma - \sqrt{\frac{2}{3} \boldsymbol{\varepsilon}_{\text{ori}} : \boldsymbol{\varepsilon}_{\text{ori}}} \right). \end{aligned} \quad (5.8)$$

The Lagrangian can be used to derive the stress-strain relation:

$$\boldsymbol{\sigma} = \frac{\partial \mathcal{L}}{\partial \boldsymbol{\varepsilon}} = \mathbf{K} : (\boldsymbol{\varepsilon} - z \boldsymbol{\varepsilon}_{\text{ori}}). \quad (5.9)$$

The thermodynamic forces \mathcal{A}_z^{d} and $\mathcal{A}_{\text{ori}}^{\text{d}}$, driving phase transformation and martensite reorientation are then derived as follows:

$$\begin{aligned} \mathcal{A}_z^{\text{d}} &= - \frac{\partial \mathcal{L}}{\partial z} = \mathcal{A}_z - \mathcal{A}_z^{\text{r}} \\ &= \boldsymbol{\sigma} : \boldsymbol{\varepsilon}_{\text{ori}} - C(\theta) - Gz - \left[(\alpha - \beta)z + \frac{\beta}{2} \right] \gamma^2 \\ &\quad - (\nu_1 - \nu_2), \end{aligned} \quad (5.10)$$

$$\begin{aligned} \mathcal{A}_{\text{ori}}^{\text{d}} &= - \frac{\partial \mathcal{L}}{\partial \boldsymbol{\varepsilon}_{\text{ori}}} = \mathcal{A}_{\text{ori}} - \mathcal{A}_{\text{ori}}^{\text{r}} \\ &= z \left\{ \boldsymbol{\sigma} - \frac{2}{3} [\alpha z + \beta(1 - z)] \boldsymbol{\varepsilon}_{\text{ori}} \right\} \\ &\quad - \frac{2\mu}{3} \frac{\boldsymbol{\varepsilon}_{\text{ori}}}{\sqrt{\frac{2}{3} \boldsymbol{\varepsilon}_{\text{ori}} : \boldsymbol{\varepsilon}_{\text{ori}}}}, \end{aligned} \quad (5.11)$$

where \mathcal{A}_z and \mathcal{A}_{ori} are the thermodynamic forces without internal constraints, \mathcal{A}_z^{r} and $\mathcal{A}_{\text{ori}}^{\text{r}}$ are the thermodynamic forces due to the internal constraints. The evolution of martensite volume fraction z and martensite reorientation strain $\boldsymbol{\varepsilon}_{\text{ori}}$ are governed by the following positive, convex dissipation

pseudopotential \mathcal{D} :

$$\begin{aligned}\mathcal{D} := D(\dot{z}, \dot{\boldsymbol{\varepsilon}}_{\text{ori}}) &= P(z, \dot{z})\dot{z} + R(z)\sqrt{\frac{2}{3}\boldsymbol{\varepsilon}_{\text{ori}} : \boldsymbol{\varepsilon}_{\text{ori}}} \\ &= [a(1-z) + bz]|\dot{z}| + z^2Y\sqrt{\frac{2}{3}\boldsymbol{\varepsilon}_{\text{ori}} : \boldsymbol{\varepsilon}_{\text{ori}}},\end{aligned}\quad (5.12)$$

and the thermodynamic forces \mathcal{A}_z^{d} and $\mathcal{A}_{\text{ori}}^{\text{d}}$ are chosen to be sub-gradients of the pseudopotential \mathcal{D} to ensure thermodynamic consistency:

$$\mathcal{A}_z^{\text{d}} \in \partial_{\dot{z}} \mathcal{D}, \quad (5.13)$$

$$\mathcal{A}_{\text{ori}}^{\text{d}} \in \partial_{\dot{\boldsymbol{\varepsilon}}_{\text{ori}}} \mathcal{D}. \quad (5.14)$$

The above relations yield the following inequalities:

$$\mathcal{F}_z = |\mathcal{A}_z^{\text{d}}| - [a(1-z) + bz] \leq 0, \quad (5.15)$$

$$\mathcal{F}_{\text{ori}} = \|\mathcal{A}_{\text{ori}}^{\text{d}}\|_{\text{VM}} - z^2Y \leq 0, \quad (5.16)$$

which defined loading functions for phase transformation and martensite orientation, respectively.

5.3 Shakedown analysis of SMAs

The shakedown theory provides a necessary condition for fatigue safety in structures subjected to time-varying load. The elastic shakedown of a structure corresponds to a situation where energy dissipation becomes bounded and the response elastic after a certain number of loading cycles. This path-independent state, which is also independent of the initial state of the structure, corresponds to a high-cycle fatigue regime. The shakedown theorem for elastic perfectly plastic materials was initially proposed by [Melan \(1936\)](#) and [Koiter \(1960\)](#) and was later extended to hardening plasticity by [Nguyen \(2003\)](#) and to non-smooth mechanics by [Peigney \(2010\)](#).

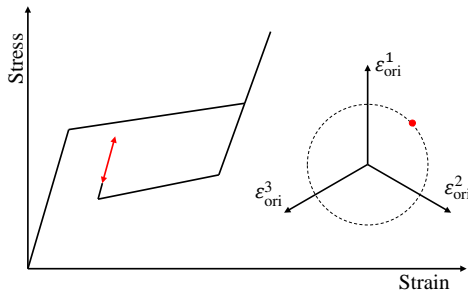
An elastoplastic structure subjected to cyclic loading may present one of the following three asymptotic responses: (i) elastic shakedown, in which the material settles into a pure elastic response, (ii) elastoplastic shakedown, in which the response corresponds to a stabilized elastoplastic cycle, (iii) cyclic ratcheting, where no stabilization takes place and therefore inelastic strains continue to accumulate. A structure that undergoes elastic shakedown can usually achieve high-cycle fatigue life, whereas elastoplastic shakedown usually corresponds to low-cycle fatigue life.

Compared to elastoplastic structures, the behavior of SMA structures under cyclic loading is significantly more complex. This is mainly due to solid-solid phase transformation taking place within SMAs and to the possible influence of thermomechanical coupling. An early analysis of shakedown in SMAs was proposed by [Feng and Sun \(2007\)](#), in which elastic–plastic deformation and phase transformation are considered with the assumption of small strains and isothermal conditions.

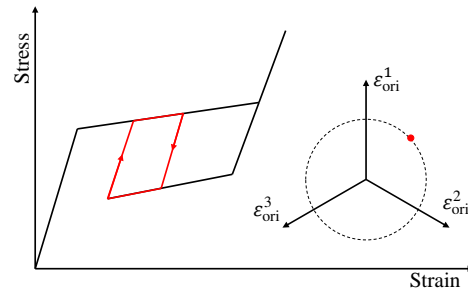
A SMA structure subjected to cyclic loading below the plastic yield strength may present one of the

following four asymptotic responses:

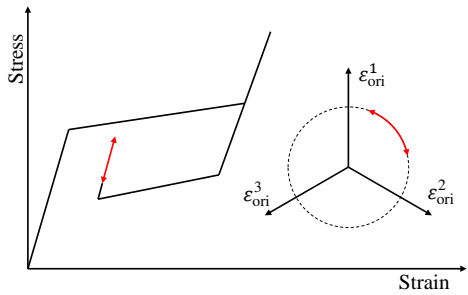
- Elastic shakedown, which corresponds to pure elastic response as illustrated in Fig. 5.1a,
- Alternating phase transformation without martensite reorientation, which corresponds to stabilized cyclic evolution of the martensite volume fraction as illustrated in Fig. 5.1b,
- Alternating martensite reorientation without phase transformation, which corresponds to stabilized cyclic evolution of martensite reorientation strain at constant volume fraction of martensite as illustrated in Fig. 5.1c,
- Alternating phase transformation and martensite reorientation, which corresponds to stabilized cyclic evolution of both martensite volume fraction and martensite reorientation strain as illustrated in Fig. 5.1d.



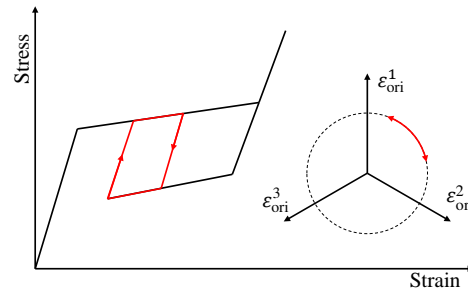
(a) Elastic shakedown.



(b) Alternating phase transformation without martensite reorientation.



(c) Alternating martensite reorientation without phase transformation.



(d) Alternating phase transformation and martensite reorientation.

Figure 5.1 Possible responses of SMAs under varying loads.

Out of these possible states, only elastic shakedown can be reasonably expected to result in high-cycle fatigue life. For SMAs obeying the ZM model, we propose the following statement of the shakedown theorem based on the work of Peigney (2014a,b):

Conjecture 1 (elastic shakedown of SMAs obeying the ZM model) *If there exists $m > 1$, $T > 0$ and time-independent fields $(\rho^*, z^*, \varepsilon_{\text{ori}}^*, \mathcal{A}_z^{\text{L}*}, \mathcal{A}_{\text{ori}}^{\text{L}*})$ such that*

$$\mathcal{A}_z \left(m\sigma^{\text{E}}(t) + \rho^*, z^*, \varepsilon_{\text{ori}}^* \right) - \mathcal{A}_z^{\text{L}*} \in \partial_z \mathcal{D}, \quad (5.17)$$

$$\mathcal{A}_{\text{ori}} \left(m\sigma^{\text{E}}(t) + \rho^*, z^*, \varepsilon_{\text{ori}}^* \right) - \mathcal{A}_{\text{ori}}^{\text{L}*} \in \partial_{\varepsilon_{\text{ori}}} \mathcal{D}, \quad (5.18)$$

are satisfied for all $t \geq T$, then elastic shakedown will be achieved regardless of the initial state of the material.

5.4 Fatigue analysis based on a multiscale approach

In order to achieve high-cycle fatigue performance, the asymptotic macroscopic behavior of a SMA structure is expected to be purely elastic. In this case, defects appear and are then confined in certain grains because of stress concentration due to anisotropy and heterogeneity of the material at this scale. A mesoscopic analysis is therefore important in investigating high-cycle fatigue.

In this regard, [Dang Van \(1973\)](#) proposed a multiscale approach for analyzing high-cycle fatigue in elastoplastic metallic materials. Starting with the assumption of elastic shakedown and from mesoscopic considerations ([Ballard et al., 1995](#)), the authors derived a multiaxial fatigue criterion based on the following fundamental assumption: “*fatigue rupture will not occur if and only if the elastic shakedown takes place at all scales of the structure, at the macroscopic scale as well as at the mesoscopic scale. In particular the local plastic dissipation must be bounded.*” ([Dang Van, 2002](#)). In order to reduce the computational time, [Papadopoulos \(1987\)](#) proposed a criterion using von Mises’s criterion instead of Schmidt’s law for the grain plasticity criterion.

In contrast to elastoplastic metals, where the governing dissipation mechanism is slip plasticity, dissipation in shape memory alloys is due to a combination of phase transformation and martensite reorientation. Uniaxial or multiaxial loading of SMA can induce phase transformation accompanied by the nucleation or shrinking of martensite variants ([Otsuka and Wayman, 1999](#); [Bodaghi et al., 2013](#)). More specifically, when the direction of the applied loading changes locally at a material point, preferred martensite variants begin to form at the expense of others leading to a change in orientation of the inelastic strain in the martensite phase. Both phase transformation and martensite reorientation can take place at the same time in presence of multiaxial nonproportional loading.

As shown in [Fig. 5.2](#), at the macroscopic scale, the mechanical state of a shape memory alloy is described by a set of *macroscopic* variables considered to be uniform in a representative elementary volume (REV). These variables include the stress Σ , strain E , martensite volume fraction Z and martensite orientation strain E_{ori} . In reality, however, the REV consists of grains with different shapes, orientations and internal states. At the scale of these grains, *i.e.* the mesoscopic scale, the mechanical state is defined by mesoscopic variables, which include the stress σ , strain ε , martensite volume fraction z and martensite orientation strain ε_{ori} . Within a SMA crystal, austenite and martensite phases are

separated by habit planes, whereas different variants of martensite are separated by martensite plate boundaries. According to the crystallographic theory of martensitic transformation, phase transformation is achieved by means of habit plane motion, whereas the reorientation of variants is associated with the motion of plate boundaries.

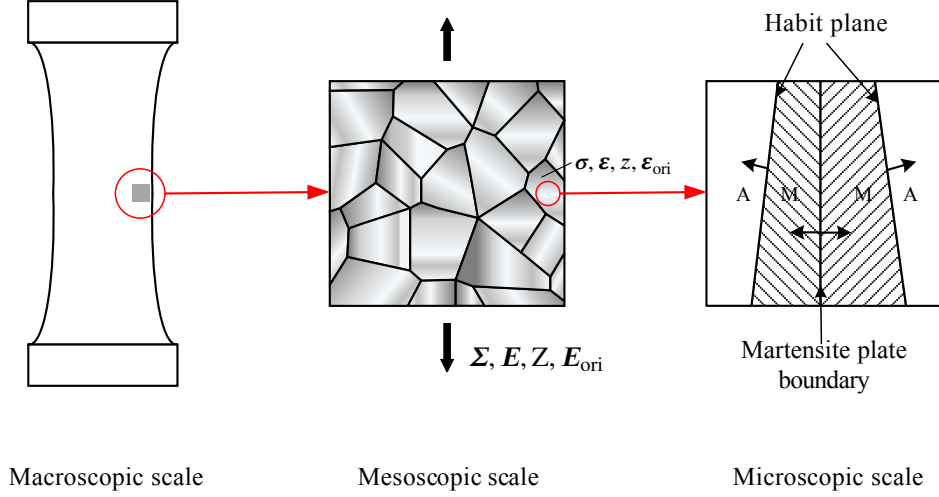


Figure 5.2 Multiscale representation of SMA volume elements.

In high-cycle fatigue, relatively few grains undergo phase transformation and martensite orientation. These grains can be thought of as inclusions in a SMA matrix. Following [Dang Van \(1973\)](#)'s assumption based on the Lin-Taylor model, the macroscopic total strain of the matrix and the mesoscopic strain in the inclusion are considered identical. In this case,

$$\mathbf{E} = \boldsymbol{\epsilon} \Rightarrow \mathbf{E}^{el} + \mathbf{Z}\mathbf{E}_{ori} = \boldsymbol{\epsilon}^{el} + z\boldsymbol{\epsilon}_{ori}. \quad (5.19)$$

Moreover, if \mathbf{L} and \mathbf{l} represent the macroscopic and the mesoscopic elastic stiffness tensors of the SMA, Eq. (5.19) can be written

$$\mathbf{L}^{-1} : \boldsymbol{\Sigma}^{el} + \mathbf{Z}\mathbf{E}_{ori} = \mathbf{l}^{-1} : \boldsymbol{\sigma} + z\boldsymbol{\epsilon}_{ori}. \quad (5.20)$$

Multiplying both sides by \mathbf{l} then gives

$$\boldsymbol{\sigma} = \mathbf{l} : \mathbf{L}^{-1} : \boldsymbol{\Sigma}^{el} + \mathbf{l} : (\mathbf{Z}\mathbf{E}_{ori} - z\boldsymbol{\epsilon}_{ori}). \quad (5.21)$$

The double inner product of the meso-stiffness \mathbf{l} by the macro-compliance \mathbf{L}^{-1} is the fourth rank localization tensor. If one further assumes that

$$\mathbf{L} = \mathbf{l}, \quad (5.22)$$

the localization tensor ($\mathbf{l} : \mathbf{L}^{-1}$) becomes the fourth-order identity tensor.

The mesoscopic residual stress $\boldsymbol{\rho}$ is defined as

$$\boldsymbol{\rho} = \boldsymbol{l} : (\boldsymbol{Z}\boldsymbol{E}_{\text{ori}} - z\boldsymbol{\varepsilon}_{\text{ori}}), \quad (5.23)$$

so that

$$\boldsymbol{\sigma} = \boldsymbol{\Sigma}^{\text{el}} + \boldsymbol{\rho}. \quad (5.24)$$

Because $\boldsymbol{\rho}$ is deviatoric, the mesoscopic and macroscopic hydrostatic pressures are equal. Indeed, if P denotes the hydrostatic pressure at the mesoscale, one has

$$P = \frac{1}{3}\text{tr}\boldsymbol{\sigma} = \frac{1}{3}\text{tr}(\boldsymbol{\Sigma}^{\text{el}} + \boldsymbol{\rho}) = \frac{1}{3}\text{tr}\boldsymbol{\Sigma}^{\text{el}}. \quad (5.25)$$

According to the fundamental assumption used to derive the Dang Van criterion for high-cycle fatigue, infinite fatigue life is conditioned by the achievement by the structure of a mesoscopic elastic shakedown state. This entails the existence of a time-independent field $\boldsymbol{\rho}^*$ such that

$$\boldsymbol{\sigma}(\boldsymbol{x}, t) = \boldsymbol{\Sigma}^{\text{el}}(\boldsymbol{x}, t) + \boldsymbol{\rho}^*(\boldsymbol{x}), \quad (5.26)$$

satisfies the crystal loading condition:

$$\forall \boldsymbol{x}, t, \mathcal{F}(\boldsymbol{\sigma}(\boldsymbol{x}, t)) \leq 0. \quad (5.27)$$

If $\mathcal{F} = \{\mathcal{F}_z, \mathcal{F}_{\text{ori}}\}$ is a loading function for the crystal, corresponding to phase transformation and martensite reorientation functions at the macroscopic scale, then based on the ZM model (Zaki and Moumni, 2007a), the loading conditions can be written as

$$\mathcal{A}_z^{\text{d}} \in \partial_z \mathcal{D}, \text{ and } \mathcal{A}_{\text{ori}}^{\text{d}} \in \partial_{\boldsymbol{\varepsilon}_{\text{ori}}} \mathcal{D}. \quad (5.28)$$

leads to the following inequalities:

$$\mathcal{F}_z = \left| \boldsymbol{s} : \boldsymbol{\varepsilon}_{\text{ori}} - C(\theta) - Gz - \left[(\alpha - \beta)z + \frac{\beta}{2} \right] \gamma^2 - (\nu_1 - \nu_2) \right| - [a(1 - z) + bz] \leq 0, \quad (5.29)$$

$$\mathcal{F}_{\text{ori}} = \left\| \boldsymbol{s} - \frac{2}{3\gamma^2} (\boldsymbol{s} : \boldsymbol{\varepsilon}_{\text{ori}}) \boldsymbol{\varepsilon}_{\text{ori}} \right\|_{\text{VM}} - zY \leq 0. \quad (5.30)$$

For a given material point, if $\boldsymbol{\varepsilon}_{\text{ori}}(\boldsymbol{x})$ is the local martensite orientation strain tensor and $\boldsymbol{s}(\boldsymbol{x}, t)$ is the local stress deviator, denoting $\boldsymbol{s}_p(\boldsymbol{x}, t)$ the projection of $\boldsymbol{s}(\boldsymbol{x}, t)$ parallel to $\boldsymbol{\varepsilon}_{\text{ori}}(\boldsymbol{x})$ and $\boldsymbol{s}_o(\boldsymbol{x}, t)$ the projection normal to $\boldsymbol{\varepsilon}_{\text{ori}}(\boldsymbol{x})$ as shown in Fig. 5.3a, the loading conditions in Eqs. (5.29) and (5.30) can be rewritten as follows:

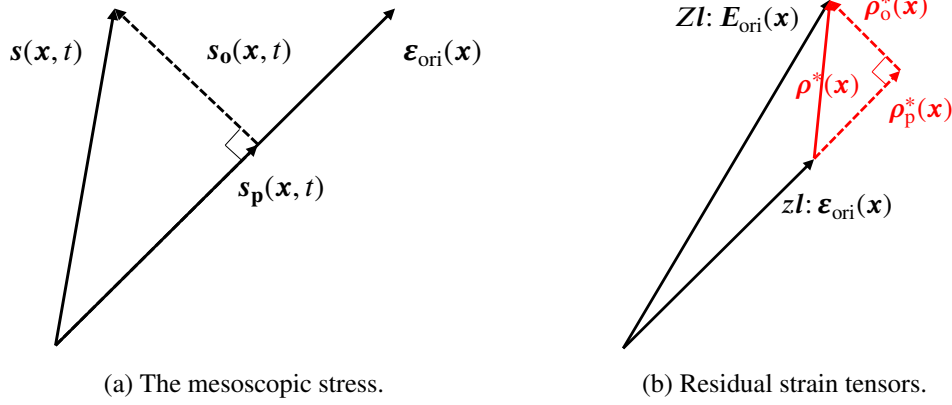


Figure 5.3 Projections parallel and normal to the orientation strain.

$$\mathcal{F}_z = \left| \left\| s_p(\mathbf{x}, t) \right\|_{\text{VM}} - f_z^*(\mathbf{x}) \right| \leq \frac{1}{\gamma} [a(1-z) + bz], \quad (5.31)$$

$$\mathcal{F}_{\text{ori}} = \left\| s_o(\mathbf{x}, t) \right\|_{\text{VM}} \leq zY, \quad (5.32)$$

where $f_z^*(\mathbf{x})$, defined as

$$f_z^*(\mathbf{x}) = \frac{1}{\gamma} \left\{ C(\theta) + Gz + \left[(\alpha - \beta)z + \frac{\beta}{2} \right] \gamma^2 + (v_1 - v_2) \right\}, \quad (5.33)$$

is independent of $s_p(\mathbf{x}, t)$ and $s_o(\mathbf{x}, t)$. Because of the fundamental assumption of elastic shakedown, $f_z^*(\mathbf{x})$ is also time-independent at shakedown at constant temperature because z no longer changes. By examining the above expressions of the loading functions, it is seen that a stress aligned with the direction of martensite orientation, for which $s_o(\mathbf{x}, t) = 0$ and $s(\mathbf{x}, t) = s_p(\mathbf{x}, t)$, will not modify this orientation but rather contribute to further phase transformation within the bounds of the physical constraints $0 \leq z \leq 1$. Conversely, a stress perpendicular to the direction of martensite orientation, for which $s_p(\mathbf{x}, t) = 0$ and $s(\mathbf{x}, t) = s_o(\mathbf{x}, t)$, will favor reorientation of the variants in directions that are more in-line with the direction of the applied load and therefore more energetically favorable.

Using the meso-macro scale relationship (5.26), Eqs. (5.31) and (5.32) become

$$\mathcal{F}_z = \left| \left\| S_p^{\text{el}}(\mathbf{x}, t) + \rho_p^*(\mathbf{x}) \right\|_{\text{VM}} - f_z^*(\mathbf{x}) \right| \leq \frac{1}{\gamma} [a(1-z) + bz], \quad (5.34)$$

$$\mathcal{F}_{\text{ori}} = \left\| S_o^{\text{el}}(\mathbf{x}, t) + \rho_o^*(\mathbf{x}) \right\|_{\text{VM}} \leq zY. \quad (5.35)$$

Following the work of Peigney (2014b), a geometric interpretation of the above relations is that a loading path $\phi(t)$ described by $\{S^{\text{el}}(\mathbf{x}, t) + \rho^*(\mathbf{x})\}$ is translated by $f_z^*(\mathbf{x})$. Shakedown occurs if the translated loading path $\phi(t)$ is enclosed in the elastic domain. The loading conditions under the

assumption of elastic shakedown become

$$\forall \mathbf{x}, t \begin{cases} \left| \|\mathbf{S}_p^{\text{el}}(\mathbf{x}, t) + \boldsymbol{\rho}_p^*(\mathbf{x})\|_{\text{VM}} - f_z^*(\mathbf{x}) \right| \leq \sqrt{3}\bar{w}^*, \\ \|\mathbf{S}_o^{\text{el}}(\mathbf{x}, t) + \boldsymbol{\rho}_o^*(\mathbf{x})\|_{\text{VM}} \leq \sqrt{3}\bar{r}^*. \end{cases} \quad (5.36)$$

A geometric interpretation of the conditions (5.36) is shown in Figs. 5.4a and 5.4b. In Fig. 5.4a, it can be seen that the phase transformation conditions define an admissible stress domain bounded by two hyperplanes orthogonal to $\boldsymbol{\varepsilon}_{\text{ori}}(\mathbf{x})$. Similarly, the loading conditions for martensite reorientation define an admissible stress domain bounded by a hypercylinder with infinite length, parallel to $\boldsymbol{\varepsilon}_{\text{ori}}(\mathbf{x})$. If $f_z^*(\mathbf{x})$

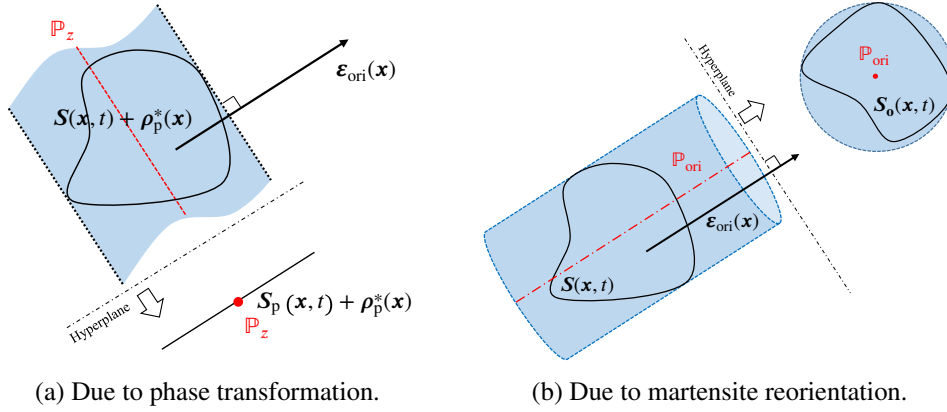


Figure 5.4 Admissible stress domains.

and $\boldsymbol{\rho}_o^*(\mathbf{x})$ are chosen such that

$$\begin{cases} f_z^*(\mathbf{x}) = \mathbf{f}_{\text{VM}}, \mathbf{f} \in \mathbb{P}_z, \\ -\boldsymbol{\rho}_o^*(\mathbf{x}) \in \mathbb{P}_{\text{ori}}, \end{cases} \quad (5.37)$$

where

$$\begin{cases} \mathbb{P}_z = \left\{ \mathbf{f} \mid \mathbf{f} = \frac{1}{2} \left\{ \max_t [\mathbf{S}_p^{\text{el}}(\mathbf{x}, t) + \boldsymbol{\rho}_p^*(\mathbf{x})] - \min_t [\mathbf{S}_p^{\text{el}}(\mathbf{x}, t) + \boldsymbol{\rho}_p^*(\mathbf{x})] \right\} \right\}, \\ \mathbb{P}_{\text{ori}} = \left\{ \boldsymbol{\rho} \mid \min_{\boldsymbol{\rho}} \left\{ \max_t \sqrt{\frac{2}{3}} [\mathbf{S}_o^{\text{el}}(\mathbf{x}, t) - \boldsymbol{\rho}] : [\mathbf{S}_o^{\text{el}}(\mathbf{x}, t) - \boldsymbol{\rho}] \right\} \right\}. \end{cases} \quad (5.38)$$

\mathbb{P}_z is the central hyperplane of the elastic region and \mathbb{P}_{ori} is the axis of the hypercylinder that contains $\mathbf{S}(\mathbf{x}, t)$. Combining the two loading conditions leads to an elastic domain consisting of the smallest hypercylinder that contains $\mathbf{S}(\mathbf{x}, t) + \boldsymbol{\rho}_p^*(\mathbf{x})$. The hypercylinder is parallel to the orientation strain tensor $\boldsymbol{\varepsilon}_{\text{ori}}(\mathbf{x})$, as shown in the left figure of Fig. 5.5.

Introducing the following definitions:

$$\begin{cases} \bar{w}^* = \max_{t_1, t_2} \frac{1}{2\sqrt{3}} \left[\|\mathbf{S}_p^{\text{el}}(\mathbf{x}, t_1) + \boldsymbol{\rho}_p^*(\mathbf{x})\|_{\text{VM}} - \|\mathbf{S}_p^{\text{el}}(\mathbf{x}, t_2) + \boldsymbol{\rho}_p^*(\mathbf{x})\|_{\text{VM}} \right], \\ \bar{r}^* = \max_{t_3} \frac{1}{\sqrt{3}} \|\mathbf{S}_o^{\text{el}}(\mathbf{x}, t_3) - [-\boldsymbol{\rho}_o^*(\mathbf{x})]\|_{\text{VM}}. \end{cases} \quad (5.39)$$

Because $\mathbf{S}_p^{\text{el}}(\mathbf{x}, t)$ and $\boldsymbol{\rho}_p^*(\mathbf{x})$ are parallel, one has

$$\|\mathbf{S}_p^{\text{el}}(\mathbf{x}, t) + \boldsymbol{\rho}_p^*(\mathbf{x})\|_{\text{VM}} = \|\mathbf{S}_p^{\text{el}}(\mathbf{x}, t)\|_{\text{VM}} + \|\boldsymbol{\rho}_p^*(\mathbf{x})\|_{\text{VM}}, \quad (5.40)$$

Eq. (5.39) becomes

$$\begin{cases} \bar{w}^* = \max_{t_1, t_2} \frac{1}{2\sqrt{3}} \|\mathbf{S}_p^{\text{el}}(\mathbf{x}, t_1) - \mathbf{S}_p^{\text{el}}(\mathbf{x}, t_2)\|_{\text{VM}}, \\ \bar{r}^* = \max_{t_3} \frac{1}{\sqrt{3}} \|\mathbf{S}_o^{\text{el}}(\mathbf{x}, t_3) - [-\boldsymbol{\rho}_o^*(\mathbf{x})]\|_{\text{VM}}. \end{cases} \quad (5.41)$$

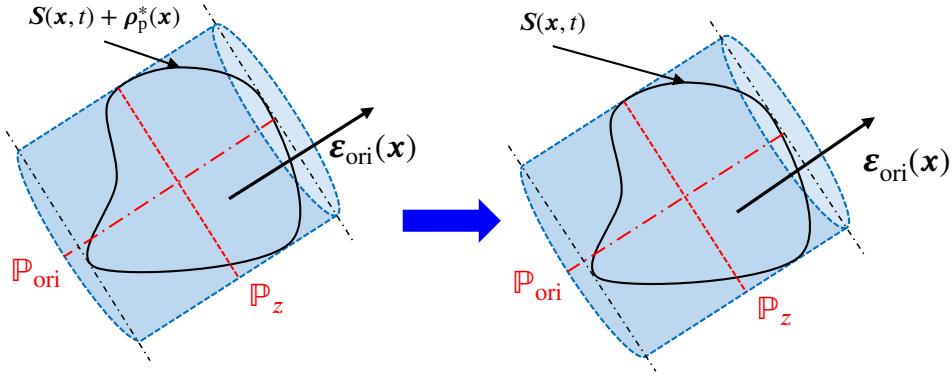


Figure 5.5 Elastic domain containing the loading path.

From a geometric point view, $2\sqrt{2}\bar{w}^*$ and $\sqrt{2}\bar{r}^*$ represent the height and radius of the smallest hypercylinder in which the macroscopic stress deviator $\mathbf{S}(\mathbf{x}, t)$ is contained, as shown in the right figure of Fig. 5.5. \bar{w}^* and \bar{r}^* can be rewritten as

$$\begin{cases} \bar{w}^* = \max_{t_1, t_2} \frac{1}{2\sqrt{2}} \sqrt{[\mathbf{S}_p^{\text{el}}(\mathbf{x}, t_1) - \mathbf{S}_p^{\text{el}}(\mathbf{x}, t_2)] : [\mathbf{S}_p^{\text{el}}(\mathbf{x}, t_1) - \mathbf{S}_p^{\text{el}}(\mathbf{x}, t_2)]}, \\ \bar{r}^* = \max_{t_3} \frac{1}{\sqrt{2}} \sqrt{\{\mathbf{S}_o^{\text{el}}(\mathbf{x}, t_3) - [-\boldsymbol{\rho}_o^*(\mathbf{x})]\} : \{\mathbf{S}_o^{\text{el}}(\mathbf{x}, t_3) - [-\boldsymbol{\rho}_o^*(\mathbf{x})]\}}. \end{cases} \quad (5.42)$$

A fatigue factor $G(\mathbf{x})$ can then be defined as follows:

$$G(\mathbf{x}) := \frac{1}{2} \left| \frac{\bar{w}^*}{\bar{b}} + \frac{\bar{r}^*}{\bar{c}} \right| + \frac{1}{2} \left| \frac{\bar{w}^*}{\bar{b}} - \frac{\bar{r}^*}{\bar{c}} \right|, \quad (5.43)$$

where \bar{b} and \bar{c} are two material constants corresponding to fatigue limits with respect to phase transformation and martensite orientation, which define the maximum size of the safe domain of the SMA material.

For $z = 0$, the martensitic phase is absent and the elastic domain reduces to a hypersphere. With the

definition

$$\begin{aligned}\bar{v}^* &= \max_t \frac{1}{\sqrt{3}} \|\mathbf{S}^{\text{el}}(\mathbf{x}, t) - [-\boldsymbol{\rho}^*(\mathbf{x})]\|_{\text{VM}} \\ &= \max_t \frac{1}{\sqrt{2}} \sqrt{\{\mathbf{S}^{\text{el}}(\mathbf{x}, t) - [-\boldsymbol{\rho}^*(\mathbf{x})]\} : \{\mathbf{S}^{\text{el}}(\mathbf{x}, t) - [-\boldsymbol{\rho}^*(\mathbf{x})]\}}.\end{aligned}\quad (5.44)$$

The fatigue factor $G(\mathbf{x})$ becomes

$$G(\mathbf{x}) := \frac{\bar{v}^*}{\bar{b}'}, \quad (5.45)$$

where \bar{b}' is the material constant corresponding to fatigue limit with respect to phase transformation when $z = 0$. Combining Eqs. (5.43) and (5.45) then gives

$$G(\mathbf{x}) := \begin{cases} \frac{1}{2} \left| \frac{\bar{w}^*}{\bar{b}} + \frac{\bar{r}^*}{\bar{c}} \right| + \frac{1}{2} \left| \frac{\bar{w}^*}{\bar{b}} - \frac{\bar{r}^*}{\bar{c}} \right|, & 0 < z < 1, \\ \frac{\bar{v}^*}{\bar{b}'}, & z = 0. \end{cases} \quad (5.46)$$

Fig. 5.6 illustrates situations in which the factor $G(\mathbf{x})$ is less than, equal to, or greater than 1 for $z \in (0, 1)$. In this figure, the macroscopic loading path $\mathbf{S}(\mathbf{x}, t)$ is bounded by a minimum hypercylinder (blue dashed lines in 2D) for which the height and radius are \bar{w}^* and \bar{r}^* . The safe domain for high-cycle fatigue is represented with a solid red line, corresponding to a cylinder of height \bar{b} and radius \bar{c} . $G(\mathbf{x})$ is less than 1 whenever the loading path is strictly within the safe domain. It becomes equal to 1 when the loading path reaches the safe domain boundary and exceeds 1 outside the safe domain. Indeed, the value of $G(\mathbf{x})$ as given by Eq. (5.43) is decided by the larger of \bar{w}^*/\bar{b} and \bar{r}^*/\bar{c} . It can be regarded as a measure of the degree of closeness between the hypercylinder boundaries and the fatigue limits such that

$$\begin{cases} G(\mathbf{x}) \leq 1 \Rightarrow \text{the material point at } \mathbf{x} \text{ is safe,} \\ G(\mathbf{x}) > 1 \Rightarrow \text{the material point at } \mathbf{x} \text{ is not safe.} \end{cases} \quad (5.47)$$

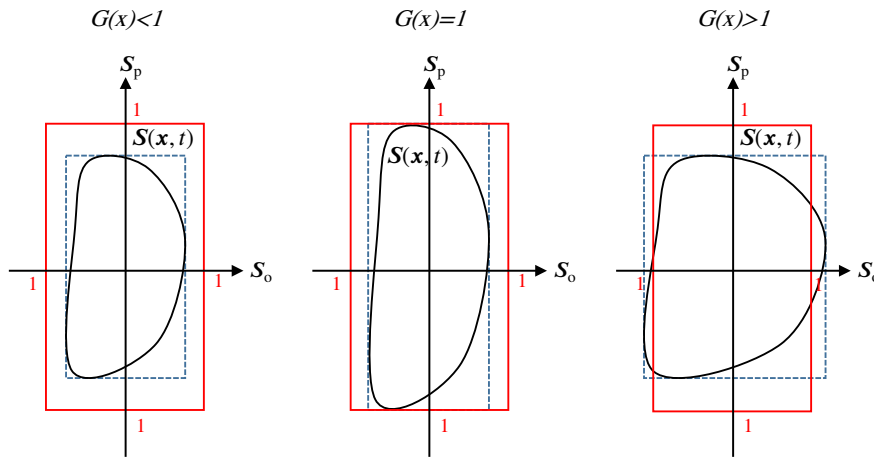


Figure 5.6 The cases when the factor $G(\mathbf{x})$ changes to different values.

Furthermore, because hydrostatic pressure is expected to also influence fatigue life, the following fatigue criterion is proposed for SMAs:

$$G(\mathbf{x}) + \bar{a}P_{\max}(\mathbf{x}) \leq 1, \quad (5.48)$$

in which $P_{\max}(\mathbf{x})$ represents the maximum value of the hydrostatic stress at material point \mathbf{x} and \bar{a} is a material constant. It should be noted that if the material is fully austenite, $z = 0$ reduces the fatigue criterion (5.48) to

$$\bar{v}^* + \frac{\bar{a}}{\bar{b}'}P_{\max}(\mathbf{x}) \leq \bar{b}'. \quad (5.49)$$

In this case, the form of the criterion is consistent with the one given by Papadopoulos (1987) for elastoplastic metals.

5.5 Non-smoothness of the safe domain

As shown in Fig. 5.7a, the safe domain is not smooth, in general, for values of z between 0 and 1. It transitions from a hypersphere for $z = 0$, consistent with conventional von Mises plasticity, to a hypercylinder aligned with the direction of orientation of martensite for strictly positive values of z .

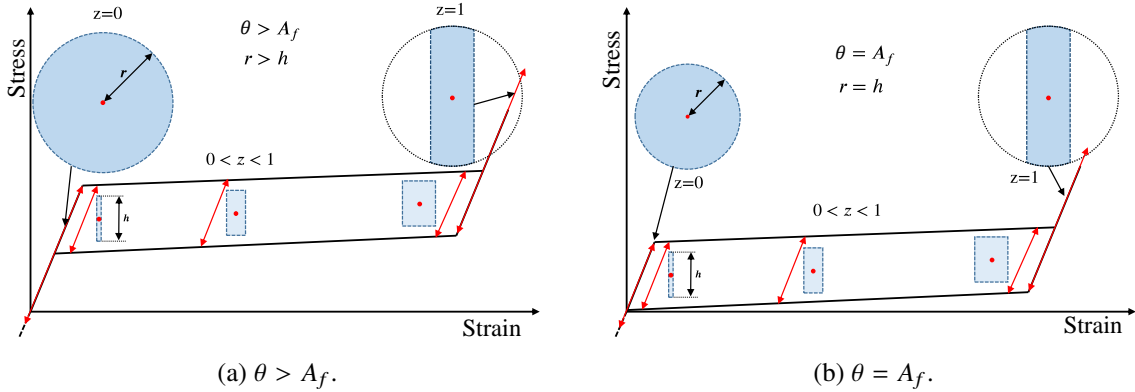


Figure 5.7 Elastic domain.

The diameter of the hypercylinder increases with z from an infinitesimal value when martensite starts to nucleate to a maximum value when the martensitic transformation is complete, *i.e.* for $z = 1$. The cylindrical domain is delimited, along its axis, with plastic yield surfaces that are not considered in this work and the size of the domain changes non-monotonically with the volume fraction z of martensite. Indeed, the domain is smaller in the mixed phase region ($0 < z < 1$) compared to the single-phase regions corresponding to either $z = 0$ or $z = 1$. This observation is consistent with the experimental observations in Tabanlı et al. (1999), where the number of cycles to failure upon elastic shakedown was found to be lowest in the mixed-phase region. The authors carried out 5 fatigue experiments corresponding to the loading cases in Fig. 5.8, where the red lines illustrate cyclic loading paths. The number of cycles to failure for the different loading cases is shown in Fig. 5.8, tests A and B were

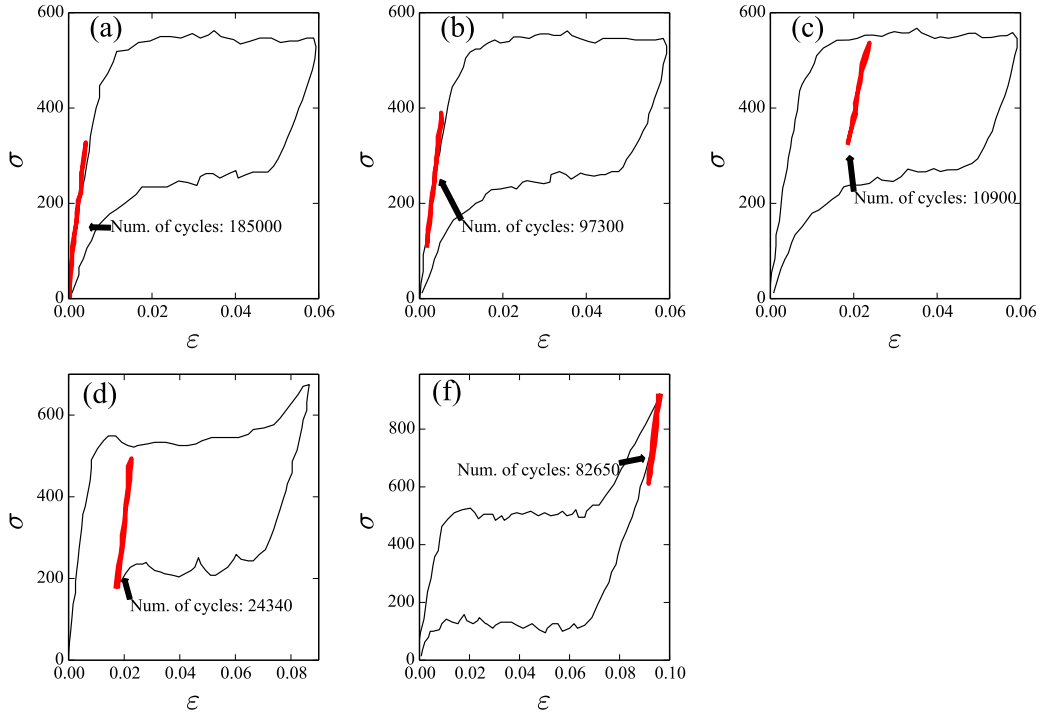


Figure 5.8 Fatigue tests for different mean stress/strain values (Tabanlı et al., 1999).

conducted using fully austenitic samples, test E was conducted using a fully martensitic sample, and tests C and D were conducted on a mixed-phase material. For similar stress amplitudes, the number of cycles to failure of mixed-phase SMAs is lower than that of single-phase SMAs. Similar phenomenon also been observed by Zheng et al. (2016) with a series of fatigue experiment using SMA samples with different martensite volume fraction. A fixed nominal strain amplitude of 0.25% was applied on all samples, as shown in Fig. 5.9, the number of cycles to failure of mixed-phase SMAs is almost the same but lower than that of single-phase SMAs.

Moreover, as shown in Fig. 5.10, for temperatures higher than the austenite finish temperature A_f , the radius r of the elastic hypersphere when $z = 0$ is greater than the height h of the elastic hypercylinder when z becomes strictly positive. r and h become equal for $\theta = A_f$, shown in Fig. 5.7b.

$$\begin{cases} r > h, & \theta > A_f, \\ r = h, & \theta = A_f. \end{cases} \quad (5.50)$$

Experimental determination of the dimension h of the hypercylinder for values of the martensite volume fraction strictly between 0 and 1 is not straightforward. Instead, h can be determined directly in the fully austenite state ($z = 0$) when $\theta = A_f$. In this situation, the radius r and the height h are equal.

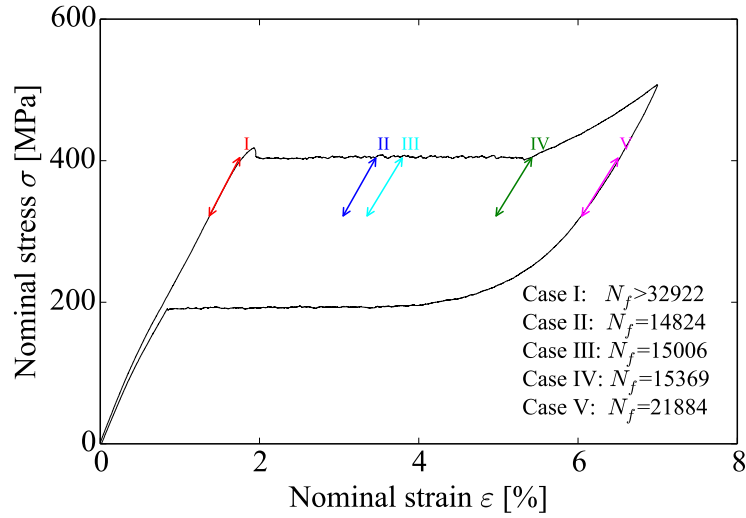


Figure 5.9 Fatigue tests with fixed nominal strain amplitude (Zheng et al., 2016).

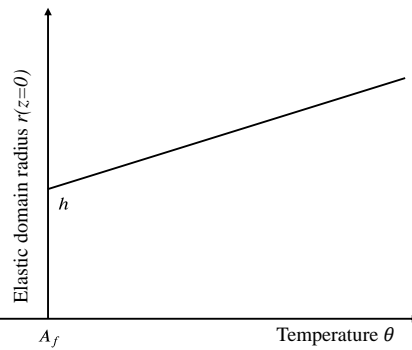


Figure 5.10 Influence of temperature on the radius of the elastic domain for $z = 0$.

5.6 Example of SMA applications

5.6.1 Identification of material constants

The fatigue criterion given by the relation (5.48) requires the identification of four material constants \bar{a} , \bar{b} , \bar{c} and \bar{b}' . The four constants can be determined from the following uniaxial fatigue experiments:

- Test 1: fully reversed bending above the austenite finish temperature A_f , which gives the fatigue limit α_{-1} , as shown in Fig. 5.11a,
- Test 2: repeated torsion at the austenite finish temperature A_f , which gives the fatigue limit β_0 , as shown in Fig. 5.11b,
- Test 3: alternating torsion below the martensite finish temperature M_f , which gives the fatigue limit γ_{-1} , as shown in Fig. 5.11c,

- Test 4: alternating torsion above the austenite finish temperature A_f , which gives the fatigue limit β'_{-1} , as shown in Fig. 5.11d.

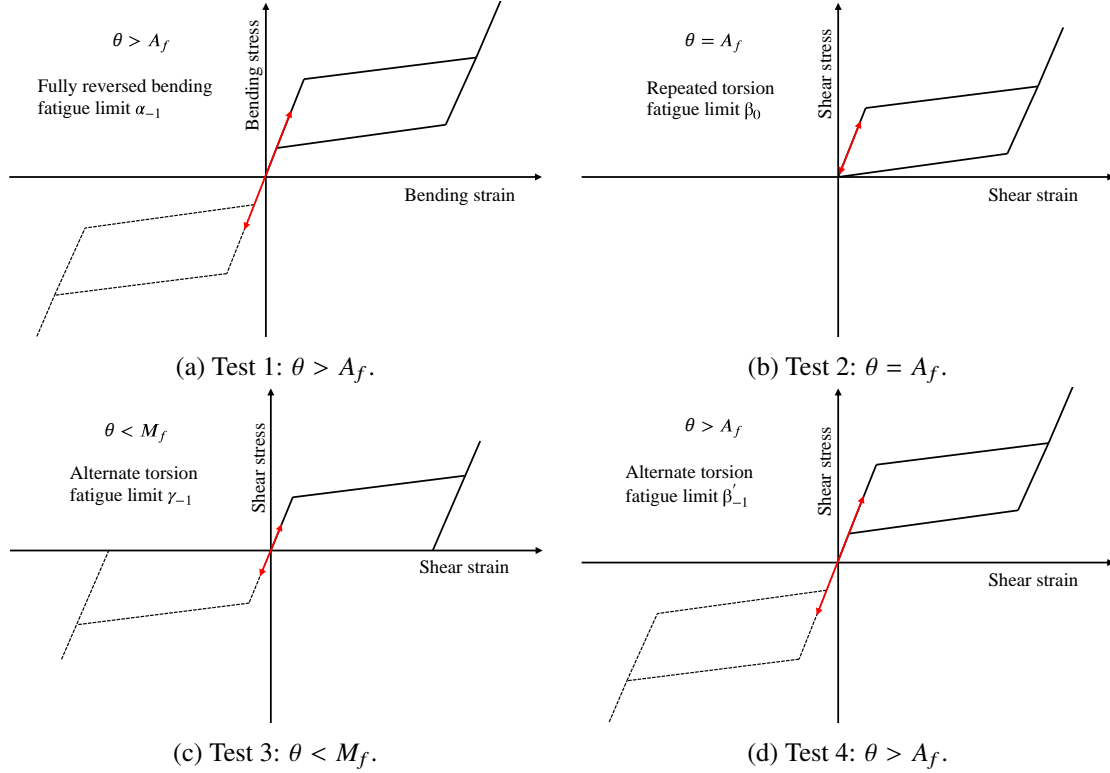


Figure 5.11 Uniaxial fatigue experiments needed for the determination of the material constants α_{-1} , β_0 , γ_{-1} and β'_{-1} .

Eq. (5.48) gives for $z \in [0, 1)$

$$\begin{cases} \bar{a} = \frac{3}{\alpha_{-1}} - \frac{\sqrt{3}}{\beta'_{-1}}, \\ \bar{b} = \frac{1}{2}\beta_0, \\ \bar{c}(z) = z\gamma_{-1}, \\ \bar{b}' = \beta'_{-1}, \end{cases} \quad (5.51)$$

where the fatigue limit due to martensite reorientation depends on the volume fraction of martensite.

5.6.2 Fatigue analysis of a SMA brick under multiaxial nonproportional loading

A SMA brick is subjected to the multiaxial nonproportional cyclic loading cases shown in Fig. 5.12 under isothermal conditions. In each case, the loading is applied according to the sequence $o \rightarrow a \rightarrow b \rightarrow c \rightarrow d \rightarrow e \rightarrow a$ for the first cycle then $a \rightarrow b \rightarrow c \rightarrow d \rightarrow e \rightarrow a$ for the following cycles. The simulations are performed on a single 8-node hexahedral element, using the material parameters listed in Table 5.1. The uniaxial tensile stress-strain response of the material is shown in Fig. 5.13.

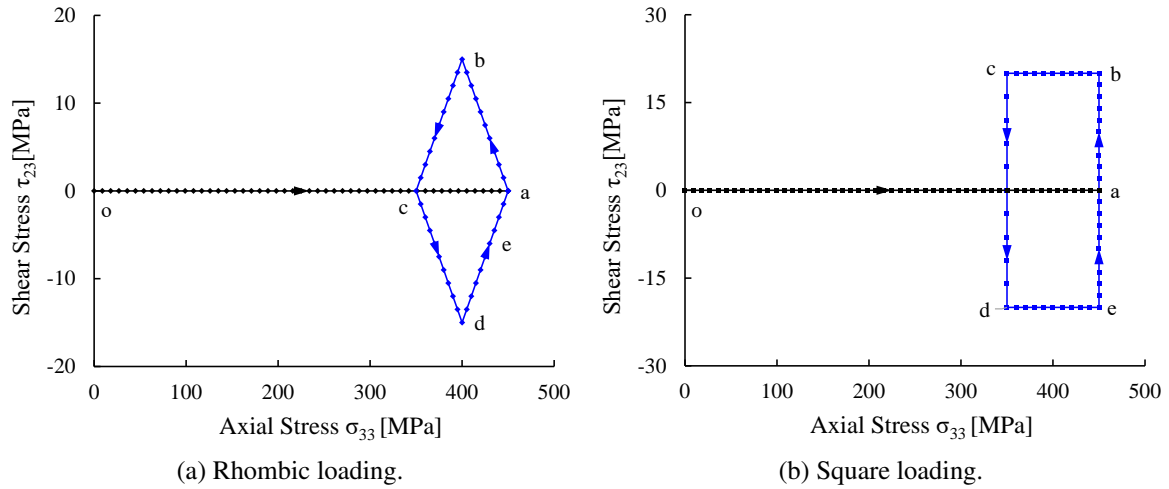


Figure 5.12 Two loading path: (a) the rhombic type and (b) the square type.

Table 5.1 Material parameters used for simulating SMA brick.

E_A	40 000	MPa	E_M	40 000	MPa
ν	0.3		Y	80	MPa
a	4.0	MPa	b	4.0	MPa
G	7.2	MPa	ε_0	0.04	
α	500	MPa	β	2500	MPa
ξ	0.4	MPa K ⁻¹	κ	2	MPa
A_f^0	273	K	θ	293	K

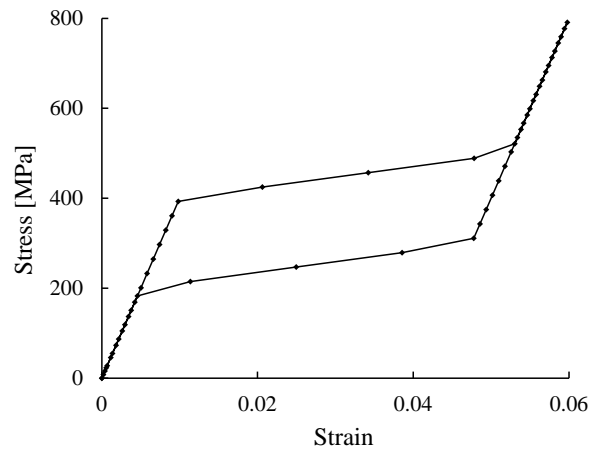


Figure 5.13 Uniaxial stress-strain response of the material.

The evolution of the martensite volume fraction and the resulting axial stress-strain behavior are shown in Fig. 5.14. From the figure, it can be seen that the material does achieve a state of elastic shakedown.

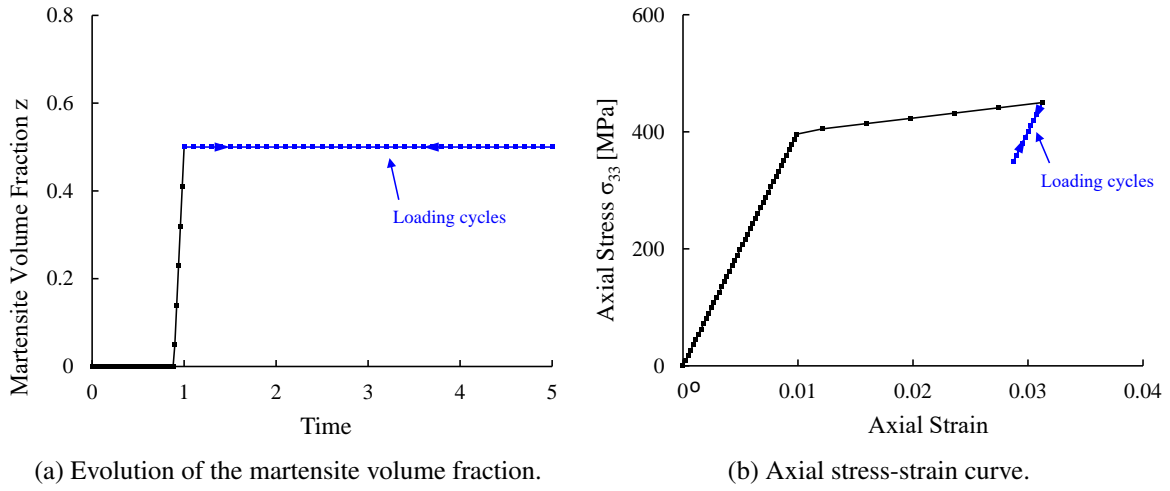


Figure 5.14 Responses to the rhombic and square loading cases in Fig. 5.12.

Melton and Mercier (1979b) performed fatigue tests for both pseudoelastic austenite ($\theta > A_f$) and thermal martensite ($\theta < M_s$) under stress-controlled, fully reversed ($R = -1$) tension-compression loading. According to Robertson et al. (2012), the 10^7 cycles fatigue limit in both conditions corresponds to a stress amplitude in the linear elastic range at $\sim 80\%$ of the plateau stress. Based on this observation, the SMA fatigue limits at 10^7 cycles are set to $\beta_0 = 92.4$ MPa and $\gamma_{-1} = 37.0$ MPa in the present simulations.

For the obtained martensite volume fraction $z = 0.5$, Eq. (5.51) gives the material parameters $\bar{b} = 46.2$ MPa and $\bar{c} = 18.5$ MPa. The loading paths are shown in Fig. 5.15, in which the directions of \mathbf{S}_p and \mathbf{S}_o are defined by the unit vectors

$$\begin{cases} \mathbf{n}_{s_p} = \left[\frac{-1}{\sqrt{6}}, \frac{-1}{\sqrt{6}}, \frac{2}{\sqrt{6}}, 0, 0, 0 \right]^T, \\ \mathbf{n}_{s_o} = [0, 0, 0, 0, 0, 1]^T. \end{cases} \quad (5.52)$$

As shown in Figure 5.15a, the rhombic loading path corresponds to $\bar{w}^* = 28.9$ MPa and $\bar{r}^* = 15$ MPa, for which a fatigue factor $G(\mathbf{x}) = 0.81$ is computed using Eq. (5.46). The material point at \mathbf{x} is therefore safe for this loading case. In contrast, the square loading path in Fig. 5.15b corresponds to $\bar{w}^* = 28.9$ MPa and $\bar{r}^* = 20$ MPa, for which $G(\mathbf{x}) = 1.08$, indicating that the material point at \mathbf{x} is not safe.

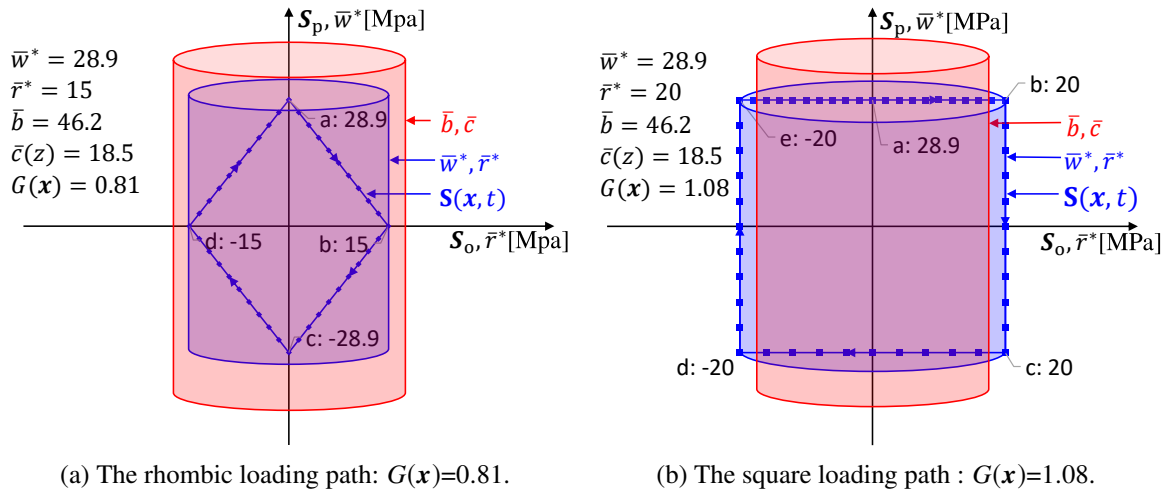


Figure 5.15 Fatigue factor $G(\mathbf{x})$ for different loading paths.

5.7 Conclusion

A shakedown-based high-cycle fatigue criterion for shape memory alloys was presented in this paper. The proposed analysis accounts for phase transformation as well as reorientation of martensite variants as possible sources of fatigue damage. Possible shakedown states are analyzed and conditions for elastic shakedown are established using a multiscale approach. Based on the observation that unlimited fatigue life is conditioned by elastic shakedown at the mesoscopic scale, which precludes inelastic deformation at this scale, a safe domain with regard to high-cycle fatigue is established in stress deviator space. The domain consists of a finite hypercylinder parallel to the direction of martensite orientation, the size of which is function of the martensite volume fraction. A procedure for determining the material constants for the fatigue criterion is also described. The proposed criterion permits to compute a fatigue factor at each material point indicating its degree of safeness with respect to high cycle fatigue. Hence, it is possible to localize critical points and predict whether the SMA structure would undergo or not fatigue. In this chapter, the second step of the efficient approach for fatigue design and optimization is completed. The proposed criterion can be used to design and optimize SMA structures against fatigue, which is the focus of the next chapter.

Chapter 6

Shape optimization of SMA structures with respect to fatigue

This chapter introduces the third step of the efficient approach for fatigue design and optimization. The chapter deals with the development of optimization tools capable of enhancing the fatigue life of a SMA structure subjected to cyclic loading. The unique ability of SMAs to accommodate recoverable deformation has motivated increased usage of these materials in engineering applications ranging from biomedicine ([Duerig et al., 1999](#)) to automotive engineering ([Jani et al., 2014](#)) and aerospace industry ([Hartl et al., 2009a,b](#)). A good understanding of fatigue in SMAs is necessary to improve the safety of SMA structures in industrial applications. Designing and optimizing SMA structures against fatigue require an efficient optimization approach to improve the design as well as a reliable fatigue criterion. In the literature, research and development efforts related to the optimized design of SMA devices have been numerous. Using SMA wire actuators, [Strelec et al. \(2003\)](#) designed an airfoil considering the coupled fluid–structure interaction problem and utilized a genetic algorithm (GA) based optimization tool with local search steps. Wind tunnel tests indicated an increase in lift for a given flow velocity and angle of attack by activating the optimized SMA wire actuators. [Langelaar and van Keulen \(2007\)](#); [Langelaar and van Keulen \(2008a,b\)](#) proposed detailed SMA structural design methods incorporating gradient-based optimization, both topology and shape optimization procedures for the design of SMA devices are described. [Hartl et al. \(2011\)](#); [Oehler et al. \(2012\)](#) proposed a general design optimization framework for SMA components and assemblies thereof actuation applications. A structural response model with respect to concerned design variables is proposed using design of experiments (DOE) techniques, and then been used to search the desired configuration using gradient or non-gradient based optimizer. By relying on commercially available software and utilizing tools already well established in design optimization, the proposed approach is shown to be very efficient for analyzing morphing aerostructures. In spite of their high quality, most of these publications are based on sensitivity analysis or applied on morphing aerostructures and remain qualitative. We focus our analyses on improving the fatigue lifetime of pseudoelastic SMAs structures under multiaxial cyclic loading.

This chapter is organized as follows: after a brief review of low- and high-cycle fatigue of shape

memory alloys in Section 6.1, detailed description of the optimization method used in the chapter is introduced in Section 6.2. Low- and high-cycle fatigue study cases are presented in Section 6.3 and Section 6.4, respectively. General conclusions and outlook are finally provided in Section 6.5.

6.1 Fatigue criterion for SMAs

6.1.1 Energy based low-cycle fatigue criterion for SMAs

Under cyclic loading, the mechanical response of pseudoelastic SMAs stabilizes and settles into a closed stress-strain loop, after several transient cycles, as shown in Fig. 6.1. For low-cycle fatigue, it is shown that the dissipated energy of the stabilized cycle is a relevant parameter for the estimation of fatigue life (Moumni et al., 2005).

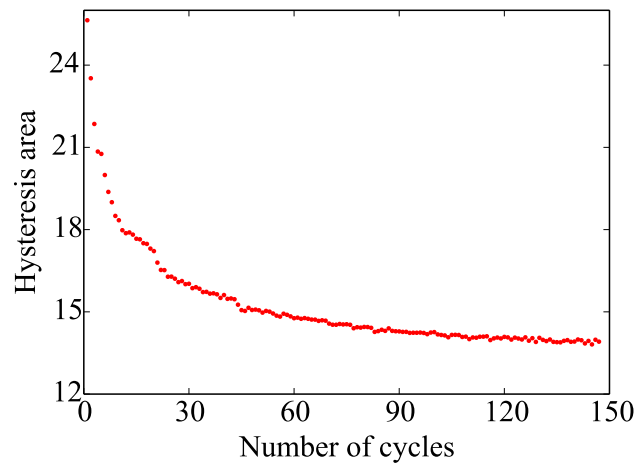


Figure 6.1 Evolution of the hysteresis area with the number of cycles.

To calculate low-cycle fatigue life of SMAs, Morin (2011) introduced the effect of hydrostatic pressure based on the work of Moumni et al. (2005). The fatigue criterion proposed by Morin (2011) is used here:

$$W_d(\mathbf{x}) + aP_{\max}(\mathbf{x}) = m[N_f(\mathbf{x})]^p, \quad (6.1)$$

where \mathbf{x} is a material point in a SMA structure, $W_d(\mathbf{x})$ is the hysteresis area of the stabilized cycle, $P_{\max}(\mathbf{x})$ is the maximum hydrostatic pressure of the stabilized cycle, $N_f(\mathbf{x})$ is the number of cycles to failure, a , m and p are material parameters. For the tensile-compressive results from Morin (2011), $a = 0.0025$, $m = 5.19 \text{ mJ/m}^3$ and $p = -0.2196$. The results are reported in Fig. 6.2.

To apply the low-cycle fatigue criterion in Eq. (6.1) on shape optimization, a fatigue factor, which indicates the degree of safeness with respect to low-cycle fatigue, is defined as

$$f_{\text{low}}(\mathbf{x}) = W_d(\mathbf{x}) + aP_{\max}(\mathbf{x}). \quad (6.2)$$

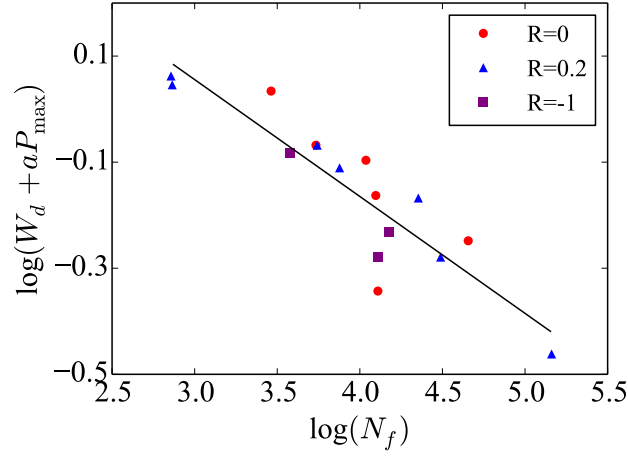


Figure 6.2 Energy based low-cycle fatigue criterion from Morin (2011).

6.1.2 Shakedown based high-cycle fatigue criterion for SMAs

In order to achieve high-cycle fatigue performance, the asymptotic macroscopic behavior of a SMA structure is expected to be purely elastic. In this case, defects appear and are then confined in certain grains because of stress concentration due to anisotropy and heterogeneity of the material at this scale. The shakedown theory provides a necessary condition for fatigue safety in structures subjected to time-varying load. The elastic shakedown of a structure corresponds to a situation where energy dissipation becomes bounded and the response elastic after a certain number of loading cycles. This path-independent state, which is also independent of the initial state of the structure, corresponds to a high-cycle fatigue regime. In the previous chapter, a shakedown based high-cycle fatigue criterion for SMAs is presented.

$$G(\mathbf{x}) + \bar{a}P_{\max}(\mathbf{x}) \leq 1, \quad (6.3)$$

where \mathbf{x} is a given material point, $G(\mathbf{x})$ is a fatigue factor calculated based on the state of point \mathbf{x} , $P_{\max}(\mathbf{x})$ is the maximum hydrostatic pressure at the stabilized cycle and \bar{a} is a material constants. The proposed criterion permits to compute a fatigue factor at each material point indicating its degree of safeness with respect to high-cycle fatigue.

$$\begin{cases} G(\mathbf{x}) + \bar{a}P_{\max}(\mathbf{x}) \leq 1 \Rightarrow \text{the material point at } \mathbf{x} \text{ is safe,} \\ G(\mathbf{x}) + \bar{a}P_{\max}(\mathbf{x}) > 1 \Rightarrow \text{the material point at } \mathbf{x} \text{ is not safe.} \end{cases} \quad (6.4)$$

Detailed definition of the high-cycle fatigue criterion defined in Eq. (6.3) can be found in the previous chapter. The fatigue factor defined as

$$f_{\text{high}}(\mathbf{x}) = G(\mathbf{x}) + \bar{a}P_{\max}(\mathbf{x}), \quad (6.5)$$

which indicates the degree of safeness with respect to high-cycle fatigue at material point \mathbf{x} .

6.2 Optimization methods

6.2.1 Boundary value problem

The boundary value problem is written here for the case of quasi-static evolution of a SMA structure occupying a volume $\Omega \in \mathbb{R}^3$ subjected to prescribed loading in the time interval $[0, T]$. Body forces $\mathbf{f}(\mathbf{x}, t)$ act in the domain Ω . The boundary Γ is defined by the following mechanical boundary components: The contact forces $\mathbf{T}^d(\mathbf{x}, t)$ are applied on a static boundary Γ_t , displacement $\mathbf{u}^d(\mathbf{x}, t)$ is prescribed on a kinematic boundary Γ_u , the design variable for shape optimization is applied on a design boundary Γ_d . The condition $\Gamma_t \cap \Gamma_u \cap \Gamma_d = \emptyset$ makes $\mathbf{T}^d(\mathbf{x}, t)$ and $\mathbf{u}^d(\mathbf{x}, t)$ design-independent, meaning that they remain unchanged with the variation of the design configuration. Using Fourier's law of heat conduction $\mathbf{q}(\mathbf{x}, t) = -k\nabla\theta(\mathbf{x}, t)$, the thermal boundary conditions are defined as follows: The inner heat generation $Q(\mathbf{x}, t)$ acts over Ω . Heat convection conditions act on the portion Γ_h of the boundary Γ , and the specified temperature $\theta^d(\mathbf{x}, t)$ is constrained over the remaining portion Γ_θ such that $\Gamma_\theta + \Gamma_h = \Gamma$. Starting from an initial configuration at time $t = 0$ in which the state variables are known, the problem consists in solving the following set of equations over Ω for $t \in [0, T]$:

Static and kinematic admissibility

$$\boldsymbol{\sigma} \in \mathbb{K}_\sigma, \mathbf{u} \in \mathbb{K}_u, \quad (6.6)$$

where the set \mathbb{K}_σ , \mathbb{K}_u are defined by

$$\begin{aligned} \mathbb{K}_\sigma &= \{ \boldsymbol{\sigma} \mid \operatorname{div} \boldsymbol{\sigma} + \mathbf{f} = 0 \text{ in } \Omega, \boldsymbol{\sigma} \cdot \mathbf{n} = \mathbf{T}^d \text{ on } \Gamma_T \}, \\ \mathbb{K}_u &= \{ \mathbf{u} \mid \mathbf{u} = \mathbf{u}^d \text{ on } \Gamma_u \}, \end{aligned} \quad (6.7)$$

and \mathbf{n} is an outward unit vector normal to the boundary Γ_T .

Heat equations

$$\mathbf{q} \in \mathbb{K}_q, \theta \in \mathbb{K}_\theta, \quad (6.8)$$

where the set \mathbb{K}_q , \mathbb{K}_θ are defined by

$$\begin{aligned} \mathbb{K}_q &= \{ \mathbf{q} \mid -\operatorname{div} \mathbf{q} + \dot{Q} = \rho C_p \dot{\theta} \text{ in } \Omega, \mathbf{q} \cdot \mathbf{n} = h(\theta - \theta_r) \text{ on } \Gamma_h \}, \\ \mathbb{K}_\theta &= \{ \theta \mid \theta = \theta^d \text{ on } \Gamma_\theta \}, \end{aligned} \quad (6.9)$$

where θ_r is the ambient temperature of the surrounding environment and h is the heat transfer coefficient. \mathbf{n} is an outward unit vector normal to the boundary Γ_h .

6.2.2 Shape optimization problem

Structural optimization problems are commonly formulated as constrained minimization problems. The typical shape optimization problem is formulated as:

$$\begin{aligned}
 &\text{find: } \Gamma_d(\mathbf{X}), \mathbf{X} = (x_1, x_2, \dots, x_n) \\
 &\text{min: } f(\mathbf{X}), \\
 &\text{s.t.: } g_j(\mathbf{X}) \geq 0 \quad (j = 1, 2, \dots, p), \\
 &\quad \quad h_k(\mathbf{X}) = 0 \quad (k = 1, 2, \dots, m), \\
 &\quad \quad \Gamma_d(\mathbf{X}) \in \Omega_d,
 \end{aligned} \tag{6.10}$$

where \mathbf{X} are design variables describing the design boundary, $\Gamma_d(\mathbf{X})$ is the optimal boundary of Γ_d . $f(\mathbf{X})$ is the objective function, $g_j(\mathbf{X})$ are inequality constraints for $j = 1$ to p , $h_k(\mathbf{X})$ are equality constraints for $k = 1$ to m . Ω_d is the design space that constrained by the design boundary Γ_d .

The solution of a constrained optimization problem in Eq. (6.10) can often be found by using the so-called Lagrangian method. The Lagrangian is defined as

$$\mathcal{L}(\mathbf{X}, \boldsymbol{\lambda}, \boldsymbol{\eta}) = f(\mathbf{X}) - \sum_{j=1}^p \lambda_j g_j(\mathbf{X}) - \sum_{k=1}^m \eta_k h_k(\mathbf{X}), \tag{6.11}$$

where λ_j and η_k are Lagrange multipliers. In general, the Lagrangian $\mathcal{L}(\mathbf{X}, \boldsymbol{\lambda}, \boldsymbol{\eta})$ is the sum of the original objective function and terms that involve Lagrange multipliers and the constraints. The Kuhn-Tucker conditions, which are necessary condition for objective function $f(\mathbf{X})$ at solution point \mathbf{X} to be a minimum are:

$$\begin{aligned}
 \frac{\partial \mathcal{L}}{\partial x_i} &= \frac{\partial f(\mathbf{X})}{\partial x_i} - \sum_{j=1}^p \lambda_j \frac{\partial g_j(\mathbf{X})}{\partial x_i} - \sum_{k=1}^m \eta_k \frac{\partial h_k(\mathbf{X})}{\partial x_i} = 0 \quad (i = 1, 2, \dots, n), \\
 \frac{\partial \mathcal{L}}{\partial \lambda_j} &= \lambda_j g_j(\mathbf{X}) = 0, \quad \lambda_j \geq 0 \quad (j = 1, 2, \dots, p), \\
 \frac{\partial \mathcal{L}}{\partial \eta_k} &= \eta_k h_k(\mathbf{X}) = 0 \quad (k = 1, 2, \dots, m).
 \end{aligned} \tag{6.12}$$

The Kuhn-Tucker conditions above only guarantee that the solution point \mathbf{X} is a local optimum. A sufficient condition for optimality in the whole solution space is that the Hessian matrix of the Lagrangian function is positive definite:

$$\mathbf{s}^T \frac{\partial^2 \mathcal{L}}{\partial \mathbf{X}^2} \mathbf{s} > 0, \quad \forall \mathbf{s} \neq \mathbf{0}. \tag{6.13}$$

In practice, to solve the shape optimization problem in Eq. (6.10), a numerical iterative search procedure is applied. It starts from an initial configuration $\mathbf{X}^{(0)}$ and proceeds in small steps:

$$\mathbf{X}^{(n+1)} = \mathbf{X}^{(n)} + \alpha \mathbf{D}^{(n)}, \tag{6.14}$$

where n is the iteration number, $\mathbf{D}^{(n)}$ is the step direction and α is the distance along this direction. The search steps improve the satisfaction of the objective function, or the degree of compliance with the constraints, or both. The iterative search procedure is terminated when the solution $\mathbf{X}^{(n+1)}$ satisfies the Kuhn-Tucker conditions (6.12).

To compute the step direction $\mathbf{D}^{(n)}$ and the distance α , several strategies are used in shape optimization. A nonparametric shape optimization approach based on optimality criteria is applied. Physical intuitive based optimality criteria postulate criteria that describe the optimum. The redesign rule is derived from the optimality criteria and the response behavior of the system for modifications of the design variables. The design space for so called nonparametric shape optimization is build up by implicit parameter from a chosen set of surface nodes from the finite element model. As shown in Fig. 6.3, the outer normal on the node is taken as the optimization displacement vector, while for nodes on the perimeter of the set of design nodes the one sided normal from the adjoining element surface is taken.

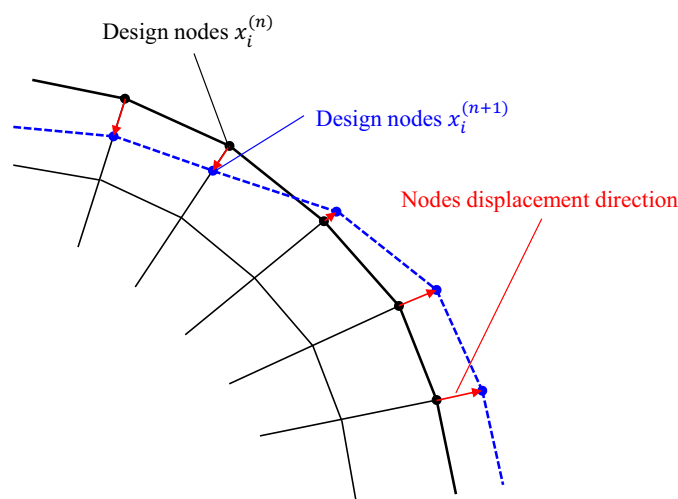


Figure 6.3 Design nodes update strategy.

6.2.3 Description of the optimization process and tools

The objective of this work is the optimization design of SMA structure with respect of low- and high-cycle fatigue. In this section, the detailed description of optimization process and tools utilized is presented. The framework of the optimization process can be described at three levels:

- Optimization iteration, which integrates the structural responses to change the structural configuration to improve fatigue performance.
- Calculation of the solution of the global boundary value problem and fatigue life for a given structural configuration.
- Calculation of the local constitutive responses at a given material point.

As shown in Fig. 6.4, the optimization tool used in this work is Tosca Structure¹ from Simulia. It can run any command-based analysis tools during the optimization iteration automatically. The finite element analysis tool used here is Abaqus from Simulia. Combining Abaqus' user material subroutine (UMAT) interface, the structural responses of a given configuration is calculated using Abaqus. The quantitative structural responses is read by the fatigue life solver, which is written in Python. The Python script is executed by Abaqus/CAE without GUI, and read the structural responses from the Abaqus result ODB file. fatigue factors for every material points are written in ASCII files, which will be read by optimization tool Tosca to change the structural configuration according to the redesign rule. The new structural configuration will be the new input of the finite element analysis tool to start the next iteration.

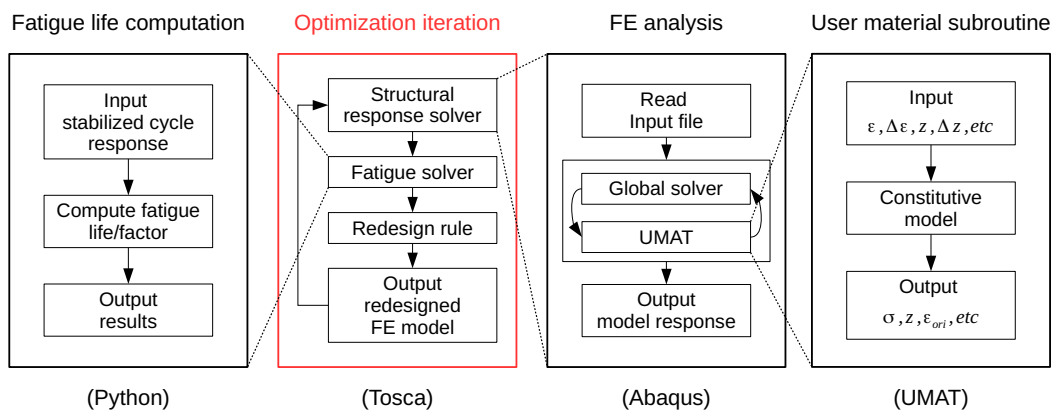


Figure 6.4 Optimization process.

6.3 Optimization case 1: SMA plate with a hole in the center

In this section, a center-holed SMA plate case is presented to demonstrate the optimization process. The shape of the center hole is optimized to enhance the low-cycle fatigue life of the plate under uniaxial tensile-unloading condition. The geometry of the model is shown in Fig. 3.10a, which is also used in Chapter 3. Due to symmetry, only one quarter of the model is used in the simulations. The plate is 100 mm × 120 mm × 15 mm in size and contains a hole 25 mm in radius at the center. The mesh consists of 128 hexahedral elements with linear integration (C3D8) for a total of 747 degrees of freedom. uniaxial loading is considered, involving vertical traction of 50 MPa. The material parameters used for this simulation is shown in Table 2.2.

In this optimization case, the objective is to minimize the maximum low-cycle fatigue factor of the SMA plate under the vertical traction. The design variable is the shape of the center hole. The constraint is the total volume of the new design cannot larger than the one of the initial configuration. The shape

¹Tosca Structure is a platform for structural optimization based on industry standard FEA packages (Abaqus, ANSYS, MSC Nastran, etc.)

optimization problem is formulated as:

$$\begin{aligned}
 &\text{find: } \Gamma_d(\mathbf{X}), \mathbf{X} = (x_1, x_2, \dots, x_n) \\
 &\text{min: } \max(f_{\text{low}}(\mathbf{X})), \\
 &\text{s.t.: } V(\mathbf{X}) \leq 37.7, \\
 &\quad \Gamma_d(\mathbf{X}) \in \Omega_d,
 \end{aligned} \tag{6.15}$$

where $f_{\text{low}}(\mathbf{X})$ is the low-cycle fatigue factor defined in Eq. (6.2), $V(\mathbf{X})$ is the total volume of the SMA plate, which is constrained to be less than the initial configuration value of 37.7 cm^3 .

A desktop equipped with Intel hexa-core Xeon processors @1.6 GHz and 16 GB of RAM is used to run the simulations. The simulation process converged after 15 iterations. The total solution time is 6 min. The iterative curve is shown in Fig. 6.5. As we can see, during the iterative process, the volume of the center hole almost remains constant, the shape of the hole in the center changes its shape gradually from a circle to a “rectangle”. The maximum of the fatigue factor $f_{\text{low}}(\mathbf{X})$ decrease from 0.328 to 0.073, the distributions of fatigue factor $f_{\text{low}}(\mathbf{X})$ before and after optimization are shown in Fig. 6.6. Meanwhile, the stress also decreases, which means that less phase transformation occurs during the loading-unloading process. Fig. 6.7 shows the maximum stress at time step 0.5 decreases from 141.9 MPa to 99.4 MPa, the corresponding maximum martensite volume fraction decreases from 0.96 to 0.16, as shown in Fig. 6.8.

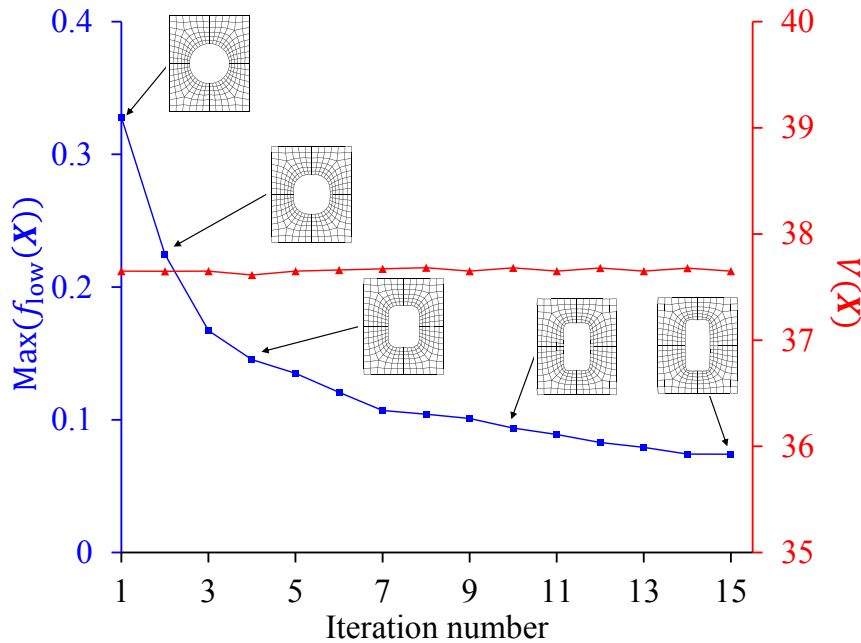


Figure 6.5 The convergence history of the objective function (blue) and the constraint (red).

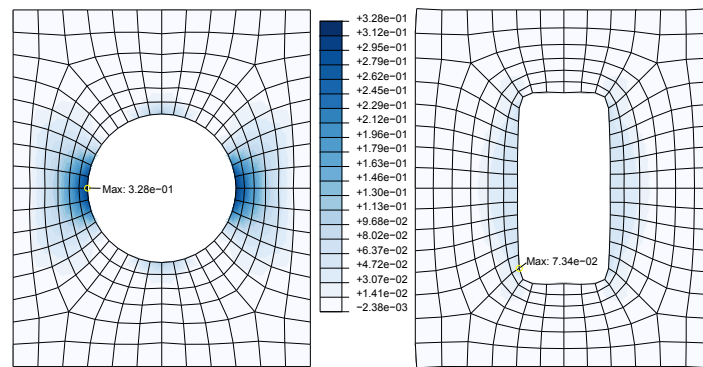


Figure 6.6 Comparison of the low-cycle fatigue factor distribution before and after optimization.

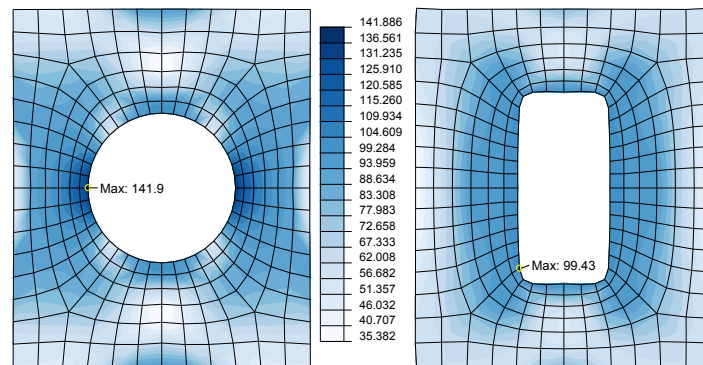


Figure 6.7 Comparison of the stress distribution at step time 0.5 before and after optimization.

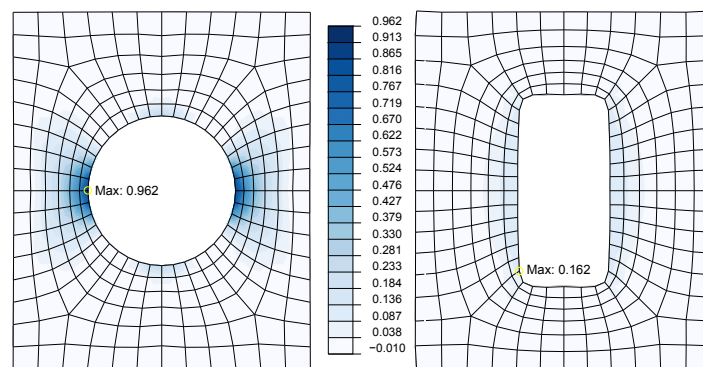


Figure 6.8 Comparison of the martensite volume fraction distribution at step time 0.5 before and after optimization.

6.4 Optimization case 2: self-expanding SMA stent

In this section, a self-expanding stent is used as the optimization case study. Stent implantation is one of the most effective minimally invasive treatments for the obstruction of coronary arteries (Gu

et al., 2012). Based on different deployment approaches, stents can be classified as two types: balloon-mounted and self-expanding stents. Balloon-mounted stents are manufactured in a crimped state and mounted onto a tightly-folded balloon catheter and expanded plastically and deployed by inflating the balloon. Self-expanding stents are manufactured at a diameter slightly above the artery and are crimped and constrained by a delivery catheter to the smaller diameter until the intended deployment position is reached, where the constraint is removed and the stent deployed (Duerig and Wholey, 2002). Nickel titanium, also known as Nitinol, exhibits pseudoelastic and biocompatible properties that make it particularly suitable for self-expanding stents. Compared to a balloon-mounted stent, a Nitinol self-expanding stent can be designed to provide constant gentle outward pressure with minimal influence on the geometry and properties of the anatomy (Duerig et al., 2000; Duerig and Wholey, 2002; Gong et al., 2003).

Experimental evaluation of the fatigue behavior involves long lasting fatigue test. Even with an accelerated fatigue test, a 400 million cycles test can last months. Finite element analysis (FEA) is an extremely useful complement and has proven its effectiveness and capacity to provide a better and more detailed understanding for fatigue analysis and design. The aim of this section is to provide a fast and cost-effective method to evaluate fatigue resistance of Nitinol stent components, which is then applied to a specific stent geometry to illustrate the effectiveness of the method.

6.4.1 FEM implementation

Geometric model and boundary conditions

Numerous Nitinol stent designs are used in clinical practice, most of which having two fundamental constituents: expandable ring elements and connecting elements (Bonsignore, 2003). The geometry of the stent in this study is based on the design of self-expanding Nitinol stent manufactured by Covidien™, shown in Fig. 6.9b, which can also be found in Bonsignore (2003). The stent is cut from a Nitinol tube into an open lattice design with “peak-to-peak” connectors. Since the stent pattern repeats itself, only a unit cell of the stent with appropriate boundary conditions is considered (Fig. 6.9b). For the boundary planes K+ and K−, the periodic boundary conditions can be written as

$$u_{\rho}^{K+} = u_{\rho}^{K-}, u_{\phi}^{K+} = u_{\phi}^{K-}, \text{ and } u_z^{K+} = u_z^{K-}, \quad (6.16)$$

where u_{ρ} , u_{ϕ} and u_z are the displacements along ρ , ϕ and z directions in cylindrical coordinates, respectively. The constraints in Eq. (6.16) means that a pair of corresponding nodes on plane K+ and K− have the same displacements. The same periodic boundary conditions is also enforced on the boundary planes J+ and J−. It is notable that the three translational movement of one node on the stent is constrained to avoid rigid motion. The unit cell stent model is meshed with 3 elements through the thickness direction and the total number of elements used to mesh the unit cell is 5000. The coronary artery is modeled as a cylinder with an outer diameter of 2.5 mm and thickness of 0.5 mm. Reduced integration 8-node elements (C3D8R) are used to mesh the artery with 5 element layers through the

thickness direction. The total number of elements used to mesh the artery is 6000. As shown in Figs. 6.9c and 6.9d, the expanded stent has a bigger diameter compared to the artery, which can expand the artery after deployment.

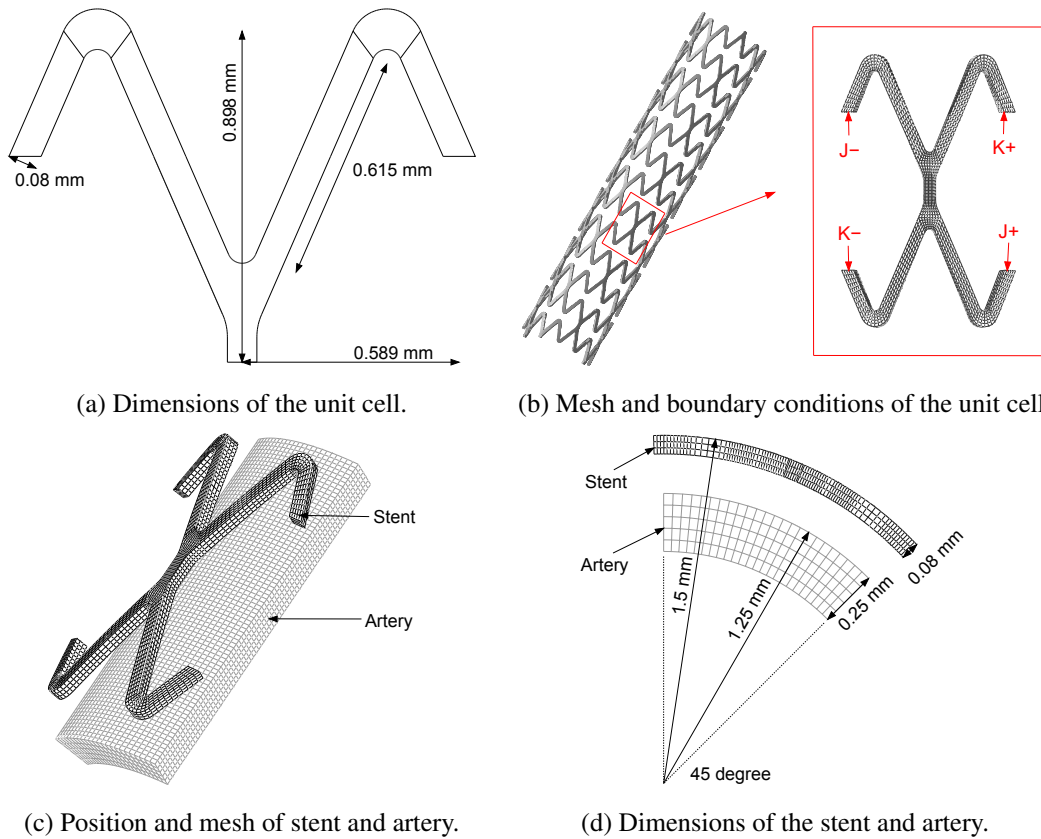


Figure 6.9 Stent and artery modeling.

Material properties

The finite element simulation of the stent is performed with the following loading conditions: (i) Stent crimping and deployment, whereby an initially expanded nitinol stent is compressed by prescribing inward radial displacement conditions on the outer surface at a low temperature of 263 K (-10°C), the displacement is then removed at the human body temperature of 310 K (37°C), which makes the stent self-expand and come into contact with the artery wall. (ii) Stent operation under cyclic diastolic-systolic loading.

The stent is assumed to be made of pseudoelastic Nitinol (52 Ni %wt). The transformation temperatures of the material are determined by differential scanning calorimetry (DSC), which is shown in Fig. 6.10a. Fig. 6.10b shows the stress-strain response under the stress-controlled cyclic tensile loading, performed at room temperature 298 K. The hysteresis loop evolves and reaches a stabilized state when the number of cycles increases.

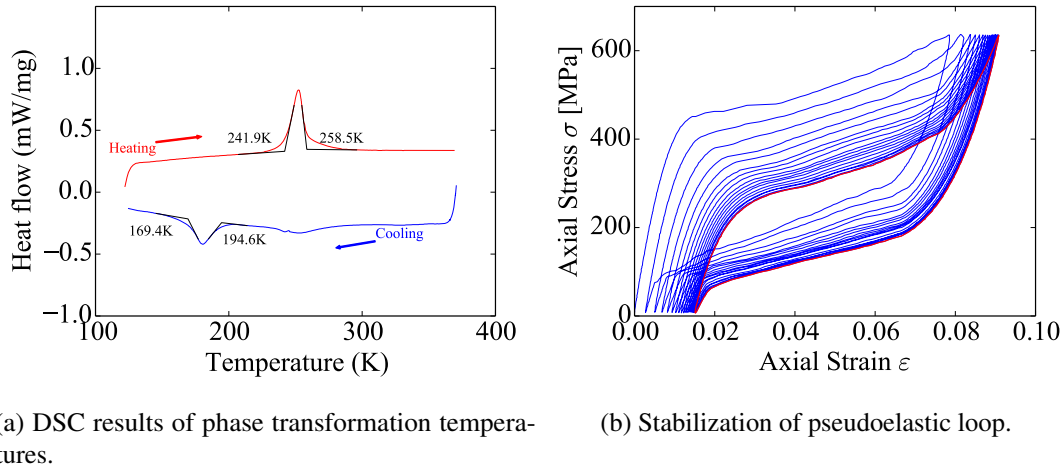


Figure 6.10 Material parameters of Nitinol used for manufacturing stent.

The material parameters used for stent simulation, which are characterized from the uniaxial experimental data in Fig. 6.10b, are listed in Table 6.1. Figs. 6.11a and 6.11b show the uniaxial stress-strain response of the Nitinol SMA at temperatures 263K and 310K respectively, which are the temperature conditions for stent crimping and stent operation. It's notable from the figures that the phase transformation stress decreases when the temperature decreases. This is helpful to crimping the stent in lower temperature, which makes the material “softer”.

Table 6.1 Material parameters used for finite element simulations.

E_A	40 000	MPa	E_M	30 000	MPa
ν	0.3		ρ	6400	kg m^{-3}
C_p	470	$\text{J kg}^{-1} \text{K}^{-1}$	$B^{(\text{sat})}$	100	MPa
α_A	1.1×10^{-5}	K^{-1}	α_M	1.1×10^{-5}	K^{-1}
k	18	$\text{W m}^{-1} \text{K}^{-1}$	τ	10	
σ_{rs}	30	MPa	σ_{rf}	80	MPa
$\sigma_{ms}^{(0)}$	455	MPa	$\sigma_{ms}^{(\text{sat})}$	260	MPa
$\sigma_{mf}^{(0)}$	605	MPa	$\sigma_{mf}^{(\text{sat})}$	470	MPa
$\sigma_{as}^{(0)}$	340	MPa	$\sigma_{as}^{(\text{sat})}$	235	MPa
$\sigma_{af}^{(0)}$	80	MPa	$\sigma_{af}^{(\text{sat})}$	90	MPa
$\gamma^{(0)}$	0.058		$\gamma^{(\text{sat})}$	0.054	
ϕ	0	K^{-1}	ν	0.016	
A_f^0	258.5	K	θ_r	310	K

The modeling of arterial mechanical behavior is based on the work of Danpinid et al. (2010); Khamdaeng et al. (2012), who performed arterial stiffness identification of the human carotid artery and proposed the characterization of the aortic wall stress-strain relationship. In particular, an isotropic

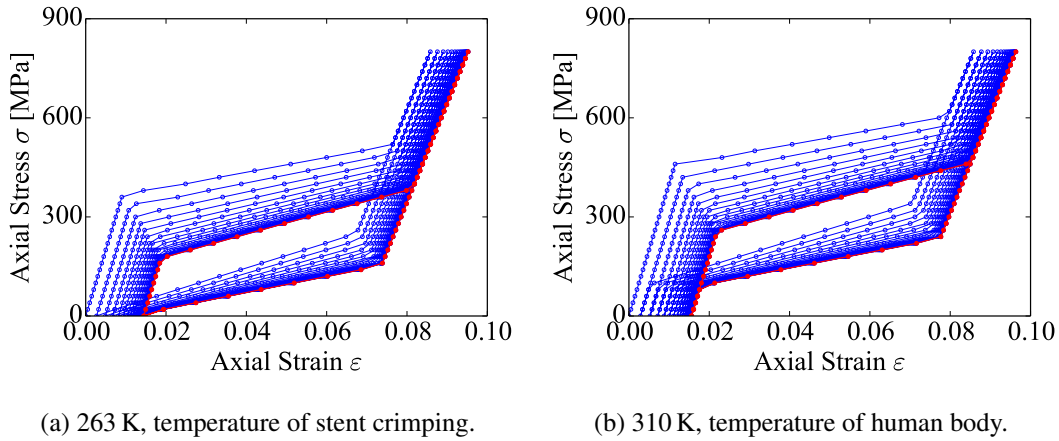


Figure 6.11 Stress-strain curve at different temperatures.

“bilinear” constitutive model consistent with the mean values of their experimental measurement in the circumferential direction is used. The relation between Young’s modulus E_{artery} and strain ε are

$$E_{\text{artery}} = \begin{cases} 160 \text{ kPa}, & \varepsilon \leq 0.025, \\ 900 \text{ kPa}, & \varepsilon > 0.025, \end{cases} \quad (6.17)$$

which is also implemented in Abaqus using user material subroutine UMAT.

Stent crimping and deployment

First, the expanded stent is compressed by a delivery catheter at 263 K (-10°C), which makes the stent deform easier. A displacement of 0.85 mm in the radial direction is applied on the outer surface of the stent, resulting in a folded diameter of 1.3 mm of the folded stent. To simplify the simulation, self-contact of the stent during crimping is not considered here. The artery material is not considered in analyzing stent crimping. Then, the stent is released from the catheter inside the artery. During the deployment stage, contact condition is applied between the outer surface of crimped stent and the inner surface of the artery. The displacement applied during the crimping process is then removed and the stent is allowed to expand progressively by itself. When the self-expanding stent reaches the inner surface of the artery, the contact is activated and the stent continues to expand outward against the artery wall until reaching a position in which the outward forces due to expansion of the stent are balanced by the compressive forces exerted by the artery wall on the stent.

Pulsating loading

After deployment of the stent, the stent-artery system is subjected to a continuous cyclic diastolic-systolic loading at the human body temperature of 310 K (37°C). This cyclic loading condition is a result of physiologic blood pressure loading acting on the internal surface of the stent and artery. The pulsatile

loading ranges between 80 mmHg for diastolic pressure and 160 mmHg for systolic pressure, which followed the US Food and Drug Administration (FDA) Guidance and based on the ASTM fatigue testing standard for vascular stents (ASTM F2477–07) (ASTM F2477-07, 2013). The cyclic loading makes the stent reach elastic shakedown state after a certain number of cycles, In this case, ten cycles are needed in this case.

6.4.2 High-cycle fatigue analysis

Since the stent is found to achieve elastic shakedown, failure by fatigue may only take place after a large number of cycles. In order to evaluate the fatigue endurance of the stent, the high-cycle fatigue criterion defined in Eq. (6.5) is used. It is notable that only phase transformation is considered in this case:

$$G(\mathbf{x}) = \begin{cases} \frac{\bar{w}^*}{\bar{b}}, & 0 < z < 1, \\ \frac{\bar{v}^*}{\bar{b}'}, & z = 0. \end{cases} \quad (6.18)$$

The material parameters \bar{b} and \bar{b}' in the criterion are used the 30% of the stress, under which the material remains elastic under mixed-phase and pure austenite phase, respectively. The material parameter \bar{a} is obtained from Auricchio et al. (2016).

$$\begin{cases} \bar{b} = 27.6 \text{ MPa}, \\ \bar{b}' = 76.8 \text{ MPa}, \\ \bar{a} = 0.011 \text{ MPa}^{-1}. \end{cases} \quad (6.19)$$

The material parameters used here are for reference only. They are used to figure out which can figure out danger zones, before proceeding to optimizing the geometry with respect to fatigue..

6.4.3 Simulation results and optimization process

The stent release, followed by operation under diastolic-systolic blood pressure cycles is simulated using the original stent design shown in Fig. 6.9. Fig. 6.12 shows the martensite volume fraction in the stent at fully crimped, systolic and diastolic blood pressure, respectively. As shown in Fig. 6.12b and Fig. 6.12c, the martensite volume fractions are the same, which means there is no phase transformation during the cyclic diastolic-systolic blood pressure loading. This is a necessary condition for the stent to have high-cycle fatigue. Fig. 6.13a is the stress distribution after being completely crimped, and the maximum stress is 860.37 MPa. Fig. 6.13b and Fig. 6.13c are the stress distributions in the stent under systolic and diastolic blood pressure, respectively, and the maximum stresses are 130.02 MPa and 156.74 MPa, respectively. Fig. 6.13d is the high-cycle fatigue factor calculated using Eq. (6.5), the maximum fatigue factor is 0.92. The danger zones in terms of fatigue, which are the locations having large fatigue factor, are pointed out in Fig. 6.13d. These danger zones are the locations subjected to the highest stress, also under hydrostatic tension, which are bad for fatigue due to tensile loads assisting the opening of cracks..

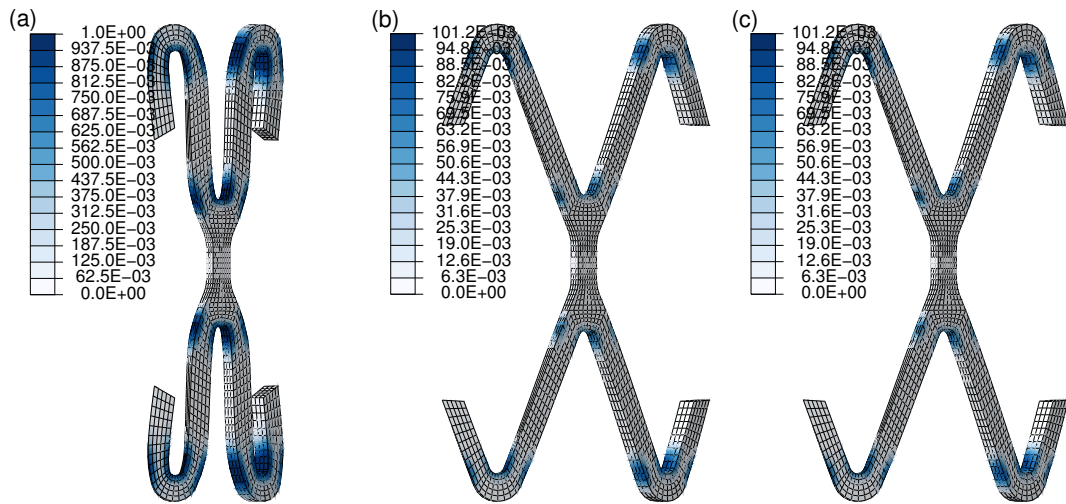


Figure 6.12 Simulated martensite volume fraction for the original stent design under: (a) fully crimped loading; (b) systolic pressure; (c) diastolic pressure.

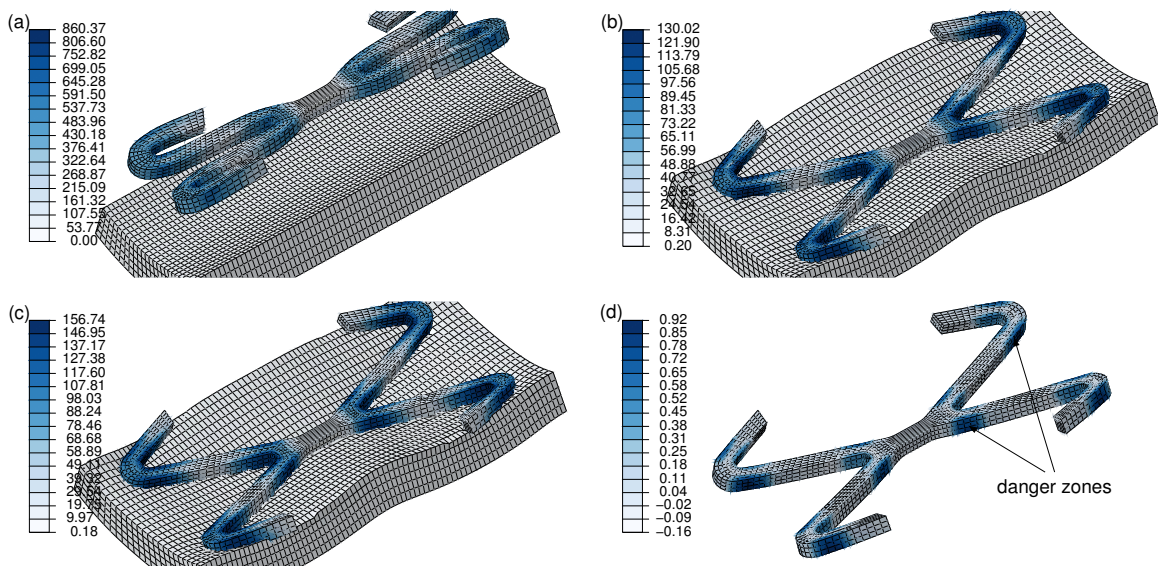


Figure 6.13 Simulated results for the original stent design: (a) stress distribution fully crimped; (b) stress distribution under systolic pressure; (c) stress distribution under diastolic pressure; (d) high-cycle fatigue factor distribution.

Shape optimization is carried out to improve high-cycle fatigue performance under cyclic diastolic-systolic blood pressure loading conditions. The reduced geometric model shown in Fig. 6.14 is used to simplify the optimization process and reduce computation time. The objective of the optimization is to minimize the maximum high-cycle fatigue factor of the SMA stent under cyclic diastolic-systolic blood pressure loading. The constraint is the total volume of the new design cannot be larger than that the original design. The design variable is the free edge of the stent in Fig. 6.14. The shape optimization

problem is formulated as:

$$\begin{aligned}
 &\text{find: } \Gamma_d(\mathbf{X}), \mathbf{X} = (x_1, x_2, \dots, x_n) \\
 &\text{min: } \max(f_{\text{high}}(\mathbf{X})), \\
 &\text{s.t.: } V(\mathbf{X})/\bar{V} \leq 1, \\
 &\quad \Gamma_d(\mathbf{X}) \in \Omega_d,
 \end{aligned} \tag{6.20}$$

where $f_{\text{high}}(\mathbf{X})$ is the high-cycle fatigue factor defined in Eq. (6.5), $V(\mathbf{X})$ is the total volume of the SMA stent, which is constrained to be less than the original design \bar{V} .

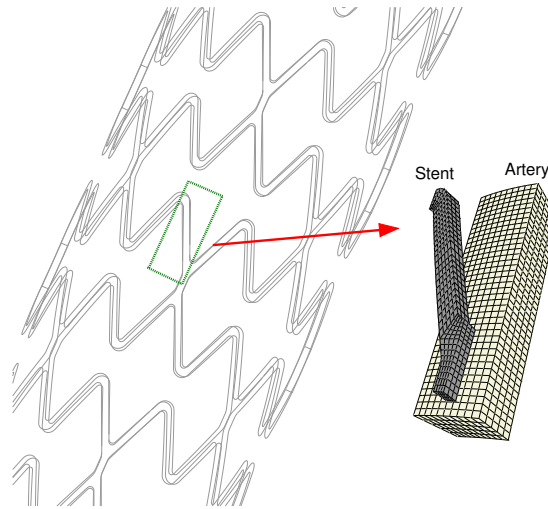


Figure 6.14 The single strut reduced stent model considered for the optimization problem.

The optimization process converged after 8 iterations. The total solution time is 3 h 37 min. The convergence curves are shown in Fig. 6.15. As we can see, during the iterative optimization process, the strut geometry evolves gradually from a rectangular block to a dogbone-like shape, meanwhile, the volume of the stent is kept almost constant. The maximum fatigue factor $f_{\text{high}}(\mathbf{X})$ decreases from 0.899 to 0.571, the distributions of the fatigue factor $f_{\text{high}}(\mathbf{X})$ before and after optimization are shown in Fig. 6.16, with a more uniform distribution reached after 8 iterations. Meanwhile, the stress also decreases, as shown in Figs. 6.17 and 6.18, the maximum stress in the stent under systolic and diastolic blood pressure decreases from 151.3 MPa to 139.8 MPa, and from 126.3 MPa to 121.3 MPa, respectively. The martensite volume fraction decreases from 0.081 to 0.016, as shown in Figure 6.19.

A new CAD model of the stent is built according to the optimized stent configuration illustrated in Fig. 6.15. The original design and new design of the stent are shown in Fig. 6.20, It's notable that these two designs have the same volume.

The optimized stent model is simulated under crimp-release, cyclic diastolic-systolic blood pressure loading. Fig. 6.21 shows the martensite volume fraction in the stent at fully crimped, systolic and diastolic blood pressure, respectively. Compare to the original design shown in Fig. 6.12, The maximum stabilized martensite volume fraction is reduced from 0.101 to 0.025. Fig. 6.22a is the stress distribution after being completely crimped, and the maximum stress is 665.10 MPa. Compared to the original

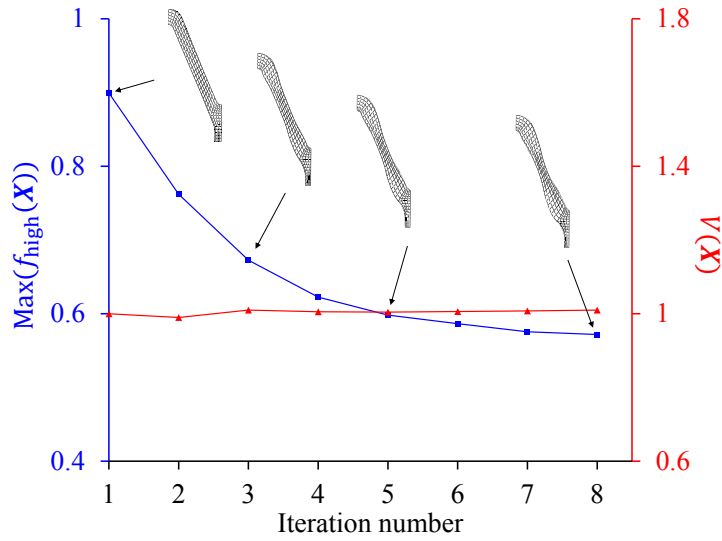


Figure 6.15 The convergence history of the objective function (blue) and the constraint (red).

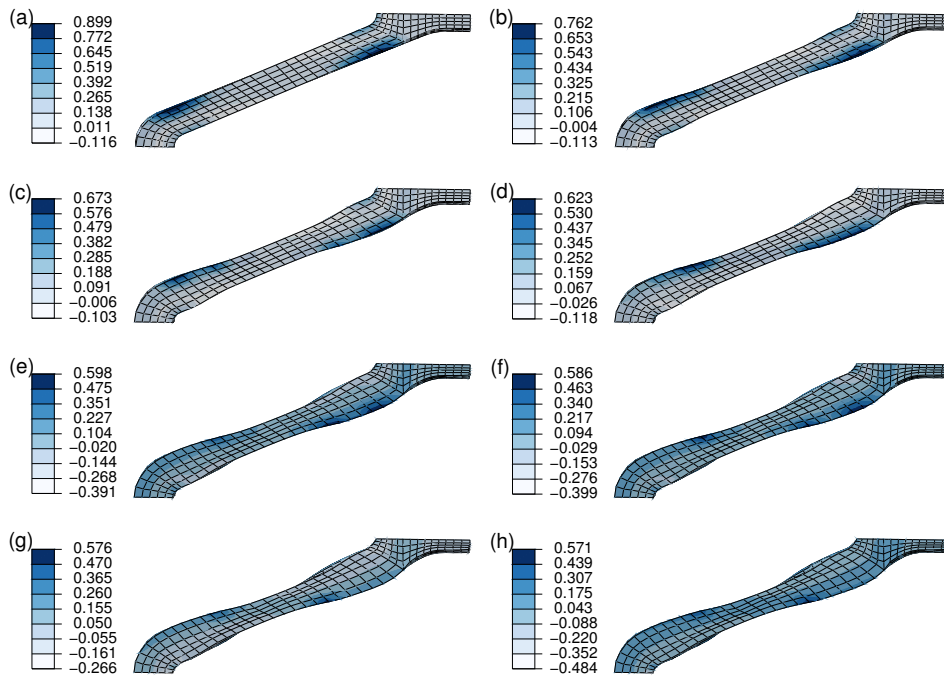


Figure 6.16 Evolution of the high-cycle fatigue factor in iterations 1 to 8, corresponding to Figs. (a) to (h).

design (860.37 MPa), it's reduced 22.7%. Fig. 6.22b and Fig. 6.22c are the stress distribution of the stent under systolic and diastolic blood pressure, respectively, and the maximum stress are 122.67 MPa and 139.70 MPa, respectively. Compared to the original design (130.02 MPa and 156.74 MPa), it is reduced 5.7% and 10.9%, respectively. Fig. 6.22d shows the high-cycle fatigue factor calculated using Eq. (6.5), the maximum fatigue factor is 0.69, a reduction of 25% compared to the original design.

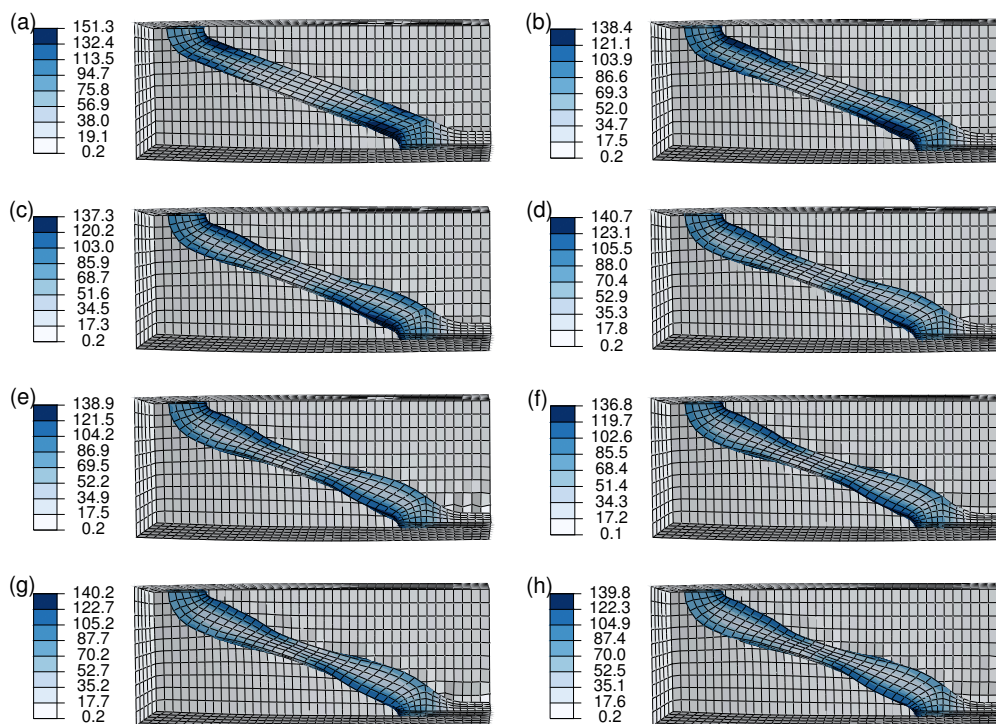


Figure 6.17 Evolution of the von Mises stress in the stent under systolic pressure in iterations 1 to 8, corresponding to Figs. (a) to (h).

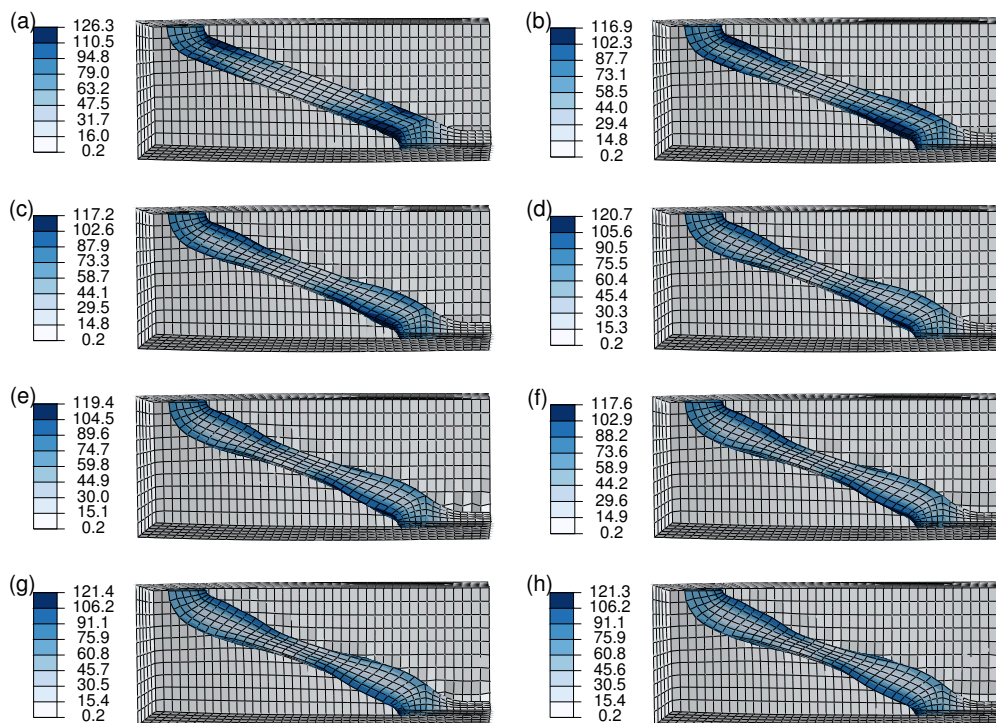


Figure 6.18 Evolution of the von Mises stress in the stent under diastolic pressure in iterations 1 to 8, corresponding to Figs. (a) to (h).

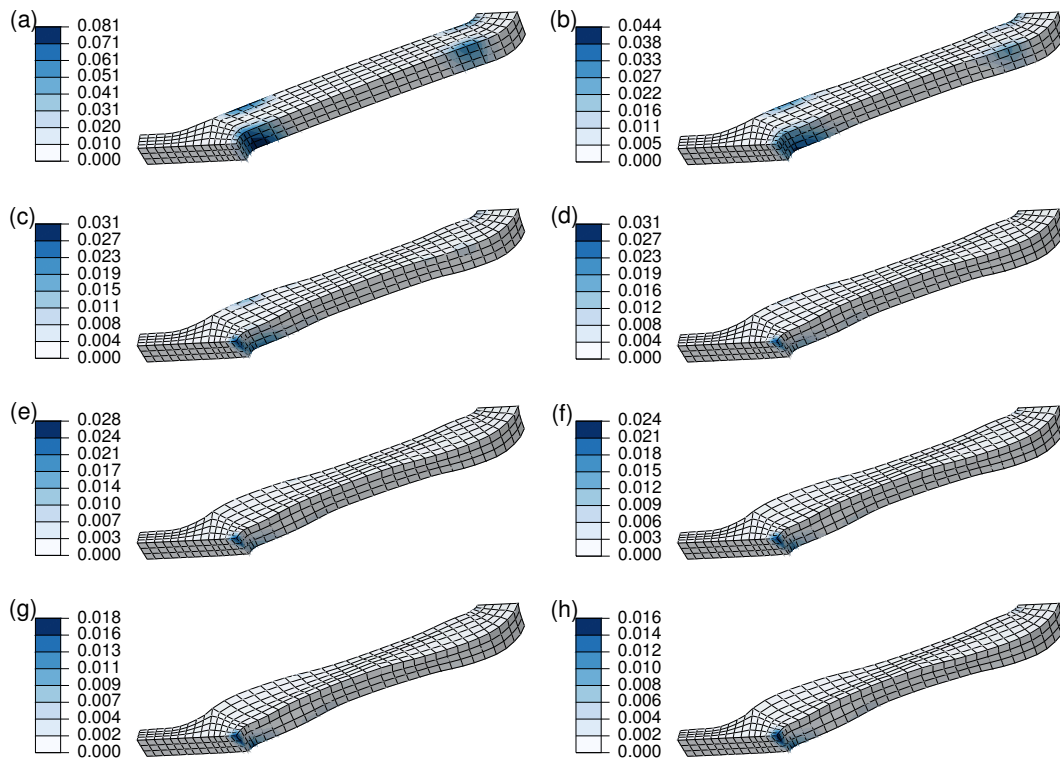


Figure 6.19 Evolution of the maximum martensite volume fraction in the stent in iterations 1 to 8, corresponding to Figs. (a) to (h).

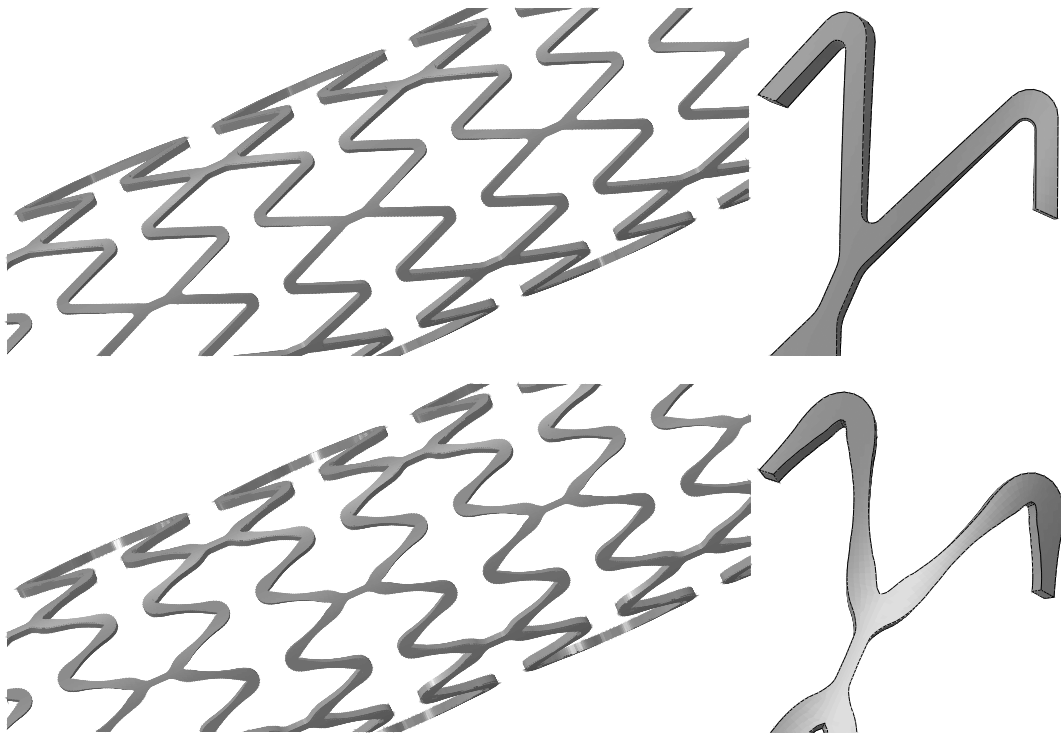


Figure 6.20 Geometric comparison of the original and new stent designs.

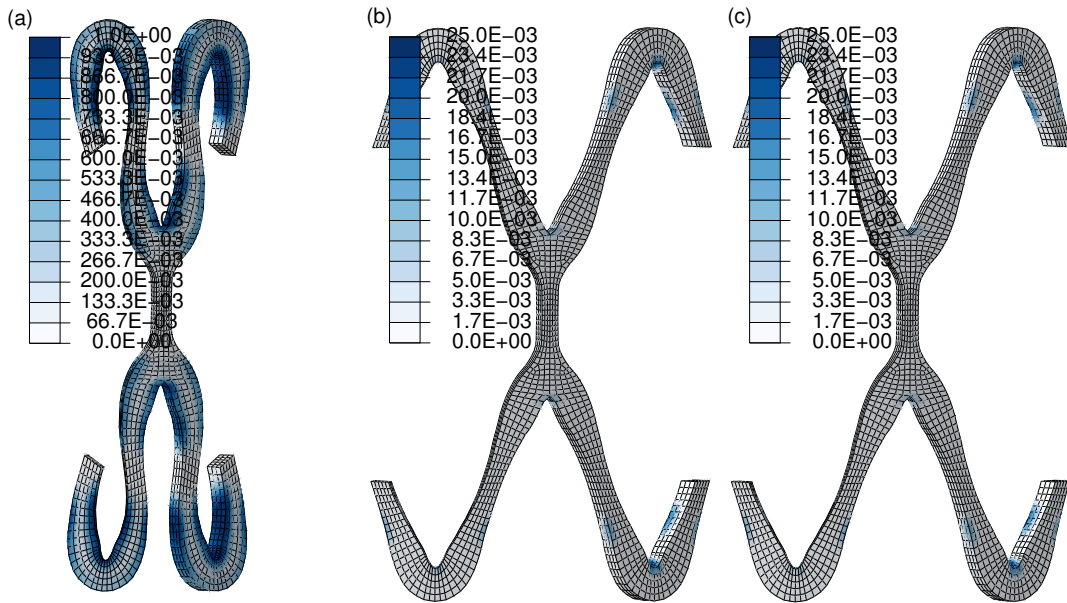


Figure 6.21 Simulated martensite volume fraction of the new stent design under: (a) fully crimped loading; (b) systolic pressure; (c) diastolic pressure.

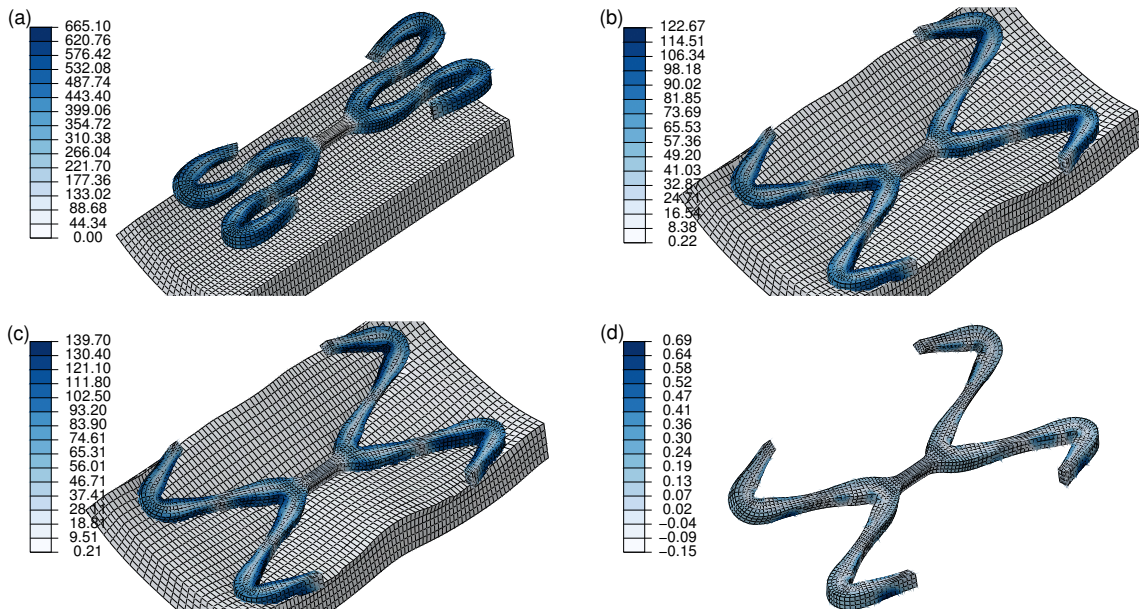


Figure 6.22 Simulated results of the new stent design: (a) stress distribution fully crimped; (b) stress distribution under systolic pressure; (c) stress distribution under diastolic pressure; (d) high-cycle fatigue factor distribution.

6.5 Conclusion

In this chapter, engineering analysis tools are utilized to develop an efficient methodology for enhancing the fatigue life of SMA structures. Specifically, an energy based low-cycle fatigue model and a shakedown based high-cycle fatigue model have been implemented in a flexible nonparametric shape optimization framework. Two optimization case studies are provided, one is a SMA plate with a hole in the center, the other is a self-expanding stent. For each case study, the optimization problem is formulated. The design objective in each case is the minimization of the maximum fatigue factor, and the constraint is the total volume of the structure. The optimized results for each case indicated that the new configuration improved the fatigue behavior dramatically, compared to the original one. Further work is needed in order to experimentally validate the optimization procedure, which can then be utilized in designing SMA structures of arbitrary geometry with respect to fatigue.

Chapter 7

Conclusions

This thesis developed a comprehensive and efficient approach for design and optimization of SMA structures with respect to fatigue. This approach is split into three major steps.

The first step, devoted in Chapters 2 to 4, is the development of a suitable constitutive law, that is able to predict with good accuracy the cyclic thermomechanical response of SMAs. Time integration and assessment of ZM model for SMAs under multiaxial nonproportional loading is provided. In order to solve numerical convergence problems in situations where the phase transformation process presents little or lack of hardening, LATIN method is integrated with ZM model for simulation of pseudoelastic SMAs. Then an extended thermomechanically coupled 3D rate-dependent model for pseudoelastic SMAs under cyclic loading is developed, including the influence of load rate and temperature on both the rate and value at saturation of residual strain. The time-integration procedures are programmed into the software Abaqus by means of a user material subroutine (UMAT) and several simulation cases are presented and discussed.

The second step, detailed in Chapter 5, deals with high-cycle fatigue of SMAs. A shakedown based fatigue criterion is developed to predict whether a SMA structure submitted to high-cycle loading would undergo fatigue. The analysis accounts for phase transformation as well as reorientation of martensite variants as possible sources of fatigue damage. In the case of high-cycle fatigue, once the structure has reached an asymptotic state, damage is assumed to become confined at the mesoscopic scale, or the scale of the grain, with no discernable inelasticity at the macroscopic scale. Using a multiscale approach, a high-cycle fatigue criterion analogous to the Dang-Van model for elastoplastic metals is derived for SMAs obeying the ZM model for SMAs.

Finally, the third step, introduced in Chapter 6, is the development of a structural optimization approach, which can be used to improve the fatigue lifetime measured by the predefined fatigue criterion. Both low- and high-cycle fatigue are considered. The proposed approach is used to optimize two 3D SMA structures, namely, a SMA plate with a hole in the center and a self-expanding SMA stent. Significant fatigue safety improvement is obtained with new designed configurations.

To summarize, this approach can be used as follows: by given the geometry of a SMA structure with its boundary condition and thermomechanical loading, the constitutive law allows the determination of

its thermomechanical response by incremental method. If the phase transformation process presents little or lack of hardening under non-cyclic loading, LATIN method can be used to solve the numerical convergence problems. Then, the shakedown based fatigue criterion can be used to compute a fatigue factor, which indicates the degree of safeness with respect to high-cycle fatigue at every material point of the structure. Finally, the calculated fatigue factors are unitized by integrated optimization tools to improve the fatigue life by changing the structure configuration. The optimized structure configuration is determined after limited iterations.

This work can be continued in different aspects. Firstly, anisotropic behavior in tension-torsion loading. SMAs under cyclic nonproportional loading is very challenging to model (Song et al., 2014), indeed, even under monocyclic nonproportional loading (Fig. 4.8b), there is observable disagreement of the tension-torsion stress curves compared to experimental data due to the use of the von Mises equivalent stress in formulating the loading functions in our the model. Secondly, the proposed high-cycle fatigue criterion has several material constants, which are the fatigue limits under different loading conditions. Traditionally, experimental methods correlate the high-cycle fatigue limits are time-consuming and expensive. Efficient approach of evaluating the fatigue limit of elastoplastic metals using infrared thermographic technique can be found in the literature (Luong, 1998). This could be an interesting but challenging topic for SMA material due to its unique thermomechanical coupled phase transformation phenomena. Thirdly, the fatigue optimized SMAs structures, such as stents, need to be validated for larger range of experiments. Finally, SMA structures can be manufactured by 3D printing technology. Fatigue problem is also important for these type of structures. The proposed approach can be used in this field in the future.

Appendix A

Derivation of the continuous tangent operators for Chapter 4

Temperature distribution in SMAs influences the mechanical behavior of the material and vice versa, resulting in strong thermomechanical coupling. In order to account for this coupling, an incremental finite element method is utilized that couples temperature and displacement fields. The numerical integration procedure requires the definition, at each integration point, of tangent operators representing the local rate of change in stress and heat with respect to the total strain and temperature, considered as control variables. The increments of the stress σ and heat Q can then be written in linearized form in terms of the increments of strain and temperature as follows:

$$d\sigma = \mathcal{J}_{\sigma\varepsilon} : d\varepsilon + \mathcal{J}_{\sigma\theta}d\theta, \quad (\text{A.1})$$

$$dQ = \mathcal{J}_{Q\varepsilon} : d\varepsilon + \mathcal{J}_{Q\theta}d\theta, \quad (\text{A.2})$$

where $\mathcal{J}_{\sigma\varepsilon}$ and $\mathcal{J}_{Q\varepsilon}$ are the tangent stiffness tensors with respect to the increments of stress and internal heat generation, respectively. $\mathcal{J}_{\sigma\theta}$ and $\mathcal{J}_{Q\theta}$ are the tangent thermal modulus tensors with respect to the increments of stress and internal heat generation, respectively. The tangent stiffness and thermal modulus tensors are assembled to calculate the simultaneous increase in total strain and temperature for the next load increment. The accuracy of the tangent modulus directly influences the convergence rate. The derivation of the continuous tangent modulus tensors for simultaneous processes proceeds as follows:

The time-continuous stress-strain relation Eq. (4.9) can be written in differential form as

$$d\sigma = \mathbf{K} : [d\varepsilon - (\mathbf{R}dz + zN d\eta + \alpha d\theta)], \quad (\text{A.3})$$

where the second-order tensor \mathbf{R} is given by

$$\mathbf{R} := \left(\mathbf{K}_M^{-1} - \mathbf{K}_A^{-1} \right) : \sigma + \varepsilon_{\text{ori}} + (\alpha_M - \alpha_A)(\theta - \theta_r) + \frac{\varepsilon_r^{(\text{sat})}}{\tau} \left(\frac{3}{2} \frac{s}{\sigma_{\text{VM}}} \right) \exp\left(-\frac{z_e}{\tau}\right) \text{sgn}(z). \quad (\text{A.4})$$

The volumetric heat generation per unit time \dot{Q} can be written in differential form as follows:

$$\begin{aligned} dQ = & [\xi - \sigma : (\alpha_M - \alpha_A)] \theta \frac{dz}{dt} + Yz^2 \frac{d\eta}{dt} \\ & + \left[a(1-z) + bz + \left(\frac{B^{(\text{sat})}}{\tau} z\varepsilon_0 + \frac{\varepsilon_r^{(\text{sat})}}{\tau} \sigma_{\text{VM}} \right) \exp\left(-\frac{z\varepsilon}{\tau}\right) \right] \left| \frac{dz}{dt} \right|. \end{aligned} \quad (\text{A.5})$$

Consistency with the loading functions \mathcal{F}_z and \mathcal{F}_{ori} requires that

$$\partial_{\sigma} \mathcal{F}_z : d\sigma + \partial_z \mathcal{F}_z dz + \partial_{\varepsilon_{\text{ori}}} \mathcal{F}_z : N d\eta + \partial_{\theta} \mathcal{F}_z d\theta = 0, \quad (\text{A.6})$$

$$\partial_{\sigma} \mathcal{F}_{\text{ori}} : d\sigma + \partial_z \mathcal{F}_{\text{ori}} dz + \partial_{\varepsilon_{\text{ori}}} \mathcal{F}_{\text{ori}} : N d\eta + \partial_{\theta} \mathcal{F}_{\text{ori}} d\theta = 0, \quad (\text{A.7})$$

where $\mathcal{F}_z \in \{\mathcal{F}_z^1, \mathcal{F}_z^2\}$. Combining Eqs. (A.3), (A.6) and (A.7) gives

$$\mathbf{A}_{\varepsilon} : d\varepsilon + A_z dz + A_{\text{ori}} d\eta + A_{\theta} d\theta = 0, \quad (\text{A.8})$$

$$\mathbf{B}_{\varepsilon} : d\varepsilon + B_z dz + B_{\text{ori}} d\eta + B_{\theta} d\theta = 0, \quad (\text{A.9})$$

where

$$\begin{aligned} \mathbf{A}_{\varepsilon} & := \mathbf{K} : \partial_{\sigma} \mathcal{F}_z, \\ A_z & := \partial_z \mathcal{F}_z - \partial_{\sigma} \mathcal{F}_z : \mathbf{K} : \mathbf{R}, \\ A_{\text{ori}} & := \partial_{\varepsilon_{\text{ori}}} \mathcal{F}_z : \mathbf{N} - z \partial_{\sigma} \mathcal{F}_z : \mathbf{K} : \mathbf{N}, \\ A_{\theta} & := \partial_{\theta} \mathcal{F}_z - \partial_{\sigma} \mathcal{F}_z : \alpha, \\ \mathbf{B}_{\varepsilon} & := \mathbf{K} : \partial_{\sigma} \mathcal{F}_{\text{ori}}, \\ B_z & := \partial_z \mathcal{F}_{\text{ori}} - \partial_{\sigma} \mathcal{F}_{\text{ori}} : \mathbf{K} : \mathbf{R}, \\ B_{\text{ori}} & := \partial_{\varepsilon_{\text{ori}}} \mathcal{F}_{\text{ori}} : \mathbf{N} - z \partial_{\sigma} \mathcal{F}_{\text{ori}} : \mathbf{K} : \mathbf{N}, \\ B_{\theta} & := -\partial_{\sigma} \mathcal{F}_{\text{ori}} : \alpha. \end{aligned} \quad (\text{A.10})$$

Solving Eqs. (A.8) and (A.9) for the unknowns dz and $d\eta$ gives

$$dz = \mathbf{C}_{\varepsilon} : d\varepsilon + C_{\theta} d\theta, \quad (\text{A.11})$$

$$d\eta = \mathbf{D}_{\varepsilon} : d\varepsilon + D_{\theta} d\theta, \quad (\text{A.12})$$

where for combined phase transformation and martensite reorientation

$$\begin{aligned}
C_{\varepsilon} &:= \frac{A_{\text{ori}}\mathbf{B}_{\varepsilon} - B_{\text{ori}}\mathbf{A}_{\varepsilon}}{A_z B_{\text{ori}} - B_z A_{\text{ori}}}, \\
C_{\theta} &:= \frac{A_{\text{ori}}\mathbf{B}_{\theta} - B_{\text{ori}}\mathbf{A}_{\theta}}{A_z B_{\text{ori}} - B_z A_{\text{ori}}}, \\
D_{\varepsilon} &:= \frac{B_z \mathbf{A}_{\varepsilon} - A_z \mathbf{B}_{\varepsilon}}{A_z B_{\text{ori}} - B_z A_{\text{ori}}}, \\
D_{\theta} &:= \frac{B_z \mathbf{A}_{\theta} - A_z \mathbf{B}_{\theta}}{A_z B_{\text{ori}} - B_z A_{\text{ori}}}.
\end{aligned} \tag{A.13}$$

In the absence of martensite reorientation the above relations become

$$\begin{aligned}
C_{\varepsilon} &:= -\frac{\mathbf{A}_{\varepsilon}}{A_z}, \\
C_{\theta} &:= -\frac{\mathbf{A}_{\theta}}{A_z}, \\
D_{\varepsilon} &:= 0, \\
D_{\theta} &:= 0,
\end{aligned} \tag{A.14}$$

and in the absence of phase transformation one has

$$\begin{aligned}
C_{\varepsilon} &:= 0, \\
C_{\theta} &:= 0, \\
D_{\varepsilon} &:= -\frac{\mathbf{B}_{\varepsilon}}{B_{\text{ori}}}, \\
D_{\theta} &:= -\frac{\mathbf{B}_{\theta}}{B_{\text{ori}}}.
\end{aligned} \tag{A.15}$$

Eqs. (A.11) and (A.12) can be used to eliminate dz and $d\eta$, respectively. Eqs. (A.3) and (A.5) then give

$$d\boldsymbol{\sigma} = (\mathbf{K} - \mathbf{K} : \mathbf{R} \otimes \mathbf{C}_{\varepsilon} - z\mathbf{K} : \mathbf{N} \otimes \mathbf{D}_{\varepsilon}) : d\boldsymbol{\varepsilon} + (-\mathbf{K} : \mathbf{R}\mathbf{C}_{\theta} - z\mathbf{K} : \mathbf{N}\mathbf{D}_{\theta}) d\theta, \tag{A.16}$$

$$dQ = \frac{G_z \mathbf{C}_{\varepsilon} + H_{\text{ori}} \mathbf{D}_{\varepsilon}}{dt} : d\boldsymbol{\varepsilon} + \frac{G_z \mathbf{C}_{\theta} + H_{\text{ori}} \mathbf{D}_{\theta}}{dt} d\theta, \tag{A.17}$$

where

$$G_z := [\xi - \boldsymbol{\sigma} : (\boldsymbol{\alpha}_M - \boldsymbol{\alpha}_A)]\theta + \left[a(1-z) + bz + \left(\frac{B_{\text{sat}}}{\tau} z\varepsilon_0 + \frac{\varepsilon_r^{(\text{sat})}}{\tau} \sigma_{\text{VM}} \right) \exp\left(-\frac{z\varepsilon}{\tau}\right) \right] \text{sgn}(\dot{z}), \tag{A.18}$$

$$H_{\text{ori}} := Yz^2. \tag{A.19}$$

The tangent stiffness and thermal moduli tensors are given by

$$\mathcal{J}_{\sigma\varepsilon} = \mathbf{K} - \mathbf{K} : \mathbf{R} \otimes \mathbf{C}_\varepsilon - z\mathbf{K} : \mathbf{N} \otimes \mathbf{D}_\varepsilon, \quad (\text{A.20})$$

$$\mathcal{J}_{\sigma\theta} = -\mathbf{K} : \mathbf{R}\mathbf{C}_\theta - z\mathbf{K} : \mathbf{N}\mathbf{D}_\theta, \quad (\text{A.21})$$

$$\mathcal{J}_{Q\varepsilon} = \frac{G_z \mathbf{C}_\varepsilon + H_{\text{ori}} \mathbf{D}_\varepsilon}{dt}, \quad (\text{A.22})$$

$$\mathcal{J}_{Q\theta} = \frac{G_z \mathbf{C}_\theta + H_{\text{ori}} \mathbf{D}_\theta}{dt}. \quad (\text{A.23})$$

In the absence of martensite reorientation, one has

$$\mathcal{J}_{\sigma\varepsilon} = \mathbf{K} - \mathbf{K} : \mathbf{R} \otimes \mathbf{C}_\varepsilon, \quad (\text{A.24})$$

$$\mathcal{J}_{\sigma\theta} = -\mathbf{K} : \mathbf{R}\mathbf{C}_\theta \quad (\text{A.25})$$

$$\mathcal{J}_{Q\varepsilon} = \frac{G_z \mathbf{C}_\varepsilon}{dt}, \quad (\text{A.26})$$

$$\mathcal{J}_{Q\theta} = \frac{G_z \mathbf{C}_\theta}{dt}, \quad (\text{A.27})$$

and in the absence of phase transformation,

$$\mathcal{J}_{\sigma\varepsilon} = \mathbf{K} - z\mathbf{K} : \mathbf{N} \otimes \mathbf{D}_\varepsilon, \quad (\text{A.28})$$

$$\mathcal{J}_{\sigma\theta} = -z\mathbf{K} : \mathbf{N}\mathbf{D}_\theta, \quad (\text{A.29})$$

$$\mathcal{J}_{Q\varepsilon} = \frac{H_{\text{ori}} \mathbf{D}_\varepsilon}{dt}, \quad (\text{A.30})$$

$$\mathcal{J}_{Q\theta} = \frac{H_{\text{ori}} \mathbf{D}_\theta}{dt}. \quad (\text{A.31})$$

Appendix B

Mathematical derivations for Chapter 5

For completeness, this section presents a detailed derivation of the key relations that appear in Chapter 5.

B.1 Dimensions of the elastic domain

In Section 5.4, \bar{w}^* and \bar{r}^* are related to the height and radius of the hypercylinder as follows:

$$\begin{cases} \bar{w}^* = \max_{t_1, t_2} \frac{1}{2\sqrt{3}} \|\mathbf{S}_p^{\text{el}}(\mathbf{x}, t_1) - \mathbf{S}_p^{\text{el}}(\mathbf{x}, t_2)\|_{\text{VM}}, \\ \bar{r}^* = \max_{t_3} \frac{1}{\sqrt{3}} \|\mathbf{S}_o^{\text{el}}(\mathbf{x}, t_3) - [-\boldsymbol{\rho}_o^*(\mathbf{x})]\|_{\text{VM}}, \end{cases} \quad (\text{B.1})$$

which can be fully expanded into

$$\begin{cases} \bar{w}^* = \max_{t_1, t_2} \frac{1}{2\sqrt{3}} \sqrt{\frac{3}{2} [\mathbf{S}_p^{\text{el}}(\mathbf{x}, t_1) - \mathbf{S}_p^{\text{el}}(\mathbf{x}, t_2)] : [\mathbf{S}_p^{\text{el}}(\mathbf{x}, t_1) - \mathbf{S}_p^{\text{el}}(\mathbf{x}, t_2)]}, \\ \bar{r}^* = \max_{t_3} \frac{1}{\sqrt{3}} \sqrt{\frac{3}{2} \{\mathbf{S}_o^{\text{el}}(\mathbf{x}, t_3) - [-\boldsymbol{\rho}_o^*(\mathbf{x})]\} : \{\mathbf{S}_o^{\text{el}}(\mathbf{x}, t_3) - [-\boldsymbol{\rho}_o^*(\mathbf{x})]\}}. \end{cases} \quad (\text{B.2})$$

The height and radius of the hypercylinder are given by

$$\begin{cases} h = \max_{t_1, t_2} \sqrt{[\mathbf{S}_p^{\text{el}}(\mathbf{x}, t_1) - \mathbf{S}_p^{\text{el}}(\mathbf{x}, t_2)] : [\mathbf{S}_p^{\text{el}}(\mathbf{x}, t_1) - \mathbf{S}_p^{\text{el}}(\mathbf{x}, t_2)]}, \\ r = \max_{t_3} \sqrt{\{\mathbf{S}_o^{\text{el}}(\mathbf{x}, t_3) - [-\boldsymbol{\rho}_o^*(\mathbf{x})]\} : \{\mathbf{S}_o^{\text{el}}(\mathbf{x}, t_3) - [-\boldsymbol{\rho}_o^*(\mathbf{x})]\}}. \end{cases} \quad (\text{B.3})$$

Substituting in Eq. (B.2) then gives

$$\begin{cases} h = 2\sqrt{2}\bar{w}^*, \\ r = \sqrt{2}\bar{r}^*. \end{cases} \quad (\text{B.4})$$

B.2 Material constants

In Section 5.6.1, the material constants were related to fatigue limits. The fatigue criterion given by Eq. (5.48) has four material constants: \bar{a} , \bar{b} , \bar{c} and \bar{b}' , which can be determined from four simple uniaxial fatigue tests.

The fatigue limit in repeated torsion β_0 is the height of the hypercylinder when $z = 0$, $2\bar{b}$ is the maximum height of the hypercylinder in terms of the square root of the second invariant $\sqrt{J_2}$ of the stress deviator. For $T = A_f^0$, Eq. (5.50) gives

$$\beta_0 = 2\bar{b} \Rightarrow \bar{b} = \frac{1}{2}\beta_0. \quad (\text{B.5})$$

Similarly, the maximum radius \bar{c} of the hypercylinder in terms of $\sqrt{J_2}$ is related to the fatigue limit γ_{-1} in alternating torsion at $z = 1$ by the following equation:

$$\bar{c}(z = 1) = \gamma_{-1}. \quad (\text{B.6})$$

The radius of the hypercylinder is then given in terms of z by

$$\bar{c}(z) = z\gamma_{-1}. \quad (\text{B.7})$$

When $z = 0$, the material is fully austenitic. In this case, the elastic domain is a hypersphere of radius \bar{b}' , which is related to β'_{-1} by the relation

$$\bar{b}' = \beta'_{-1}. \quad (\text{B.8})$$

The material constant \bar{a} can be obtained from a fully reversed bending test. In this case, using $\bar{v}^* = \frac{1}{\sqrt{3}}\alpha_{-1}$ and $P_{\max}(\mathbf{x}) = \frac{1}{3}\alpha_{-1}$, the fatigue criterion (5.48) gives

$$\frac{\frac{1}{\sqrt{3}}\alpha_{-1}}{\bar{b}'} + \bar{a}\frac{1}{3}\alpha_{-1} = 1 \Rightarrow \bar{a} = \frac{3}{\alpha_{-1}} - \frac{\sqrt{3}}{\bar{b}'}, \quad (\text{B.9})$$

combined with Eq. (B.8) leads to

$$\bar{a} = \frac{3}{\alpha_{-1}} - \frac{\sqrt{3}}{\beta'_{-1}}. \quad (\text{B.10})$$

Bibliography

- Andani, M. and Elahinia, M. (2014). [A rate dependent tension–torsion constitutive model for superelastic nitinol under non-proportional loading; a departure from von Mises equivalency](#). *Smart Materials and Structures*, 23(1):015012.
- Andreasen, G. and Hilleman, T. (1971). [An Evaluation of 55 Cobalt Substituted Nitinol Wire for Use in Orthodontics](#). *The Journal of the American Dental Association*, 82(6):1373–1375.
- Arghavani, J., Auricchio, F., Naghdabadi, R., Reali, A., and Sohrabpour, S. (2010). [A 3-D phenomenological constitutive model for shape memory alloys under multiaxial loadings](#). *International Journal of Plasticity*, 26(7):976–991.
- ASTM F2477-07 (2013). [Standard test methods for in vitro pulsatile durability testing of vascular stents](#). ASTM International, West Conshohocken, PA.
- Auricchio, F., Bonetti, E., Scalet, G., and Ubertini, F. (2014). [Theoretical and numerical modeling of shape memory alloys accounting for multiple phase transformations and martensite reorientation](#). *International Journal of Plasticity*, 59:30–54.
- Auricchio, F., Constantinescu, A., Menna, C., and Scalet, G. (2016). [A shakedown analysis of high cycle fatigue of shape memory alloys](#). *International Journal of Fatigue*, 87:112–123.
- Auricchio, F., Marfia, S., and Sacco, E. (2003). [Modelling of SMA materials: Training and two way memory effects](#). *Computers & Structures*, 81(24–25):2301–2317.
- Ballard, P., Dang Van, K., Deperrois, A., and Papadopoulos, I. (1995). [High cycle fatigue and a finite element analysis](#). *Fatigue & Fracture of Engineering Materials and Structures*, 2(3):397–411.
- Bo, Z. and Lagoudas, D. (1999). [Thermomechanical modeling of polycrystalline SMAs under cyclic loading Part III: evolution of plastic strains and two-way shape memory effect](#). *International Journal of Engineering Science*, 37(9):1175–1203.
- Bodaghi, M., Damanpack, A., Aghdam, M., and Shakeri, M. (2013). [A phenomenological SMA model for combined axial–torsional proportional/non-proportional loading conditions](#). *Materials Science and Engineering: A*, 587(0):12–26.
- Boisse, P., Bussy, P., and Ladeveze, P. (1990). [A new approach in non-linear mechanics: The large time increment method](#). *International Journal for Numerical Methods in Engineering*, 29(3):647–663.
- Bonsignore, C. (2003). [A decade of evolution in stent design](#). In *Proceedings of the International Conference on Shape Memory and Superelastic Technologies*, pages 519–528.
- Bouvet, C., Calloch, S., and LExcellent, C. (2002). [Mechanical behavior of a Cu-Al-Be shape memory alloy under multiaxial proportional and nonproportional loadings](#). *Journal of Engineering Materials and Technology*, 124(2):112–124.

- Bouvet, C., Calloch, S., and Lexcellent, C. (2004). [A phenomenological model for pseudoelasticity of shape memory alloys under multiaxial proportional and nonproportional loadings](#). *European Journal of Mechanics - A/Solids*, 23(1):37–61.
- Chemisky, Y., Duval, A., Patoor, E., and Ben Zineb, T. (2011). [Constitutive model for shape memory alloys including phase transformation martensitic reorientation and twins accommodation](#). *Mechanics of Materials*, 43(7):361–376.
- Dang Van, K. (1973). [Sur la résistance à la fatigue des métaux](#). *Sciences et Techniques de l'Armement : Mémorial de l'Artillerie Française*, pages 647–722.
- Dang Van, K. (2002). [Application of shakedown theory to fatigue analysis of structures](#). In *Inelastic Behaviour of Structures under Variable Repeated Loads*, volume 432 of *International Centre for Mechanical Sciences*, pages 377–393. Springer Vienna.
- Danpinid, A., Luo, J., Vappou, J., Terdtoon, P., and Konofagou, E. (2010). [In vivo characterization of the aortic wall stress-strain relationship](#). *Ultrasonics*, 50(7):654–665.
- Dordoni, E., Meoli, A., Wu, W., Dubini, G., Migliavacca, F., Pennati, G., and Petrini, L. (2014). [Fatigue behaviour of Nitinol peripheral stents: the role of plaque shape studied with computational structural analyses](#). *Medical Engineering & Physics*, 36(7):842–9.
- Dordoni, E., Petrini, L., Wu, W., Migliavacca, F., Dubini, G., and Pennati, G. (2015). [Computational modeling to predict fatigue behavior of NiTi stents: What do we need?](#) *Journal of Functional Biomaterials*, 6(2):299–317.
- Duerig, T., Pelton, A., and Stöckel, D. (1999). [An overview of nitinol medical applications](#). *Materials Science and Engineering: A*, 273-275:149–160.
- Duerig, T., Tolomeo, D., and Wholey, M. (2000). [An overview of superelastic stent design](#). *Minimally Invasive Therapy & Allied Technologies*, 9(3-4):235–246.
- Duerig, T. and Wholey, M. (2002). [A comparison of balloon- and self-expanding stents](#). *Minimally Invasive Therapy & Allied Technologies*, 11(4):173–8.
- Dunić, V., Busarac, N., Slavković, V., Rosić, B., Niekamp, R., Matthies, H., Slavković, R., and Živković, M. (2016). [A thermo-mechanically coupled finite strain model considering inelastic heat generation](#). *Continuum Mechanics and Thermodynamics*, 28(4):993–1007.
- Dunić, V., Pieczyska, E., Tobushi, H., Staszczak, M., and Slavković, R. (2014). [Experimental and numerical thermo-mechanical analysis of shape memory alloy subjected to tension with various stress and strain rates](#). *Smart Materials and Structures*, 23(5):055026.
- Eggeler, G., Hornbogen, E., Yawny, A., Heckmann, A., and Wagner, M. (2004). [Structural and functional fatigue of NiTi shape memory alloys](#). *Materials Science and Engineering: A*, 378(1-2):24–33.
- Feng, X. and Sun, Q. (2007). [Shakedown analysis of shape memory alloy structures](#). *International Journal of Plasticity*, 23(2):183–206.
- Funakubo, H., editor (1987). *Shape memory alloys*. Gordon and Breach Science Publishers, New York.
- Gong, X., Pelton, A., Duerig, T., Rebelo, N., and Perry, K. (2003). [Finite element analysis and experimental evaluation of superelastic Nitinol stent](#). In *SMST-2003 Proceedings of the International Conference on Shape Memory and Superelastic Technologies*, pages 453–462, Pacific Grove, CA.
- Grabe, C. and Bruhns, O. (2008). [On the viscous and strain rate dependent behavior of polycrystalline NiTi](#). *International Journal of Solids and Structures*, 45(7–8):1876–1895.

- Grabe, C. and Bruhns, O. (2009). [Path dependence and multiaxial behavior of a polycrystalline NiTi alloy within the pseudoelastic and pseudoplastic temperature regimes](#). *International Journal of Plasticity*, 25(3):513–545.
- Gu, L., Zhao, S., and Froemming, S. (2012). [Arterial wall mechanics and clinical implications after coronary stenting: Comparisons of three stent designs](#). *International Journal of Applied Mechanics*, 04(02):1250013.
- Gu, X., Zaki, W., Morin, C., Moumni, Z., and Zhang, W. (2015). [Time integration and assessment of a model for shape memory alloys considering multiaxial nonproportional loading cases](#). *International Journal of Solids and Structures*, 54:82–99.
- Halphen, B. and Nguyen, Q. S. (1974). [Plastic and visco-plastic materials with generalized potential](#). *Mechanics Research Communications*, 1(1):43–47.
- Hartl, D., Chatzigeorgiou, G., and Lagoudas, D. (2010). [Three-dimensional modeling and numerical analysis of rate-dependent irrecoverable deformation in shape memory alloys](#). *International Journal of Plasticity*, 26(10):1485–1507.
- Hartl, D., Lagoudas, D., and Calkins, F. (2011). [Advanced methods for the analysis design and optimization of SMA-based aerostructures](#). *Smart Materials and Structures*, 20(9):094006.
- Hartl, D., Lagoudas, D., Calkins, F., and Mabe, J. (2009a). [Use of a Ni60Ti shape memory alloy for active jet engine chevron application: I. Thermomechanical characterization](#). *Smart Materials and Structures*, 19(1):015020.
- Hartl, D., Mooney, J., Lagoudas, D., Calkins, F., and Mabe, J. (2009b). [Use of a Ni60Ti shape memory alloy for active jet engine chevron application: II. Experimentally validated numerical analysis](#). *Smart Materials and Structures*, 19(1):015021.
- Hazar, S., Zaki, W., Moumni, Z., and Anlas, G. (2015). [Modeling of steady-state crack growth in shape memory alloys using a stationary method](#). *International Journal of Plasticity*, 67:26–38.
- He, Y. and Sun, Q. (2010). [Frequency-dependent temperature evolution in NiTi shape memory alloy under cyclic loading](#). *Smart Materials and Structures*, 19(11):115014.
- Hornbogen, E. (2004). [Review thermo-mechanical fatigue of shape memory alloys](#). *Journal of Materials Science*, 39(2):385–399.
- Huang, W. (2002). [On the selection of shape memory alloys for actuators](#). *Materials & Design*, 23(1):11–19.
- Jani, J., Leary, M., Subic, A., and Gibson, M. (2014). [A review of shape memory alloy research applications and opportunities](#). *Materials & Design*, 56:1078–1113.
- Kan, Q. and Kang, G. (2010). [Constitutive model for uniaxial transformation ratchetting of super-elastic NiTi shape memory alloy at room temperature](#). *International Journal of Plasticity*, 26(3):441–465.
- Kan, Q., Yu, C., Kang, G., Li, J., and Yan, W. (2016). [Experimental observations on rate-dependent cyclic deformation of super-elastic NiTi shape memory alloy](#). *Mechanics of Materials*, 97:48–58.
- Kang, G., Kan, Q., Qian, L., and Liu, Y. (2009). [Ratchetting deformation of super-elastic and shape-memory NiTi alloys](#). *Mechanics of Materials*, 41(2):139–153.
- Khamdaeng, T., Luo, J., Vappou, J., Terdtoon, P., and Konofagou, E. (2012). [Arterial stiffness identification of the human carotid artery using the stress-strain relationship in vivo](#). *Ultrasonics*, 52(3):402–411.

- Knowles, G. and Bird, R. (2004). [Telescopic wing system](#). *U.S. Patent*, 6834835 B1.
- Koiter, W. (1960). [General theorems for elastic-plastic solids](#). *Progress in Solids Mechanics*, 11:167–221.
- Kutlucinar, I. (2005). [Aircraft with shape memory alloys for retractable landing gear](#). *U.S. Patent*, 6938416 B1.
- Lagoudas, D. and Entchev, P. (2004). [Modeling of transformation-induced plasticity and its effect on the behavior of porous shape memory alloys. Part I: constitutive model for fully dense SMAs](#). *Mechanics of Materials*, 36(9):865–892.
- Langelaar, M. and van Keulen, F. (2007). [Design optimization of shape memory alloy active structures using the R-phase transformation](#). In *The 14th International Symposium on: Smart Structures and Materials & Nondestructive Evaluation and Health Monitoring*, pages 65250W–65250W. International Society for Optics and Photonics.
- Langelaar, M. and van Keulen, F. (2008a). [Modeling of shape memory alloy shells for design optimization](#). *Computers & Structures*, 86(9):955–963.
- Langelaar, M. and van Keulen, F. (2008b). [Sensitivity analysis of shape memory alloy shells](#). *Computers & Structures*, 86(9):964–976.
- Lexcellent, C. and Bourbon, G. (1996). [Thermodynamical model of cyclic behaviour of Ti-Ni and Cu-Zn-Al shape memory alloys under isothermal undulated tensile tests](#). *Mechanics of Materials*, 24(1):59–73.
- Lexcellent, C., Leclercq, S., Gabry, B., and Bourbon, G. (2000). [The two way shape memory effect of shape memory alloys: an experimental study and a phenomenological model](#). *International Journal of Plasticity*, 16(10–11):1155–1168.
- Lim, T. and McDowell, D. (1999). [Mechanical behavior of an Ni-Ti shape memory alloy under axial-torsional proportional and nonproportional loading](#). *Journal of Engineering Materials and Technology*, 121(1):9–18.
- Luong, M. P. (1998). [Fatigue limit evaluation of metals using an infrared thermographic technique](#). *Mechanics of Materials*, 28(1):155 – 163.
- Mahtabi, M., Shamsaei, N., and Mitchell, M. (2015). [Fatigue of Nitinol: The state-of-the-art and ongoing challenges](#). *Journal of the Mechanical Behavior of Biomedical Materials*, 50:228–254.
- Maitournam, H., Pommier, B., and Thomas, J. (2002). [Détermination de la réponse asymptotique d’une structure anélastique sous chargement thermomécanique cyclique](#). *Comptes Rendus Mécanique*, 330(10):703–708.
- Maletta, C., Sgambitterra, E., Furgiuele, F., Casati, R., and Tuissi, A. (2012). [Fatigue of pseudoelastic NiTi within the stress-induced transformation regime: a modified Coffin–Manson approach](#). *Smart Materials and Structures*, 21(11):112001.
- Mehrabi, R., Kadkhodaei, M., and Elahinia, M. (2014). [A thermodynamically-consistent microplane model for shape memory alloys](#). *International Journal of Solids and Structures*, 51(14):2666–2675.
- Melan, E. (1936). [Theorie statisch unbestimmter Systeme](#). *Sitz. Berl. Ak. Wiss.*, 2:45–68.
- Melton, K. and Mercier, O. (1979a). [Fatigue of NiTi thermoelastic martensites](#). *Acta Metallurgica*, 27(1):137–144.

- Melton, K. and Mercier, O. (1979b). [The effect of the martensitic phase transformation on the low cycle fatigue behaviour of polycrystalline NiTi and CuZnAl alloys](#). *Materials Science and Engineering*, 40(1):81–87.
- Meoli, A., Dordoni, E., Petrini, L., Migliavacca, F., Dubini, G., and Pennati, G. (2014). [Computational study of axial fatigue for peripheral nitinol stents](#). *Journal of Materials Engineering and Performance*, 23(7):2606–2613.
- Miyazaki, S., Igo, Y., and Otsuka, K. (1986). [Effect of thermal cycling on the transformation temperatures of TiNi alloys](#). *Acta Metallurgica*, 34(10):2045–2051.
- Miyazaki, S., Mizukoshi, K., Ueki, T., Sakuma, T., and Liu, Y. (1999). [Fatigue life of Ti-50 at. Ni and Ti-40Ni-10Cu at. shape memory alloy wires](#). *Materials Science and Engineering: A*, 273-275:658–663.
- Miyazaki, S., Sugaya, Y., and Otsuka, K. (1989). [Effects of various factors on fatigue life of Ti–Ni alloys](#). In *Proceedings of the MRS International Meeting on Advanced Materials.*, volume 9, pages 251–256.
- Morin, C. (2011). [A comprehensive approach for fatigue analysis of shape memory alloys](#). PhD thesis, Ecole Polytechnique.
- Morin, C., Moumni, Z., and Zaki, W. (2011a). [A constitutive model for shape memory alloys accounting for thermomechanical coupling](#). *International Journal of Plasticity*, 27(5):748–767.
- Morin, C., Moumni, Z., and Zaki, W. (2011b). [Thermomechanical coupling in shape memory alloys under cyclic loadings: Experimental analysis and constitutive modeling](#). *International Journal of Plasticity*, 27(12):1959–1980.
- Morin, C., Moumni, Z., and Zaki, W. (2011c). [Direct numerical determination of the asymptotic cyclic Behavior of pseudoelastic shape memory structures](#). *Journal of Engineering Mechanics*, 137(7):497–503.
- Moumni, Z. (1995). [Sur la modélisation du changement de phase solide : application aux matériaux à mémoire de forme et à l'endommagement fragile partiel](#). PhD thesis, Ecole Nationale des Ponts et Chaussées.
- Moumni, Z., Van Herpen, A., and Riberty, P. (2005). [Fatigue analysis of shape memory alloys: energy approach](#). *Smart Materials and Structures*, 14(5):S287.
- Moumni, Z., Zaki, W., and Maitournam, H. (2009). [Cyclic behavior and energy approach of the fatigue of Shape Memory Alloys](#). *Journal of Mechanics of Materials and Structures*, 4(2):395–411.
- Moumni, Z., Zaki, W., and Nguyen, Q. S. (2008). [Theoretical and numerical modeling of solid–solid phase change: Application to the description of the thermomechanical behavior of shape memory alloys](#). *International Journal of Plasticity*, 24(4):614–645.
- Nguyen, Q. S. (2003). [On shakedown analysis in hardening plasticity](#). *Journal of the Mechanics and Physics of Solids*, 51(1):101–125.
- Nicola, L., Bower, A., Kim, K., Needleman, A., and Van der Giessen, E. (2008). [Multi-asperity contact: A comparison between discrete dislocation and crystal plasticity predictions](#). *Philosophical Magazine*, 88(30-32):3713–3729.
- Oehler, S., Hartl, D., Lopez, R., Malak, R., and Lagoudas, D. (2012). [Design optimization and uncertainty analysis of SMA morphing structures](#). *Smart Materials and Structures*, 21(9):094016.

- Otsuka, K. and Kakeshita, T. (2002). [Science and technology of shape-memory alloys: New developments](#). *MRS Bulletin*, 27(02):91–100.
- Otsuka, K. and Wayman, C., editors (1999). *Shape memory materials*. Cambridge University Press.
- Panico, M. and Brinson, L. (2007). [A three-dimensional phenomenological model for martensite reorientation in shape memory alloys](#). *Journal of the Mechanics and Physics of Solids*, 55(11):2491–2511.
- Papadopoulos, I. (1987). *Fatigue polycyclique des métaux: Une nouvelle approche*. PhD thesis, Ecole Nationale des Ponts et Chaussées.
- Patoor, E., Lagoudas, D., Entchev, P., Brinson, L., and Gao, X. (2006). [Shape memory alloys Part I: General properties and modeling of single crystals](#). *Mechanics of Materials*, 38(5):391–429.
- Peigney, M. (2010). [Shakedown theorems and asymptotic behaviour of solids in non-smooth mechanics](#). *European Journal of Mechanics - A/Solids*, 29(5):784–793.
- Peigney, M. (2014a). [On shakedown of shape memory alloys structures](#). *Annals of Solid and Structural Mechanics*, pages 17–28.
- Peigney, M. (2014b). [On shakedown of shape memory alloys with permanent inelasticity](#). In *11th World Conference on Computational Mechanics, 5th European Conference on Computational Mechanics, 6th European Conference on Computational Fluid Dynamics*, pages 1863–1871, Barcelone, Spain.
- Pelton, A. (2011). [Nitinol fatigue: A review of microstructures and mechanisms](#). *Journal of Materials Engineering and Performance*, 20(4-5):613–617.
- Pelton, A., Huang, G., Moine, P., and Sinclair, R. (2012). [Effects of thermal cycling on microstructure and properties in Nitinol](#). *Materials Science and Engineering: A*, 532:130–138.
- Pelton, A., Schroeder, V., Mitchell, M., Gong, X., Barney, M., and Robertson, S. (2008). [Fatigue and durability of Nitinol stents](#). *Journal of the Mechanical Behavior of Biomedical Materials*, 1(2):153–164.
- Porter, G., Liaw, P., Tiegs, T., and Wu, K. (2001). [Fatigue and fracture behavior of nickel-titanium shape-memory alloy reinforced aluminum composites](#). *Materials Science and Engineering A*, 314(1-2):186–193.
- Robertson, S., Pelton, A., and Ritchie, R. (2012). [Mechanical fatigue and fracture of Nitinol](#). *International Materials Reviews*, 57(1):1–37.
- Runciman, A., Xu, D., Pelton, A., and Ritchie, R. (2011). [An equivalent strain/Coffin–Manson approach to multiaxial fatigue and life prediction in superelastic Nitinol medical devices](#). *Biomaterials*, 32(22):4987–4993.
- Saint-Sulpice, L., Arbab Chirani, S., and Calloch, S. (2009). [A 3D super-elastic model for shape memory alloys taking into account progressive strain under cyclic loadings](#). *Mechanics of Materials*, 41(1):12–26.
- Saleeb, A., Dhakal, B., Dilibal, S., Owusu-Danquah, J., and Padula, S. (2015). [On the modeling of the thermo-mechanical responses of four different classes of NiTi-based shape memory materials using a general multi-mechanism framework](#). *Mechanics of Materials*, 80:67–86.
- Shaw, J. and Kyriakides, S. (1995). [Thermomechanical aspects of NiTi](#). *Journal of Mechanics Physics of Solids*, 43:1243–1281.

- Shiraishi, Y., Yambe, T., Saijo, Y., Sato, F., Tanaka, A., Yoshizawa, M., Ogawa, D., Wada, Y., Itoh, S., Sakata, R., Park, Y., Uematsu, M., Umezu, M., Fujimoto, T., Masumoto, N., Liu, H., Baba, A., Konno, S., Nitta, S., Imachi, K., Tabayashi, K., Sasada, H., and Homma, D. (2007). [Morphological Approach for the Functional Improvement of an Artificial Myocardial Assist Device using Shape Memory Alloy Fibres](#). In *29th Annual International Conference of the IEEE Engineering in Medicine and Biology Society*, pages 3974–3977.
- Simo, J. and Hughes, T. (1998). *Computational inelasticity*, volume 7 of *Interdisciplinary Applied Mathematics*. Springer, New York.
- Siredey-Schwaller, N., Eberhardt, A., and Bastie, P. (2009). [Parameters influencing the fatigue life of a Cu-Al-Be single-crystal shape memory alloy under repeated bending](#). *Smart Materials and Structures*, 18(2):025014.
- Sittner, P., Hara, Y., and Tokuda, M. (1995). [Experimental study on the thermoelastic martensitic transformation in shape memory alloy polycrystal induced by combined external forces](#). *Metallurgical and Materials Transactions A*, 26(11):2923–2935.
- Sofla, A., Meguid, S., Tan, K., and Yeo, W. (2010). [Shape morphing of aircraft wing: Status and challenges](#). *Materials & Design*, 31(3):1284–1292.
- Song, D., Kang, G., Kan, Q., Yu, C., and Zhang, C. (2014). [Non-proportional multiaxial transformation ratchetting of super-elastic NiTi shape memory alloy: Experimental observations](#). *Mechanics of Materials*, 70:94 – 105.
- Stebner, A. and Brinson, L. (2013). [Explicit finite element implementation of an improved three dimensional constitutive model for shape memory alloys](#). *Computer Methods in Applied Mechanics and Engineering*, 257(0):17–35.
- Strelec, J., Lagoudas, D., Khan, M., and Yen, J. (2003). [Design and Implementation of a Shape Memory Alloy Actuated Reconfigurable Airfoil](#). *Journal of Intelligent Material Systems and Structures*, 14(4-5):257–273.
- Tabanli, R., Simha, N., and Berg, B. (1999). [Mean stress effects on fatigue of NiTi](#). *Materials Science and Engineering: A*, 273-275:644–648.
- Tanaka, K., Nishimura, F., Hayashi, T., Tobushi, H., and Lexcellent, C. (1995). [Phenomenological analysis on subloops and cyclic behavior in shape memory alloys under mechanical and/or thermal loads](#). *Mechanics of Materials*, 19(4):281–292.
- Van Humbeeck, J. (1999). [Non-medical applications of shape memory alloys](#). *Materials Science and Engineering: A*, 273-275:134–148.
- Xia, Z., Ju, F., and Sasaki, K. (2007). [A general finite element analysis method for balloon expandable stents based on repeated unit cell RUC model](#). *Finite Elements in Analysis and Design*, 43(8):649–658.
- Yin, H., He, Y., and Sun, Q. (2014). [Effect of deformation frequency on temperature and stress oscillations in cyclic phase transition of NiTi shape memory alloy](#). *Journal of the Mechanics and Physics of Solids*, 67:100–128.
- Yu, C., Kang, G., and Kan, Q. (2014). [A physical mechanism based constitutive model for temperature-dependent transformation ratchetting of NiTi shape memory alloy: One-dimensional model](#). *Mechanics of Materials*, 78:1–10.

- Yu, C., Kang, G., Kan, Q., and Song, D. (2013). [A micromechanical constitutive model based on crystal plasticity for thermo-mechanical cyclic deformation of NiTi shape memory alloys](#). *International Journal of Plasticity*, 44:161–191.
- Yu, C., Kang, G., Kan, Q., and Zhu, Y. (2015). [Rate-dependent cyclic deformation of super-elastic NiTi shape memory alloy: Thermo-mechanical coupled and physical mechanism-based constitutive model](#). *International Journal of Plasticity*, 72:60–90.
- Zaki, W. (2010). [An approach to modeling tensile–compressive asymmetry for martensitic shape memory alloys](#). *Smart Materials and Structures*, 19(2):025009.
- Zaki, W. (2012a). [An efficient implementation for a model of martensite reorientation in martensitic shape memory alloys under multiaxial nonproportional loading](#). *International Journal of Plasticity*, 37:72–94.
- Zaki, W. (2012b). [Time integration of a model for martensite detwinning and reorientation under nonproportional loading using Lagrange multipliers](#). *International Journal of Solids and Structures*, 49(21):2951–2961.
- Zaki, W. and Moumni, Z. (2007a). [A 3D model of the cyclic thermomechanical behavior of shape memory alloys](#). *Journal of the Mechanics and Physics of Solids*, 55(11):2427–2454.
- Zaki, W. and Moumni, Z. (2007b). [A three-dimensional model of the thermomechanical behavior of shape memory alloys](#). *Journal of the Mechanics and Physics of Solids*, 55(11):2455–2490.
- Zaki, W., Moumni, Z., and Morin, C. (2011). [Modeling Tensile-Compressive Asymmetry for Superelastic Shape Memory Alloys](#). *Mechanics of Advanced Materials and Structures*, 18(7):559–564.
- Zaki, W., Zamfir, S., and Moumni, Z. (2010). [An extension of the ZM model for shape memory alloys accounting for plastic deformation](#). *Mechanics of Materials*, 42(3):266–274.
- Zhang, Y., Zhu, J., Moumni, Z., Van Herpen, A., and Zhang, W. (2016). [Energy-based fatigue model for shape memory alloys including thermomechanical coupling](#). *Smart Materials and Structures*, 25(3):035042.
- Zheng, L., He, Y., and Moumni, Z. (2016). [Lüders-like band front motion and fatigue life of pseudoelastic polycrystalline NiTi shape memory alloy](#). *Scripta Materialia*, 123:46–50.
- Zider, R. and Krumme, J. (1990). [Eyeglass frame including shape-memory elements](#). *U.S. Patent*, 4896955 A.

Titre : Optimisation structurale vis-à-vis de la fatigue des structures en alliages à mémoire de forme.

Mots clés : alliages à mémoire de forme, fatigue polycyclique, optimisation structurale, modèle constitutif, chargement non proportionnel, couplage thermomécanique, comportement cyclique.

Résumé : Cette thèse présente une approche globale d'optimisation vis-à-vis de la fatigue des matériaux et structures en alliages à mémoire de forme (AMF). Cette approche s'articule en trois étapes : i) Le développement d'une loi de comportement capable de prédire la réponse thermomécanique à l'état stabilisé d'une structure en AMF sous chargement cyclique multiaxial non proportionnel. On prend notamment en compte la dépendance de la déformation résiduelle par rapport à la température. Par ailleurs, la méthode LATIN à grand incrément de temps a été généralisée pour les AMF dans le cadre du modèle ZM. Ceci permet de résoudre les problèmes de convergence numérique rencontrés lorsque le processus de transformation de phase se produit avec une pente du plateau de transformation faible. ii) Le développement d'un critère de fatigue à grand nombre de cycles pour les AMF. Ce critère s'inscrit dans le cadre de la théorie d'adaptation à l'instar du critère de Dang Van pour les métaux élasto-plastiques. Le critère proposé permet de calculer en chaque point de la structure en AMF un facteur de fatigue indiquant son degré de dangerosité. iii) Le développement d'une approche d'optimisation structurale qui peut être utilisée pour améliorer la durée de vie en fatigue prédite par le critère proposé dans la deuxième partie. Des exemples numériques sont traités pour valider chaque étape. L'approche globale a par ailleurs été testée et validée pour l'optimisation structurale d'un stent.

Title : Optimization of Shape Memory Alloy Structures with Respect to Fatigue

Keywords : shape memory alloys, high-cycle fatigue, structural optimization, nonproportional loading, thermomechanical coupling, cyclic loading.

Abstract : This thesis presents a comprehensive and efficient structural optimization approach for shape memory alloys (SMAs) with respect to fatigue. The approach consists of three steps: First, the development of a suitable constitutive model capable of predicting, with good accuracy, the stabilized thermomechanical stress state of a SMA structure subjected to multiaxial nonproportional cyclic loading. The dependence of the saturated residual strain on temperature and loading rate is discussed. In order to overcome numerical convergence problems in situations where the phase transformation process presents little or no positive hardening, the large time increment method (LATIN) is utilized in combination with the ZM (Zaki-Moumni) model to simulate SMA structures instead of conventional incremental methods. Second, a shakedown-based fatigue criterion analogous to the Dang Van model for elastoplastic metals is derived for SMAs to predict whether a SMA structure subjected to high-cycle loading would undergo fatigue. The proposed criterion computes a fatigue factor at each material point, indicating its degree of safeness with respect to high-cycle fatigue. Third, a structural optimization approach, which can be used to improve the fatigue lifetime estimated using the proposed fatigue criterion is presented. The prospects of this work include the validation of the optimization approach with experimental data.